Alignment Properties of PBLG investigated by Rheo-NMR and their Application to Structure Determination

Zur Erlangung des akademischen Grades eines

Doktors der Naturwissenschaften

(Dr. rer. nat.)

von der KIT-Fakultät für Chemie-und Biowissenschaften des
Karlsruher Instituts für Technologie (KIT)
genehmigte
Dissertation

von
M.Sc. Fabian Michael Hoffmann
aus Schwenningen a.N.

Tag der mündlichen Prüfung: 17. Juli 2025
1. Referent: Prof. Dr. Burkhard Luy
2. Referentin: apl. Prof. Dr. Gisela Guthausen

Eidesstattliche Erklärung

Bei der eingereichten Dissertation zum Thema

Alignment Properties of PBLG investigated by Rheo-NMR and their Application to Structure Determination

handelt es sich um meine eigenständig erbrachte Leistung. Ich habe nur die angegebenen Quellen und Hilfsmittel benutzt und mich keiner unzulässigen Hilfe Dritter bedient. Insbesondere habe ich wörtlich oder singgemäß aus anderen Werken übernommene Inhalte als solche kenntlich gemacht. Die Arbeit oder Teile davon habe ich bislang nicht an einer anderen Hochschule des In- oder Auslands als Bestandteil einer Prüfungs- oder Qualifikationsleistung vorgelegt. Die Richtigkeit der vorstehenden Erklärung bestätige ich. Die Bedeutung der eidesstattlichen Versicherung und die strafrechtlichen Folgen einer unrichtigen oder unvollständigen eidesstattlichen Versicherung sind mir bekannt.

Ich versichere an Eides statt, dass ich nach dem besten Wissen die reine Wahrheit erklärt und nichts verschwiegen habe.

Karlsruhe, 04.06.2025

Ort, Datum

Fabian Michael Hoffmann

List of publications

1. **Hoffmann, F.M.**; Kouril, K.; Berger, S.T.; Meier, B.; Luy, B., "Rheo-NMR at the Phase Transition of Liquid Crystalline Poly-γ-benzyl-L-glutamate: Phase Kinetics and a Valuable Tool for the Measurement of Residual Dipolar Couplings". *Macromolecules* **2023**, *56*, 7782-7794.

2. **Hoffmann, F.M.**; Leistner, A.-L.; Kirchner, S.; Luy, B.; Muhle-Goll, C.; Pianowski, Z., "Cargo Encapsulation in Photochromic Supramolecular Hydrogels Depends on Specific Guest-Gelator Supramolecular Interactions". *Eur. J. Org. Chem.* **2023**, 26.
The topic of this publication is not part of this thesis.

3. Ferraro, V.; **Hoffmann, F.M.**; Fuhr, O.; Luy, B.; Bräse, S., "2,1,3-Benzoselenadiazole as Mono- and Bidentate N-Donor for Heteroleptic Cu(I) Complexes: Synthesis, Characterization and Photophysical Properties". *Inorganics* **2024**, *12*, 201.
The topic of this publication is not part of this thesis.

4. Krause, F.; Moser, C.; Elsing, D.; Silber, M.; **Hoffmann, F.M.**; Woordes, Y.T.; Luy, B.; Muhle-Goll, C., "Mutations alter conformations and dynamics of APP-TMDs - an RDC analysis". *Chem. Eur. J.* **2025**, *accepted.*
The topic of this publication is not part of this thesis.

5. **Hoffmann, F.M.**; Luy, B., "The Transition State of PBLG Studied by Deuterium NMR", *Polymers* **2025**, *17*, 3280.
Also available as preprint at ChemRxiv under 10.26434/chemrxiv-2025-wdl2n

Acknowledgements

Ich möchte mich bei allen Personen bedanken, die mich in den letzten Jahren begleitet und tatkräftig unterstützt haben, allen voran Prof. Dr. Burkhard Luy, der mich in seinen Arbeitskreis aufgenommen hat, mir die Welt der NMR gezeigt hat, mir große Unterstützung während meiner Promotion gegeben hat, und viele meiner Fragen beantwortet hat.

Darüber hinaus gilt ein großer Dank PD Dr. Claudia Muhle-Goll, ebenfalls für die Aufnahme in den Arbeitskreis und zahlreiche Hilfestellungen, wenn ich mal wieder nicht weiterwusste.

Mein Dank gilt Dr. Benno Meier, Dr. Karel Kouril und Dr. Masoud Minaei vor allem für ihr Know-how im Ingenieurs-Bereich ohne den es diese Arbeit nicht gegeben hätte. Aber auch für jeder Zeit ein offenes Ohr, wenn ich auch hier Fragen hatte.

Zudem möchte ich bei Prof. Dr. Manfred Wilhelm und Dr. Christopher Klein für die Zusammenarbeit der rheologischen Messungen bedanken, sowie bei Prof. Dr. Gisela Guthausen für die Zusammenarbeit bei den Image-Messungen.

Ein großer Dank gilt dem gesamten und Team des IBG-4, sowie den ehemaligen Mitgliedern, für viele schöne Stunden beim Mittagessen, Kaffee oder sonstigen Aktivitäten. Ganz besonders gilt mein Dank hier Dr. Jens Haller für tatkräftige Unterstützung, Dr. Celine Moser, die gemeinsam mit mir immer wieder verzweifelt ist und Yannik Woordes, der mir gerade in der letzten Zeit sehr geholfen hat.

Zum Schluss möchte mich noch bei meiner gesamten Familie bedanken, die mich über viele Jahre unterstützt haben und ohne die ich nicht bis zu diesem Punkt gelangt wäre. Genauso gilt der Dank meinen Freunden, die gerade die Zeit im und um das Studium, sowie der Promotion mit vielen guten Erinnerungen versehen haben. Doch der größte Dank gilt meiner Partnerin, die mich nicht nur mit allen Höhen und Tiefen durch die Promotion begleitet hat, sondern trotz allen Widrigkeiten und Eigenheiten immer für mich da war.

Abstract

The liquid crystal (LC) poly-γ-benzyl-L-glutamate (PBLG) is used for structure determination of small molecules in nuclear magnetic resonance (NMR). Using a self-made rheo-device, it changes the orientation of its alignment director by shear forces, thereby reducing signal width and increasing signal intensity. Most interestingly, under shear the phase transition from isotropic to the anisotropic liquid crystalline phases disappears, and anisotropic parameters such as residual dipolar couplings (RDCs) and residual chemical shift anisotropy (RCSA) are measurable at concentrations down to 1 wt% of PBLG, which provides far better spectral quality and opens novel types of applications.

The self-built rheo-device with Couette geometry, which was optimized in the course of this work, consists of a rotating 3 mm NMR tube inside a 5 mm NMR tube controlled by self-written pulse programs. Its shear force tilts the alignment director from 0° to 75-90° with respect to the magnetic field and also aligns seemingly isotropic PBLG solutions around the same angle Θ_D of 75-90°. The alignment strength of PBLG above its critical concentration is reduced by the factor $(3\cos^2\Theta_D - 1)/2$, resulting in a decrease of the quadrupolar splitting of deuterochloroform ($CDCl_3$) of approximately -0.5, for which the sign change of the quadrupolar splitting was confirmed with a Q.E.COSY experiment. The kinetics of the times required for the director to either align with the shear plane or relax back parallel to the magnetic field were studied for different concentrations of PBLG controlling both spectrometer pulses and shearing with explicit pulse programming. The shear rates used in this work were in a range between 408.4 and 896.6 s^{-1}.

Using the highest shear rate of 896.6 s^{-1}, RDCs and RCSA of strychnine under shear were obtained for different concentrations of PBLG, showing a significant decrease in signal width and increase in signal intensity under shear. At concentrations below the transition region, the spectral quality under shear was better than at higher concentrations, and measurement time was shortened by a factor of three. Most importantly, new ways to determine RDCs and RCSA are demonstrated without the need for an isotropic sample without PBLG as a reference.

Special attention was paid to concentrations of PBLG right at the LC phase transition. An unambiguously identified biphasic concentration range was characterized under static conditions with dilution and kinetic studies. The kinetic studies show the time required by the alignment director to fully align parallel to the magnetic field for different proportions of isotropic and anisotropic phases, and the dilution studies are used to discuss the influence of small solute molecules on PBLG. Furthermore, a biphasic sample containing the solute molecule strychnine shows simultaneous isotropic J-couplings and anisotropic T-couplings, where the isotropic and anisotropic ^{13}C chemical shifts can be distinguished, leading to direct RCSA measurements in a single sample without the need of an additional reference. Nevertheless, the sample contained tetramethylsilane (TMS), which showed no evidence of RDCs and RCSA within the obtained linewidth of 1 Hz.

In summary, PBLG shows very interesting properties at and below the isotropic-to-LC phase transition. With the rheo-device, the LC PBLG can be aligned in a magnetic field below the critical concentration, reducing multiplet and signal widths and increasing signal intensities, which is particularly useful for small molecule structure determination using RDCs and RCSA. Together with new findings on the phase transition of PBLG, rheo-NMR of LCs appears to be a new method for tunable alignment strength that is competitive with the elaborately prepared stretched polymer gels and less costly than variable-angle sample spinning (VASS).

Zusammenfassung

Der Flüssigkristall Poly-γ-benzyl-L-glutamate (PBLG) wird in der magnetischen Kernresonanz (NMR) für Strukturbestimmung genutzt. Scherkräfte eines selbstgebauten Rheo-Apparat ändern die Orientierung seines Alignmentdirektors, wodurch die Signalbreite verringert und die Signalintensität erhöht wird. Interessanterweise verschwindet der Phasenübergang von der isotropen zur anisotropen, flüssigkristallinen Phase während der Scherung, und anisotrope Parameter wie dipolare Restkopplungen (RDCs) sowie die Restanisotropie der chemischen Verschiebung (RCSA) können für PBLG-Konzentrationen bis zu 1 wt% gemessen werden, wodurch eine deutlich bessere Qualität der Spektren erzeugt wird und neue Applikationen eröffnet werden.

Die selbstgebaute Rheo-Apparatur mit Couette-Geometrie, der im Verlauf dieser Arbeit weiter optimiert wurde, besteht aus einem rotierendem 3 mm NMR-Röhrchen innerhalb eines 5 mm NMR-Röhrchens, welches durch selbstgeschriebene Pulsprogramme gesteuert wird. Die Scherkräfte dieser Apparatur neigen den Alignmentdirektor von 0° zu 75-90° in Bezug auf das Magnetfeld und richten scheinbar auch isotrope PBLG-Flüssigkeiten entlang des Winkels Θ_D (75-90°) aus. Die Stärke des Alignments von PBLG oberhalb der kritischen Konzentration wird mit dem Faktor $(3\cos^2\Theta_D - 1)/2$ verringert, wodurch die quadrupolare Aufspaltung von Deuterochloroform ($CDCl_3$) um ungefähr den Faktor -0.5 verringert wird. Der Vorzeichenwechsel wurde mit einem Q.E.COSY-Experiment bestätigt. Die Kinetik des zeitlichen Verlaufs, die der Alignmentdirektor benötigt um sich entweder entlang der Scherebene oder zurück parallel zum Magnetfeld auszurichten, wurde für verschiedene PBLG-Konzentrationen bestimmt. Hierbei wurden Spektrometerpulse und die Scherung mit explizit programmierten Pulsprogrammen kontrolliert. Die in dieser Arbeit genutzten Scherraten lagen zwischen 404.4 und 896.6 s^{-1}.

RDCs und RCSA von Strychnin wurden mit der höchsten Scherrate von 896.6 $^{-1}$ für verschiedene PBLG-Konzentrationen gemessen, wodurch die Signalbreite während der Scherung deutlich abnahm und die Signalintensität erhöht wurde. Für Konzentrationen unterhalb des Phasenübergangs war die Qualität der Spektren höher als für Konzentrationen oberhalb des Übergangs und die Messzeit konnte um das Dreifache reduziert werden. Am wichtigsten sind jedoch die neuen Möglichkeiten, mit denen RDCs und RCSA ohne PBLG-freie, isotrope Proben gemessen werden können.

Besondere Beachtung wurde PBLG-Konzentration direkt am Phasenübergang geschenkt und eine eindeutig biphasischer Konzentrationsbereich wurde unter statischen Bedingungen mit Verdünnungsreihen und kinetischen Studien charakterisiert. Die kinetischen Studien zeigen den zeitlichen Verlauf, die der Alignmentdirektor für verschiedene Anteile von isotroper und anisotroper Phase benötigt, um vollständig parallel zum Magnetfeld ausgerichtet zu werden, und die Verdünnungsreihen wurden genutzt um den Einfluss kleiner Moleküle auf PBLG zu diskutieren. Darüber hinaus zeigt eine biphasische Probe mit dem kleinen Molekül Strychnin gleichzeitig isotrope J-Kopplungen und anisotrope T-Kopplungen, wodurch isotrope und anisotrope ^{13}C chemische Verschiebungen unterschieden werden konnten und RCSA direkt in einer einzigen Probe ohne zusätzliche Referenz gemessen werden konnte. Diese Probe beinhaltete zusätzlich Tetramethylsilan (TMS), welches innerhalb der erhaltenen Linienbreite von 1 Hz keine Anzeichen von RDCs oder RCSA zeigte.

Zusammenfassend lässt sich sagen, dass PBLG am und unter dem Phasenübergang von isotroper zu flüssigkristalliner Phase sehr interessante Eigenschaften aufweist. Der Flüssigkristall PBLG kann

mit einer Rheo-Apparatur unterhalb der kritischen Konzentration in einem Magnetfeld ausgerichtet werden, wodurch Mulitplett- und Signalbreiten reduziert werden, sowie Signalintensitäten erhöht werden. Dies ist besonders nützlich für die Strukturbestimmung von kleinen Molekülen durch RDCs und RCSA. Zusammen mit neuen Entdeckungen am Phasenübergang von PBLG scheint Rheo-NMR von Flüssigkristallen eine neue Methode für einstellbare Alignment-Stärke zu sein, die mit aufwendig hergestellten, gestreckten Polymergelen konkurrieren kann und weniger kostspielig ist als VASS.

Contents

1 Introduction

1.1 Motivation

In the 1940s, the LC PBLG was first synthesized by Hanby et al.[1] in the lab of Ambrose and Elliot (Messrs. Courtaulds LTD, Maidenhead, Berks.)[2] as potential polymer fiber substituting natural fibers such as wools. Since then, it was first used in rheology as a model to determine the shear behavior of LCs. The rigid rods of this α-helical polymer do not only align under shear stress[3–6], but also in magnets, with the director parallel to the magnetic field[7,8].

The alignment in magnetic fields of PBLG depends on its concentration. At lower concentrations, PBLG does not align in magnetic fields and the sample appears to behave like an isotropic liquid. At the transition from isotropic to anisotropic LC phase, a range of approximately 0.5 wt% has been reported in which isotropic and anisotropic phases coexist. In NMR, the alignment above the critical concentration is used to induce partial alignment of the solute molecules, resulting in anisotropy in the solute molecules. Couplings such as RDCs, residual quadrupolar couplings (RQCs) and RCSA, which average to zero in isotropic solutions, are measurable in the anisotropic environment. These anisotropic parameters contain important structural information about the solute molecules, providing a better insight into their structure and dynamics of the molecules. The great advantage of PBLG compared to most other LCs is, together with its enantiomeric pair poly-γ-benzyl-D-glutamate (PBDG) that it can distinguish between enantiomers[9,10].

Despite their great benefits as an alignment medium, PBLG and PBDG require a high molecular weight and relatively high concentrations of at least 9 wt% for anisotropic solutions in which the director is oriented with the magnetic field. Therefore, the partial alignment is strong compared to other alignment media such as stretched polymer gels[11,12], often resulting in large multiplet widths for protons decreasing the overall signal width. However, its use in enantiodiscrimination led to numerous developments that increased the signal width for protons or detected atomic nuclei other than protons, which are less affected by the multiplet widths.
One of these developments was VASS first introduced by Courtieu et al. in 1982[13]. The LC was spun around an arbitrary angle between 0° and 90°, which reduces the anisotropic parameters to zero. Then, the alignment director rotates around the same angle Θ_D with respect to the magnetic field and the alignment strength is scaled by the factor $(3\cos^2\Theta_D - 1)/2$. The Thiele group[14] showed the influence of the tilt angle on a PBLG sample in $CDCl_3$ with strychnine and obtained various data sets for different angles, all of which are scalable with the quadrupolar coupling of $CDCl_3$. All spectra obtained showed less broadend multiplet widths.

8 years later[15], a new technique was introduced to theoretically change the alignment director perpendicular to the magnetic field. By combining rheology with NMR (called *rheo-NMR*), it was possible to change the director angle by shear force into the shear plane. In practice, the obtained director angle is in equilibrium between the magnetic force pulling parallel to the magnetic field and the shear force acting perpendicular to the magnetic field[16,17]. Nowadays, this technique is mainly used in imaging and velocimetry experiments to monitor the structural changes of polymers including even biologically important proteins[18,19] or to measure the responses of complex fluids[20–22] under shear stress.

The change in the director due to shear force can also be used for LCs, which reduces their alignment strength similar to VASS at angles almost perpendicular to the magnetic field. In addition, the anisotropic parameters of small solute molecules under shear are reduced, which will be investigated in this work. Hence, a rheo-device was built based on the model of Paul T. Callaghan[23]. The used rheo-device in this work is a Couette cell type, where a 3 mm NMR tube is rotating a sample inside a 5 mm NMR tube with motor frequencies up to 50 Hz corresponding to shear rates up to 896.6 s^{-1}. With this rheo-device, PBLG in $CDCl_3$ is to be aligned perpendicular to the magnetic field reducing the alignment strength by the factor $(3\cos^2\Theta_D - 1)/2$. The effects of the shear force on different concentrations of PBLG as well as kinetic studies of the switching times of the alignment director into the shear-plane and back parallel to the magnetic field shall be investigated. Subsequently, the effects on RDCs and RCSA with strychnine as a small solute molecule will be determined. Strychnine was selected because of its comparability with the earlier work of the Thiele group[14] and for its large number of couplings, which are sometimes very large under static alignment conditions with PBLG and therefore a reduction of these has a significant effect.

The phase transition of PBLG, in which the isotropic PBLG phase changes into anisotropy without shear force, will be studied in detail. In addition to a characterization by deuterium NMR methods, the influence of solute molecules on the phase transition and the effect of the phase transition on RDCs and RCSA will be measured.

2 Theory

2.1 NMR

The origin of NMR goes back to the year 1938 where the group of I. Rabi[24] observed the resonance peaks of Li and Cl in a beam of LiCl molecules passing through a magnetic field. A few years later, Purcell, Torrey and Pound in 1945 and Bloch, Hansen and Packard in 1946 detected radio signals from organic compounds. Purcell and co-workers detected the radio-frequency signals from paraffin wax[25] and Bloch with his colleagues from water[26]. All three works were later awarded with the Nobel prize in physics: Isidor Isaac Rabi in 1944[27] and Edward Mills Purcell and Felix Bloch in 1952[28]. Since then, NMR spectroscopy developed significantly in different areas rewarding two more NMR spectroscopists with a Nobel Prize in Chemistry: Richard Robert Ernst in 1991 for high resolution NMR[29,30] and Kurt Wüthrich in 2002 for three dimensional NMR spectroscopy[31,32].

2.1.1 Principle

In NMR, the most important characteristic of an atomic nuclei (*i*) is its spin I with the magnetic momentum μ and the gyromagnetic ratio γ_i

$$\hat{\mu} = \gamma_i \hat{I} \tag{2.1}$$

or as the magnetic field is oriented along z and therefore polarization only occurs along z, Equation 2.1 simplifies to

$$\mu_z = \gamma_i I_z \quad \text{with} \quad I_z = m\hbar \tag{2.2}$$

Inside this magnetic field, the ($2I$+1)-fold degenerated nuclear state of the spin will be split by the *Zeeman effect* (see Fig. 2.1A) in different nuclear spin energy levels. As the usually observed nuclei in NMR are ^{1}H, ^{13}C and ^{15}N with spin 1/2, the energy levels will split in the two eigenstates α and β with

$$E = -\mu_z B^0 = -m\gamma_i \hbar B^0 \tag{2.3}$$

where $m(\alpha)$ = + 1/2, $m(\beta)$ = - 1/2 and $\hbar$ is the reduced Planck constant. The angular momentum then rotates around the direction of the magnetic field (called *precession*) with the *Larmor-frequency* ω^0 (see Fig. 2.1B) and a corresponding energy

$$\Delta E = \hbar\omega^0 \tag{2.4}$$

where ω^0 is proportional to the magnetic field.

$$\omega^0 = \gamma_i B^0 \tag{2.5}$$

With the Boltzmann distribution the number of nuclei in each state can be calculated resulting for a temperature of 300 K and a magnetic field of 18.8 T in a difference of 1.3 out of 10000 spins. This very small difference is enough for a macroscopic magnetization in equilibrium and explains why NMR is so insensitive[33,34]

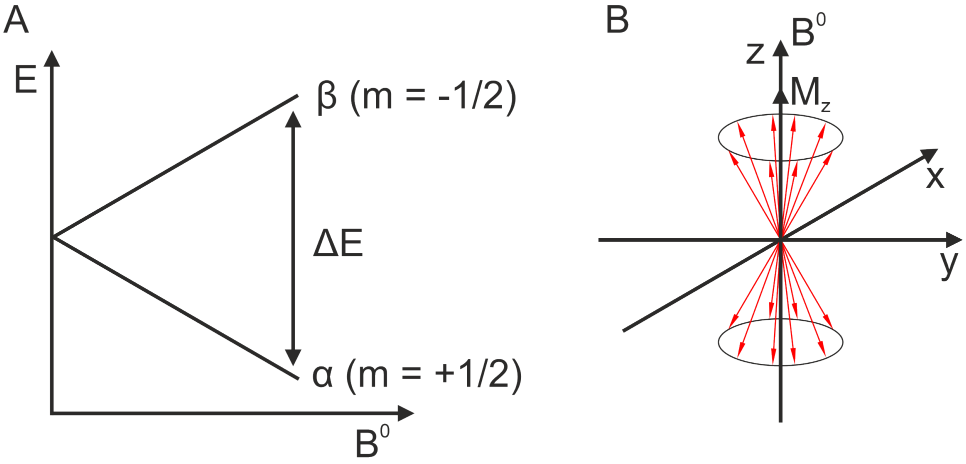

Figure 2.1: A) The Zeeman effect in a magnetic field splits the normally degenerated energy levels into their eigenstates. B) The nuclear spins are rotating around the magnetic field B^0 with the Larmor Frequency ω^0 having pure z-magnetization. (adapted from [33])

As long as the nuclear spins are rotating around B^0, no NMR signal can be measured. Therefore, a pulse with the frequency ω^1 or field B^1 (see Eq. 2.5) which is perpendicular to B^0 is needed resulting in measurable magnetization. A long enough pulse in x-direction excites the nuclei and turns the z-magnetization (M_z) completely into y-magnetization (M_y). Over time, the environment transfers its energy to spins, directing them along z until the full z-magnetization is restored. This time is called the T_1 time, *Spin-Lattice relaxation*, or *longitudinal relaxation*. Then, the magnetization over time can be described with

$$\frac{dM_z(t)}{dt} = -\frac{1}{T_1}\left[M_z(t) - M_z^0\right] \tag{2.6}$$

There is a second relaxation time T_2, called *transverse relaxation* or *spin-spin relaxation* perpendicular to the field. An example for this relaxation are spins interacting with each other in a way that each spin precesses at a slightly different frequency resulting in a dephasing in the x-y plane. This magnetization can not be recovered during the experiment. As T_2 relaxation is directly proportional to the molecular weight, spectra of high molecular weight proteins lack of sensitivity. The transverse magnetization M_{xy} over time is only determined by relaxation, because the precession does not change the value of M_{xy}

$$\frac{M_{xy}(t)}{dt} = -\frac{1}{T_2} M_{xy}(t) \tag{2.7}$$

Both time constants depend on the Larmor frequency and the correlation time τ_c which will be discussed later (see Section 2.1.5)[33–35].

In NMR, only the transverse magnetization is measured because the longitudinal nuclear spin magnetization is too weak and measuring it is impractical. The transverse magnetization oscillates around a well-defined frequency which induces an electric current in a coil with the winding axes perpendicular to the magnetic field. This electric current is the NMR signal called *free-induction decay (FID).* After detection, the FID will be Fourier-transformed and the typical spectrum with peaks at certain frequencies is obtained. With no environmental interference, only one peak in Lorentzian shape would be visible at the Larmor-frequency. Of course, the atomic nuclei always feel interference and the electrons surrounding the nuclei produce small local magnetic fields resulting in a frequency different from the unperturbed Larmor frequency - *the chemical shift* δ. As can be seen in Equation 2.5, the frequency depends on B^0 and the chemical shift δ is defined in parts per million (ppm) via a reference frequency, which typically is the signal of TMS at 0 ppm[33–35].

$$\delta = 10^6 \frac{\omega - \omega_{ref}}{\omega_{ref}} \tag{2.8}$$

2.1.2 Couplings

Before the different kinds of couplings in NMR are explained, a few quantum mechanical basics are needed. First, as Equation 2.2 already shows, the spin angular momentum $\vec{I}$ is direction dependent and can therefore be written as Cartesian operators

$$\hat{\mathbf{I}} = \begin{pmatrix} \hat{I}_x \\ \hat{I}_y \\ \hat{I}_z \end{pmatrix} \quad \text{with} \quad |\hat{\mathbf{I}}| = \hbar\sqrt{I(I+1)} \tag{2.9}$$

and together with the unity operator ($\hat{1}$), they form a complete basis set. Additionally, shift operators which increase ($\hat{I}^+$) or decrease ($\hat{I}^-$) the quantum number are needed for calculations.

$$\hat{I}^+ = \hat{I}_x + i\hat{I}_y \tag{2.10}$$

$$\hat{I}^- = \hat{I}_x - i\hat{I}_y \tag{2.11}$$

Second, the nuclei can interact with their environment in two ways: the electric charge with the electric field and the magnetic moment with the magnetic field which can be written in the spin Hamiltonian operator

$$\hat{\mathcal{H}}_j = \hat{\mathcal{H}}_j^{elec} + \hat{\mathcal{H}}_j^{mag} \tag{2.12}$$

for the nucleus I_j. Hereby, the electric spin Hamiltonian is a superposition of the total electric charge, the electric dipole moment, the electric quadrupolar moment of the nucleus and so on. The total electric charge represents the electrostatic forces between the nuclei and the electrons and is therefore of no direct importance in NMR and the electric dipole moment for a nucleus does not exist as shown by nuclear physicists. The electric quadrupolar moment exists for molecules but only if their spin $I > 1/2$ which means nuclei with spin $I = 1/2$ do not have an electric contribution to the spin Hamilton operator.

$$\hat{\mathcal{H}}_j^{elec} = 0 \quad (\text{for spin}\, I = 1/2) \tag{2.13}$$

For nuclei with higher spins, the interaction of the electric quadrupole moment to an electric field gradient is the most important one and the electric part of the spin Hamiltonian simplifies to the quadrupole interaction.

$$\hat{\mathcal{H}}_j^{elec} = \hat{\mathcal{H}}_j^{Q} \quad (\text{for spin}\, I \geq 1) \tag{2.14}$$

For the magnetic part of the spin Hamiltonian Equations 2.1 and 2.3 are rewritten as operators and the energy is substituted by the Hamiltonian.

$$\hat{\boldsymbol{\mu}}_j = \gamma_j \hat{\mathbf{I}}_j \quad \text{with} \quad \hat{\mathbf{I}}_j = \hat{I}_{jx}\mathbf{e}_x + \hat{I}_{jy}\mathbf{e}_y + \hat{I}_{jz}\mathbf{e}_z \tag{2.15}$$

$$\hat{\mathcal{H}}_j^{mag} = -\hat{\boldsymbol{\mu}}_j \cdot \mathbf{B} \tag{2.16}$$

In a three-dimensional vector e_x, e_y and e_z are unit vectors along the orthogonal directions in space. As shown in Equation 2.16, if the magnetic dipole moment is parallel to the magnetic field, the magnetic energy is at a minimum and at a maximum when turned by 180°. For a closer look at the spin Hamiltonian, the electric and magnetic parts can be divided into their external and internal interactions. The external interactions are purely magnetic and can be divided into influences of the static magnetic field, the radio-frequency field and the gradient field. The internal interactions coming from the sample itself can be magnetic and electric where the electric influences only exist for nuclei with spin $I > 1/2$ as explained earlier. The magnetic influences can be divided into influences of a single spin (chemical shift and spin-rotation) or between two spins (direct and indirect dipole-dipole coupling) (see Fig.2.2). Sorted by relative magnitude, the electric quadrupolar coupling is by far the greatest (up to a few hundred megahertz), followed by the direct dipole-dipole coupling and the chemical shift. The indirect dipole-dipole coupling ($\mathcal{J}$-coupling) is even smaller and the weakest is the influence through spin-rotation. The spin Hamiltonian operator can then also be written as

$$\hat{H}_j = \hat{H}^{CS} + \hat{H}^{J} + \hat{H}^{DD} + \hat{H}^{Q} + \hat{H}^{SR} \tag{2.17}$$

with the Hamiltonians of the chemical shift (CS), $\mathcal{J}$-coupling (J), direct dipole-dipole coupling (DD), quadrupolar coupling (Q) and spin rotation (SR)[34].

The *spin-rotation interaction* is the interaction between nuclear spins and the magnetic field generated by rapid molecular rotation. More precisely, this magnetic field is generated by electric charges which circulate due to the molecular rotation. This effect is not of importance in the NMR spectroscopy, only in microwave spectroscopy of gases. In isotropic liquids, the secular Hamiltonian averages to zero and the rotation in solids is restricted, so that this effect only occasionally causes relaxation. Before the other four influences will be explained further, motional averaging will be explained first[34].

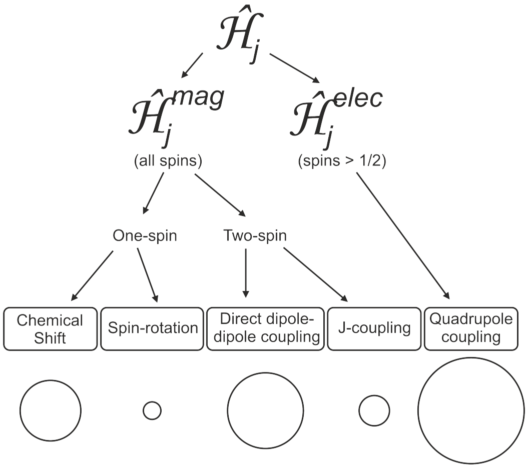

Figure 2.2: Scheme of the possible couplings in NMR experiments sorted by their characteristics and magnitudes are given through the size of the circles underneath. Hereby, the electric quadrupole coupling only exists for spins with $I > 1/2$ and the direct dipole-dipole coupling does not exit for isotropic liquids (adapted from [34])

2.1.2.1 Motional averaging

The molecular motion has three relevant ones: rotation, translation and internal molecular motions. Molecular rotation means, the molecule is changing its orientation in space which is indicated by the angle Θ with respect to the magnetic field. After long enough time, the molecule will have been in all possible orientations and the time average can be replaced with the orientational average. The Hamiltonian is then only dependent on the angle Θ of the molecular orientation. For gases and isotropic liquids where all orientations are equally probable, the Hamiltonian can be written as

$$\hat{\mathcal{H}}_{int}^{iso} = N^{-1} \int d\Theta \hat{\mathcal{H}}_{int}^{0}(\Theta) \tag{2.18}$$

where the normalization constant N is chosen in a way that the probability is one and $\hat{\mathcal{H}}_{int}^{0}$ is the orientational average of a secular interaction. For anisotropic liquids, not all orientations are equally likely. The LC is oriented along a director axis and therefore orientations close to this axis are more likely. In solids the orientation is even more restricted resulting in a very complex Hamiltonian[34].

The molecular translation is either a random motion of neighboring atoms (diffusion) or a biased one pressured by an external gradient (flow). Diffusion is mainly a motion of gases and liquids which can be measured on the time-scale of NMR with special sequences. Hereby, diffusion in gases is faster than in liquids. In solids, diffusion also exists but is usually insignificant on the NMR time-scale.
The internal molecular motions have an effect on the spin interaction terms, whereby the impact of the effect is differentiated between inter- or intramolecular interactions. Pure intramolecular interactions are the spin-rotation and J-coupling, the others (chemical shift, direct dipole-dipole and quadrupolar coupling) are inter- and intramolecular and will be explained in the following sections[34].

2.1.2.2 Chemical Shift

The influence of the main magnetic field at the position of a given nucleus is altered by its surrounding electrons. Therefore, every nucleus feels a slightly different magnetic field which implements itself as a small frequency shift, which is called the chemical shift. This effect is an inter- and intramolecular interaction where the intramolecular ones are more dominant. The most prominent intermolecular interactions are different chemical shifts in different solvents or between solids and liquids. The effect is based on the external magnetic field $\mathbf{B}^0$ inducing a current in the electron clouds of the molecule which then induces a local magnetic field $\mathbf{B}_j^{induced}$. The nuclei feel the sum of both fields,

$$\mathbf{B}_j^{loc} = \mathbf{B}^0 + \mathbf{B}_j^{induced} \tag{2.19}$$

however, the influence of the induced field is only one ten-thousandth of B^0 but still enough for a measurable shift. On top of that, the induced field is proportional to B^0 and can be written as

$$\mathbf{B}_j^{induced} = \boldsymbol{\delta}^j \cdot \mathbf{B}^0 \tag{2.20}$$

with the *chemical shift tensor* δ^j representing a 3x3 matrix[34]

$$\begin{pmatrix} B_{j,x}^{induced} \\ B_{j,y}^{induced} \\ B_{j,z}^{induced} \end{pmatrix} = \begin{pmatrix} \delta_{xx}^j & \delta_{xy}^j & \delta_{xz}^j \\ \delta_{yx}^j & \delta_{yy}^j & \delta_{yz}^j \\ \delta_{zx}^j & \delta_{zy}^j & \delta_{zz}^j \end{pmatrix} \cdot \begin{pmatrix} 0 \\ 0 \\ B^0 \end{pmatrix} \tag{2.21}$$

The tensor of a molecule can be represented as an ellipsoid. The ellipsoid has three mutually perpendicular principal axes of symmetry that define its shape, which correspond to the three principal directions of the tensor[36] (see Fig. 2.3). Along these axes the chemical shift tensor has the principal values δ_{XX}^j, δ_{YY}^j or δ_{ZZ}^j. In the principal axes system all other tensor elements (the off-diagonal elements) are zero and the isotropic chemical shift tensor is then:

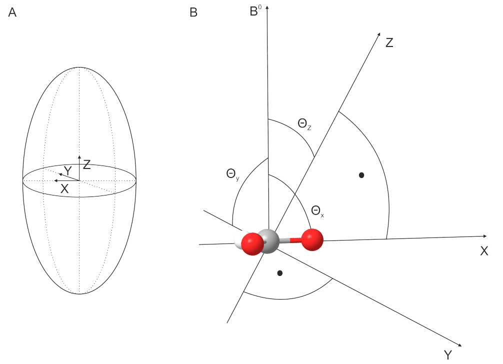

Figure 2.3: A carboxylate group is shown in the principal axes system. A) shows an ellipsoid with its principal axes. B) The principal axes of a carboxylate group if B^0 is not aligned to the Z principal axis. The Z principal axis is almost perpendicular to the CO_2 plane. Note, if B^0 is aligned to one of the axes, the three angles Θ are getting 0° for the aligned axis and 90° for the other two.

$$\delta_j^{iso} = \frac{1}{3}\left(\delta_{XX}^j + \delta_{YY}^j + \delta_{ZZ}^j\right) \tag{2.22}$$

If all three principal values are equal, this tensor determines the peak position in an isotropic spectrum - the chemical shift. If at least two are not equal, the tensor is anisotropic and a *chemical shift anisotropy* can be measured. For this calculation, the Z principal axis will be assigned furthest from the isotropic chemical shift which gives the largest deviation as

$$\delta_j^{aniso} = \delta_{ZZ}^j - \delta_j^{iso} \tag{2.23}$$

and the difference between the other two principal values, called *biaxiality* η_j, is

$$\eta_j = \frac{\delta_{YY}^j - \delta_{XX}^j}{\delta_j^{aniso}} \tag{2.24}$$

where η_j is between 0 and 1 with this definition. For two equal principal values, η_j will get zero and the tensor is *uniaxial*. So far, only the tensor was calculated but not the chemical shift frequency. In order to simplify the Hamiltonian afterwards, we need the secular approximation. With this approximation we can simplify a small, non-resonant additional interaction to first order if we maintain its components along the large main field B^0. Therefore, the full chemical shift Hamiltonian

$$\hat{\mathcal{H}}_j^{CS,full} = -\hat{\boldsymbol{\mu}}_j \cdot \mathbf{B}_j^{induced} \tag{2.25}$$

will be rewritten with the secular approximation and with Equations 2.15 and 2.20 to

$$\hat{\mathcal{H}}_j^{CS} = -\gamma_j \overline{\delta_{zz}^j(\Theta)} B^0 \hat{I}_{jz} \tag{2.26}$$

where δ_{zz}^j depends on the molecular orientation Θ. Together with the Hamiltonian of the static field

$$\hat{\mathcal{H}}_j^{static} = -\gamma_j B^0 \hat{I}_{jz} \tag{2.27}$$

the Hamiltonian for the Larmor frequency is

$$\hat{\mathcal{H}}_j^0 = \hat{\mathcal{H}}_j^{static} + \hat{\mathcal{H}}_j^{CS} = \omega_j^0 \hat{I}_{jz} \tag{2.28}$$

and the frequency itself is

$$\omega_j^0 = -\gamma_j B^0 \left(1 + \overline{\sigma_{zz}^j(\Theta)}\right) \quad \text{with} \quad \overline{\sigma_{zz}^j(\Theta)} = \overline{\delta_{zz}^j(\Theta) + \delta_{ref}} \tag{2.29}$$

and therefore depends on the motionally averaged chemical shielding σ_{zz}^j, which is the sum of the chemical shift and the chemical shift of the reference δ_{ref} (see reference [34] for further details). With the motional average and Equation 2.18

$$\overline{\delta_{zz}^j(\Theta)} = \delta_j^{iso} \tag{2.30}$$

and the frequency in the isotropic case is defined as

$$\omega_j^0 = -\gamma_j B^0 \left(1 + \sigma_j^{iso}\right) \quad \text{with} \quad \sigma_j^{iso} = \delta_j^{iso} + \delta_{ref} \tag{2.31}$$

The isotropic chemical shift is of major importance as diagnostic tool in chemistry. Qualitatively, the chemical shift range increases with the atomic weight. ^{1}H for example, has a range of around 10 ppm,

^{13}C around 200 ppm and NMR active metal nuclei of several thousands ppm. The amount of electron density decides how far the signal is shifted from a standard (e.g.TMS at 0 ppm). A higher electron density shifts to lower δ values and a lower electron density to higher values. Even negative values are possible, for example most ^{19}F chemical shifts. Nuclei with low electron density mostly have an electronegative neighbor atom which pulls the electron density out of the observed nucleus. Other influences on the electron density are ring currents induced by conjugated π electrons freely moving in the ring or other conjugated systems. For unsubstituted aromatics, the density is increased in the plane of the ring (called *deshielding*) and decreased around the local symmetry axis (called *shielding*). In the anisotropic case, $\overline{\delta^j_{zz}(\Theta)}$ is not equal δ^{iso}_j but the probability of the favored direction needs to be taken into account

$$\overline{\delta^j_{zz}(\Theta)} = \int d\Theta \delta^j_{zz}(\Theta) p(\Theta) \tag{2.32}$$

resulting in a chemical shift difference between the isotropic and anisotropic signal. In solids, it goes even one step further. As all different orientations are possible without averaging over them, one peak appears for each of these directions and the spectrum shows the so called *powder pattern*[34].

2.1.2.3 J-coupling

Very often, the signals in a spectrum are not just single lines but split into multiplets by indirect dipole-dipole coupling called *scalar coupling* or *J-coupling*. Protons magnetize the electrons, creating another local magnetic field around the neighboring nuclei. Because of this involvement of electrons, the coupling is called indirect. Next to the chemical shift, it is the second most important information a chemist can get about the investigated molecules showing the chemical bonding of atomic nuclei. A measurable J-coupling exists only through a small number of chemical bonds between two spins and is therefore only intramolecular. An index before the J indicates the distance (= number of bonds), ^1J for a direct bond (e.g. C-H), ^2J for a two bond distance (e.g. H-C-H), ^3J for three bonds (e.g. H-C-C-H) and so on. The coupling values get smaller with an increased number of bonds why normally bond distances of 5 Å or more can not be seen as they are too small. On the other hand, the coupling strength is independent of the magnetic field[33,34].
The easiest case is the coupling between a neighboring CH and CH_3 group for the spin 1/2 nucleus ^1H. The CH group has one proton and its spin can be either up (↑) or down (↓), which splits the signal of the CH_3 group in two lines (a doublet) with the same height shifted by $\pm\frac{1}{2}\,{}^3J_{HH}$ with the coupling J in Hertz (around 0-20 Hz for $^3J_{HH}$). The CH group on the other hand has three neighboring protons which all can be in the two states resulting in eight possible orientations ↑↑↑, ↑↑↓, ↑↓↑, ↓↑↑, ↑↓↓, ↓↑↓, ↓↓↑ and ↓↓↓. As ↑↑↓, ↑↓↑ and ↓↑↑ can not be distinguished due to the same energy as well as ↑↓↓, ↓↑↓ and ↓↓↑, the multiplet for the CH group will be a quartet with 1:3:3:1 intensities as can be seen in Figure 2.4.

The J coupling is not only seen in the homonuclear case, but also in the heteronuclear case. The ^{13}C of the CH group will split the hydrogen signal as well into a doublet with a higher coupling of $^1J_{CH}$ typically being between 120 - 260 Hz. This doublet will have only 1.1 % of the intensity compared with the $^3J_{HH}$ quartet due to the natural abundance of ^{13}C (1.1 %). Other nuclei than spin 1/2 can show multiplets due to couplings as well. Important during the calculations for higher nuclei is, they do not simply have ± 1/2 as possible spin quantum numbers. Nuclei with spin I = 1 for example have three states: +1, 0 and -1. The number of lines for the multiplet can then be calculated with (2nI+1) where n is the number of magnetically equivalent coupling partners[33–35].

The full Hamiltonian for the J-coupling between spin I_j and I_k can be written as

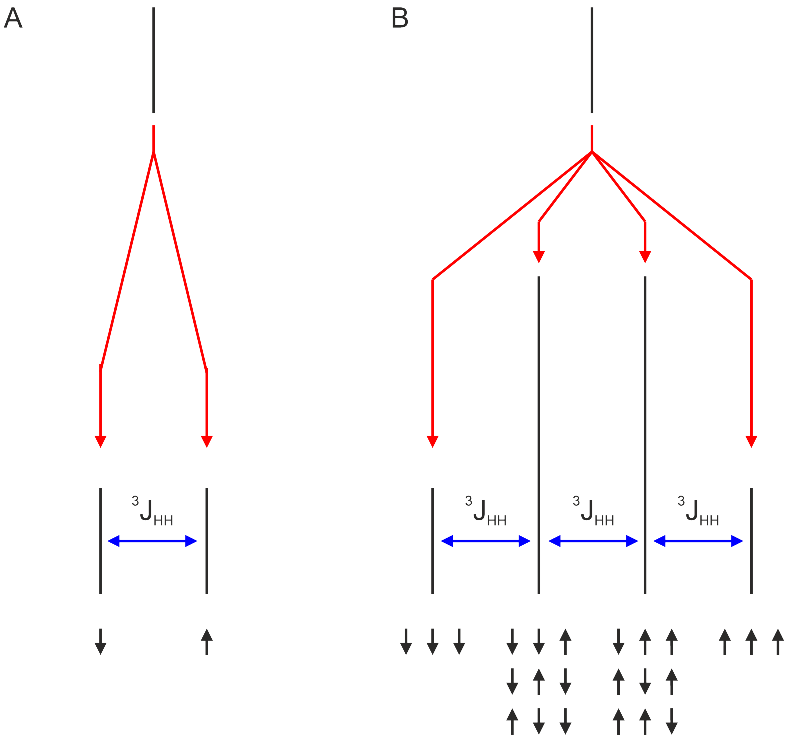

Figure 2.4: The splitting through $^3\mathcal{J}$-coupling of neighboring CH and CH$_3$ groups. A) The CH$_3$ group is split into a doublet by one proton of the CH group which can either be in the α (↓) or β (↑)state. B) The CH group is split into a quartet with the same coupling constant. As there are eight possibilities for the three protons where two times three states are indistinguishable, four lines with 1:3:3:1 intensity can be seen (adapted from [33])

$$\hat{\mathcal{H}}_{jk}^{J,full} = 2\pi \hat{\mathbf{I}}_j \cdot \mathbf{J}_{jk} \cdot \hat{\mathbf{I}}_k \tag{2.33}$$

with $\mathbf{J}_{jk}$ as the $\mathcal{J}$-coupling tensor and 2π for the conversion from radians per second to Hertz. The tensor is given by

$$\mathbf{J}_{jk} = \begin{pmatrix} J_{xx}^{jk} & J_{xy}^{jk} & J_{xz}^{jk} \\ J_{yx}^{jk} & J_{yy}^{jk} & J_{yz}^{jk} \\ J_{zx}^{jk} & J_{zy}^{jk} & J_{zz}^{jk} \end{pmatrix} \tag{2.34}$$

which will be averaged out by molecular tumbling in isotropic liquids leading to an isotropic Hamiltonian of

$$\hat{\mathcal{H}}_{jk}^{iso} = 2\pi J_{jk} \hat{\mathbf{I}}_j \cdot \hat{\mathbf{I}}_k \quad \text{with} \quad J_{jk} = \frac{1}{3}\left(J_{xx}^{jk} + J_{yy}^{jk} + J_{zz}^{jk}\right) \tag{2.35}$$

where $\mathcal{J}_{jk}$ is the isotropic $\mathcal{J}$-coupling. Comparing with δ_j^{iso} from Equation 2.22 both isotropic tensors look alike consisting only of the diagonal elements. The secular Hamiltonian on the other hand can be distinguished in two cases, homo- and heteronuclear spin coupling. Both cases are isotropic but from a different type. Hereby, the homonuclear case is exactly the same as the isotropic Hamiltonian in Equation 2.35 and the heteronuclear case, which is always in the so called weak coupling limit, only contains the z-components:

$$\hat{\mathcal{H}}_{jk}^{J,homo} = 2\pi J_{jk}\hat{\mathbf{I}}_j \cdot \hat{\mathbf{I}}_k \quad \text{and} \quad \hat{\mathcal{H}}_{jk}^{J,hetero} = 2\pi J_{jk}\hat{I}_{jz}\hat{I}_{kz} \tag{2.36}$$

The sign of the $\mathcal{J}$-coupling can be either positive or negative, positive indicating parallel spin polarizations and negative couplings indicating that the spin polarizations are opposite. The rule of thumb is here that spins with the same sign of the gyromagnetic ratio connected by one chemical bond have positive $\mathcal{J}$-coupling and with opposite signs negative $\mathcal{J}$-coupling. For two or more bonds, the sign is not that easy to predict as it depends on many factors, e.g. molecular geometry[34]. The magnitude as well depends on the structure (bond angles and torsional angles). The torsional angles are well described by the *Karplus-relationship*

$$J(\Phi) = A\cos^2(\Phi - 60) - B\cos(\Phi - 60) + C \tag{2.37}$$

where A, B and C are empirical constants (see Fig. 2.5) . This relationship is especially useful for the determination of the protein secondary structure and the assignment of protons for a CH_2 group in rigid organic molecules with six- or higher membered ring systems[33,34].

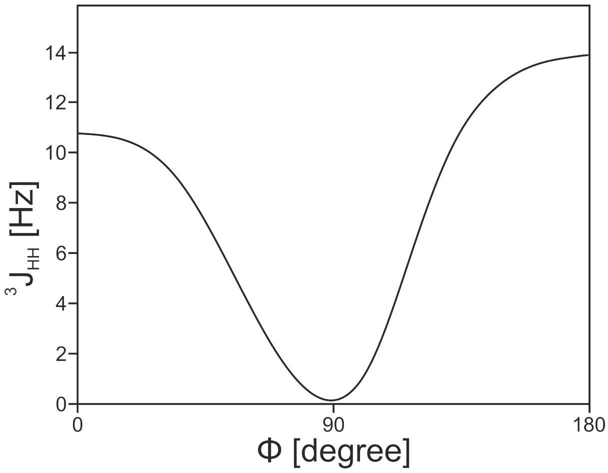

Figure 2.5: The Karplus curve shows the $^3J_{HH}$-coupling constant varying with the torsion angle Φ calculated by Equation 2.37. The curve here shows typical values for small, rigid molecules which have the highest coupling constants at an angle of 180° and the lowest at 90° (adapted from [37])

Although the $\mathcal{J}$-coupling has as well an anisotropic part which could be seen in LCs and solids, it is small compared to the practically indistinguishable direct dipole-dipole coupling in the next chapter, this $\mathcal{J}$-anisotropy will be ignored[34].

2.1.2.4 Dipolar coupling

The dipolar coupling is a direct coupling between the magnetic field generated by one nuclear spin (j) with a second nuclear spin (k) and the magnetic field generated by nuclear spin two with the first nuclear spin. This direct dipole-dipole coupling does not involve electron clouds but relates through space and can be inter- as well as intramolecular. The full Hamiltonian is

$$\hat{\mathcal{H}}_{jk}^{DD,full} = b_{jk}\left(3\left(\hat{\mathbf{I}}_j \cdot \mathbf{e}_{jk}\right)\left(\hat{\mathbf{I}}_k \cdot \mathbf{e}_{jk}\right) - \hat{\mathbf{I}}_j \cdot \hat{\mathbf{I}}_k\right) \tag{2.38}$$

where e_{jk} is a unit vector parallel to the connecting line of both nuclei with $e_{jk} \cdot e_{jk} = 1$ and b_{jk} is the dipole-dipole coupling constant consisting of

$$b_{jk} = -\frac{\mu_0}{4\pi} \frac{\gamma_j \gamma_k \hbar}{r_{jk}^3} \tag{2.39}$$

with the gyromagnetic ratios of nuclei *j* and *k*, the spin-spin distance r_{jk} between both and the magnetic constant $\mu_0 = 4\pi \times 10^{-7}$ H m^{-1}. Very important, b_{jk} is a constant and not dependent on the orientation, the Hamiltonian on the other hand is dependent on the orientation as the vector e_{jk} changes direction with molecule rotation. Hereby, the energy has its minimum when both spins are parallel as indicated by the negative sign in b_{jk}.

So far, only one pair of spins are described by the full Hamiltonian but in a sample are many spins, not just two. The full Hamiltonian is then a double summation over all pairs of spins

$$\hat{\mathcal{H}}^{DD,full} = \sum_k \sum_j^{k-1} \hat{\mathcal{H}}_{jk}^{DD,full} \tag{2.40}$$

For the dipole-dipole coupling the secular approximation is valid again, at least for high magnetic fields. However, there are two possible solutions for the reduced Hamiltonian as the spins can be either from the same isotopic species or not. The Hamiltonian in the homonuclear case is

$$\hat{\mathcal{H}}_{jk}^{DD}(\Theta) = d_{jk} \left(3\hat{I}_{jz}\hat{I}_{kz} - \hat{\mathbf{I}}_j \cdot \hat{\mathbf{I}}_k \right) \tag{2.41}$$

with the secular dipole-dipole coupling

$$d_{jk} = b_{jk} \frac{1}{2} \left(3\cos^2 \Theta_{jk} - 1 \right) \tag{2.42}$$

where Θ_{jk} is the angle between the vector e_{jk} and the external magnetic field B^0. The important difference between the dipole-dipole coupling constant b_{jk} and the secular dipole-dipole coupling d_{jk} is that the secular dipole-dipole coupling depends on the angle Θ_{jk} with respect to the magnetic field instead of only the distance between the spins.

In the heteronuclear case the Hamiltonian is again reduced due to the weak coupling limit to

$$\hat{\mathcal{H}}_{jk}^{DD}(\Theta_{jk}) = d_{jk} 2\hat{I}_{jz}\hat{I}_{kz} \tag{2.43}$$

with the same secular dipole-dipole coupling. Important angle values for d_{jk} are 0° (parallel to the magnetic field), 54.74° (the magic angle) and 90° (perpendicular to the magnetic field). Hereby, the magic angle is the solution for

$$3\cos^2 \Theta_{jk} - 1 = 0 \quad \text{with} \quad \Theta_{magic} = \arctan\sqrt{2} \cong 54.74 \tag{2.44}$$

As always, three conditions (isotropic liquids, anisotropic liquids, solids) need to be considered separately. In the isotropic case, the intramolecular and the short-range intermolecular dipole-dipole couplings average to zero. Without a predominant direction, the spin-spin vector can point into every direction with equal probability and the integral of Equation 2.44 over all angles equals zero. Hence, the dipolar coupling averages out to zero (intramolecular). Furthermore, the translational motion averages the short-range intermolecular coupling to zero. The long-range dipole-dipole coupling does not average to zero even for isotropic liquids but it is so small that it can be neglected and the isotropic Hamiltonian is approximately zero. On the other hand, in anisotropic liquids exists a predominant direction and the intramolecular dipole-dipole coupling is not averaged out and the Hamiltonian terms are as described in Equation 2.41 and 2.43 with the secular dipole-dipole coupling d_{jk}. Both intermolecular couplings can be regarded as in the isotropic case. Due to fast diffusion the short-range couplings are zero and the long-range couplings are very small. This is not the case for solids, where all three coupling classes are strong and need to be considered[34].

2.1.2.5 Quadrupolar coupling

As mentioned earlier, the electric quadrupole moment only exists for nuclei with spins > 1/2 but is the strongest interaction measurable in NMR of diamagnetic compounds between the electric field gradient induced by the surrounding electron clouds and the nuclei. This interaction is mainly intramolecular but also in parts intermolecular. Similar to the principal values for the chemical shift anisotropy tensor, the electric field gradient tensor has the principal values

$$V_{XX} + V_{YY} + V_{ZZ} = 0 \tag{2.45}$$

The largest principal value is the product of the electric charge e and the electric quadrupole moment q and set to V_{ZZ}

$$eq = V_{ZZ} \tag{2.46}$$

and the biaxiality η_Q can be written as

$$\eta^S Q = \frac{V_{XX} - V_{YY}}{V_{ZZ}} \tag{2.47}$$

The full nuclear quadrupole Hamiltonian for an arbitrary molecular orientation is a product of the electric field gradient tensor with the rotation matrix $R^Q(\Theta)$ representing the relative orientation of the electric field gradient principal axis system,

$$\mathbf{V}(\Theta) = \mathcal{R}^Q(\Theta) \cdot \begin{pmatrix} V_{XX} & 0 & 0 \\ 0 & V_{YY} & 0 \\ 0 & 0 & V_{ZZ} \end{pmatrix} \cdot \mathcal{R}^Q(\Theta)^{-1} \tag{2.48}$$

and the quadrupolar moment Q, elementary charge e, as well as the spin I

$$\hat{\mathcal{H}}^{Q,full}(\Theta) = \frac{eQ}{2I(2I-1)\hbar} \hat{\mathbf{I}} \cdot \mathbf{V}(\Theta) \cdot \hat{\mathbf{I}} \tag{2.49}$$

The full nuclear quadrupole Hamiltonian can also be written as a sum of the first-order quadrupolar Hamiltonian, second-order quadrupolar Hamiltonian and so on

$$\hat{\mathcal{H}}^{Q,full} = \hat{\mathcal{H}}^{Q,(1)} + \hat{\mathcal{H}}^{Q,(2)} + \dots \tag{2.50}$$

and in the case that the Zeeman interaction is much bigger than the quadrupolar coupling the full quadrupolar Hamiltonian can be stopped after the first-order quadrupolar Hamiltonian which is equivalent to the secular approximation. With larger quadrupolar interaction the second-order quadrupolar Hamiltonian must be included as well and sometimes even the third-order one. Hereby, the first-order quadrupolar Hamiltonian is

$$\hat{\mathcal{H}}^{Q,(1)} = \omega^{Q,(1)} \frac{1}{6} \left(3\hat{I}_z^2 - I(I+1)\hat{1} \right) \tag{2.51}$$

and $\omega^{Q,(1)}$ is the first-order quadrupolar coupling given by

$$\omega^{Q,(1)} = \frac{3eQ\overline{V}_{zz}}{2I(2I-1)\hbar} = \frac{3e^2qQ}{4I(2I-1)\hbar}(3\cos^2\Theta - 1) \tag{2.52}$$

As before, motional averaging in isotropic liquids averages the quadrupolar coupling to zero and therefore the first-order quadrupolar Hamiltonian as well. Also, approximately no influence on the peak position can be seen but an influence on the relaxation of nuclear spins with $I > 1/2$ will be seen as discussed in Section 2.1.5. For anisotropic liquids, on the other hand, a quadrupolar coupling can be seen which correlates with the ordering of the of LCs. In solids, the quadrupolar coupling is even stronger and can reach values between a few kilohertz or hundreds of megahertz[34].

2.1.3 Anisotropic NMR

$\mathcal{J}$-couplings and nuclear Overhauser enhancement (NOE) data from isotropic measurements are the main data used for the characterization of (bio-)molecules. But they do have limitations in predicting the complete and correct configuration and relative orientation leading to poorly defined structures especially in biomolecules. Only with isotropic constraints, dynamic aspects may be, missed leading to incorrect structural representations when motion is present[38]. They also cannot determine the relative configuration of long-range CH couplings that do not belong to same spin system, which means that important stereo information is lost[39]. Therefore, new sets of constraints are needed by introducing anisotropy into materials.

2.1.3.1 General Information

In NMR it is very important to distinguish between isotropic and anisotropic conditions. Normally, motional averaging caused by the relatively high thermal energies reduces any anisotropic couplings to zero[40]. However, there exist a few materials which restrict this thermal energy and force the molecule to align along the magnetic field. These materials can be divided in three general types: liquid crystalline phases, stretched gels and orientation by paramagnetic ions[41]. Paramagnetic ions are mostly used in biomolecular NMR especially for generating pseudocontact shifts which give information about structure, function and dynamics of the biomolecules. Normally, the ions will not be used with small molecules as the lines broaden by the covalently attached paramagnetic ions[41,42]. Stretched polymers are better suited for small molecules, first introduced by Deloche and Samulski[43]. Hereby, a dry, cross-linked polymer is swollen with solvent (mostly deuterated) and the investigated solute molecule. If the swollen polymer stick is put inside an NMR tube, it can be stretched and anisotropy is generated. Together with another stretchable tube inside the NMR tube, the length of the gel is adjustable and therefore the alignment as well. The induced alignment is rather small which gives less line-broadening (see Section 2.1.5) and often clear and simple spectra[11,41]. The third type, the LCs, will be explained in section 2.1.3.4.

All three types have in common that they transfer their anisotropy on the solute molecules and molecular ordering is introduced. The motional averaging is not complete any longer resulting in additional measurable couplings (RDCs) and shifts (RCSA). As most investigated molecules are natural organic compounds where the only nuclei with spin > 1 are deuterium and nitrogen, RQCs are only relevant in enriched molecules (e.g. deuterated solvents). Residual means in this context that the measured couplings and shifts are small (up to a few hundred Hertz) compared to dipolar couplings or chemical shift anisotropy in solids (up to a few hundred kilohertz). The concept of measuring residual anisotropic parameters is very important for liquid NMR as higher molecular ordering and hence higher anisotropic parameters increase the complexity of the spectra and hence smaller measurable couplings improve the spectral quality[38]. The first and most famous example for this increase in complexity was given by Saupe and Englert[44] in 1963 where the benzene solvent signal inside a LC was split in over 30 lines.

2.1.3.2 Alignment tensor

If the alignment is small enough, the RDCs give the needed information about the order of the molecule as long as the so called *alignment tensor* is known. This tensor can be calculated with the principal components of the principal axis system from Figure 2.3 in subsection 2.1.2.2. First, the probability of finding the magnetic field along the principal axes is needed. Therefore, the probability tensor P,

$$\mathbf{P} = \begin{pmatrix} P_X & 0 & 0 \\ 0 & P_Y & 0 \\ 0 & 0 & P_Z \end{pmatrix} \tag{2.53}$$

where P_X, P_Y and P_Z are its principal values ($P_X + P_Y + P_Z = 1$), is multiplied with the unit vector e_j along each of the principal axes which is equal to $\overline{\cos^2\Theta}$

$$\overline{\cos^2\Theta} = P_X e_X^2 + P_Y e_Y^2 + P_Z e_Z^2 \tag{2.54}$$

This can be inserted into the time averaged form of Equation 2.42 and hence every dipole-dipole coupling can be predicted for the arbitrary spin pair. To get from here to the alignment tensor **A**, **P** needs to be expressed as its traceless part with the unity matrix **1** which is equal to **A**

$$\mathbf{A} = \mathbf{P} - \frac{1}{3}\mathbf{1} \tag{2.55}$$

Similarly, the principal values A_X, A_Y and A_Z are written as

$$A_X = P_X - \frac{1}{3}, \quad A_Y = P_Y - \frac{1}{3}, \quad A_Z = P_Z - \frac{1}{3}, \tag{2.56}$$

and therefore the second Legendre polynomial of the time averaged dipole-dipole coupling can be written as

$$3\cos^2\Theta - 1 = A_X e_X^2 + A_Y e_Y^2 + A_Z e_Z^2 \tag{2.57}$$

and d_{jk} can be rewritten as the residual form

$$d_{jk}^{res} = b_{jk}\frac{1}{2}\mathbf{A} \tag{2.58}$$

The alignment tensor was not the first matrix describing the order of molecules. If **A** is scaled by 3/2 and the optical axis of a LC is parallel to B^0, one gets the *Saupe matrix* $\mathbf{S}$[36]

$$\mathbf{S} = \frac{3}{2}\mathbf{A} \tag{2.59}$$

The Saupe matrix or *order matrix* was published by Saupe[45] in 1968. He defined a 3x3 matrix which uses the principal axes fixed on the molecule system. This symmetrical and traceless matrix (only 5 elements are non-zero) is significant for determining the order of any molecule in an anisotropic environment.

$$S_{ij} = \frac{1}{2} < 3\cos\Theta_i \cos\Theta_j - \delta_{ij} > \quad \text{with} \quad \delta_{ij} = 0 \text{ for } i \neq j;\ \delta_{ij} = 1 \text{ for } i = j \tag{2.60}$$

Hereby, *i* and *j* represent the three principal angles (Θ_X, Θ_Y and Θ_Z) of the molecular system and δ_{ij} is the Kronecker symbol. Therefore, the five elements are S_{XZ}, S_{YZ}, S_{XY}, S_{XX}-S_{YY} and S_{ZZ} (with S_{XX} + S_{YY} + S_{ZZ} = 0)[45]. Programs like PALES from M. Zweckstetter[46,47] use singular value decomposition (SVD) based calculations for **A** and **S** with given molecular structures and correlate experimental parameters like RDCs with the ones calculated by the tensors.
The Saupe matrix not only gives the orientational information about the molecule but of its alignment medium as well. Hence, the orientation of the medium itself is given by the quadrupolar coupling of the deuterated medium or solvent with Equation 2.52. From the splitting of the deuterated solvent with the known quadrupolar coupling constant, the director angle Θ_D of the alignment medium or all five elements of the Saupe matrix can be calculated if the solvent has a threefold synthesis such as chloroform[48,49].

2.1.3.3 Extraction of RDCs, RCSA and RQCs

All residual anisotropic parameters require partial alignment in the sample so that they can be measured with minimal complexity and line broadening. Mostly, a set of isotropic parameters is needed from which the anisotropic parameters can be subtracted. The RCSA for example is the difference between the isotropic chemical shift and the anisotropic chemical shift. This sounds simple, but a correct RCSA assignment requires several steps. First, one peak needs to be assigned as reference in both spectra from which the other chemical shift differences can be measured. Ideally, this peak does not change its chemical shift value under aligning conditions. This reference should show no RCSA itself which can theoretically achieved with a perfect tetrahedral symmetry. Hence, TMS with its tetrahedral symmetry and a chemical shift of 0 ppm is a good choice[50]. However, it is not the perfect choice as only the silicone is truly tetrahedral and RDCs and RCSA were reported several times for the other nuclei in TMS and other tetrahedral molecules. One explanation for the reported anisotropic parameters are distortions of the tetrahedral symmetry for example through internal vibrational motion[51,52].
Second, the susceptibility χ of the sample should not be changed which means the solvent needs to be the same in both samples and even the very same sample container should be used. R. Hoffman[53] showed that even the tetrahedral TMS has a measurable chemical shift difference in various solvents

with different susceptibilities. This comes from the relation of χ with B^0 for the magnetic field inside the sample (B^{sample})

$$B^{sample} = \frac{B^0}{1 + 2\pi\chi_{zz}} \tag{2.61}$$

where χ_{zz} is the volume susceptibility in z-direction to the magnetic field[13,40]. One approach to reduce the effect of susceptibility to a minimum is measuring the chemical shift difference of two anisotropic spectra at slightly different alignment conditions with stretched gels by VASS. Here, the stretched sample is completely unaltered and only the director angle Θ_D respective to the magnetic field is changed which results in a different alignment tensor[50].

For RDCs the magnetic characteristics of the isotropic and anisotropic sample do not need to match as precisely as for the RCSA. Dipolar couplings are simply added to J-couplings in the anisotropic case resulting in the so called *total coupling T*.

$${}^{1}T_{CH} = J_{CH} + \frac{1}{2}\left(3\cos^2\Theta_D - 1\right) D_{CH} \tag{2.62}$$

which simplifies for a sample aligned along B^0 ($\Theta_D = 0°$) to

$${}^{1}T_{CH} = J_{CH} + D_{CH} \tag{2.63}$$

where the J-coupling and the dipolar coupling are both independent of the magnetic field and the susceptibility[54]. Hereby, the RDCs can be of positive or negative sign and T can increase or decrease with respect to the isotropic case where only the J-coupling was measured. Even in the same molecule RDCs can have different signs.

In stronger alignments it might be possible that the RDCs are larger than the J-coupling. In such a case, the T-coupling can change the sign if RDCs and J-coupling are different in their sign. For example, a C-H group shows an isotropic J-coupling of +120 Hz and a T-coupling in the anisotropic case of 20 Hz. In a conventional spectrum the sign cannot be determined. If ${}^{1}T_{CH}$ = +20 Hz, then ${}^{1}D_{CH}$ = -100 Hz, but if ${}^{1}T_{CH}$ = -20 Hz, ${}^{1}D_{CH}$ = -140 Hz. One possible way to determine the correct value is to measure the total couplings at different alignment strengths and compare it with the quadrupolar coupling. Both are scalable and therefore the rate of D_1/D_2 should be the same as Q_1/Q_2 where Q is the value of the RQCs. In the example with the T-coupling of 20 Hz, another anisotropic spectrum with a different alignment strength was measured with a 70 Hz T-coupling resulting in RDCs of either -50 Hz or -190 Hz. The corresponding quadrupolar couplings of the solvent showed 300 Hz for the 20 Hz T-coupling and 150 Hz for the 70 Hz T-coupling. Now the rates of the quadrupolar coupling and the RDCs are compared. 300/150 = -100/-50 = 2 and -140/-190 ≈ 0.74. Therefore, the correct T-couplings are +20 Hz and +60 Hz and the corresponding RDCs -100 Hz and -50 Hz[55]. However, for small induced alignments, the measured T-coupling is exactly the frequency difference of the doublet in the spectra and no additional spectra under different alignment strengths are needed. Still, there is one major disadvantage measuring RDCs, the multiplet broadening by the dipolar couplings.

Last, RQCs can be measured if nuclei with spins $I > 1/2$ are involved, which in non-enriched systems means mostly the deuterium nuclei of the solvent. In isotropic solutions no dipolar or quadrupolar couplings are observed and all molecules with either only a single quadrupolar nucleus or with only symmetric quadrupolar nuclei will produce one line.
For non-symmetric molecules with more than one quadrupolar nucleus, J-coupling can be observed if

the linewidth is smaller than the coupling. In anisotropic solutions, both the dipolar and quadrupolar coupling are present and the lines will be split for nuclei with spin $I = 1$. Nuclei with spin $I > 1$ like chlorine will not show any splittings due to rapid relaxation and their large quadrupolar coupling values will not give resolved high resolution spectra[40].

For spin $I = 1$ nuclei, one can distinguish three cases: a single nucleus, only symmetric nuclei and at least two not symmetric nuclei (Fig.2.6). A single nucleus which is not coupled to any other magnetic nuclei will split in two lines where the distance is the quadrupolar coupling (Fig.2.6A).

Is the nucleus (e.g. deuterium) coupled to another magnetic nucleus (e.g. ^{1}H), the splitting will be a doublet of a doublet where the bigger doublet is the quadrupolar coupling of deuterium and the smaller doublet is (J_{HD} + $2D_{HD}$) (Fig.2.6B). This rule is valid for all A_nX systems where X is the spin 1 nucleus and the resulting spectra show a doublet of a multiplet[40].

As soon as more than one quadrupolar nucleus is involved, the obtained splitting pattern gets more complicated and goes beyond the scope of this thesis, which is why the interested reader is referred to further reading.

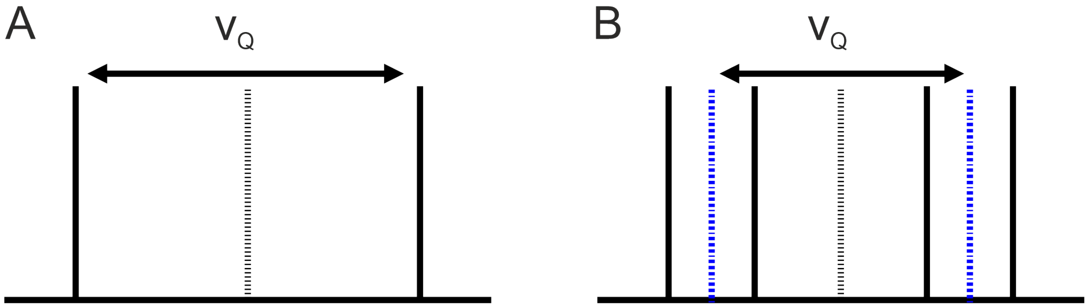

Figure 2.6: Two cases of quadrupolar couplings. The solid black lines are the observed peaks, the dotted grey line is the isotropic chemical shift and the dotted blue lines in B) are the hypothetical peaks by the quadrupolar coupling without the second coupling. A) A single quadrupolar nucleus is split only by the quadrupolar coupling. B) A single quadrupolar nucleus is split by the quadrupolar coupling and another magnetic nucleus (adapted from [40]).

The main profit NMR spectroscopists gain from the RQCs is the information about the order of the whole system by the deuterated solvents. Especially, if solvents with only one deuterium and no other magnetic coupling nuclei like $CDCl_3$ are used and the splitting of the signal is exactly the quadrupolar coupling and hence the strength of the alignment. Also, the lineshape and width give great indication of the homogeneity of the whole sample[56].

2.1.3.4 Liquid Crystals

F. Reinitzer[57] in 1888 and O. Lehmann[58] with his book published 1904 in Karlsruhe were the first finding and introducing *liquid crystals* to the scientific community. The initial scepticism of something being liquid and solid at the same time, followed a rising interest provoked by the first conference on LCs in 1965[59] for these birefringent and therefore anisotropic materials. Nowadays, LCs are well established (e.g. in TV or computer screens) resulting in a Nobel prize in physics for Pierre-Gilles de Gennes in 1991[60].

The phase of a LC is mostly referred to as mesophase as they lie between liquid and solid phases. These mesophases need special structured molecules which can align in one direction for example induced by a magnetic field[40]. So far, three types of structures are known: discotic (shaped like discs)[61], conic (shaped like a rice bowl)[62] and rod-like structures (e.g. α-helical)[40]. All three structure types have in common that they are thermotropic, lyotropic or metallotropic. Thermotropic LCs exhibit the mesophase in a specific temperature range, the mesophase of a lyotropic LC is not temperature-dependent, but is formed with solvent molecules[40]. Another more recently found mesophase is the metallotropic phase where inorganic melts are incorporated into anisotropic molecules[63]. The mesophase of all these kinds of LCs can mix homogeneously with solute molecules transferring anisotropy on these solutes. If the concentration of the solute molecule in the LC is too high, it can break the mesophase and destroy the anisotropy. Therefore, care must be taken by preparing LCs[40]. As this work focuses on a LC in a rod-like shape, the interested reader is referred to other literature on discotic and conic structures.

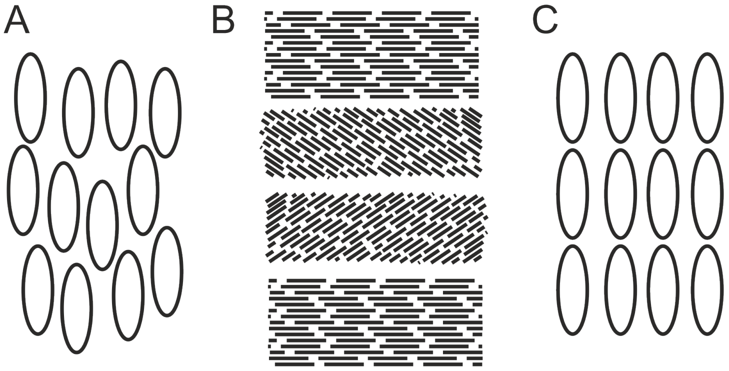

Figure 2.7: The three possible mesophases of a LC, in A) the nematic phase, in B) the cholesteric phase and in C) a smectic phase (adapted from [40]).

Looking at the molecular ordering, different classes of mesophases can be seen. For rod-like structures the three most important ones are: nematic, cholesteric and smectic (Fig. 2.7). Hereby, the nematic phase has the lowest ordering where large groups of the rod-like molecules are arranged in parallel. An external constraint like a magnetic field orients all groups in the same direction, without the constraint these groups can have different directions still with parallel rods inside the groups. The nematic phase has a preferred orientation which is described by a unit vector called *director*.

If no field is applied, optically active (chiral) molecules form the cholesteric phase which is a special case of the nematic phase. Instead of having a preferred direction over a large volume along one axis, the groups twist around this axis in a helical ordering. A famous example is the α-helix PBLG. The cholesteric phase does not only have to consist of chiral molecules. Adding chiral solutes to a nematic phase changes them into a cholesteric phase as well. Normally, cholesteric phases are unsuitable for high resolution NMR, but magnetic fields will untwist this helical order and the phase becomes nematic and therefore more suitable for high resolution NMR.

The third type can be subdivided into eight subdivisions, three of them are smectic A, smectic B and smectic C. All the smectic phases are layered structures in which the molecules in a layer are arranged parallel to each other and the layers can move freely against each another. In the smectic A phase, the molecules are more perpendicular to the layer plane, in the smectic C phase, they are tilted to the layer phase. The smectic B phase has higher symmetry than the other two phases. Because smectic phases have a higher degree of ordering than nematic and cholesteric phases, they lie lower in temperature. Hereby, the smectic B phase exists at the lowest temperature just above the melting point and the smectic A phase exists at the highest temperature of these three. With even stronger heating, the smectic phase transforms into a nematic phase and finally to a complete isotropic liquid[40].

NMR mainly focuses on a nematic or a cholesteric LC if liquid crystalline alignment is wanted. Especially, the cholesteric ones like PBLG are of great interest to NMR spectroscopists as they can discriminate between chiral enantiomers. If both enantiomers are dissolved in a cholesteric phase, both molecules have different chemical shifts for the chiral groups as one molecule is directly interacting with the cholesteric LC and the other one only indirect[9,64]. Another advantage of LCs with very long rods is that the LC is not interfering with the measured spectra. It only broadens the signal width which can be painful in ^{1}H but no additional peaks show up due to their large size and very short T_2 time (see Section 2.1.5)[9]. This signal broadening mainly comes from large multiplet widths, which the higher alignment of LCs produce in comparison to other alignment media.

2.1.4 Two-dimensional NMR

In subsection 2.1.1, it was mentioned that an Fourier-transformed FID results in frequency related spectrum. This spectrum is one-dimensional. In NMR, there are also two- and three-dimensional experiments where two (ω^1 and ω^2) or three frequencies directly correlate with each other generating so-called *cross-peaks* which are visible on a two-dimensional map. For 3D experiments, the evaluation is more complex and the reader is referred to additional literature, for example from M. Zweckstetter[33]. Still, the question is, how can two frequencies correlate with each other generating visible cross-peaks. The basic principle will be shown with the simplest 2D experiment, the COSY (COrrelation SpectroscopY) seen in Figure 2.8.

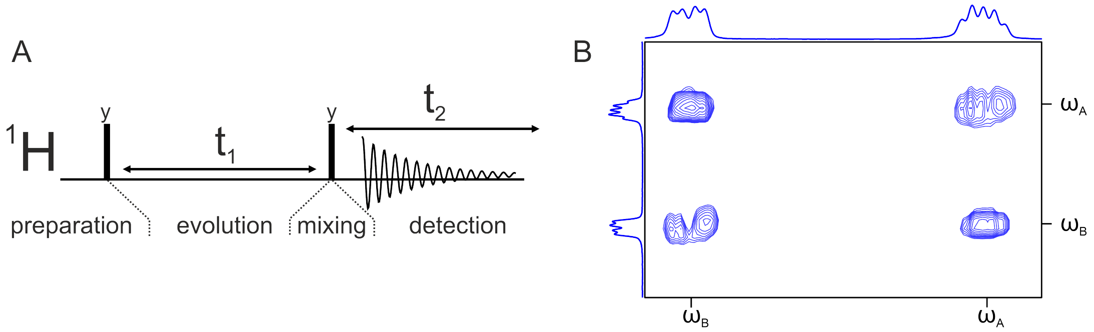

Figure 2.8: A) The basic COSY experiment consists of two 90° pulses in y-direction which are separated by the evolution time t_1. With the first 90° pulse the preparation ends and the second 90° pulse is the mixing period. After the second pulse, the FID will be detected in a second waiting period t_2. (adapted from [33] B) Two frequencies ω_A and ω_B generate the typical COSY cross peaks (ω_A/ω_B and ω_B/ω_A) and diagonal peaks (ω_A/ω_A and ω_B/ω_B).

Each 2D experiment consists of the preparation time where the equilibrium magnetization is transformed via a 90° pulse into the transverse magnetization. This magnetization can now evolve during the evolution time t_1 until a second 90° pulse changes the evolved signal into an observable one. During this mixing time, magnetization can be transferred from one spin to another (coupling). After the last pulse, the observable magnetization is detected during the detection time t_2. A Fourier transformation in t_2 would lead again to a 1D spectrum with the signals evolved in t_1. For the second dimension, the experiment is repeated several times and t_1 is extended by a second time interval Δ_1 for each new experiment (called increment). Hence, each increment has a different total evolution time t_1 and a Fourier transformation in t_1 results in the second dimension. Therefore, both Fourier transformed time domains give spectra in the frequency domains ω^1 and ω^2 and the typical 2D cross peaks can be seen. Hereby, for homonuclear experiments four peaks per frequency pair ω_A and ω_B are visible as shown in Figure 2.8: The two cross peaks at ω_A/ω_B and ω_B/ω_A and two diagonal peaks at ω_A/ω_A and ω_B/ω_B[33,35].

2.1.5 Relaxation and NOE

In section 2.1.1 the two types of relaxation (T_1 and T_2) were shortly discussed. The T_1 time is the relaxation from the "spin-reservoir" to the equilibrium z-magnetization and the T_2 time shows how fast the excited magnetization dephases to a net magnetization of zero. Both relaxation times are very

important to consider as both limit the time a pulse sequence needs for optimal results. If there is no excited magnetization left before the acquisition starts, no signal is detectable. Luckily, both relaxations are on the order of seconds and normally enough magnetization is left for the acquisition. On the other hand, the next experiment needs to wait until the magnetization is back to equilibrium. Otherwise, the starting magnetization is reduced and potential signal is lost. Especially, if more than one scan is acquired in an experiment, this needs to taken into account. As the theory of relaxation in NMR is a complex topic which can fill books by its own, it follows only a short description and for more and deeper knowledge, the reader is referred to other literature (e.g. from James Keeler[35])
The mechanism behind the relaxation is that small local fluctuating fields in the sample transfer energy between the magnetic energy of spins and the energy of thermal motion. After the spins get excited by a pulse, they gain energy which they loose again over time into the energy reservoir of thermal motion (T_1). The local fields vary for all spins in the sample, hence their precession frequency is slightly different. Over time, more and more spins will be out of step (= dephased) until they are all randomly oriented in the x,y direction and the net magnetization is zero (T_2). The local field is influenced by many sources. The most dominant ones for spin 1/2 nuclei are the chemical shift and the dipole-dipole coupling. This means, the main parameters influencing the local fields are the gyromagnetic ratios, the distance r between two spins ($1/r^3$) and the orientation of the vector between both spins relative to the magnetic field[35].

The random thermal motion depends on vibration and rotation. Vibration of molecules is at much higher frequencies than the Larmor frequency and can thus be neglected for the relaxation. Rotations are on the same order of magnitude as the Larmor frequency in gases. In liquids, rotations are more constrained due to the density of the liquids. Nevertheless, a molecule will move randomly through the solution which is called *rotational diffusion*. After some time, the molecule will be at some other place. This average time the molecule needs to move one radian from its starting position, is then called *rotational correlation time* τ_c. The correlation time varies from 10 ps for small molecules to 10 ns for small proteins and its reciprocal ($1/\ \tau_c$) is the frequency of this movement which is then as well in the range of ω^0. For quantifying this motion, two functions are needed: the correlation function $G_c(\tau)$ and the spectral density $\mathcal{J}(\omega)$ which is the Fourier transformed of $G_c(\tau)$. For a spherical molecule these are approximately

$$G_c(\tau) = \overline{B_{loc}^2} exp\left(\frac{-|\tau|}{\tau_c}\right) \tag{2.64}$$

$$J(\omega) = \overline{B_{loc}^2}\frac{2\tau_c}{1+\omega^2\tau_c^2} = \overline{B_{loc}^2} j(\omega) \tag{2.65}$$

The maximum of $\mathcal{J}(\omega)$ is at $\omega = 0$ and decreases for higher frequencies. The rate of the decrease is determined by τ_c where shorter correlation times spread the spectral density to higher frequencies. On the other hand, if the spectral density function is plotted for a given Larmor frequency as a function of τ_c, it will have a maximum when $\omega^0\tau_c = 1$ which means that the rate of longitudinal relaxation will have its maximum at $\tau_c = 1/\omega^0$, too[35]. Mathematically, the spectral density function has two limits which can be called in terms of relaxation, the *fast motion* and *slow motion* limits. In the fast motion limit $\omega\tau_c \ll 1$ and the denominator ≈ 1, hence

$$j(\omega) = 2\tau_c \tag{2.66}$$

and the spectral density is independent of the Larmor frequency. In the slow motion limit $\omega\tau_c \gg 1$ and the spectral density can be written as

$$j(\omega) = \frac{2\tau_c}{\omega^2\tau_c^2} \tag{2.67}$$

and therefore $j(\omega)$ gets much smaller than $2\tau_c$[35].

Another very important effect is the cross relaxation of two spins via dipolar interaction (Fig. 2.9). The two spins can be either in the α or β state which gives four different energy levels where two have approximately the same energy in the homonuclear case ($\alpha\beta$ and $\beta\alpha$). The relaxation-induced transitions can be between all of these energy levels resulting in four transitions where one spin changes (W_1), one transition where both spins change and the quantum number changes by two (W_2) and one where both spins change but the quantum number does not change (W_0). $W_{\Delta M}$ is hereby the rate constant for the transitions with the change in the quantum number ΔM as index.

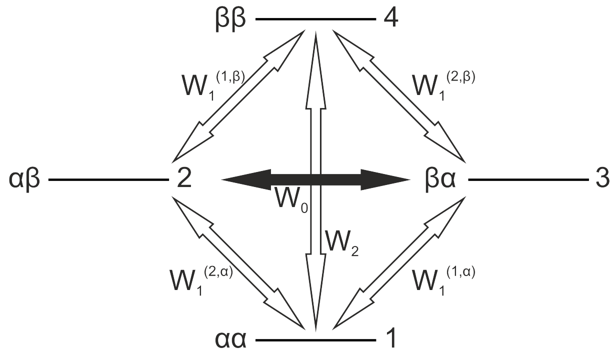

Figure 2.9: The possible transitions of dipolar relaxation in a two-spin system with all four energy levels. The index of W shows the change in the quantum number, the superscript shows which spin is flipping during the transition. 1-4 are simply the names for the four different energy levels. The shown energy levels are for the homonuclear case, in the heteronuclear case $\alpha\beta$ and $\beta\alpha$ will have different energies (adapted from [35]).

As the z-magnetization depends on the population difference (n_i - n_j) between two states i and j, the z-magnetization can be written in form of the spin operator $\hat{I}_{1z}$ for spin one or $\hat{I}_{2z}$ for spin two instead of $M_{1,z}$ or $M_{2,z}$ respectively.

$$I_{1z} = (n_1 - n_3) + (n_2 - n_4) \quad \text{and} \quad I_{2z} = (n_1 - n_2) + (n_3 - n_4) \tag{2.68}$$

The magnetization does not only depend on the sum of both possible transitions but also on the difference which is denoted $2I_{1z}I_{2z}$

$$2I_{1z}I_{2z} = (n_1 - n_3) - (n_2 - n_4) = (n_1 - n_2) - (n_3 - n_4) \tag{2.69}$$

and it has a equilibrium value which is given by

$$I_{1z}^0 = n_1^0 - n_3^0 + n_2^0 - n_4^0 \quad \text{and} \quad I_{2z}^0 = n_1^0 - n_2^0 + n_3^0 - n_4^0 \tag{2.70}$$

The equilibrium value of $2I_{1z}I_{2z}$ is zero. With these equations, the rate equations for the populations can be written as

$$\frac{dI_{1z}}{dt} = -R_z^{(1)}(I_{1z} - I_{1z}^0) - \sigma_{12}(I_{2z} - I_{2z}^0) - \Delta^{(1)}2I_{1z}I_{2z} \tag{2.71}$$

$$\frac{dI_{2z}}{dt} = -\sigma_{12}(I_{1z} - I_{1z}^0) - R_z^{(2)}(I_{2z} - I_{2z}^0) - \Delta^{(2)} 2I_{1z}I_{2z} \tag{2.72}$$

$$\frac{d2I_{1z}I_{2z}}{dt} = -\Delta^{(1)}(I_{1z} - I_{1z}^0) - \Delta^{(2)}(I_{2z} - I_{2z}^0) - R_z^{(1,2)} 2I_{1z}I_{2z} \tag{2.73}$$

where the constants are defined as follows:

$$R_z^{(1)} = W_1^{(1,\alpha)} + W_1^{(1,\beta)} + W_2 + W_0 \tag{2.74}$$

$$R_z^{(2)} = W_1^{(2,\alpha)} + W_1^{(2,\beta)} + W_2 + W_0 \tag{2.75}$$

$$\sigma_{12} = W_2 - W_0 \tag{2.76}$$

$$\Delta^{(1)} = W_1^{(1,\alpha)} - W_1^{(1,\beta)} \tag{2.77}$$

$$\Delta^{(2)} = W_1^{(2,\alpha)} - W_1^{(2,\beta)} \tag{2.78}$$

$$R_z^{(1,2)} = W_1^{(1,\alpha)} + W_1^{(1,\beta)} + W_1^{(2,\alpha)} + W_1^{(2,\beta)} \tag{2.79}$$

$\mathrm{R}_z^{(1)}$ and $\mathrm{R}_z^{(2)}$ are the self relaxation constants of spin one and two which means the magnetization of these spins relax back to equilibrium without the involvement of the other spin magnetization and $R_z^{(1,2)}$ is the same for the $2I_{1z}I_{2z}$ term. The rate constant σ_{12} is the relaxation between spin one and two which is called *cross relaxation*. This cross relaxation is (almost) unique for dipolar relaxation and responsible for the NOE. The two other rate constants $\Delta^{(1)}$ and $\Delta^{(2)}$ describe the interconversion from I_{1z} with $2I_{1z}I_{2z}$ and I_{2z} with $2I_{1z}I_{2z}$. Actually, $\mathrm{W}_1^{(1,\alpha)}$ and $\mathrm{W}_1^{(1,\beta)}$ are equal for dipolar relaxations as well as $\mathrm{W}_1^{(2,\alpha)} = \mathrm{W}_1^{(2,\beta)}$ which simplifies $\Delta^{(1)}$ and $\Delta^{(2)}$ to zero and the rate equations 2.71, 2.72 and 2.73 to

$$\frac{dI_{1z}}{dt} = -R_z^{(1)}(I_{1z} - I_{1z}^0) - \sigma_{12}(I_{2z} - I_{2z}^0) \tag{2.80}$$

$$\frac{dI_{2z}}{dt} = -\sigma_{12}(I_{1z} - I_{1z}^0) - R_z^{(2)}(I_{2z} - I_{2z}^0) \tag{2.81}$$

$$\frac{d2I_{1z}I_{2z}}{dt} = -R_z^{(1,2)} 2I_{1z}I_{2z} \tag{2.82}$$

The rate constants simplify then the same way to

$$R_z^{(1)} = W_1^{(1)} + W_2 + W_0 \tag{2.83}$$

$$R_z^{(2)} = W_1^{(2)} + W_2 + W_0 \tag{2.84}$$

$$\sigma_{12} = W_2 - W_0 \tag{2.85}$$

$$R_z^{(1,2)} = W_1^{(1)} + W_1^{(2)} \tag{2.86}$$

The cross relaxation between I_{1z} and I_{2z} is still there but no more interconversion with $2I_{1z}I_{2z}$. Equations 2.80, 2.81 and 2.82 are called the *Solomon equations*[35].

As the cross relaxation is a dipolar interaction, $W_{\Delta M}$ depends on the spectral density and the dipole-dipole coupling b_{jk} (here with spins 1 and 2)

$$W_1^{(1)} = \frac{3}{40} b_{12}^2 j\left(\omega^{0,1}\right) \quad W_1^{(2)} = \frac{3}{40} b_{12}^2 j\left(\omega^{0,2}\right) \quad W_2 = \frac{3}{10} b_{12}^2 j\left(\omega^{0,1} + \omega^{0,2}\right) \quad W_0 = \frac{1}{20} b_{12}^2 j\left(\omega^{0,1} - \omega^{0,2}\right) \tag{2.87}$$

where the factor in front of the equation comes from the Hamiltonian of the interaction causing relaxation. As the rate constants $R_z^{(1)}$, $R_z^{(2)}$ and $R_z^{(1,2)}$ are always positive, only the cross relaxation rate constant σ_{12} needs a closer look

$$\sigma_{12} = b_{12}^2 \frac{3}{10} j\left(2\omega^0\right) - b_{12}^2 \frac{1}{20} j(0) \tag{2.88}$$

where $j(\omega^{0,1} + \omega^{0,2})$ becomes $j(2\omega^0)$ for homonuclear spins and $j(\omega^{0,1} - \omega^{0,2})$ becomes $j(0)$ with $j(0) = 2\tau_c$. Again the fast and slow motion limit can be calculated where $j(2\omega^0) = 2\tau_c$ in the fast motion limit

$$\sigma_{12} = \frac{1}{2} b_{12}^2 \tau_c \tag{2.89}$$

and in the slow motion limit the spectral density is negligible due to a high value of $\omega^0\tau_c$

$$\sigma_{12} = -\frac{1}{10} b_{12}^2 \tau_c \tag{2.90}$$

So, in the fast motion limit σ_{12} is positive and in the slow motion limit it is negative. When $W_2 = W_0$, $\sigma_{12} = 0$ which is the crossover point where

$$b_{12}^2 \frac{3}{10} j\left(2\omega^0\right) = b_{12}^2 \frac{1}{20} j(0) \tag{2.91}$$

and hence the product $\omega^2\tau_c = \sqrt{\frac{5}{4}}$ if $j(\omega)$ is substituted in the equation[35].
The cross relaxation gets very important in the so called *NOE*. The z-magnetization of spin one changes with the dipolar relaxation of spin two (Eq. 2.80) which is proportional to σ_{12} and hence to $1/r^6$ as $\sigma_{12} \sim b_{12}^2$. Approximately, only protons in a distance of up to 5 Å will be close enough to observe cross relaxation due to $1/r^6$. As the dipolar interaction is through space, the corresponding NOESY (NOE SpectroscopY) spectra will normally show cross peaks for all nuclei in a distance less than 5 Å.

Depending on the correlation time, the NOE can be either positive for small τ_c (fast motion limit) or negative for high τ_c (slow motion limit)[33,35].

With the Solomon equations, the longitudinal relaxation T_1 can be calculated as well. The whole z-magnetization is the sum of both individual spins in Equation 2.80 and 2.81.

$$\frac{dI_z}{dt} = \frac{dI_{1z}}{dt} + \frac{dI_{2z}}{dt} = -R_z^{(1)}(I_{1z} - I_{1z}^0) - \sigma_{12}(I_{2z} - I_{2z}^0) - \sigma_{12}(I_{1z} - I_{1z}^0) - R_z^{(2)}(I_{2z} - I_{2z}^0) \tag{2.92}$$

This equation can be simplified by substituting $R_z^{(1)} + \sigma_{12}$ with $R_{sum,1}$ and the same for $R_z^{(2)}$ in case of intramolecular dipole-dipole couplings, leading to

$$\frac{dI_z}{dt} = -(R_{sum,1} + R_{sum,2})(I_z - I_z^0) \tag{2.93}$$

where

$$R_{sum,1} + R_{sum,2} = W_1^{(1)} + W_2 + W_0 + W_2 - W_0 + W_1^{(2)} + W_2 + W_0 + W_2 - W_0 = W_1^{(1)} + W_1^{(2)} + 2W_2 \tag{2.94}$$

which simplifies even further if both spins are from the same nuclei to the reciprocal of T_1

$$\frac{1}{T_1} = 2W_1 + 2W_2 = \frac{3}{20} b_{11}^2 \left(j(\omega^0) + 4j(2\omega^0) \right) \tag{2.95}$$

and therefore

$$\frac{1}{T_1} = \frac{3}{20} b_{11}^2 \left(\frac{2\tau_c}{1 + \omega^2\tau_c^2} + \frac{8\tau_c}{1 + 4\omega^2\tau_c^2} \right) \tag{2.96}$$

Again, the fast and slow motion limit can be calculated. For the fast motion limit with $\omega^0\tau_c \ll 1$, both denominators are 1 which gives $10\tau_c$ in the brackets and

$$\frac{1}{T_1^{fast}} = \frac{3}{2} b_{11}^2 \tau_c \tag{2.97}$$

for the slow motion limit, the brackets will be $2/\omega^2\tau_c$ and

$$\frac{1}{T_1^{slow}} = \frac{3b_{11}^2}{10\omega^2\tau_c} \tag{2.98}$$

For the spectroscopist, the qualitative interpretation is that for small correlation times T_1 only depends on the reciprocal of the correlation time, which means $1/\tau_c$ increases for decreasing τ_c and hence T_1 is increasing. On the other hand, for high correlation times, T_1 is proportional to τ_c and therefore increases with increasing τ_c[34,65].

Similar, the transverse relaxation T_2 can be calculated for intramolecular dipole-dipole relaxation giving

$$\frac{1}{T_2} = \frac{3}{40} b_{11}^2 \left(3j(0) + 5j(\omega^0) + 2j(2\omega^0)\right) \tag{2.99}$$

or rewritten with the spectral density functions

$$\frac{1}{T_2} = \frac{3}{40} b_{11}^2 \left(6\tau_c + \frac{10\tau_c}{1+\omega^2\tau_c^2} + \frac{4\tau_c}{1+4\omega^2\tau_c^2}\right) \tag{2.100}$$

The fast motion limit for a small correlation time shows an increase for T_2 which is exactly like the one for T_1

$$\frac{1}{T_2^{fast}} = \frac{3}{2} b_{11}^2 \tau_c \tag{2.101}$$

The slow motion limit on the other hand is different from T_1

$$\frac{1}{T_2^{slow}} = \frac{3}{40} b_{11}^2 \left(6\tau_c + \frac{11}{\omega^2\tau_c}\right) \approx \frac{9b_{11}^2\tau_c}{20} \tag{2.102}$$

The fraction will get negligibly small compared to $6\tau_c$ and T_2 decreases for higher correlation times. This effect can be observed qualitatively as spectral line broadening where the full width at half-maximum (FWHM) = $1/(\pi T_2)$ in units of Hertz[34,35]. The correlation time does not only depend on the size of the molecule but it is also proportional to η/T as Debye assumed,

$$\tau = \frac{4\pi\eta a^3}{kT} \tag{2.103}$$

where η is the viscosity, a the radius of a sphere approximating the molecule and T the temperature of the sample[65,66].

2.2 Rheology

In 1920, the chemistry professor Eugene Bingham embossed the word *rheology* which comes from the Greek verb to flow ($\rho\epsilon\iota\nu$). The field of rheology studies everything which deals with flow behavior (aeronautics, hydraulics, fluid dynamics and solid mechanics) and deformation. A rheologist focuses on the material behavior, mostly of liquids[67]. A special case are hereby complex fluids (like a LC) which show mechanical properties of solid- and liquid-like behavior with not only viscous response but also elastic response (called viscoelasticity). As will be seen later in section 2.4.2, such materials exhibit effects after shear cessation depending on the history of the applied strain[68]. The everyday person can "feel" rheology for example in food. The ketchup in the bottle, which only starts to come out of the bottle by some force (hitting on the bottom) and then very fast and nearly not controllable. It is a nice example for a shear-thinning effect which will be discussed later. Another rheological example from everyday life is the production of ice cream where some additives and stirring create a foam with a certain viscosity so that the consumer does not just drink a liquid with flavor[69].

2.2.1 Basics

The fundamental equation in rheology is Hooke's law where the force is proportional to the deformation.

$$\tau = G\gamma \tag{2.104}$$

Hereby, τ is the force per unit area (stress), γ the relative length change (strain) and G the constant of proportionality (elastic modulus) for solids. For liquids on the other hand, the constant of proportionality is the Newtonian viscosity η where the stress is proportional to the rate of straining after Newton's law[67].

$$\tau = \eta\dot{\gamma} = \eta\frac{d\gamma}{dt} \tag{2.105}$$

The viscosity of the liquid is temperature dependent according to Arrhenius law

$$\eta(T) = c_1 exp\left(-\frac{E_A}{RT}\right) \tag{2.106}$$

where c_1 is material constant in [Pas], E_A is the activation energy, R the gas constant ($R = 8.314 \cdot 10^{-3}$ kJ/(mol·K) and T the temperature of the system[70].
Viscoelastic experiments are a combination of Hook's spring and Newton's dashpot where after the Maxwell model for viscoelastic liquids the spring and the dashpot are arranged in series as can be seen in Figure 2.10. Under stress, first the spring will show a deformation until the maximum deflection where the dashpot starts to move under the continuous stress. After cessation of the stress, the spring will directly fall back in the starting position but the dashpot stays in its deformation which is irreversible[70].

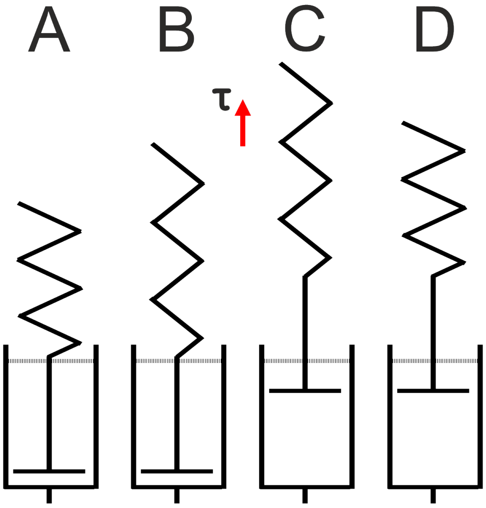

Figure 2.10: The Maxwell-model shows the viscoelastic response of a system where the viscous part can be described as a dashpot and the elastic part as a spring. The red arrow indicates the stress direction in B and C. A) Both are in the starting position as no stress is on the system yet. B) Only the spring answers to stress and is deformed. The dashpot does not show a reaction on the stress yet. C) The spring is fully deformed and hence the dashpot is reacting to the continuous stress with deformation. D) After cessation of stress the spring directly bounces back in the original state. The dashpot does not relax back and the deformation of the whole system is irreversible (adapted from [70]).

The time-dependent response of the whole system can be described with the relaxation modulus G(t)

$$G(t) = \frac{\tau(t)}{\gamma} \tag{2.107}$$

which is identical to Hook's law only that elastic solids do not show any relaxation. As the response is mostly an sinusoidally oscillation, the stress and the strain can be written as

$$\gamma = \gamma_0 \sin(\omega t) \tag{2.108}$$

$$\tau = \tau_0 \sin(\omega t + \delta) \tag{2.109}$$

with the phase angle δ. The stress for the system is then analyzed as two waves of the same frequency where both waves are shifted by 90° to each other

$$\tau = \tau' + \tau'' = \tau_0' \sin(\omega t) + \tau_0'' \cos(\omega t) \tag{2.110}$$

After insertion of the sine modulated equations and solving for the angle, following equation is obtained

$$\tan(\delta) = \frac{\tau_0''}{\tau_0'} \tag{2.111}$$

Similar, the relaxation modulus can be differentiated in the elastic (storage) modulus *G'* and the viscous (loss) modulus *G"*

$$G' = \frac{\tau_0'}{\gamma_0} \tag{2.112}$$

$$G'' = \frac{\tau_0''}{\gamma_0} \tag{2.113}$$

where both are only different by the angle δ as well

$$\tan(\delta) = \frac{G''}{G'} \tag{2.114}$$

The curves of *G'* and *G"* describe how well energy is stored or lost in the system[67]. From Equations 2.108 and 2.109 one can see that both moduli are not only dependent on time but also on the frequency ω of the oscillation. If displayed logarithmically, both moduli increase linearly for liquid-like polymers with rising ω. Similar, the stress increases linear with the shear rate for liquid-like systems, but with time the stress stays constant. The viscosity also stays constant for liquid-like polymers with increasing shear rate. Special attention must be paid to the rotating walls of a rheometer where the so called *wall-slip* is possible. If the investigated liquid behaves solid-like at these walls, it can slip against the wall and the flow is completely different at this boundary compared to the rest of the gap[69]. For a characterization if the polymer behaves liquid- or solid-like and behaves linear or nonlinear viscoelastic, the dimensionless

Deborah number De can help. It is defined as the materials relaxation time τ_{relax} divided by the flow time t

$$De = \frac{\tau_{relax}}{t} = \frac{\eta_0}{Gt} \quad \text{with} \quad \tau_{relax} \approx \frac{\eta_0}{G} \tag{2.115}$$

where the materials relaxation time can roughly be described as the zero shear viscosity η_0 divided by the relaxation modulus[67,69]. The responses of the polymer can then be classified as De » 1 where the response is solid-like, De « 1 where the response is liquid-like and $De \approx 1$ where the response is viscoelastic. To characterize a polymer in the nonlinear viscoelastic regime, the three most important nonlinear phenomena need to be investigated: *normal stress differences*, *shear thinning* and *extensional thickening*[67].

2.2.1.1 Normal stress difference

The shearing of viscoelastic material between two parallel plates produces not only stress, but also the so called normal stress differences N_1 and N_2. If the stress is written as a tensor **T** for its direction along the material volume is

$$\mathbf{T}^{p}_{ij} = \begin{pmatrix} \tau_{xx} & \tau_{xy} & \tau_{xz} \\ \tau_{yx} & \tau_{yy} & \tau_{yz} \\ \tau_{zx} & \tau_{zy} & \tau_{zz} \end{pmatrix} \tag{2.116}$$

then the normal stress differences are

$$N_1 = \tau_{xx} - \tau_{yy} \tag{2.117}$$

and

$$N_2 = \tau_{yy} - \tau_{zz} \tag{2.118}$$

where x is the direction of the flow, y is perpendicular to the surfaces between the fluid is sheared and z is a neutral perpendicular direction. N_1 is normally larger than N_2 and usually of positive sign (exceptions are LCs) and N_2 of negative sign. The typical ratio of -N_1/N_2 for non linear viscoelastic materials is around 0.05 and 0.3. Experimentally, N_1 is for example the thrust per unit area in a cone and plate rheometer. For positive values the plates are pushed apart, for negative values they are pulled together by N_1[67,69,70].

2.2.1.2 Shear thinning

Shear thinning behavior is when the viscosity of the sheared material decreases with increasing shear rate which is especially developed in polymer melts and in concentrated polymer solutions. It can be explained with the entangled concept where chains and loops at rest of the macromolecule build a huge network. Under shear, this network partially breaks up and the chains and loops are aligned in the direction of shear. This reduces the flow resistance and hence the viscosity. Once shearing stops, the material accumulates again[67,70]. If the shear rate is low enough, many materials have a constant shear rate until the shear thinning starts. This first critical value is the zero shear viscosity η_0[70]. LC polymers show a special response of their viscosity under shear. They exhibit shear thinning and shear plateaus (viscosity is not changing with shear) in different regions which will be explained further in section 2.4.2. Some materials show an increase in viscosity with rising shear rates instead which is called *shear thickening*. The polymer molecules will entangle more with each other which increases the flow resistance and therefore the viscosity[70]. Some materials even show shear thinning and shear thickening behavior for different shear rate regimes[69].

2.2.1.3 Extensional thickening

In an extensional flow, the polymers are not sheared or rotated but stretched or extended with special devices. These devices pull on both sides of the polymer and lengthen the whole material over time. For polymer melts which are difficult to grip at their ends rupturing of the polymer is possible. Other materials like sticky polymers are easier to handle. During this extension, the viscosity of the stretched polymer increases. The same material which is shear thinning under shear, can thicken under extension. But there is no correlation between extensional thickening and shear thinning, the magnitude of both effects can be similar or not. For each new material the shear and extension viscosity needs to be measured separately. A polymer can be stretched until it ruptures without ever showing a steady-state plateau in its extension viscosity[67,69].

2.2.2 Rheological devices

Rheological characteristics (e.g. viscosity, shear stress) need very precise measurement devices, a so called *rheometer* which can measure stress and deformation history (strain). Equation 2.105 consists only of stress, strain and the material constant viscosity. Hence, it is clear that a rheometer either measures stress with a given strain or measures the strain with a given stress as the viscosity is always calculated out of stress and strain. Nowadays, many rheometers exist, each slightly different and perfected for special types of liquids or measurement regimes. All of these rheometers need to fulfill two requirements for accurate measuring. The sample adheres on both walls without any sliding effects and inside the rheometer has to be a laminar flow without any turbulences[67,70].

The strain rheometers are divided into homogeneous deformation where stress and strain are independent of the position in the sample, nonhomogeneous deformation where the applied stress is a function of the position, and the complex or indexer deformation where constitutive equations are needed to relate stress and strain inside the rheometer as the device is build more complex. Hereby, a strain rheometer with homogeneous deformation can measure all three regions of straining: small, large and steady. With nonhomogeneous deformation only small and steady straining are reliably measured, large straining is not measurable. The indexer rheometer does not measure any straining reliably and is therefore of no use for fundamental rheological work but is often used if data does not need to be precise. Their big advantage is that they are lower in cost and easier to operate. Examples for homogeneous deformation are the sliding plates, concentric cylinders or cone and plate, for nonhomogeneous deformation are flow through a capillary or parallel disks and for indexer rheometers are quality control rheometers in food industry. A second discrimination of rheometer hardware types can be made by the type of flow used: a drag flow where a moving surface produces shear on a fixed surface and the pressure-driven flows where a pressure difference generates shear[67].

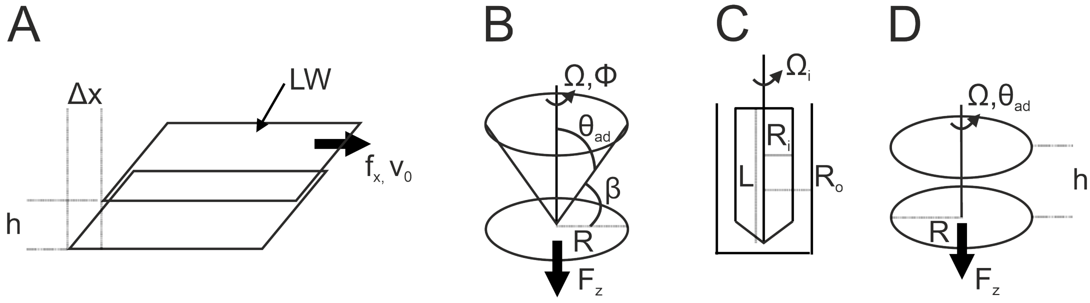

Figure 2.11: Four different types of rheometers are shown A) The top plate with the area LW of the sliding plates is pulled at constant shear in x-direction with a gap height h which is filled with the sample. B) A concentric cylinder is rotating with the angular frequency Ω on a flat surface with a cone angle β. The measured liquid is between the plate at the bottom and the cone on top. C) The Couette geometry consists of two cylinders where either the inner or outer cylinder is rotating or both with the respective angular frequencies Ω_i or Ω_o. The gap between both cylinders is difference R_o - R_i. D) In the parallel disk rheometer two round plates are on top of each other with the sample between with the gap height h. The top plate is rotating with the angular frequency Ω (adapted from [67, 70]).

2.2.2.1 Sliding plates

The sliding plates rheometers (Fig. 2.11A) are very simple. On a fixed surface lies the investigated liquid. Another plate on top moving in constant velocity creates homogeneous shear stress over the whole sample if inertial and edge effects are neglected. Therefore, shear strain, shear rate and shear stress are

$$\gamma = \frac{\Delta x}{h} = \frac{v_0 t}{h} \tag{2.119}$$

$$\dot{\gamma} = \frac{v_0}{h} \tag{2.120}$$

$$T_{xy} = \frac{f_x}{LW} \tag{2.121}$$

where Δx is the distance the top plate is moving in the time t with the velocity v_0, h is the distance between the two plates, f_x is the thrust in x-direction and LW is the area of the plate. Inertial effects can be neglected for very short times or at high frequency oscillation, edge effects on the other hand are more difficult and increase with strain. Unless LW is much greater than h, buckling (≈ the structure bends sideways) occurs for solids and and it is difficult to reach large strains and normal forces as the plates need to stay exactly parallel the whole time. On top, liquids have the problem that they spread easily unless the viscosity is high enough which gives then the problem of buckling like in solids[67].

2.2.2.2 Concentric cylinders

The concentric cylinders or *Couette geometry* (Fig. 2.11C) after Maurice Couette[71] was the first built concentric cylinder in 1890. He took an outer rotating cup (Cup) and a static inner cylinder (Bob). The torque on the inner cylinder could be measured by a mirror showing the angular deflection of a torsion wire which connected Cup and Bob. The instruments today use similar concepts. For calculations, a few assumptions must be made in this geometry. The flow inside the cylinders is steady, laminar and isothermal, gravity and end effects are negligible, there is a symmetry in the angular displacement Θ_{ad} with $\partial/\partial\Theta_{ad} = 0$ and the velocity can be calculated as

$$v_{\Theta_{ad}} = r\Omega \quad \text{and} \quad v_r = v_z = 0 \tag{2.122}$$

with the radius r and the angular frequency Ω. The boundary conditions for the concentric cylinders are

$$v_{\Theta_{ad}} = \Omega_i R_i \quad \text{at} \quad r = R_i \tag{2.123}$$

$$v_{\Theta_{ad}} = 0 \quad \text{at} \quad r = R_o \tag{2.124}$$

or when both cylinders rotate

$$v_{\Theta_{ad}} = \Omega_o R_o \quad \text{at} \quad r = R_o \tag{2.125}$$

Here, R_i and Ω_i are the radius and angular frequency of the inner cylinder, R_o and Ω_o of the outer cylinder. The shear stress distribution $\tau_{r\Theta_{ad}}$ inside the gap of both cylinders can be described either with the torque on the inner cylinder M_i or equally on the outer cylinder M_o

$$\tau_{r\Theta_{ad}}(R_i) = \frac{M_i}{2\pi R_i^2 L} \tag{2.126}$$

$$\tau_{r\Theta_{ad}}(R_o) = \frac{M_o}{2\pi R_o^2 L} \tag{2.127}$$

with the length L of the Bob. For the shear strain and shear rate exist two possible solutions. If the gap between both cylinders is very narrow ($\kappa = R_i/R_o > 0.99$), the curvature can be disregarded and shear strain and shear rate behave the same way as between parallel plates

$$\gamma = \frac{\Delta x}{\Delta r} = \frac{\Theta_{ad}\overline{R}}{R_o - R_i} \tag{2.128}$$

$$\dot{\gamma}(R_i) \cong \dot{\gamma}(R_o) = \frac{\Delta v}{\Delta r} = \frac{\Omega_i \overline{R}}{R_o - R_i} \quad \text{with} \quad \overline{R} = \frac{R_o + R_i}{2} \tag{2.129}$$

Mostly, this is not the case and the gap is bigger which means the shear rate changes over the gap with the highest shear rate at the rotating wall and the lowest at the non-rotating wall (can be zero in a large gap). Normally, the velocity profile needs to be measured for an exact solution of the shear rate at each position. But as a function of the stress $\tau_{r\Theta_{ad}}$, the shear rates can be calculated quite efficiently with

$$\dot{\gamma}(R_i) - \dot{\gamma}(R_o) = 2\tau_{Ri}\frac{d\Omega_i}{d\tau_{Ri}} \tag{2.130}$$

which leads to

$$\dot{\gamma}(R_i) = \frac{2\Omega_i}{n\left(1 - \kappa^{\frac{2}{n}}\right)} \tag{2.131}$$

$$\dot{\gamma}(R_o) = \frac{2\Omega_o}{n\left(1 - \kappa^{\frac{-2}{n}}\right)} \quad \text{with} \quad n = \frac{dlnM_i}{dln\Omega_i} \tag{2.132}$$

where the Maclaurin series was used to derive both equations out of Equation 2.130. As the concentric cylinders are calculated in cylindrical coordinates, the first normal stress difference N_1 is then

$$\tau_{xx} - \tau_{yy} = \tau_{\Theta_{ad}\Theta_{ad}} - \tau_{rr} = \frac{(\tau_{rr}(R_i) - \tau_{rr}(R_o))\overline{R}}{R_o - R_i} \tag{2.133}$$

where $\overline{R}$ is the distance to the midpoint of the cylinder and the stress difference $\tau_{rr}(R_i)$ - $\tau_{rr}(R_o)$ is the pressure difference between both cylinders. If N_1 is a large positive number in concentric cylinders, the so called *Weissenberg effect* can be observed which means the liquid is climbing on the inner rod to the top[67]. The molecules at the outer wall do not have enough energy to follow the shear at the outer wall and will all be pushed into the middle where the lowest energy is needed for following the shear. As there is not enough place, the molecules evade into the only free direction which is climbing up the middle rod[70].

In this geometry end effects need to be considered as well. One end is the bottom, where inner cylinder and outer cylinder approximately behave like parallel disks which is an extra torque contribution for this end and can be minimized by changing the inner cylinder geometry at the bottom. For example, it can be built as a double Couette cylinder with a recessed bottom or with a conic cylinder which is then a cone and plate at the bottom. The other end is the top where the liquid is in contact to a gas phase (mostly air). Therefore, the top end does not give any geometrical problems, but the surface tension and evaporation of the liquid might trouble. Especially, if the liquid is easily evaporating, a stiff and solid-like crust is generated at the top which has a huge impact on the characteristics at this spot. Also, the rod climbing effect plays a role here if it happens. Nevertheless, solutions at this end are all trying to reduce the amount of free surface at the top (e.g. by low density oils or a second conic cylinder design) which reduces these effects[67].

The last effect which plays a major role in this geometry is frictional heat produced by the rotation. Equation 2.106 shows that this increase in temperature is decreasing the viscosity and volatile solvents will evaporate faster at the top end at higher temperatures. For this reason, most rheometers are temperature controlled with cooling outside of the cell reducing this frictional heat[67].

2.2.2.3 Cone and plate

The cone and plate rheometer (Fig. 2.11B) is the most used one studying non-Newtonian effects. It has a constant rate of shear and directly measures N_1 by total thrust. For calculations, here are some assumptions needed as well. Similar to the Couette geometry, a steady, laminar and isothermal flow is needed and $v_r = v_{\Theta_{ad}} = 0$ and hence only the velocity of the angular displacement Φ ($v_\Phi(r, \Theta_{ad})$ is of importance. The angle β between the cone and the bottom plate should always be smaller than 0.1 rad ($\approx 6°$) and body forces are negligible. The last assumption is that the liquid is spherical meaning the curvature at the edge of the geometry is spherical due to surface tension reducing slip at the edge. The boundary conditions for the whole geometry are then

$$v_\Phi \left(\frac{\pi}{2}\right) = 0 \tag{2.134}$$

$$\begin{aligned} v_\Phi \left(\frac{\pi}{2} - \beta\right) &= \Omega r \sin\left(\frac{\pi}{2} - \beta\right) = \Omega r \\ \text{for} \quad \sin\left(\frac{\pi}{2} - \beta\right) &= \cos\beta = 1 - \frac{\beta^2}{2!} + \frac{\beta^4}{4!} + \ldots \cong 1 \quad \text{if} \quad \beta \leq 0.1 \end{aligned} \tag{2.135}$$

and the shear stress inside is

$$\tau_{\Phi\Theta_{ad}}(\Theta_{ad}) = \frac{3M}{2\pi R^3 \sin^2 \Theta_{ad}} \tag{2.136}$$

which can be reduced to

$$\tau_{xy} = \tau_{\Phi\Theta_{ad}} = \frac{3M}{2\pi R^3} \tag{2.137}$$

with the boundary condition of $\beta < 0.1$ rad which gives for $\sin^2\left(\frac{\pi}{2} - \beta\right) = 0.990 \approx 1$. Therefore, the shear stress is approximately constant over the whole geometry for $\beta < 6°$. The same applies to the shear strain and the shear rate, which are constant with an error of less than 0.7 % for $\beta < 6°$.

$$\gamma = \frac{\Phi}{\beta} \quad \text{and} \quad \dot{\gamma} = \frac{\Omega}{\beta} \tag{2.138}$$

That is the reason why the cone and plate rheometer is so attractive for rheologists. Also the normal stress difference can be calculated very easily.

$$\tau_{xx} - \tau_{yy} = \tau_{\Phi\Phi} - \tau_{\Theta_{ad}\Theta_{ad}} = \frac{2F_z}{\pi R^2} \tag{2.139}$$

with the thrust in z-direction F_z. Contrary to the Couette rheometer, the fluid inside does not climb on a cylinder. Instead, the measured normal forces in a cone and plate are negative and therefore the plates are pulled together and the torque will be increased by secondary flow effects. One of the major problems of this rheometer is with high viscosity samples. At low shear rates they flow out of the plates and a hole in the middle originates. It seems, there will be a critical edge velocity for materials. With increasing viscosity and decreasing surface tension, the critical velocity decreases. Similar as in the Couette geometry, the solvent will evaporate at the edge of the cone and plate and sample crust will be left there. The frictional heating is not that big of a problem in this geometry and with Newtonian fluids mostly negligible[67].

2.2.2.4 Parallel disks

The parallel disks rheometer (Fig. 2.11D) is very similar to the cone and plate. Instead of the cone rotating on a flat surface, a second flat plate is rotating on top. The main difference between both rheometers is the flow. For parallel disks it s not homogeneous but still steady, laminar and isothermal. The velocities v_r and v_z are both zero and the only velocity $v_{\Theta_{ad}}(r,z)$ is around the angular displacement Θ_{ad}. The body forces are negligible and a cylindrical edge is assumed. The shear rate for one stationary disk and one rotating at Ω is given by

$$\dot{\gamma}(r) = \frac{r\Omega}{h} \quad \text{with the velocity} \quad v_{\Theta_{ad}}(r,z) = \frac{r\Omega_z}{h} \tag{2.140}$$

if the inertial forces are neglected and no slip at the surfaces occur. Similar, the strain can be calculated with

$$\gamma = \frac{r\Theta_{ad}}{h} \tag{2.141}$$

depending on the position on the plate. In the middle, the strain is zero and at the edge it has its maximum. Additionally, the shear stress depending on the torque M is given by

$$\tau_{xy} = \tau_{\Theta_{ad}z} = \frac{M}{2\pi R^3}\left(3 + \frac{dlnM}{dln\dot{\gamma}_R}\right) \tag{2.142}$$

and the normal stress difference by

$$N_1 - N_2 = \frac{F_z}{\pi R^2}\left(2 + \frac{dlnF_z}{dln\dot{\gamma}_R}\right) \tag{2.143}$$

An advantage of the parallel disks against the cone and plate is the sample loading. It is much easier for viscous and soft solid samples. Also, data at higher shear rates can be obtained much better. By decreasing the gap, secondary flow effects as well as edge effects and shear heating effects can be reduced. This is not possible for the cone and plate rheometer. On the other hand, shear strain and shear rate are not constant over the whole rheometer as in the cone and plate[67].

2.2.2.5 Pressure-driven flow rheometer

The origin for pressure-driven flows goes back to Hagen[72] in 1839 and Poiseuille[73] in 1840 who both measured independently the viscosity of water in a small capillary. They observed that at the center of the flow the velocity is at its maximum but the velocity gradient, the shear rate and shear strain are zero. At the wall, the opposite is the case: the velocity is zero and the velocity gradient, the shear rate and shear strain are at their maximum. All pressure-driven rheometer induce a nonhomogeneous flow and can therefore only measure steady shear functions. Still, they are widely used because of their simplicity and low costs. Also, the most accurate viscosity data can be obtained by long capillaries. Another advantage is their fully closed frame where no gas-liquid interfaces can be found except at the start and end of the capillary. Hence, the edge effects of, for example, the cone and plate do not exist as well as solvent evaporation and other effects at a free surface. The two most famous types of pressure-driven flow rheometers are the capillary flow and the slit flow. Table 2.1 shortly summarizes the most important characteristics of these two rheometers[67].

Table 2.1: The most important characteristics of a capillary flow and a slit flow rheometer taken from reference [67]

Capillary flow	Slit flow
Pressure through gravity, compressed gas or a piston	Pressure through a piston
Capillary tube of radius R and length L	Slit with thickness H and length L
Viscosity is determined by pressure drop and flow rate	Viscosity is determined by pressure
Wall slip due to lower viscosity at the wall	Wall slip due to lower viscosity at the wall
Shear heating for high shear rates and high viscosity at the wall	shear heating general problem
Viscosity is independent of pressure	Direct pressure measurement with pressure transducer

2.2.2.6 General information

All non-flow rheometers are controlled by a motor which induces the rotation. In the beginning, ac synchronous motors coupled to a gear box were often used. They generated a wide range of constant rotation ranges. Nowadays, this motor type is still found but not very often. Instead, dc motors with closed-loop servo control are mainly chosen. This type allows infinite speed variation and programming of the deformation. A dc motor can be coupled directly or indirectly to the shaft. An indirectly coupled motor gives flexibility in size and location, but it limits the deformations which can be programmed due to backslash in the gears. Contrary, in a direct coupled motor a wide range of deformations can be programmed if combined with a servo control system. In this motor a capacitance transducer controls the angular position and a tachometer the angular velocity[67].

For exact measurements, the alignment of parts like the shaft with bearings need high accuracy for the most rheometers, especially for parallel disks and the cone and plate type. Otherwise, the shear rate for example will not be constant over the whole plate surface. Similar, the vertical motion needs to be precise for an optimal loading and unloading of the samples. Also, very often the tip of the cone is removed avoiding unwanted normal forces (around 50 µm). Concentric cylinders on the other hand do not need a perfect alignment if their gap size is ≥ 0.5 mm increasing the play in this type[67].

The other big problem in all rheometer types is the temperature control inside the sample chamber. Without any special equipment, there can be large temperature gradients in the instruments and shear heating will falsify results. By installing an oven or a cooling bath around the sample and shearing part, control of temperature can be regained. Unfortunately, there is not always enough space for such a control in the intended application[67].

The last major issue is the sample evaporation mainly due to exposure to the environment at free surfaces of the rheometer. Porous pads filled with the sample or a suitable solvent for example will prevent evaporation by maintaining a proper humidity inside the device. Or, coating with low viscosity oil is sometimes used for this reason. A more simple way would be to seal the whole rheometer, but this is not possible or affordable for most of the intended applications[67]. A comparison of advantages and disadvantages for the mentioned rheometers can be seen in Table 2.2.

Table 2.2: The advantages and disadvantages of the sliding plates, cone and plate, concentric cylinders and parallel disks[67,70]

	Sliding plates	**Cone and plate**	**Concentric cylinders**	**Parallel disks**
Advantages	Simple design	Small sample volume	Low viscosity fluids cannot flow out of the rheometer	No limits for particle size and three-dimensional structures
	Easy to clean	Easy to clean	one-time outer measuring cylinders if hard to clean	Easy to clean or one-time plates can be used
		air bubbles will be pressed to the outside of the geometry	can be closed on top preventing evaporation	Easy to load viscous samples
	Homogeneous flow	Homogeneous flow if $\beta \leq 0.1$ rad	Homogeneous flow if $R_i/R_o \geq 0.95$	bigger gaps lead to shorter resting time
	Constant shear rate, linear shear strain	Shear rate and shear stress are constant	Good for suspension settling	Shear rate can be changed by gap width
			Easy temperature control due to a high contact surface of the outside cylinder	Temperature effects have less influence on the sample due to the bigger gap
Disadvantages	The sample loading	The sample loading	Difficult to clean which takes a long time	Nonhomogeneous flow
	The edges limit to $\gamma < 10$	Edge effect strongly (turbulences, evaporation)	Turbulences with low-viscosity fluids at high shear rates	Edge effect strongly (turbulences, evaporation)
		Temperature gradient if only the plate is heated	Paste-like fluids often have invisible air bubbles	Temperature gradient if only the plate is heated
	Hard to keep the gap constant	Particle size is limited	High sample volume	Shear conditions dependent on position
		Needs a long equilibration time and a constant temperature due to the small gap		

Rheometers which do not fulfill the DIN and ISO norms are called relative measuring systems and are not allowed to use for official industry characterization of fluids. Devices not fulfilling these norms have turbulences and other unwanted effects which makes exact measurements impossible and therefore all gained characteristics are only relative. On the other hand, this is efficient for most scientific laboratories which reduces the cost and complexity of the system. Sometimes, it might not be possible to explain and repeat some results. The rheologist calls this the *rheo-chaos*[70].

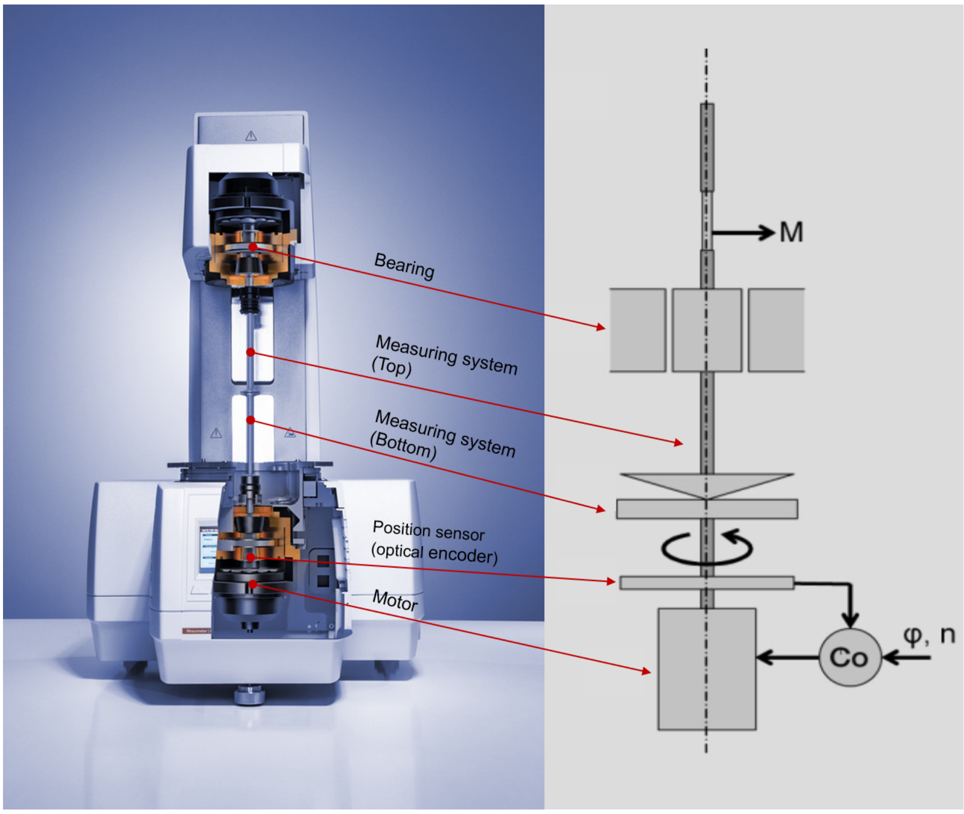

Figure 2.12: An example of a strain-controlled rheometer from Anton Paar GmbH. At the controller (Co) the speed n or the deflection angle ϕ is applied, rotating the cell (here a cone and plate) and the resulting torque M is measured with the transducer (taken without changes from [74] under the CC BY license).

2.3 Rheo-NMR

The non-invasive nature of NMR and its wide range of applications have a major impact in chemical engineering. Together with rheology, which in its simplest form is a device that rotates a sample and applies shear forces on the sample, the application of *rheo-NMR* offers new insights into material properties. The use of NMR during rheology adds the measurement of chemical properties to the originally measured mechanical properties. On the other hand, the NMR community gains a new method that orchestrates the alignment properties of the sample by shear force. The most used NMR tools are so far imaging and velocimetry experiments[17].

In 1990, Nakatani and coworkers[15] were the first ones introducing rheo-NMR as fusion of rheology and NMR. They wanted to monitor the behavior of shear-induced anisotropy in polymers by NMR. In a cone and plate rheometer, poly(dimethylsiloxane) (PDMS) known from stretched gels[43] and poly(isobutylene) (PIB) known from a first attempt under elongational shear strain[75], were used as test-polymers. They were able to prove the principle with their apparatus, but the limitations of non-NMR-active and non-metallic components for the apparatus and a small active volume of the chosen cone and plate cell left room for improvement. Independently around the same year, various groups have tried to measure NMR images of the Couette flow, but their apparatus did not allow to measure NMR and shear flow simultaneously[76–80]. From these groups, P.T. Callaghan was the first to build a Couette cell inside a NMR magnet measuring NMR images during shear flow[81]. In 1994, the group of C. Schmidt developed the cone and plate cell inside a magnet further allowing simultaneous measurement of shear viscosity and director orientation where they could turn the director up to 70° into the x-y plane[82]. These two types of cells are the most commonly used geometries inside a magnet. Which one to choose depends on the experiments which shall be measured. The cone and plate offers a unique and stable shear rate over the whole sample but only a single shear rate. The Couette cell on the other hand, can vary the shear rate but does not provide the same shear rate at every location in the cell[81]. On top of that, the Couette cell can be build by two NMR tubes of different size which is easier and cheaper than a precise cone and plate cell at a specific angle. For some cells it might be necessary to build the NMR coil directly around the sample volume and therefore to create a probehead with the rheometer. Especially, the cone and plate type is often built this way[68]. Next to the type of cell, it is important choosing the correct magnet for the chosen experiments. Are the rheological results most important and home-built permanent magnets sufficient or are superconducting magnets required for more sensitive NMR measurements such as flow imaging. Examples for all possible ideas can be seen in the group of M. Wilhelm[83], in the group of P.T. Callaghan[81] or in the group of C. Schmidt[82]. In all these studies and many other rheo-NMR related studies, ^{2}H-NMR is the most powerful tool giving insight on director orientation and molecular ordering[84].

The group of Callaghan investigated the influence of the flow on the quadrupolar coupling of deuterium in a Couette cell which represents the angle Θ_D the alignment director is oriented with respect to the magnetic field. If the gap between the outer cylinder and inner cylinder is narrow ($R_i/R_o > 0.99$), the shear rate in the Couette cell is constant(Section 2.2.2.2). As for rheo-NMR no small gaps are used, the shear rate changes from the highest one at the inner rotating wall to the lowest one at the outer wall. With deuterium imaging experiments and their 1D slices, they could show that the quadrupolar splitting of deuterated benzene stays approximately constant. Hence, the tilt of the alignment director is approximately constant over the gap and the effect of the shear rate on the director as well. On top, they could simulate the 1D slices taken over the whole gap revealing that the appearance of a secondary peak in the middle of the split signal is an artifact of the flow and not a second phase. This shows that in flow aligning regimes, only one director orientation is given which can be calculated from the quadrupolar coupling of the deuterated solvent. Nevertheless, there probably will be some flow artifacts which need to be identified first[85].

As the quadrupolar splitting is proportional to the second Legendre polynomial (see Eq. 2.52) with a material specific proportionality constant A, the angle Θ_D of the sheared director can be calculated from the zero shear splitting at $\Theta_D = 0°$ where the polynomial equals

$$\Delta \nu_Q = AP_2(cos\Theta_D) \quad \text{with} \quad P_2(cos(0)) = \frac{3cos^2(0)-1}{2} = 1 \tag{2.144}$$

The new angle under shear will increase with the shear rate until an asymptote is reached where the mechanical torque dominates over the magnetic torque. This angle corresponds to the alignment angle which would be possible for all shear rates without a magnetic field pulling the director back to parallel to the magnetic field[17,86].

With magnetic resonance imaging (MRI) and MRI velocimetry flow behavior is the best observed during NMR experiments. By measuring radial maps, wall slip and shear-thinning can be observed for different

rotational frequencies and therefore the behavior of the fluid over the whole gap[87]. Additionally, the generated velocity profiles can show the effect of shear-banding where a fluid is subdivided into two fluids which experience the same rotational frequency and the same shear stress but different shear rates and a different viscosity. This phenomenon can be seen in pulsed gradient spin echo (PGSE) experiments combined with velocimetry as flow curves with coexisting shear rates for a single shear stress[87,88]. However, the shear bands observed in velocimetry experiments could only be seen so far for wormlike micelles, onion type LCs and a few other. It is associated with a plateau in the flow curve and an average shear rate applied in the unstable region. In optical birefringent measurements such bands occur as well but their complex relationship is unsolved so far[16].
Callaghan[84] showed that proton NMR is possible as well. It is the most sensitive nucleus in NMR and therefore the sample volume can be reduced. 20 µl were enough for measuring chemical shift differences and changes in the spin relaxation times during shear. Nevertheless, proton NMR has some disadvantages with flow. The small ppm range leads to overlap of the signals making them hard to distinguish. The different spin relaxation times of solids and liquids as well as deuterating the solvent can help to differentiate these peaks. The second major disadvantage for proton NMR are dipolar interactions due to the used LCs which are strongly influencing proton signals[84].
With the right setup, it is possible to measure if the director of the rotated liquid is tumbling or flow-aligning. It depends on the shear rate, the magnetic field, the rotational viscosity and the anisotropy of the magnetic susceptibility. Generally, the higher the shear rate and the higher the magnetic field is the higher is the possibility for the liquid to be in the flow-aligning regime[86].

2.4 PBLG

The LC poly-γ-benzyl-L-glutamate (PBLG) is a well studied polymer which can align in a magnetic field. It was often used in rheology as model testing shear responses on LCs. The ability to align in a magnetic field and transfer the anisotropy on solute molecules, made it a frequently used choice in NMR as well. Especially since PBLG is a cholesteric LC which can distinguish enantiomers.

2.4.1 General information

PBLG (Fig. 2.13) was first synthesized by Hanby, Waley and Watson[1] in the lab of Ambrose and Elliott (Messrs. Courtaulds LTD, Maidenhead, Berks.)[2] in the 1940s as potential polymer fiber substituting natural fibers (for example wools). The rod-like polymer forms an α-helix with a diameter of 16 Å. 18 benzene residues contribute to five turns of the helix with a length of 27 Å. Therefore, one turn is $\approx$ 5.4 Å and the helix length per residue is 1.5 Å. The 3.4 Å thick benzene rings are at an angle of 49° to each other but still π-stacking is possible between the rings of the same helix. Additionally, the benzene rings of different helix strains can stack, this is why up to four helices can form a bundle resulting in macroscopic clusters and sub-regimes as proven by x-ray scattering[89]. Seen from the molecular level, the coil of the helix is build up by 3.6 monomers per helical turn. Hereby, the oxygen of the carbonyl group and the hydrogen of the amide group build hydrogen bonds which prevent flexibility inside the helix and the polymer gets its rigid rod-like character. This effect only happens as long as the solvent is not interrupting the hydrogen bonds. These non-interrupting solvents are called 'helicoidal solvents'. Examples are the non-polar solvents m-cresol, chloroform ($CHCl_3$), dimetyhlformamide (DMF) and dioxane. In all other solvents, like dichloroacetic acid, PBLG will be in the random coil structure[90,91].

As a consequence of the long rods, PBLG macromolecules have a positive diamagnetic susceptibility. Therefore, cholesteric PBLG aligns with the external magnetic field untwisting the cholesteric helix

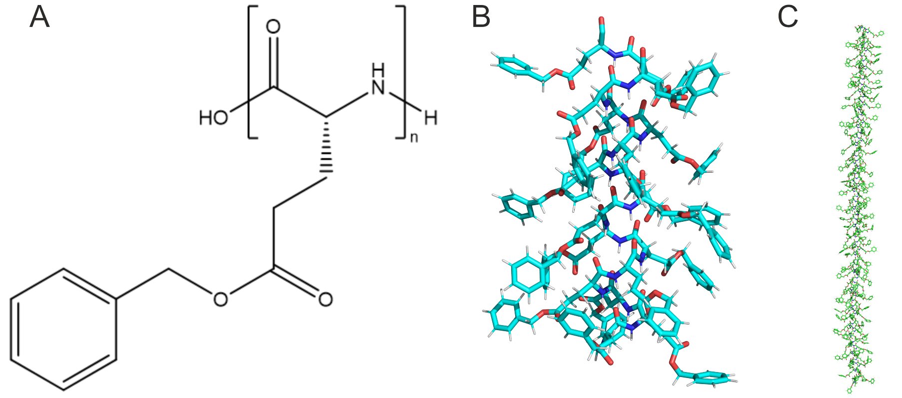

Figure 2.13: A) The molecular structure of PBLG. B) The 18/5 helix element of PBLG. C) Many of the 18/5 helix elements build a long rod of PBLG.

bundle into nematic order[92]. Under a polarization microscope, the nematic order of the lyotropic LC PBLG can be seen as different regions with regular arranged patterns (striations). Although, PBLG forms an α-helical LC in all helicoidal solvents, the rotation and the distances between the striations vary widely. Each specific solvent has an huge impact on the exact structure but macroscopically they often look and behave similar[93].

Polymers, especially stiff polymers, depend strongly on the orientational order of the molecules as well as on their concentration. Therefore, Doi and Edwards[94] classified rigid rod-like polymers into four different regimes: The dilute, semi-dilute, concentrated isotropic and nematic regime. A sample counts as diluted when all dissolved rods inside the solution do not feel any interaction with each other. As soon as the rotation of the rods is disturbed by other molecules but the distance between them is still large compared to the diameter of the rods, the solution is semi-diluted[95]. The transition from dilute to semi-dilute can be estimated with

$$\Phi_0 = 24 \left(\frac{D}{L} \right)^2 = \frac{24}{x^2} \tag{2.145}$$

where the aspect ratio x is the length (L) divided by the diameter (D) and Φ_0 is the volume fraction. For an aspect ratio of 50, the volume percentage would only be 1 %[69]. The concentrated isotropic regime begins when the diameter becomes large compared to the distance between molecules and the macroscopic sample still behaves isotropic ($\Phi_0 \approx \pi D/4L$). At the point, where the macroscopic sample behaves anisotropic, the nematic regime begins[69,95]. In 1949, Onsager had already shown the electrostatic effect in calculations as to why rod-shaped particles undergo the transition from isotropic to anisotropic. He even showed a possible coexistence of both phases at the same concentration[96].

2.4.1.1 Transition from the isotropic to anisotropic phase

Almost 10 years later, Flory[97] published a whole theory on this biphasic behavior for LCs like PBLG. The transition from a pure isotropic phase to a pure anisotropic phase always goes through a transition region. A rough estimate of the biphasic phase can be calculated if the aspect ratio of the polymer is known (starting from $8/x$ until $12.5/x$ (in w/w %)). With this estimation it is easy to see that the biphasic phase shifts to a smaller concentration range the higher x is, where the range is decreasing simultaneously. The aspect ratio itself depends on the molecular weight[97]. Hereby, different solvents show different ranges. Sakomoto[98] tested 10 solvents with critical concentrations ranging from 6.5 wt% for tetrahydrofuran (THF) to 12.4 wt% for DMF. Additionally, Miller et al.[99] showed that different rod-lengths of PBLG are biphasic for dioxane between 7.0 ± 0.5 wt% and 9-11 wt%, for methylene chloride between 8.0 ± 0.5 wt% and 12-15 wt% and for DMF between 8.5 wt% and 11.5 wt%. There is an effective aspect ratio x^*, which additionally depends on the temperature as the effective rod length L^* depends on the temperature. Wu et al.[100] estimated a model for PBLG with DMF for the temperature:

$$x^*_{\mathrm{PBLG}} = \frac{L^*_{\mathrm{PBLG}}}{D_{\mathrm{PBLG}}} = \frac{35003.82}{T/K} - 21.3179 \tag{2.146}$$

Additionally, they took the known temperature - concentration phase from other authors[89,90,101,102] describing the influence of the temperature on the orientational order and calculated them again for different rod-lengths. Such a diagram can be seen in Figure 2.14. Below a certain temperature, the two phases coexist over a very wide concentration range. In this wide range, the polymer is a gel (do not confuse with the LC state) which means it forms a solid-like chemical or physical (for PBLG purely physical) network. Also, a pure isotropic phase hardly exists below this temperature and for a pure anisotropic phase, very high concentrations are needed. Above this temperature, the biphasic region suddenly gets very small in concentration and looks like a chimney. The width and location of this chimney varies for different conditions. For example, the amount of water has a larger impact. A completely dry sample has a very small biphasic chimney and with rising water concentration the chimney gets broader. Horton et al.[90] found a maximum temperature for PBLG in DMF, where this biphasic chimney ends and only pure phase behavior can be found at 80 °C.

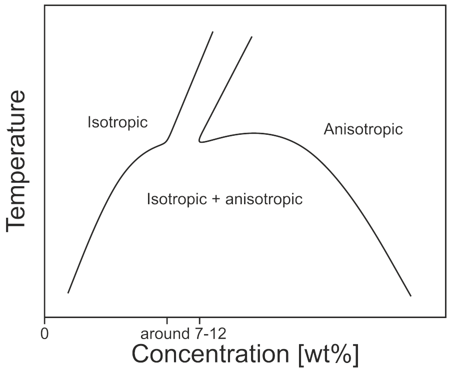

Figure 2.14: A simplified temperature - concentration phase diagram of PBLG with any solvent. At lower temperatures, PBLG is biphasic in a wide concentration range, at higher temperatures only in a small region (often called chimney). As the exact temperature range strongly depends on solvent and rod-length, no temperature range can be given in this simplified figure. For more details, the reader is advised to look at the cited references (adapted from[90, 100, 102]).

Around the same time as Flory published his theory, Robinson[103,104] saw this biphasic region in polarizing images. In his images the isotropic part always looked exactly as the pure isotropic phase and the anisotropic part as the pure anisotropic phase. Only the amount of the birefringent anisotropic phase increased which could be seen first as numerous small monocrystals (spherulites) and later as spherulites melt together. These spherulites can only be seen in the small biphasic region, the pure anisotropic phase shows other birefringent and periodic band like structures (texture). His findings could also be shown by other authors with different techniques[102,105]. A few years later, independent groups showed that it is possible to separate the biphasic phase into the isotropic and anisotropic phase after a long enough waiting period[90,106]. But this is only possible in the chimney region, in the wide biphasic region where PBLG is a gel, the network is too strong to allow separation[69].

2.4.2 PBLG in rheology

In 1958, Yang was the first to measure the viscosity dependency of shear stress for PBLG in m-cresol and dichloroacetic acid where PBLG forms an α-helix in the first case and a random coil structure with the second solvent[107]. Until the early 2000s, PBLG and its enantiomer PBDG (or a racemic mixture of both called PBG) was used among others as a model for the rheological behavior of LCs by many rheologists[5]. In the following section, the special rheological responses of PBLG will be summarized.

Rheological experiments strongly depend on the persistence length of the polymer. The persistence length λ_p describes the stiffness of the polymer

$$\lambda_p = \frac{\kappa_{br}}{k_b T} \tag{2.147}$$

where κ_{br} is the finite bending rigidity[69]. The higher the molecular weight, the longer the persistence length and the lower is the needed concentration for a fully anisotropic phase[108]. Nevertheless, the persistence length of PBLG does not change dramatically above a molecular weight $\approx$ 200 000, only the flexibility of this LC. Therefore, the influence of the persistence length on rheological experiments is very low above a molecular weight of 200 000[5]. Another advantage of PBLG during rheological experiments is its stability at high shear rates. Even shear rates of several thousands per second do not disrupt the helix or lead to mechanical degradation[3,109]. These high shear rates are needed, if an isotropic LC solution shall be sheared resulting in anisotropic behavior. More precisely, an anisotropic solution will change its direction of orientation already at low shear rates because the direction changes from one orientation to another one. Isotropic solutions do not have one direction of orientation, therefore higher shear rates are needed inducing the orientation along the flow[110].

One of the most important characteristics in rheology is the viscosity of the liquid or solid. It is mostly measured as a function of temperature where the viscosity gets smaller for higher temperatures. One unusual observation for LCs is that the viscosity increases heavily at the transition temperature from nematic to isotropic. This is due to the packing of the rods inside the sample. In the nematic state which is reached at lower temperatures, the rods are aligned, do not tumble freely and need less space compared to the isotropic state where each rod has a different orientation due to tumbling and a large hydrodynamic volume. The same reason explains the behavior of the viscosity, measured as a function of the concentration. At first, the viscosity increases with concentration until it reaches the transition from isotropic to anisotropic where it starts to decrease. Then, when the sample is fully packed and the local ordering can not be increased anymore at a concentration of 20-24 wt%, the rods do not have enough space left and the viscosity increases again[5,109,111].

The viscosity response to the shear force for PBLG can be divided into three different regions. At low shear-rates and high concentrations, PBLG exhibits shear-thinning until a plateau is reached (also called Newtonian region) leading to a third region where again shear-thinning can be observed (Fig. 2.16)[111,112]. As Walker and co-workers[5] show, region I shear-thinning is only reached at concentrations above 30 wt%. Moreover, they show that reaching 40 wt%, PBLG samples get solid like (transition into a gel) whereby the viscosity increases even more strongly, which can be observed by NMR as a decrease in the quadrupolar coupling above this concentration[113]. Another big influence on the viscosity decrease during shearing is the texture of the sample before shearing. If the sample was isotropic before and the shear force is strong enough ordering the rods into anisotropy, the viscosity decreases even more than for a sample which was anisotropic before due to the stronger change in ordering. This explains the decrease in viscosity for increasing concentrations for low shear stress (< 100 s^{-1})[110,114].

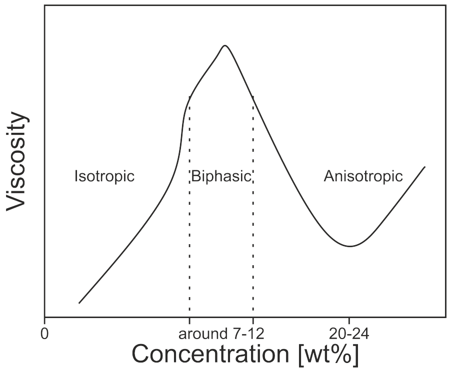

Figure 2.15: The viscosity of PBLG as a function of the concentration is shown. First, it rises in the isotropic area and has it maximum in the biphasic region. Purely anisotropic, it decreases to a minimum at approximately 20-24 wt% and increases again afterwards for higher concentrations (adapted from[109]).

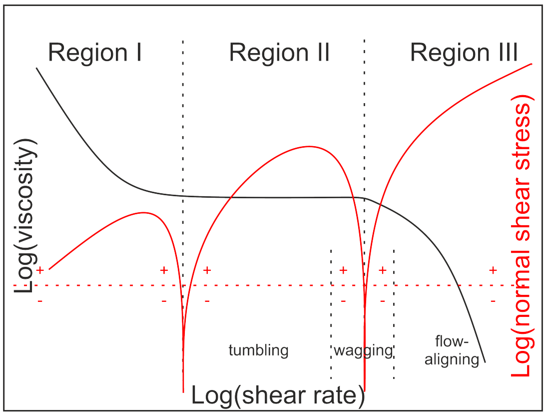

Figure 2.16: The viscosity (black) and normal shear stress (red) of a LC depending on the shear rate. First, a shear-thinning effect occurs until a plateau is reached (region II) where the director tumbles. At high shear rates the shear-thinning effect occurs again with the director aligning in the flow. During the transition from region II to III where negative values of the normal stress can be found, the director is in a wagging regime (adapted from[109, 111]).

In contrast to viscosity, the normal shear stress N_1 increases linearly with the shear rate for PBLG. During this increase, two small regions of negative normal stress can be found at anisotropic PBLG concentrations. Isotropic PBLG solutions show a non linear increase for a short region as well. Compared with viscosity measurements, this region is at shear rates where the sample goes from the plateau region II to the shear-thinning region III. Exactly in this region negative N_1 values can be found. The second negative region is the transition from region I to region II which is only found for concentrations over 30 wt%[109,115]. These negative values of the normal stress at intermediate shear rates are not fully understood. They are mostly explained by second order shear artifacts where the flow is not strong enough for only one director angle and the degree of molecular orientation is decreased[112,116].

A closer look at the director angle shows that for low shear rates in the Newtonian region II the director tumbles periodically in the shear plane without a definite angle. During this tumbling regime, the order parameter S oscillates. Then, when N_1 changes to negative values at intermediate shear rates, the tumbling regime transfers into the wagging regime where the director oscillates between two limiting angles and S as well. Hereby, the degree of the molecular orientation decreases. As soon as N_1 gets positive again, the director aligns with the flow (so called flow aligning regime), S gets in a steady-state and the molecular orientation of the system increases with higher shear rates[69,115,117].

It is also possible to measure the second normal stress N_2, which is always negative except for intermediate concentrations (around 10-15 wt%) at intermediate shear rates (50-200 s^{-1})[4]. Both normal shear

stresses increase with concentration[5,118].
In 1991, Larson and Doi[119] corrected the original theory of Doi[94] for polymer LCs predicting most of the behavior of viscosity and both normal shear stresses correctly. For example, the theory truly predicts the tumbling, wagging and flow aligning regimes as well as the higher viscosity of isotropic phases compared to anisotropic ones[118,120,121].

The storage modulus G' and the loss modulus G'' of PBLG describe how well energy is stored or lost in the system. The interaction between the two reflects whether the polymer is more liquid- ($G''/G' \gg 1$) or solid-like ($G''/G' \ll 1$)[69]. G' behaves in its concentration dependence similar to the viscosity. First, it increases with concentration until a maximum is reached between 9 and 11 wt% and then decreases again. Directly after the maximum the biphasic region begins. Contrary to the viscosity, G' increases with the shear rate[109]. After the cessation of flow, G' decreases again for some time to a minimum after which G' increases slightly. The loss modulus G'' also decreases after shear cessation but does not increase again. The decrease after cessation of flow is for both independent of the previous shear rate but it takes longer the higher the concentration of PBLG is[114].
Another phenomenon after the cessation of flow is the building of a transverse banded texture, called shear banding. If the previous shear rates were high enough, periodic bands can be observed in polarizing imaging experiments. The build up can take several minutes for intermediate shear rates or start immediately for high shear rates. The length and width of the bands increase with the concentration and slightly by time, but decrease with higher shear rates[5,108,122].

All these flow dependent characteristics of PBLG were measured in the solvent m-cresol. This aromatic solvent is not the only one leading to a liquid crystalline phase with PBLG. Therefore, Chidambaram et al.[123] compared m-cresol with its isomer deuterated benzyl alcohol (DBA). The response in viscosity was similar and the relaxation effects after shear cessation were faster for DBA but followed the same trend as in m-cresol. Additionally, the general amount of alignment was slightly higher in m-cresol than DBA. They showed with their work, that the general properties of a liquid crystalline PBLG are similar for different solvents but there are some differences even for the isomeric solvents m-cresol and DBA[123].

2.4.3 PBLG and its role in NMR

As previously mentioned, PBLG aligns in a magnetic field due to its anisotropic behavior at a certain concentration. This can be used in NMR to induce anisotropy in other molecules for the measurement of RDCs, RQCs and RCSA. The high molecular weight and thus the very short T_2 time of PBLG strongly influences the spectra[124]. On the one hand, no peaks of PBLG can be seen in the spectrum due to the short T_2 time. On the other hand, the induced alignment of PBLG is strong as it only fully aligns at a concentration of about 9 wt%. Due to the strong alignment, the dipolar and quadrupolar couplings are large which increase the multiplet widths of the investigated molecules and increase the signal width[124,125]. However, the cholesteric PBLG is a LC in a variety of non-polar solvents and it can distinguish enantiomers[9,10]. For these two reasons, it is still frequently used as an alignment medium. This section shows some further characteristics of PBLG and improvements in data acquisition.

The dipolar or quadrupolar coupling of the solvent signal measured by ^{1}H or ^{2}H NMR indicates the degree of order. Marx and Thiele[124] used this to determine the minimum concentration at which PBLG aligns for different molecular weight samples of PBLG and showed that higher concentrations are required for lower molecular weights. At the same time, the quadrupolar splitting of $CDCl_3$ at the critical concentration decreases with the molecular weight and reaches a final value for high molecular

weights (above 200 000 similar to Subsection 2.4.2), showing that the higher the molecular weight, the lower the alignment strength at the critical concentration until the threshold value of approximately 200 000 wt. The same effect can be seen on the solute molecule resulting in a decreased degree of order for the solute molecule at the critical concentration for higher molecular weights and therefore lower values for the RDCs. The orientation of the molecule on the other hand does not change as shown by unchanged Euler angles. Interestingly, preparing two samples different in the molecular weight at the same concentration results in approximately the same quadrupolar splitting and therefore the same degree of orientation. These findings clearly show that for optimal analysis of the solute molecule, higher molecular weight PBLG should be used reaching lower concentrations and lower degree of order. As a result, RDCs are reduced which reduces the linewidth in the spectrum. A drawback is the minimum concentration of at least 6 wt% of PBLG needed which still results in a strong degree of order and high values of RDCs.
Especially in ^{1}H 1D spectra, the strong homonuclear couplings and the big background produced by the polymer make data acquisition quite hard. The less sensitive ^{13}C 1D spectra are in much better agreement with the high molecular weight of PBLG. The long T_1 and short T_2 times of PBLG result in a non-interfering background and together with the multiple scans needed for natural abundance ^{13}C measurements, better spectral quality is obtained[125]. Similarly, the data acquisition for ^{19}F or ^{31}P spectra are qualitatively better than for ^{1}H as PBLG does not contain both atoms resulting in background free spectra with only peaks of the solute molecule[126,127]. Duke and coworkers[128] found a way to reduce the anisotropy and quadrupolar splittings of PBLG by adding trifluoroacetic acid (TFA). Up to 20 % TFA can be added to PBLG without destroying the α-helix and therefore the anisotropy. Hereby, the amount of TFA which can be added increases with the amount of PBLG in the sample[129]. The group of C. Thiele[129] tested more additives with dimethlysulfoxid (DMSO) and CCl_4. The non-polar additive CCl_4 showed the best results with a maximum of 30 wt% CCl_4 reducing the RDCs significantly.

A big advantage of PBLG and its enantiomer PBDG is that together with chiral solutes, information like chemical shift, scalar and dipolar couplings allows chiral discrimination. For example, small chemical shift differences can be seen between solute enantiomers in their chiral center[9,10]. Especially, because PBLG forms a LC in a lot of organic solvents ranging from polar to weakly polar, the system can be optimized for the solute molecule. Experiments have shown that enantiodiscrimination improves with more polar solvents, but highly polar or water-compatible analytes can not be dissolved with PBLG[130]. Other examples are amines which are best measured with DMF as the solvent for PBLG as it seems to break the strong intermolecular interaction of the amines with PBLG resulting in less broad lines[131]. Or methylene groups of fatty acids could be better distinguished by changing the solvent for PBLG from $CDCl_3$ to pyridine[132]. Another method for distinguishing enantiomers was published in 1998 by Lesot et al.[133]. They used natural abundance deuterium NMR with proton decoupling, first introduced by Martin et al.[134] to determine the different chemical shifts for the chiral centers. Since the chemical shifts of protons and deuterium in NMR are approximately the same, the peak assignment of protons can be used. Although the signal intensity is only of the order of 1.45×10^{-6} that of protons, the C-D coupling is $\approx$ 170 kHz instead of 46 kHz for protons. This allows a visible separation of the chiral signals in the deuterium 1D experiment. For overcrowded deuterium spectra, the same group developed 2D experiments that can be used with PBLG and natural abundance deuterium NMR[135]. The method enabled the enantiomeric discrimination of chiral alkanes, which had not been possible before[10].
Previously, ^{1}H STD-NMR was used to selectively irradiate PBLG at a chemical shift where no solute signals are present. Via intermolecular NOE and spin-diffusion magnetization from PBLG will be transferred to the binding solute molecule during the saturation. This leads to a spectrum where only the peaks of the bound enantiomer can be seen and all other solute molecules will not show any peaks[136].

2.4.3.1 PBLG in rheo-NMR

Martins with his group[137–140] and after his retirement Leal with her group[22] investigated PBLG in m-cresol via rheo-NMR through sudden rotation of the sample tube and later in a Couette cell on a 300 MHz spectrometer with applied shear rates between 5 and 350 s^{-1}. As their Couette cell is rheologically well defined with the possibility of measuring viscosity data, they could calculate the tumbling and wagging regime of PBLG in m-cresol for three concentrations (12, 14 and 17 wt%). The tumbling regime lasted up to 20 s^{-1} for the 12 wt% sample and the wagging regime up to 60 s^{-1}, while for the 14 wt% sample the limits were 40 s^{-1} and 150 s^{-1}, respectively. The 17 wt% sample showed the same limits. At shear rates higher than 150 s^{-1} all three samples were flow-aligning[22,140]. With their apparatus, they could reach director angles up to 80-85° where the full angle was reached after 10 s for the shear rate of 150 s^{-1} and for the shear rate of 5 s^{-1}, the full angle (70-75°) was reached after 100 s. The cessation of shear and the relaxation of the director back in the direction of the magnetic field was independent of the previous shear rate and takes around 700 - 1000 s[140]. Additionally, they were able to calculate the probability distributions of the director angle and from this they calculated the deuterium NMR spectra which are in full agreement with their experimental recordings (see Fig. 2.17).

In 2015, Ben Munro used PBLG in $acCDCl_3$ to obtain RDCs of a small molecule under shear conditions in his master thesis at the Massey University in New Zeeland. For average shear rates up to 108 s^{-1}, the shear profiles for these low shear rates show a change in quadrupolar couplings and director angle between 29° and 85°. The alignment tensor calculated from the measured RDCs of the used molecule isopinocampheol under each shear condition gave poor quality factors and not sufficient results for a correct structure determination. The results with ubiquitin in Pf1 phage provided better quality factors and more reliable sets of RDCs, but all sets provided the same structural information and no additional information could be obtained from measurements at different shear rates[141].

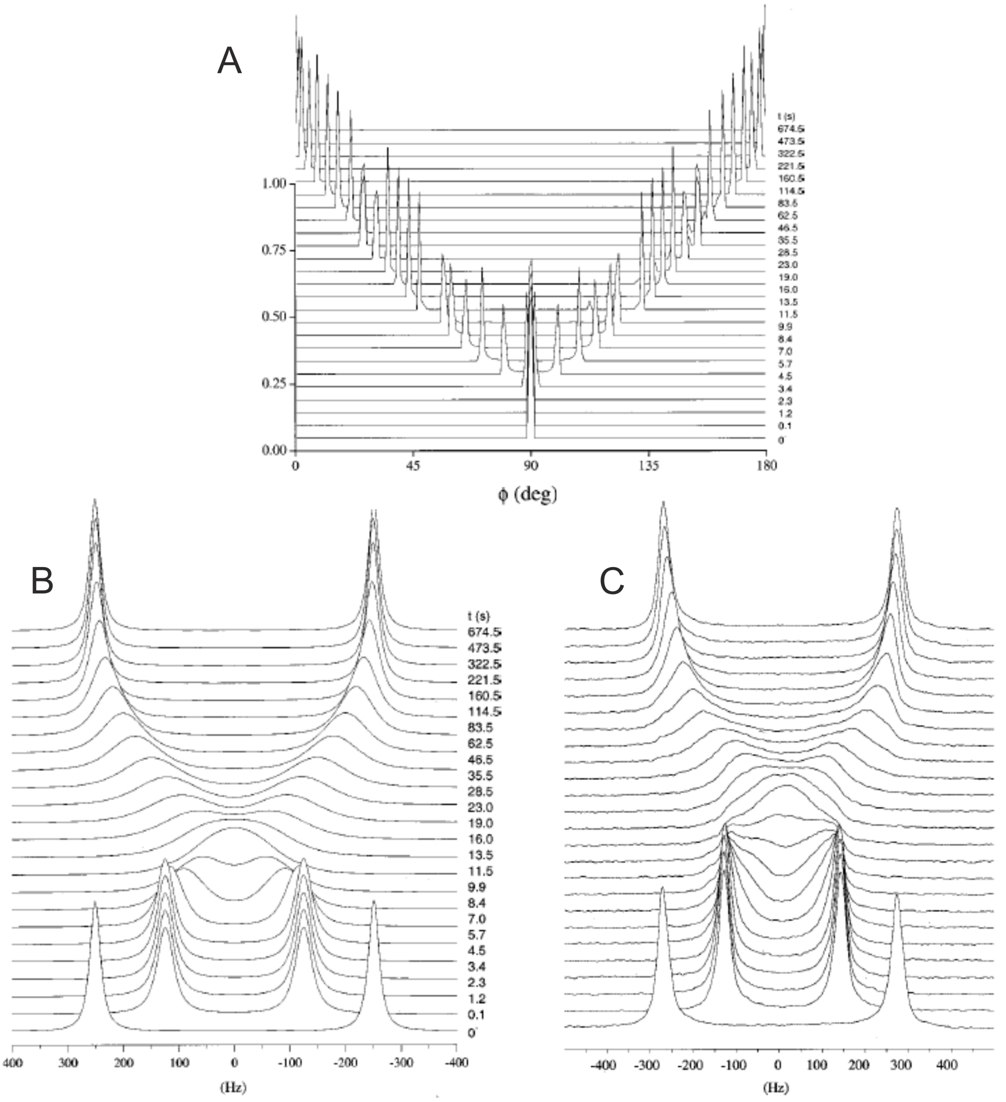

Figure 2.17: A) The calculated director distributions of a 14 wt% PBLG sample in m-cresol at different time points after sudden rotation of the sample tube inside the magnet. B) The calculated deuterium NMR spectra obtained from the director distributions in A. C) The measured deuterium NMR spectra after sudden rotation of the sample tube inside the magnet for the same time points as in A and B (with permission from [139]).

3 Material and methods

3.1 Samples

Most anisotropic samples in this section need an isotropic sample as reference. Therefore, the following isotropic samples were prepared: 4-fluorobiphenyl (Sigma), strychnine (Fluka BioChemica), 1-fluornaphtalene (Sigma), (+)-menthol (Sigma) and (-)-menthol (Sigma) all dissolved separately in stabilized $CDCl_3$ (> 99.8 %, Euroisotop). For the tetrafold experiments two samples were prepared. One, where $CDCl_3$ and $CHCl_3$ were used 1:1 by volume as solvent. Hereby, 10 v/v% TMS (Euroisotop) was added to $CDCl_3$. As molecules of interest CCl_4 (Merck) and CBr_4 (Merck) were added with identical molar amount. The second tetrafold sample was prepared with the molar ratio of $CDCl_3$:CCl_4:$CDCl_3$:$CHBr_3$:TMS:CBr_4 as 5:2.5:1:1:1:1.

3.1.1 PBLG

All PBLG samples (mol wt 150000 - 350000 purchased from Merck) were prepared by weight percentage with $CDCl_3$ (> 99.8 %, Euroisotop) as published by Sarfati et al.[9]. The solvent was used without further purification and stored over silver foil. In most of the PBLG samples, a small molecule solute was added (5 - 38 mg). PBLG, $CDCl_3$ and the solute were each directly weighed into the NMR tube and thoroughly centrifuged until the samples were fully homogenized which was checked by deuterium NMR 1D and 2D image spectra. The samples are listed in Table 3.1.

One additional PBLG sample was prepared for the tetrafold experiments. It contained 60.3 mg PBLG, 251.3 mg $CDCl_3$ with 10 % TMS, 259.4 mg $CHCl_3$ (Merck), 65.0 mg CCl_4 (Merck) and 110.1 mg CBr_4 (Merck) which results in 10.6 wt% PBLG. This sample was later diluted with 589.5 mg $CDCl_3$ with 10 % TMS and 64.3 mg CCl_4 to 5.2 wt%.

The very first PBLG sample inside the apparatus (15.4 wt% with flurbiprofen) was diluted several times (see Table 3.2) for a first characterization of the behavior of PBLG with rotation for different concentrations and shear rates. Later, a systematic dilution study of the transition region outside the rheo-device was performed. For the dilution steps see Tables 3.3 and 3.4.

3.1.2 Pf1-phage

The filamentous bacteriophage Pf1 from *Pseudomonas aeruginosa* is a ≈ 20,000 Å long particle with a diameter of 60 Å. At a physiological pH (pI ~4.0), the phage is negatively charged and can induce alignment to biomolecules[142]. As Hansen and coworkers showed[143,144], already at low concentrations the phage gets liquid crystalline and their alignment is linearly tunable with the concentration. Hereby, the long axis of the LC aligns along the magnetic field at any biologically compatible concentration and temperature. The phage was purchased from ASLA Biotech and was delivered in a 10 mM K-phosphate buffer at pH 7.6 with 2 mM $MgCl_2$ and 0.05 % NaN_3 (90 % H_2O/10 % D_2O). For the measurements the phage was put in 10 mM tris(hydroxylmethyl)aminomethane (Tris) buffer with

Table 3.1: The used PBLG samples in this work

weight percentage [wt%]	mg PBLG	mg $CDCl_3$	solute (supplier) [mg]
15.4	77.1	422.1	flurbiprofen (Sigma) [19.9]
18.2	97.7	440.0	flurbiprofen (Sigma) [36.8]
18.4	96.5	427.5	4-fluorobiphenyl (Sigma) [38.0]
13.8	77.5	484.1	ergosterol (Sigma) [19.7]
3.8	18.6	466.0	ergosterol (Sigma) [19.5]
13.1	72.6	483.5	strychnine (Fluka BioChemica) [24.8]
11.7	72.1	541.5	strychnine (Fluka BioChemica) [25.5]
11.3	71.4	560.5	strychnine (Fluka BioChemica) [24.6]
11.1	72.3	579.1	strychnine (Fluka BioChemica) [25.1]
9.0	44.0	446.3	1-fluornapthalene (Sigma) [20 µl]
14.0	75.0	460.0	(+)-menthol (Sigma) [*]
14.5	75.1	443.9	(-)-menthol (Sigma) [*]
13.2	72.4	476.0	strychnine (Fluka BioChemica) [26.4]
2.0	9.4	451.5	none
4.0	19.1	453.5	none
5.9	28.4	453.7	none
7.8	38.8	456.9	none
9.9	50.1	457.6	none
11.9	61.2	451.1	none
9.1	44.6	445.7	none
8.1	39.2	447.0	none
8.2	39.2	437.8	flurbiprofen (Sigma) [9.9]
8.3	39.0	430.4	flurbiprofen (Sigma) [20.6]
8.7	39.7	417.5	flurbiprofen (Sigma) [30.1]
8.5	40.9	441.5	none
8.1	39.0	441.8	none
9.9	49.1	446.2	TMS (Euroisotop) [*2]
10.9	54.4	444.8	TMS (Euroisotop) [*2]
6.0	28.7	449.2	strychnine (Sigma) [25.0], TMS (Euroisotop) [*3]
10.1	50.3	448.4	TMS (Euroisotop) [*2]
10.0	49.6	447.1	strychnine (Sigma) [25.8], TMS (Euroisotop) [*3]
10.3	73.7	644.2	TMS (Euroisotop) [*2]
10.2	72.7	641.4	(+)-borneol (Sigma) [14.0], TMS (Euroisotop) [*2]
9.8	69.8	644.2	(1S)-(-)-camphor (Sigma) [14.0], TMS (Euroisotop) [*2]
3.8	303.6	7535	none
8.6	660.3	7355	none
7.0	60.8	807.5	strychnine (Fluka BioChemica) [23.8]

[*] 100 mM menthol was dissolved in 1 ml $CDCl_3$ instead of directly weighing into the NMR tube.

[*2] TMS was dissolved in 25 ml $CDCl_3$ with 0.1 v/v%

[*3] TMS was dissolved in 10 ml $CDCl_3$ with 10 v/v%

0.1 mM ethylenediaminetetraacetic acid (EDTA) at pH 8 containing NaN_3 (90 % H_2O/10 % D_2O). Two samples were prepared this way with a final concentration of the Pf1 phage of 10 mg/ml for both

Table 3.2: The dilution series of PBLG with flurbiprofen for measurements with the rheo device. As the solvent evaporates in the open NMR tube and an unknown amount of PBLG is lost due to adherence at the inner tube, this dilution series is given by the quadrupolar splitting.

dilution step	splitting without rotation	splitting during rotation
0	615.1 Hz	271.8 Hz
1	535.0 Hz	239.3 Hz
2	234.2 Hz	118.7 Hz
3	225.1 Hz	109.1 Hz
4	219.1 Hz	96.7 Hz
5	214.0 Hz	97.1 Hz
6	215.2 Hz	93.8 Hz
7	0 Hz	68.1 Hz
8	0 Hz	52.0 Hz
9	0 Hz	59.3 Hz
10	0 Hz	23.1 Hz
11	0 Hz	12.0 Hz
12	0 Hz	6.2 Hz
13	0 Hz	3.0 Hz

samples. The second sample had additionally 30 µl of acetonitrile (ACN)-d_3 as additional deuterium signal.

3.1.3 DNA

Similar to PBLG, DNA is an α-helical rod with a persistence length of ~50 nm which can build liquid crystalline phases. The semiflexible and biological polymer is water soluble and best handled with NaCl as additive[145]. We prepared one sample of deoxyribonucleic acid sodium salt from herring testes Type XIV (Sigma) with 211.7 mg D_2O and 17.1 mg ACN-d_3. As the concentration of DNA was too high to handle and the ACN-d_3 signal not observable, the sample was further diluted with 206.3 mg D_2O and 55.7 mg ACN-d_3.

3.2 Methods

All rheo-NMR experiments were performed on a 400 MHz Bruker Avance III spectrometer with a BBI room temperature probehead (Bruker Biospin GmbH, Rheinstetten, Germany). Some of the non-rheological experiments were performed on this spectrometer as well. Additionally, non-rheological experiments were performed either on a 600 MHz Bruker Avance III spectrometer equipped with a cyro-TCI probehead (^{1}H, ^{13}C, ^{15}N) with z-gradient or on a 600 MHz Bruker Avance III HD spectrometer with a BBI room temperature probehead. The used pulse-sequences during all the experiments on these spectrometers can be seen in Table 3.5. The obtained spectra were processed with TopSpin (Bruker Biospin, Rheinstetten, Germany).

For the measurements with the rheo-device, the 3 mm NMR tube was filled with DMSO-d_6 (first open, later sealed and prepared under argon) and the sample was filled in a 5 mm NMR tube cut to the correct

Table 3.3: The dilution series of PBLG without a solute molecule, with borneol and with camphor

without solute molecule		**borneol**		**camphor**	
mg $CDCl_3$	**wt%**	**mg $CDCl_3$**	**wt%**	**mg $CDCl_3$**	**wt%**
59.5	9.47	55.4	9.45	21.1	9.50
28.0	9.15	20.4	9.20	24.0	9.20
16.8	8.96	25.0	8.92	22.8	8.93
17.7	8.77	20.1	8.71	17.1	8.74
16.4	8.61	16.6	8.54	15.5	8.57
18.1	8.43	22.9	8.31	20.6	8.36
30.0	8.15	14.3	8.18	14.3	8.22
19.1	7.98	16.5	8.03	22.7	8.00
20.7	7.81	29.6	7.78	25.6	7.78
25.7	7.60	24.6	7.58	24.5	7.57
28.9	7.38	23.6	7.39	25.8	7.36
28.5	7.17	28.7	7.19	25.6	7.17
28.7	6.98	28.6	6.99	31.4	6.95
28.8	6.79	30.3	6.79	21.3	6.80
19.0	6.68	16.4	6.69	17.4	6.69
12.7	6.60	15.4	6.59	15.8	6.59
18.0	6.50	21.2	6.47	17.5	6.48
15.4	6.41	12.4	6.40	16.7	6.38
20.1	6.30	20.9	6.28	19.7	6.27
19.5	6.20	14.3	6.21	12.0	6.20
20.8	6.09	20.1	6.10	19.1	6.10
16.9	6.01	19.3	6.00	21.1	5.99
23.4	5.89	24.6	5.89	*	*
22.7	5.79	23.6	5.77	*	*

* sample broke during centrifugation

length. Both tubes were fixed on the apparatus outside of the magnet and the whole device transferred into the magnet. The isotropic signal of the inner DMSO was used for automatic shimming.

RDCs were extracted by the CLIP/CLAP method for heteronuclear single quantum coherence (HSQC) experiments developed in our group[146]. A clean inphase (CLIP) and a clean antiphase (CLAP) HSQC were both acquired with the same settings for optimal addition of both spectra gaining in theory double intensity for the peaks. For all isotropic spectra, a self written Python program was used determining the isotropic J-coupling. In the anisotropic spectra, the Python program was only used if the signal was intense enough and no major spectral artifact was interfering. Otherwise, the coupling determination was done manually. Afterwards, the RDCs were run through the program PALES by M. Zweckstetter[46,47] which uses SVD to calculate theoretical RDCs for the given structure and the obtained quality factor Q and the Pearson's R factor were used to determine whether the collected RDCs represent the correct structure.

The imaging experiments were performed by Prof. Dr. Gisela Guthausen from the Institute of Mechanical Process Engineering and Mechanics at the KIT on a 400 MHz Bruker Avance Neo spectrometer equipped with a mirco 5 ^{1}H, ^{2}H double resonant probehead (loan from Bruker BioSpin, Rheinstetten, Germany). ^{2}H images were performed with chemical shift imaging (CSI) and ^{1}H images with fast

Table 3.4: The second dilution series of PBLG contained no solute molecule and started at 8.6 wt%

mg $CDCl_3$	wt%
44.6	8.17
25.0	7.96
27.1	7.73
32.3	7.48
26.4	7.29
26.6	7.11
31.5	6.90
32.1	6.70
29.8	6.53
19.8	6.42
29.0	6.26
12.9	6.19
12.6	6.13
9.5	6.08
10.7	6.03
11.8	5.97
11.6	5.92
14.5	5.85
14.1	5.79
14.9	5.72
15.4	5.66
17.6	5.58
17.0	5.51

low angle shot (FLASH) both using ParaVision 360 V3.5 (Bruker BioSpin, Rheinstetten, Germany). Processing was first done by ParaVision and the ^{1}H images additionally refined with self written MATLAB-scripts.

The viscosity measurements of the 3.8 wt% and 8.6 wt% samples were done on a ARES-G2 shear rheometer (high sensitivity, strain controlled from TA-Instruments) in the group of Prof. Dr. M. Wilhelm at the Institute of Technical Chemistry and Polymeric Chemistry at the KIT with supervising help of Dr. Christopher Klein. As measuring cell, a sliding plate type was used with a radius of 12.5 mm using around 500 µl sample volume for optimal results. Every filling of the plate was measured with two runs consisting of a first frequency sweep, than a flow sweep test and another frequency sweep. As time was crucial with the evaporating $CDCl_3$, after a set up test ranging from 0.01 s^{-1} to 300 s^{-1}, all other sweeps were performed in six steps from 30 to 300 s^{-1}. The tested temperatures for both samples were 20 and 27 °C. The rheometer gave consistent results for both samples and temperatures.

3.3 The rheo-device

My home-built rheo-NMR apparatus was designed as a Couette cell following the example of Callaghan[23]. A motor is controlled by an outer power source rotating a long rod with a 3mm NMR tube at the end. On this rotating 3mm tube (Bob), a 5mm NMR tube (inner diameter $\approx$ 4.2 mm) containing the sample for investigation is used as Cup and the sample will now be sheared by the inner 3mm tube. This

Table 3.5: The pulse sequences used in this work

pulse program file name	description	dimension
zg	^{1}H and ^{19}F	1D
zg2h	^{2}H	1D
zgig	^{13}C and ^{29}Si	1D
zgig30	^{13}C and ^{29}Si	1D
YW_ZGSP	^{13}C	1D
zgspig30_yw	^{13}C	1D
bulusatsup	^{19}F with satellite suppression	1D
bulu19fcliphsqc	^{19}F, ^{13}C CLIP-HSQC	1D
rheo2hSon	^{1}H with rheo-device	1D
rheo2hSoff	^{1}H with rheo-device	1D
mkmc_phaseenc2_2h	^{2}H image	2D
patz_D_QECOSY_av3	^{2}H, ^{13}C Q.E.COSY	2D
hsqcedetgp	^{1}H, ^{13}C HSQC	2D
hsqcetgp	^{1}H, ^{13}C HSQC	2D
hsqcetgpsi	^{1}H, ^{13}C HSQC	2D
patz_gk_clipHSQC.SP	^{1}H, ^{13}C CLIP-HSQC	2D
patz_gk_clapHSQC.SP	^{1}H, ^{13}C CLAP-HSQC	2D
bulu_cob3_clip_hsqc	^{1}H, ^{13}C CLIP-HSQC with COB3	2D
bulu_cob3_clap_hsqc	^{1}H, ^{13}C CLAP-HSQC with COB3	2D
hmbcetgp13nd	^{1}H, ^{13}C HMBC	2D
SIRiggpsp.yw2	^{13}C and ^{29}Si T_1 measurement	2D
t1irigsp	^{13}C and ^{29}Si T_1 measurement	2D
HETCOR_Adjust-BIRD-sp2.yw	^{13}C, ^{1}H Jres $^1T_{CH}$ with BIRD filter	2D
jresqf	^{1}H, ^{1}H Jres	2D
rheo_1h13c2Djres	^{1}H, ^{13}C Jres with rheo-device	2D
rheo_2Djres	^{1}H, ^{1}H Jres with rheo-device	2D
rheo_2Djres_13c	^{13}C, ^{1}H Jres with rheo-device	2D
rheo_2h2Djres	^{2}H, ^{2}H Jres with rheo-device	2D
rheo_2hjres	^{2}H, ^{2}H Jres with rheo-device	2D

whole device is compatible with conventional standard-bore high resolution NMR spectrometers and probeheads.

The device (Fig. 3.1) can be split into three major sections. The bottom end with the NMR tubes and the stator, the long acrylic tube in the middle and the top part with the motor. The motor (Faulhaber 4221G024BXTR) is fixed on a 3D printed holder on the acrylic tube and is controlled by a speed controller (Faulhaber SC5008S 6340) with speeds up to 50 Hz. Between the speed controller and the transistor-transistor logic (TTL) signal source is a MOSFET driver (TC4428) inverting the TTL signal into a pulse-width-modulated (PWM) signal with an amplitude of 10 V which the speed controller requires. The TTL signal source is either the console or an arbitrary waveform generator (Teledyne LeCroy T3AFG80). Controller and motor are powered with a +48 V, 10 A DC power supply (Mean Well DRP-480S-48), and the MOSFET driver uses a lab power supply (Voltcraft DIGI 35) set to 10 V DC as power source. Inside the 1 m long acrylic tube is a carbon fiber shaft connecting the motor with the rotor at the bottom. To minimize the misalignments, several ceramic bearings are placed around the shaft and a flexible rotary coupling as connection to the rotor. The rotor consists of a lower shaft held

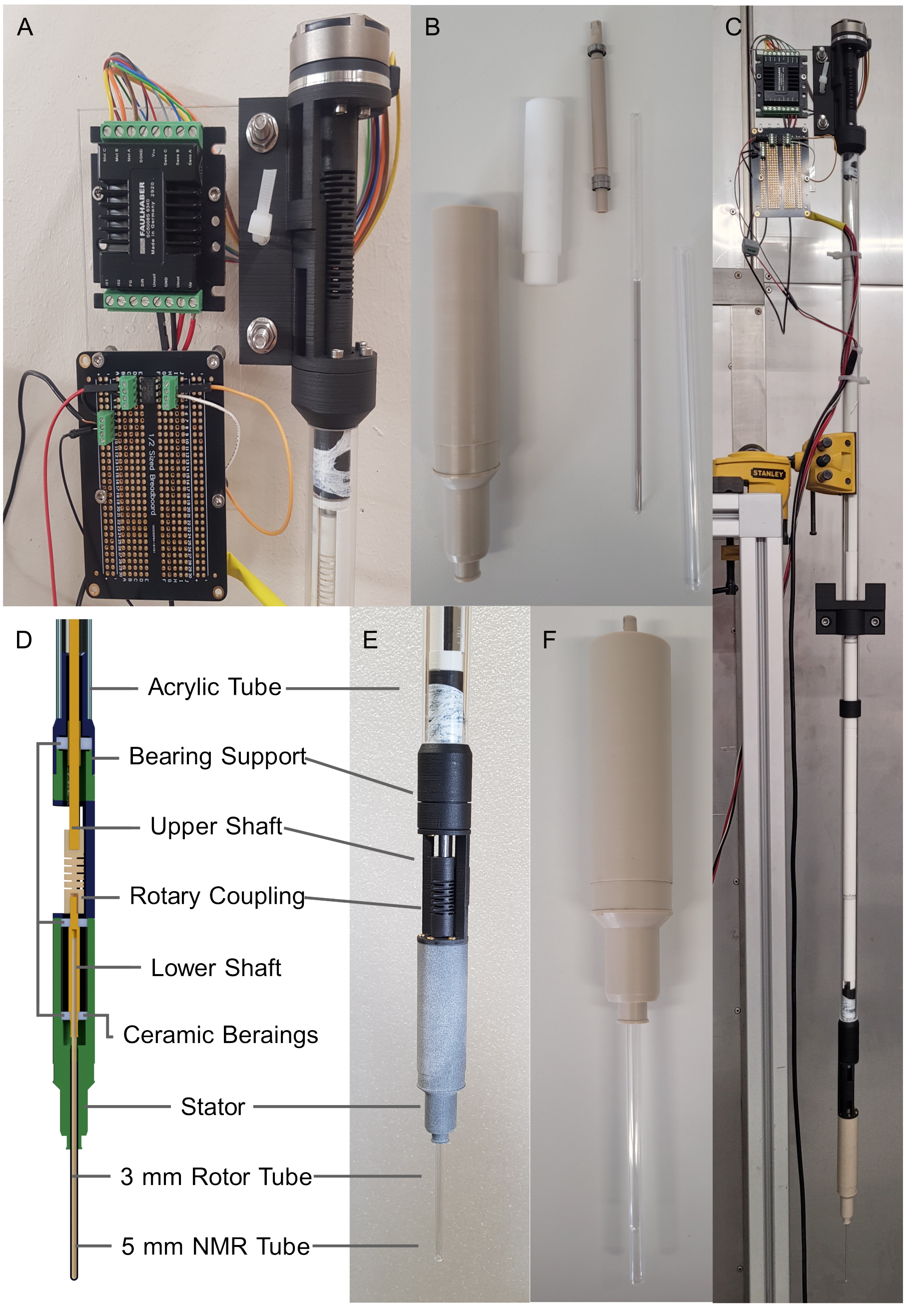

Figure 3.1: Pictures and schematics of the Rheo-device. A) The top of the device can be seen with the motor and the connection to its controller as well as the TTL inverter. B) The second generation of the stator out of PEEK and the inner parts are taken out. The inner parts are a white spacer out of Teflon, the lower shaft out of PEEK for the 3mm tube on which three non-magnetic bearings (one on top, two at the bottom) are put and the 3mm tube with DMSO-d_6 inside. The empty 5mm tube is held only by the stator. C) The whole device outside the magnet. The bigger black part in the middle of the rod is adjustable and shall hold the whole device at the correct height in the magnet and probehead. D) A cross-sectional view of the stator. The parts are named in the figure. E) The first generation of the stator screwed to the 3D printed connection between stator and acrylic tube. The lower shaft is connected over a rotary coupling to the upper shaft, while the stator is connected over a bracket to the bearing support. F) The second generation stator from B but now all parts are put together. The small PEEK part outside the stator is from the lower shaft.

by two ceramic bearings and a 3 mm NMR tube connected to the lower shaft. Around the rotor is the stator holding the 5 mm NMR sample tube and centering the whole apparatus in the magnetic bore.

Stator and acrylic tube are connected by a bracket surrounding the rotary coupling. All custom parts (rotor, stator, rotary coupling, etc.) are 3D printed from nylon using multijet fusion.
In a second generation, the 3D printed stator and lower shaft were substituted by the chemical inert material polyether ether ketone (PEEK). Also, the ceramic bearings were replaced by non magnetic steel bearings with balls out of silicon nitride or zirconia (type: HYQ NMMR85 T17HB A5 C8/13 EQ L39-4, HQW, Kürnach, Germany). These new bearings have an outer radius of 5 mm and therefore a spacer out of teflon holds the lower shaft with 3 bearings inside the stator. The rest of the apparatus stayed unchanged as no other part came in contact with the solvent chloroform or its evaporated gas.

In experiments where explicit pulse programming cannot be used and therefore no TTL signals can be sent from the console to the speed controller, the arbitrary waveform generator is used as TTL signal source. Additionally, this generator was used to test several rotation speeds which are used in the explicit pulse programming as well. After these tests, I decided to go with four different duty cycles (0.70, 0.75, 0.80 and 0.85) of the arbitrary waveform generator. With a laser, I measured the corresponding revolutions per minute of the rotor and calculated the frequencies and shear rates of our device as can be seen in Table 3.6. I calculated the shear rates with Equation 2.128 with the outer radius of 2.1 mm and the inner radius of 1.5 mm. Normally, Equation 2.128 only accounts for $\kappa = R_i/R_o > 0.99$ (our κ is 0.71), but as the torque cannot be measured on this apparatus, I cannot use the exact solution. Also, the exact solution does not account for errors like shear heating and imperfections anyway and therefore Equation 2.128 is often used for rheo-NMR devices[147].

Table 3.6: Revolutions per minute, rotation frequencies, angular frequencies and corresponding shear-rates of the rheo-device for the used duty cycles of the waveform generator

duty cycle	revolutions per minute [s^{-1}]	rotation frequency [Hz]	angular frequencies [s^{-1}]	shear-rates [s^{-1}]
0.70	2854	47.6	298.9	896.6
0.75	2335	38.9	244.5	733.6
0.80	1819	30.3	190.5	571.5
0.85	1300	21.7	136.1	408.4

The group of Callaghan[23] with their similar apparatus of a 3 mm tube inside a 5 mm tube on a long rod rotated by a motor on top, were able to measure the torque on their apparatus in a 500 MHz spectrometer. With this torque, they calculated the maximum and average shear rates with these formulae

$$\dot{\gamma}_{max} = \frac{2\omega}{1 - \left(\frac{R_i}{R_o}\right)^2} \tag{3.1}$$

and

$$\dot{\gamma}_{av} = \frac{4\omega \left(\frac{R_i}{R_o}\right)^2 ln\left(\frac{R_i}{R_o}\right)}{\left(1 - \left(\frac{R_i}{R_o}\right)^2\right)^2} \tag{3.2}$$

Using these formulae for my apparatus, I get similar average shear rates compared with Equation 2.128 for a perfect system with $\kappa > 0.99$. This shows, the approximation made for rheo-NMR devices fits sufficiently well. With Equation 3.2 I get negative values for the average shear rate. This is not surprising from the equation itself, as it has no additional minus sign and except the natural logarithm and ω everything is squared where the angular frequency ω is always positive and the natural logarithm of R_i/R_o is always negative. The negative natural logarithm comes from the fact that the inner radius has to be smaller than the outer radius and therefore R_i/R_o is always smaller than one. And a $ln(x)$ with $x < 1$ is always negative. However, the source itself only presents results with positive shear rates[23].

Table 3.7: The maximum and average shear rates after the group of Callaghan[23] in comparison to the shear rates calculated with the formula for $\kappa > 0.99$.

shear-rates [s^{-1}], $\kappa > 0.99$	average shear-rates [s^{-1}] after Callaghan	maximum shear-rates [s^{-1}] after Callaghan
896.6	-855.5	1220.4
733.6	-699.9	998.5
571.5	-545.2	777.8
408.4	-389.7	555.9

Before I decided for PEEK as material for the stator and rotor for the second generation, I tested various cheaper materials in their stability against chloroform which I can use in our 3D printer. Unfortunately, none of these materials are stable with chloroform (Table 3.8) and I had to go for the expensive and not 3D printable PEEK.

Table 3.8: Materials tested in $CHCl_3$ for the shaft

plastic	composition	stable in $CHCl_3$
PVA	polyvinyl alcohol	swells
PLA	polylactic acid	dissolves
CPE	a branched glycol-modified polyethylene terephtalate	dissolves
CPE$^+$	glycol-modified polycyclohexylenedimethylene	dissolves
Breakaway	PLA/TPU mixture	swells
TPU 95A	thermoplastic polyurethane	swells
PC	polycarbonate	dissolves
Nylon	polyamide	swells minimal
PEEK	polyether ether ketone	stable
Rheo	nylon after 3D printing	gets brittle

The first tests for the utility in NMR were done with 99.9 % D_2O. 1D deuterium spectra were acquired resulting in linewidths comparable to spectra obtained in conventional 5 mm tubes. The signal intensity compared to the conventional tube was 40 %. Hereby, the inner 3mm tube reduces the active volume to 48 % and the residual 8 % signal loss is due to a barely noticeable decreased shim. The rotation of 50 Hz is increasing the linewidth only negligible, mostly with some broadening of the foot and the signal intensity is approximately the same as without rotation.

4 Results and Discussion

4.1 Changing the Alignment Director

The 1D deuterium spectrum of pure $CDCl_3$ shows one isotropic peak at 7.28 ppm as it is referenced relatively to TMS. Adding the LC PBLG in high enough amounts, anisotropy is induced in the sample and the deuterated solvent peak splits into two separated ones. In the anisotropic environment, the quadrupolar coupling is not averaged to zero anymore and the whole sample aligns with the magnetic field indicated by this signal splitting. Nevertheless, if the PBLG concentration is not high enough, no splitting occurs and the spectrum still looks isotropic to the eye (fig. 4.1A and B). In this case, a 13 wt% PBLG sample showed a quadrupolar splitting of $|\Delta\nu_Q|$ = 482 Hz while aligned parallel to the magnetic field (alignment angle Θ_D = 0°). The tilt of the alignment director and the splitting are proportional to the second Legendre polynomial $3cos^2\Theta_D$ - 1 and as earlier works with VASS showed, the splitting changes from 0° to a deviating tilt angle[14,50]. Instead of a VASS probehead, the tilt of the alignment director can be changed by shear force, which, according to literature, results in a direction nearly perpendicular to the magnetic field[82,140]. This change of the director perpendicular to the magnetic field, was the first goal with the home-built rheo-device (these results and the following ones were already published in 2023[148]). The resulting 1D deuterium spectrum of the 13 wt% PBLG sample under shear force can be seen in Figure 4.1C with a quadrupolar splitting of $CDCl_3$ of $|\Delta\nu_Q|$ = 193 Hz. Hereby, the linewidth at FWHM increases from 13.4 Hz (static) to 26.2 Hz (sheared), which is about twice the linewidth. This indicates either a reduced quality of the shim or a slightly increased distribution of aligned polymers. If the theoretically Θ_D = 90° would be reached, the splitting under shear should be exactly half of the splitting without shear and change its sign. However, the splitting under shear is approximately 40 % of the splitting without shear. Without knowing the sign, this corresponds either to an angle of 39.2° or 75.1° calculated with

$$\frac{Q_{ns}}{Q_s} = \frac{3cos^2\Theta_{ns} - 1}{3cos^2\Theta_s - 1} = \frac{2}{3cos^2\Theta_s - 1} \tag{4.1}$$

where Q is shortly written for $\Delta\nu_Q$ in the spinning (s) and non spinning (ns) case. Solved for $cos\Theta_D$, the equation converts to

$$cos\Theta_s = \sqrt{\frac{2Q_s}{3Q_{ns}} + \frac{1}{3}} \tag{4.2}$$

An experiment developed in our group, the Q.E.COSY[149], allows sign sensitive measurements of the quadrupolar coupling. The corresponding 2D spectra for all three cases (isotropic, static anisotropic and anisotropic under shear) can be seen in Figure 4.1. The left tilt of the static case indicates a negative quadrupolar coupling $\Delta\nu_Q$ = - 482 Hz and the right tilt in the sheared case indicates a positive quadrupolar coupling $\Delta\nu_Q$ = 193 Hz. The isotropic spectrum does not show any quadrupolar coupling as expected. The second measurable coupling in the Q.E.COSY experiment is the ${}^1T_{CD}$-coupling (or

$^1J_{CD}$ = 64 Hz in the isotropic case) of 45 Hz (static) and of 26 Hz (under shear). With the Q.E.COSY, the unambiguous proof of the sign change is given and therefore the proof that the home-built rheo-device changes the alignment director by 75.1°.

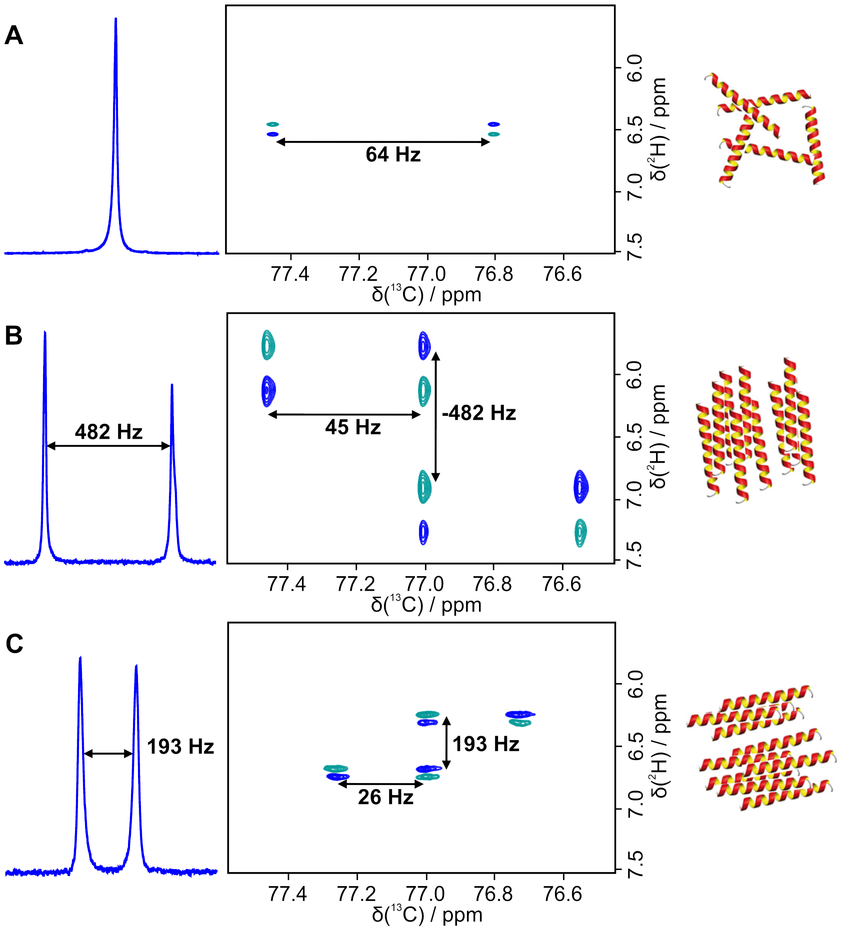

Figure 4.1: 1D deuterium spectra (left), 2D Q.E.COSY spectra (center) and the respective alignment (right) for different PBLG/$CDCl_3$ conditions. Arrows with the corresponding coupling values indicate quadrupolar $\Delta\nu_Q$ and total $^1T_{CD}$ = $^1J_{CD}$ + $^1D_{CD}$ couplings for the three conditions. (A) A 4% PBLG/$CDCl_3$ sample without shear stress shows no quadrupolar couplings and appears as an isotropic polymer orientation. (B) A 13% PBLG/$CDCl_3$ sample without shear stress shows large alignment. The director in the Q.E.COSY tilts to the left indicating a negative sign for the quadrupolar coupling. (C) The sample from B under shear stress shows a strongly reduced alignment. On top of that indicates the Q.E.COSY a sign change to a positive quadrupolar coupling[148].

4.1.1 Influence of concentration on the alignment

After I could show that the device works for fully anisotropic PBLG samples, I diluted a 15.4 wt% PBLG/$CDCl_3$ sample with flurbiprofen step by step. The goal was a complete and systematic characterization of the quadrupolar splitting behavior under shear for different concentrations. Additionally, the second goal was to align and observe quadrupolar splittings underneath the critical concentration as the rheological theory of liquid crystals tells about PBLG sheared in a rheometer.

Due to the open NMR tube, $CDCl_3$ is lost over time and I had to roughly estimate every dilution step. Nevertheless, within a small error the expected correlation between amount of alignment and concentration could be seen. As can be seen in Figure 4.2 and in the appendix in Figure 6.1, the quadrupolar splitting of $CDCl_3$ decreased almost linearly until the critical concentration of alignment induced splitting and below this concentration no splitting could be seen for the static case. Above the critical concentration, the quadrupolar splitting during rotation behaved the same way, always with approximately 40 - 50 % of the static splitting. Then, for a short concentration range, the splittings stayed nearly equal and afterwards decreased again, this time exponentially, down to a measurable splitting of 2 Hz for less than 2 wt% PBLG/$CDCl_3$. The sheared sample was always aligned between 75-90° against B^0. The exact angles for the dilution steps with a static alignment can be seen in Table 4.1. The table shows the approximately calculated concentrations, the static and rotational splittings and the calculated angles under rotation. Interestingly, dilution step 2 with approximately 9.5 wt% showed a quadrupolar coupling under rotation which was larger than half of the size of the static quadrupolar coupling. As Equation 4.2 can only calculate for splittings up to half of the size of the static alignment (otherwise there is a negative value inside the square root), this angle had to be set as the full 90°. The linewidth for these spectra are 6 Hz under rotation and 8 Hz without rotation and with an estimated error of approximately 2 Hz, the director might be slightly less than 90°.

Table 4.1: The dilution series of PBLG with flurbiprofen while measuring at the rheo device. This table shows only the concentrations with an alignment without rotation and the tilt angle of the alignment director reached by rotation in the apparatus.

dilution step	approximated concentration	splitting without rotation	splitting during rotation	tilt angle to the magnetic field
0	15.4 wt%	-615.1 Hz	271.8 Hz	78.6°
1	13.9 wt%	-535.0 Hz	239.3 Hz	79.2°
2	9.5 wt%	-234.2 Hz	118.7 Hz	90°
3	8.7 wt%	-225.1 Hz	109.1 Hz	84.2°
4	8.3 wt%	-219.1 Hz	96.7 Hz	78.6°
5	8.1 wt%	-214.0 Hz	97.1 Hz	79.9°
6	8.2 wt%	-215.2 Hz	93.8 Hz	78.1°

The short range where the values of the splittings show the plateau during rotation, was the biphasic region where PBLG is isotropic and anisotropic at the same time without shear-force. In the static case, the quadrupolar splitting of the anisotropic peaks stay nearly the same but the height of the isotropic and anisotropic peaks change within dilution. More on this biphasic phenomenon will be discussed in Section 4.2.

As a comparison to this dilution study with uncertainties in the concentration values, various PBLG/$CDCl_3$ samples at different concentrations without a solute molecule were measured (see Fig. 4.2 and in the appendix Fig. 6.1). The overall behavior was equal to the dilution series of the flurbiprofen sample. Above the critical concentration, the splittings decreased nearly linear in both cases, static and under rotation. Below, the static measurements showed no sign of a splitting and under rotation the decrease was exponential. Unfortunately, not one sample of the concentrations I chose did show the biphasic region. The tilt angles of the three concentrations above the biphasic region were 88.5° for the 9 wt% sample, 88.7° for the 10 wt% sample and 83.7° for the 12 wt% sample. Similar to the diluted concentrations with flurbiprofen, they showed angles > 80° for concentrations directly above the transition region. Hereby, the angles were even higher than for the diluted concentrations with flurbiprofen. This might be due to the influence of flurbiprofen, as the same effect could be seen with other samples containing a solute molecule. All the samples with strychnine, for example, never showed a tilt angle under rotation of more than 80° even for concentrations directly above the transition region. Solute molecules have quite an impact on the alignment of PBLG as will be further discussed in Section 4.2.

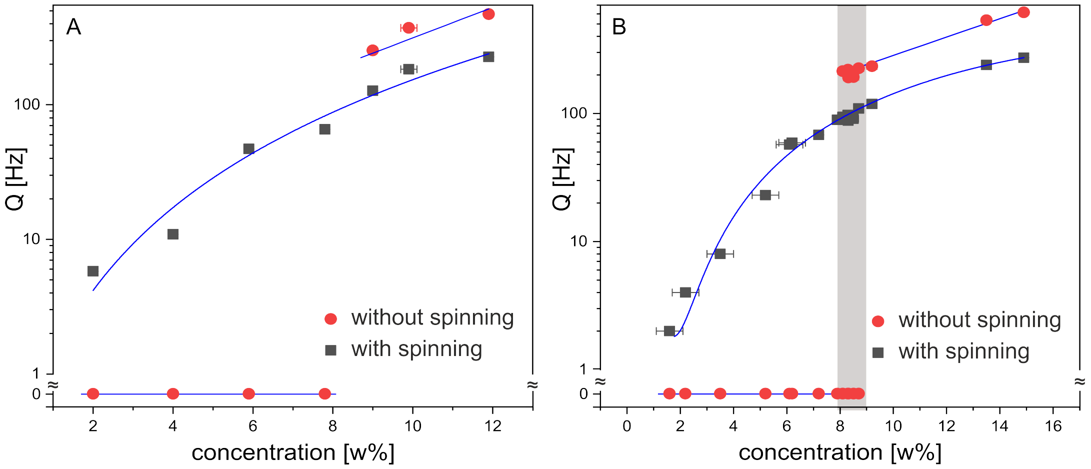

Figure 4.2: Logarithmic plots of the quadrupolar splitting of PBLG/$CDCl_3$ without solute molecule (A) and with flurbiprofen as guest (B) versus the concentration. The red dots indicate the static case and the grey squares the splitting under 48 Hz rotation. Below 8 wt%, red dots at 0 Hz for the non existing quadrupolar splitting in the isotropic phase are added. In the grey-shaded area highlighting the coexistence of isotropic and anisotropic phase red dots at 0 Hz are added as well[148].

In both series, the deuterium 1D spectra look alike. The static ones as shown very often in literature with either the isotropic peak directly at the chemical shift of $CDCl_3$ or the pure anisotropic peaks as a doublet split by the quadrupolar coupling. During rotation, the two peaks were not always narrow signals. At higher concentrations (>11 wt%), the linewidths are broad. The 13 wt% for example had a static FWHM linewidth of 13.4 Hz and 26.2 Hz during rotation. Probably due to the rotation, either a slightly increased distribution of aligned polymers or a reduction of shim quality was seen, or both together at the same time. Even with the possibility of shimming on the inner 3 mm tube with isotropic DMSO, the linewidths for these high concentrations could not be lowered. At lower concentrations, the linewidths were slightly better and as soon as an isotropic $CDCl_3$ signal was seen in the static case, the linewidth drops to 3-4 Hz for narrow peaks at both, static and shearing conditions. Unfortunately, there were some concentration regions, where no narrow peaks were seen but a peak form reminiscent to a Pake-pattern. In the measurements, these patterns were seen for some samples around 10 wt% and between 3.5 and 6 wt% (see Fig. 4.5 in Section 4.1.3 for an example). Since the deuterium spectrum reflects the tilt angle of PBLG and the alignment tensor, these patterns probably show that more than one sheared angle exists simultaneously. This phenomenon may be caused by one or more of the following effects. The first one was observed for PBLG in rheological literature and is called 'wagging' or 'kayaking', if the multiple angles correspond to a single shear rate. Both describe the waving behavior of the alignment angle between two values in regions where a single angle is not stable. The second one is due to the fact that in a Couette cell we have a distribution of shear rates over the gap, especially over wide gaps as in the used apparatus. However, Atkin et al.[85] showed in their work, that the different shear rates over the gap did not affect the size of the quadrupolar coupling too much and the quadrupolar couplings were approximately constant over the gap. The last reason might be the effect of shear banding which is often observed for wormlike micelles. Hereby, the solution under shear subdivides into two separate phases with the same shear stress and rotational frequency but exhibiting two different shear rates[87,88]. Two different shear rates would then lead to two different alignment angles. The observed pattern in the shown spectra could be described as four symmetrical peaks where the two peaks on either side of the chemical shift with zero quadrupolar coupling were overlapping. This would correspond to two quadrupolar couplings, hence two different alignment angles. With the equipment of our group, I could not measure the needed imaging experiments and thus cannot answer this question so far. Between 6 and 10 wt% always two narrow peaks could be seen even in the biphasic region and below 3.5 wt% the narrow peaks vanished into one combined peak where the linewidth is equal to the splitting and therefore full separation is not achievable anymore.

4.1.2 Influence of temperature and shear rate

Not only the concentration has a strong influence on the LC behavior but the temperature and the used shear-rate as well. Therefore, the temperature was changed in the magnet with the temperature control unit (TCU) from 284 K to 313 K in 5 K steps and the shear-rate by adjusting the rotation frequency to 21.7 Hz, 30.3 Hz, 38.9 Hz and 47.6 Hz (Fig. 4.3). With the TCU, the lowest possible temperature is 284 K and 313 K is just 20 K below the boiling point of $CDCl_3$ which I chose as last safe-to-use temperature without high evaporation or even boiling in the magnet. The frequencies and therefore the shear rates were chosen through the adjustable duty cycles of 0.70, 0.75, 0.80 and 0.85.

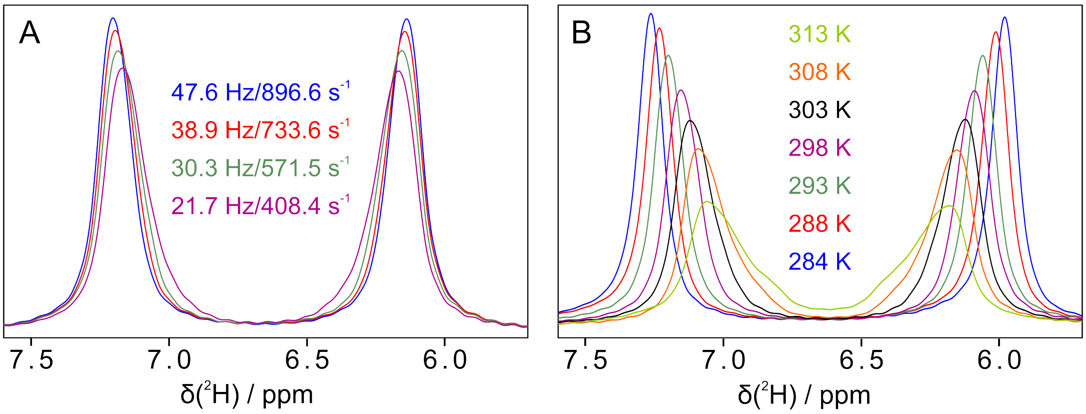

Figure 4.3: The influence of different shear-rates at 298 K (A) and of various temperatures at 48 Hz rotation (B) for a 7.8 wt% PBLG/$CDCl_3$ sample. In (A), the shear rates are given in s^{-1} and the corresponding rotation frequencies in Hz[148].

A shear rate of 400 s^{-1} is already very high. So, it did not surprise that the difference between the lowest (408.4 s^{-1}) and the highest shear rate (896.6 s^{-1}) is only tenuous. The higher the shear rate, the sharper was the signal with slightly higher intensity. Additionally, at the highest shear rate at 298 K for a 7.8 wt% sample a quadrupolar splitting of 64.4 Hz could be seen and at the lowest of 61.5 Hz. Because the sample showed no splitting under static conditions, the exact angle of the alignment tensor could not be calculated. If the 64.4 Hz are assumed as 44 % of the static splitting, the theoretical static splitting would be 146.3 Hz and the 64.4 Hz splitting would represent a tilt angle of 78.6°. The angle at the lowest shear rate with 61.5 Hz compared to the theoretical 146.3 Hz would then be 76.8°. Therefore, both shear rates showed approximately the same results and the used shear rates in the range of rotation frequencies did not matter.

The temperature on the other hand, matters quite a bit. Between 284 K and 298 K, the results were similar to the ones differing in the shear rate. The 64.4 Hz splitting increased to 78.7 Hz at 284 K with even sharper signals and higher intensity. Towards higher temperatures up to 313 K, the splitting and intensity did not only decrease, but the peaks were getting broader and started to show the pattern of a distributed alignment tilt. Fung and Martin[150] found already in 1974 that the quadrupolar splittings of $CDCl_3$ and CD_2Cl_2 in liquid crystalline solutions of PBLG increase with 1/T as we observe here. According to Arrhenius (Equation 2.106), the viscosity decreases with higher temperatures and according to Debye (Equation 2.103), the correlation time decreases for higher temperatures as well as for lower viscosities. Hence, T_2 increases for higher temperatures and lower viscosities (see Equation 2.101) and the linewidth decreases which is opposite to the observations. Thus, there must be another effect playing a bigger role. From the phase diagram of PBLG (Fig. 2.14) is known that higher temperatures lead to less anisotropic behavior and to a more isotropic behavior. Especially if the concentrations are lower than 20 wt% (as used in this work). Furthermore, the solvent mobility increases with higher temperatures, which is decreasing the anisotropic order and increasing the isotropic order. This explains at least the increasing quadrupolar splitting for lower temperatures where higher anisotropy results in higher quadrupolar couplings. As linewidths under shear are compared, one should not forget the tilt of the alignment director. Broader linewidths represent a higher distribution of alignment angles due to varying shear rates over the gap in a Couette cell or due to a slight oscillation of the director angle. Therefore, the moderately rising isotropic character of PBLG probably increases the distribution of the alignment angles and hence the linewidth of the observed peaks.

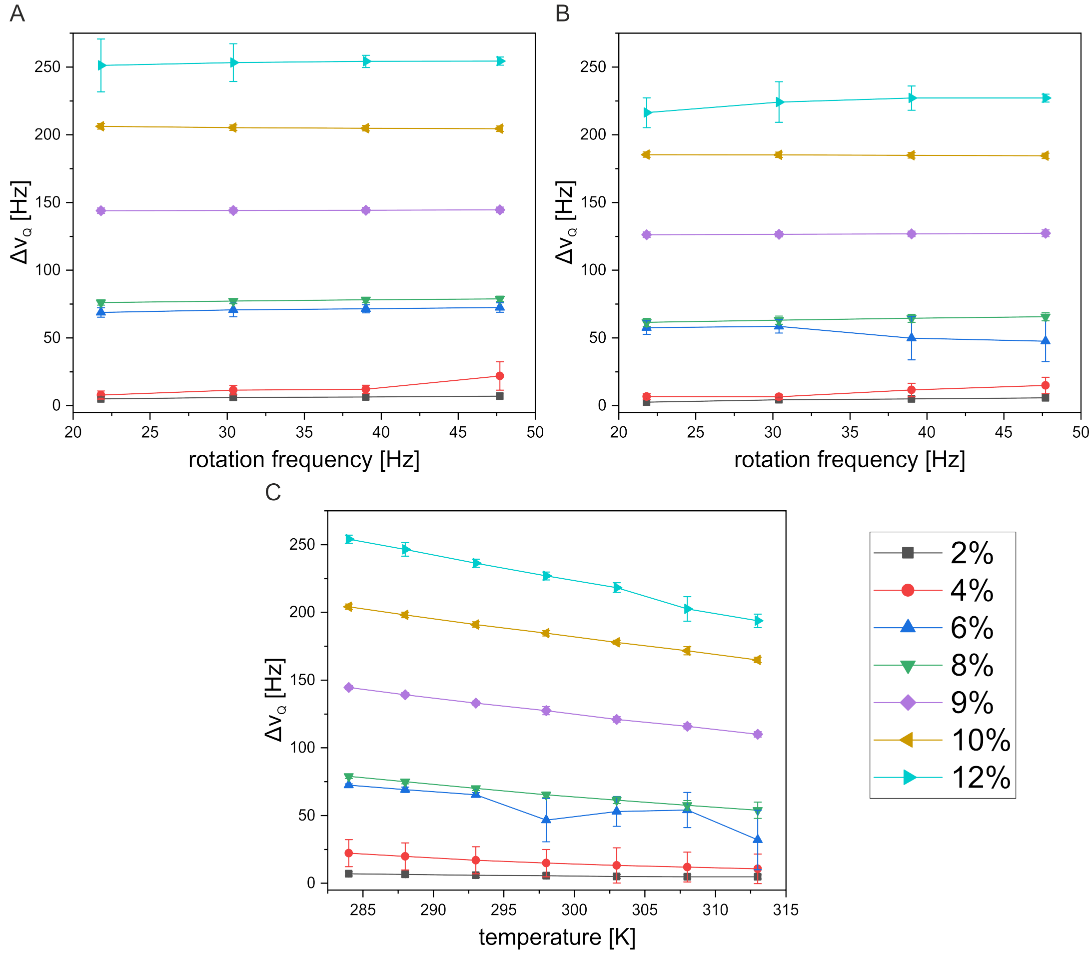

Figure 4.4: The influence of shear-rate (rotation frequency), temperature and concentration on the quadrupolar splitting of $CDCl_3$. In (A) the quadrupolar splittings at different shear-rates at 284 K are shown, in (B) at 298 K. In (C) the temperature was changed and the shear-rate was constantly at 48 Hz. The seven concentrations of PBLG/$CDCl_3$ are measured without a guest molecule[148].

The same effect could be seen for all tested concentrations (Fig. 4.4). The quadrupolar splittings increased with shear rate and rotation frequency only by a few hertz. Hereby, the temperature did not matter, the trend was the same for all concentrations at every temperature. Changing the temperature showed the opposite effect, independent from the concentration, the quadrupolar splitting always decreased with higher temperature. The quadrupolar splittings between 6 and 8 wt% did not change much, neither for the temperature nor the shear rate plots. The same happened between 2 and 4 wt%. The second is easy to explain. Reaching the lower limit of the concentration with very small quadrupolar splittings (2-20 Hz), the decrease could not be linear anymore but decayed exponentially to zero at these low concentrations. The small region between 6 and 8 wt% might be due to the biphasic region where the anisotropic fraction did not change the amount of splitting. On the other hand, this 8 wt% sample was already below the biphasic area and the quadrupolar splittings should already decrease exponentially. On top of that, the 6 wt% showed the biggest deviations in the linear behavior compared to the other concentrations in the shear rate and temperature behavior. The splitting values of the outliers of the 6 wt% sample would make more sense and maybe these were the actual correct values. Also, as could be seen in the next section and in the Figures 4.8 and 4.9, the deuterium spectra at approximately 6 wt% did not show always two nice resolved peaks but all kinds of different distribution patterns which made it difficult measuring the correct values of the quadrupolar coupling for such spectra.

4.1.3 Kinetic studies

The following kinetic studies were measured on the 15.4 wt% PBLG/$CDCl_3$ sample containing flurbiprofen which was used for the dilution series with $CDCl_3$. Exemplary, the studies for three different concentrations in the high, intermediate and low concentration area are shown. Figure 4.5 shows their deuterium spectra during rotation and without. The intermediate concentration at 8 wt% is in the biphasic area with a slightly broadend doublet during rotation while the low concentration at 6 wt% with the isotropic peak under static conditions shows a peak form reminiscent to a Pake pattern during rotation. The splitting for the high concentration of 15.4 wt% is around 44.2 % representing an alignment tilt of 78.7°, for the intermediate concentration the splitting is around 45.0 % with representing an alignment tilt of 79.4° relative to the magnetic field. The linewidth for the intermediate concentration in the static case reduced to 3.5 Hz without apodization due to the possible automatic shimming on the isotropic $CDCl_3$ signal. Under rotation the linewidth reduced even more to 2.8 Hz. The distribution pattern for the 6 wt % concentration consisted of only positive quadrupolar couplings as could be seen in a Q.E.COSY spectrum. Hence, the corresponding alignment angles Θ_D to the quadrupolar coupling must all be larger than the magic angle. As discussed before, these multiple angles can be either due to a response to several shear rates in the gap, the effect of kayaking or wagging, or to shear banding.

For the acquisition of all three kinetic studies, we programmed our own pulse sequence where I could control the rotation of the 3 mm inner tube via TTL signals from the spectrometer console instead of the waveform generator. As the insert of the TTL output for my purposes needs explicit pulse programming and therefore separation of the time unit from the other channels, this form of pulse programming is only possible for sequences without gradients. Nevertheless, standard 1Ds (here the ^{2}H 1D) do not use gradients and therefore two types of experiments were created. One, where the time the director needs for full alignment in the shear plane was measured and the second where the time the director needs to relax back parallel to B^0 after shear cessation. The deuterium channel was similarly programmed for both. The sequence starts with a waiting time interval d_{eq} for equilibration of the alignment (only needed for the relaxation back parallel to B^0) followed by a second time interval d_r and a third one Δ and finishes with the 90° pulse directly before the acquisition. The interval d_r was set either to 10 s for the shear cessation experiments or to 600 s for the experiments switching the alignment into the shear plane. The delay d_{eq} was set to 500 s and Δ was varied between 10 µs and 10000 s for the relaxation back to 0° and between 10 µs and 10 s for the switching into the shear plane during rotation. In the second channel for the rotation two cases needed to be distinguished. The first one where I was interested in the time Δ the system needs to switch the alignment back after rotation and the second one where Δ represents the time the system needs to tilt the alignment into the shear plane. Therefore, in the first case, it was rotated during d_r and Δ started directly when the rotation stopped and in the second case, it was not rotated in the beginning but the rotation started together with the time interval Δ and it was rotated during the acquisition. The delay d_{eq} for the first case was

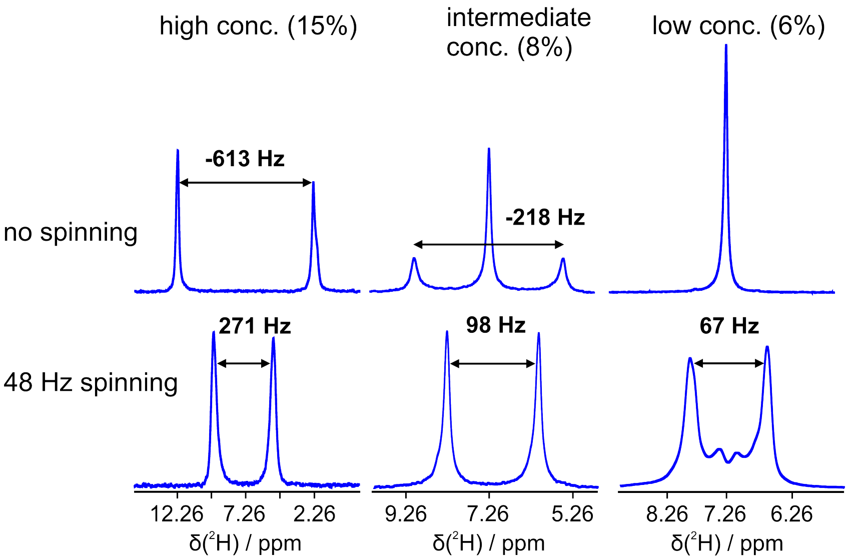

Figure 4.5: ^{2}H 1D spectra of PBLG/CDCl$_3$ with 20 mg flurbiprofen diluted to different concentrations. The top row shows the spectra without rotation and the bottom row with 48 Hz rotation. The high concentration (15 wt%) shows a large quadrupolar coupling for CDCl$_3$ with the known doublet which is reduced by 44.2 % in its size under rotation. Diluting to around 8 wt%, the spectra without rotation shows the transition from anisotropic to isotropic as a small biphasic region. Spinning mixes the phases with the coupling reduced to 45.0 % of the anisotropic phase. At 6 wt%, the sample is completely isotropic without rotation, which changes to a distribution of quadrupolar couplings during rotation[148].

used for two reasons: reduce the time of rotation and therefore less heat produced by the rotation and as recovery for the alignment if Δ was shorter than 500 s.

First, a look at the time the alignment needs to get back parallel to the magnetic field after shear cessation for the high concentration (Fig. 4.6A). In the first second, the two peaks broaden and loose intensity until they reached a coalescence after already 5 seconds. The coalescence indicates the change of sign from positive quadrupolar couplings under rotation back to negative couplings. Another 5 seconds later, the peaks for the z-alignment show up, still very broad with a connected baseline and the full quadrupolar splitting is not reached yet. After around 50 s, the final quadrupolar splitting is reached. A negligible few Hertz is missing but the peaks are still broad with tails pointing to the center. After around 500 s this hump is not distinctive and no change in the quadrupolar splitting can be observed anymore. Still, signal intensity and sharpness increase even after 5000 s in the 400 MHz spectrometer. The long time the alignment needs to be back parallel to the magnetic field is due to the used 9.4 T magnet. At lower fields, the time is even longer. For example, in a 2.2 T magnet, the alignment needs up to 24 hours[151]. Or, as will be seen in Section 4.2, a higher magnetic field shortens this time.
The switching time for orienting magnetization perpendicular to the magnetic field induced by rotation is on a different time scale (Fig. 4.6B). After 5 seconds the final quadrupolar splitting and the full symmetric Lorentzian shape is reached. Afterwards, the peaks increase only slightly in intensity and sharpness. It even takes not more than 100 - 200 ms reaching the final doublet under rotation with a negligible difference in the quadrupolar splitting compared to the maximum splitting. The coalescence from the other switching time could be seen here as well, only this time already after 10 ms. After 50 ms, the final peaks start to show up still as a part of the coalescence. Interestingly, even the lowest delay Δ of 10 µs shows that the original alignment along z is already vanished and broad peaks with a lower quadrupolar splitting can be seen.

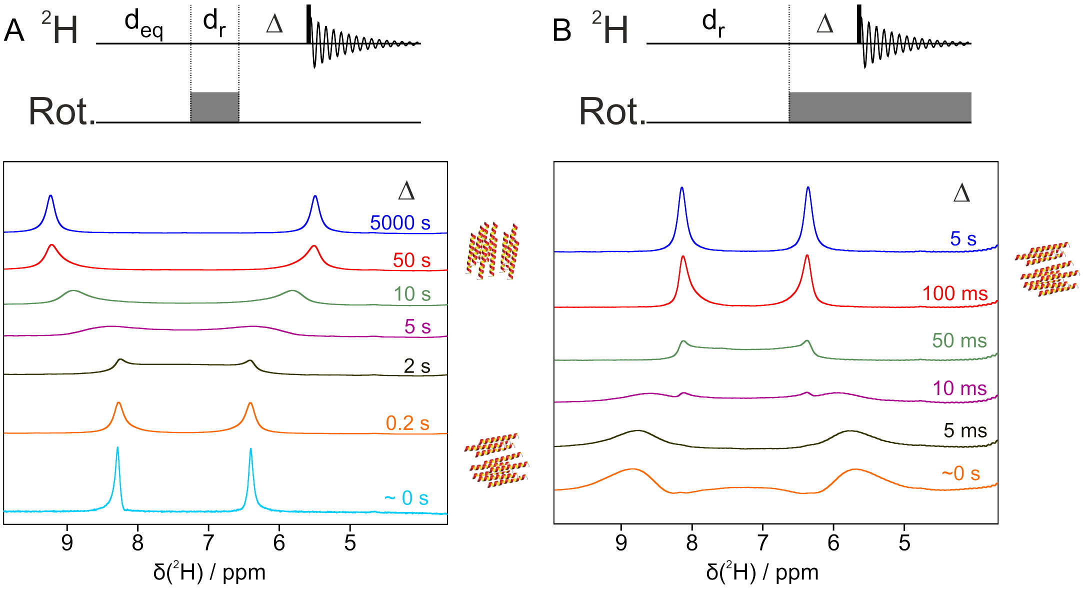

Figure 4.6: Deuterium spectra of a 15 wt% sample PBLG/$CDCl_3$ with 20 mg Flurbiprofen showing the behavior during switching from rotation to no rotation (A) and vice versa (B). On the right side of the spectra are the values for Δ and next to it helices visualize the corresponding phases. The delays were set to d_{eq} = 500 s, d_r = 10 s for (A) and d_r to 600 s[148].

The behavior for the relaxation time after shear cessation at the intermediate concentration had one similarity (Fig. 4.7A). It takes up to 300 s until the final quadrupolar splitting for the outer anisotropic peaks can be seen and afterwards narrowing of the linewidth and increasing in the intensity is observed. The other behavior is quite different. The coalescence for example is between 50 and 100 s and changes from one broad isotropic peak to another broad isotropic peak at the chemical shift of $CDCl_3$. The first isotropic peak, which can be seen after around 20 s comes after a distribution pattern where the distance between both peaks decreases until no quadrupolar couplings are observed. The distribution patterns in both peaks show up after 500 ms. Before, the two sheared alignment peaks increase in linewidth and decrease in intensity and quadrupolar splitting. As will be discussed later in Section 4.2, it is typical for a biphasic sample needing more time to build up both phases. Therefore, it is not surprising that the change of sign of the quadrupolar coupling (the coalescence) takes places almost 50 seconds later than for the high concentration sample.
The switching time from no rotation into rotation looks similar to the one from the high concentration sample (Fig. 4.7B). Again, both anisotropic peaks show up after 50 ms, this time somewhat more clearly, and the coalescence vanishes a few milliseconds earlier. In addition, this time the coalescence begins during the FID.

Last, the kinetic studies for the low concentration behave very similar to the intermediate one (Fig 4.8A). From 20 s on, they look alike with the coalescence between 20 and 100 s and even the anisotropic peaks show up after 300 s. After a few thousand seconds they vanish again. These peaks probably pop up due to an increase in concentration through evaporation of the solvent over time which fastens by rotation. Or, it was a kind of memory effect where complex fluids show viscous and elastic responses that depend on the history of shear[17]. As the sample was close to the transition region, some PBLG mesophases might have "remembered" the alignment under shear until a sufficiently long waiting time converted them to an isotropic phase. All more diluted samples do not show these small aligned peaks. Contrary to the intermediate concentration, none of the deuterium spectra in the shear cessation study show any sign of a distribution pattern. Only the first few milliseconds show different kinds of spectra with two peaks and a negative spectral dropout in the middle.

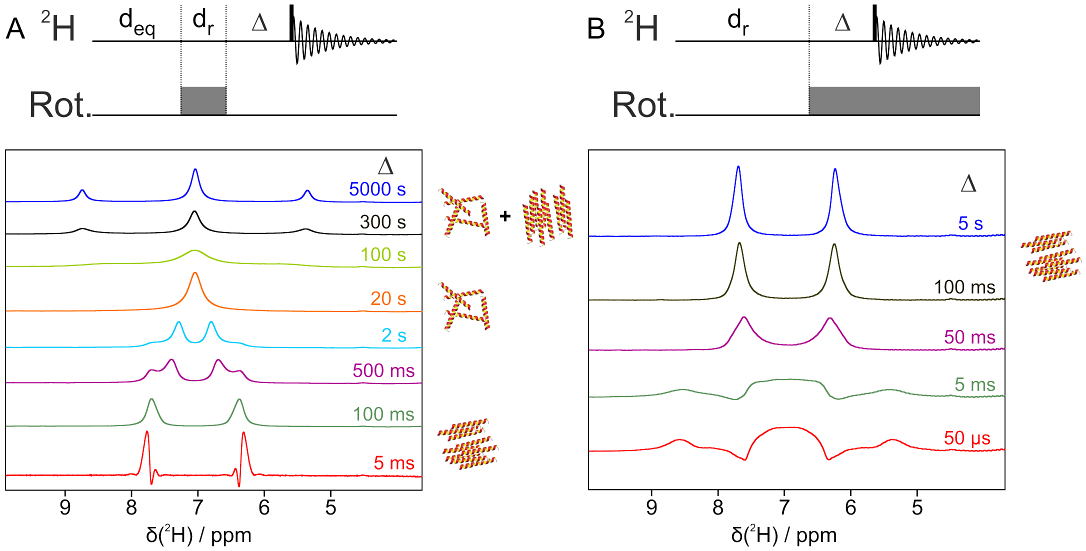

Figure 4.7: Deuterium spectra of a 8 wt% concentration PBLG/$CDCl_3$ with 20 mg Flurbiprofen showing the behavior during switching from rotation to no rotation (A) and vice versa (B). On the right side of the spectra are the values for Δ and next to it helices visualize the corresponding phases. The delays were set to d_{eq} = 500 s, d_r = 10 s for (A) and d_r to 600 s[148].

The switching time, after the rotation started, does not show the coalescence anymore (Fig 4.8B). A broad peak in the middle with distribution patterns and two small negative spectral dropouts can be seen right from the beginning. The peak broadens in the first milliseconds with more distribution on top separating in two peaks after 50 ms at both ends still with a distribution pattern in the middle. After 100 ms these peaks are more clear and the distribution pattern in the middle can also look like a big hump or two very small peaks. Up to 5 seconds, the outer two peaks increase in intensity and become narrower and the small peaks in the middle decrease but never vanish. Lepper et al.[152] observed a similar behavior for their wormlike micelles during their highest shear rates (shear rates of 1-2 s^{-1} as highest shear rates). They call these pattern "ridges" and explain it with a disassembly of the micelles into two different orientation angles which reassemble after some shearing time to the larger angle ending in two completely separated peaks at the expected orientation angle under shear. If in the shown case, the distribution pattern at room temperature after 5 s also changes into two complete separated peaks after a long enough waiting period, cannot be said for sure. The 5 s interval was the last one measured with specific pulse sequences and the first 1D deuterium spectrum under rotation with the waveform generator was taken sometime between 30 and 60 s showing this pattern as well.

The last measurements were repeated at a lower temperature (290 K, Fig. 4.9). The first five milliseconds show barely noticeable differences. After 50 milliseconds on the other hand, the second smaller quadrupolar coupling is not visible anymore, only a broader linewidth for the resulting quadrupolar coupling. Already after 100 ms, the signals are sharp and afterwards the linewidth and signal intensity increase slightly. These results support the disassembly and reassembly theory of Lepper et al.[152] and this concentration shortly underneath the transition region needs more than 30 to 60 s for a complete reassembly of the orientation angles at room temperature. As two different orientation angles probably disturb following measurements (for example as in Section 4.3), preshearing and a 1D deuterium spectrum evaluating the orientation angle are essential.

For the high and intermediate concentration, it was possible to determine the tilt angle Θ_D under rotation. Additionally, I took the tilt angle of the approximately 9.5 wt% dilution step as this one showed a tilt angle of 90°. The corresponding 1D deuterium spectra of this concentration are similar to the 15.4 wt% with barely noticeable differences and hence will not be shown here. During both type of

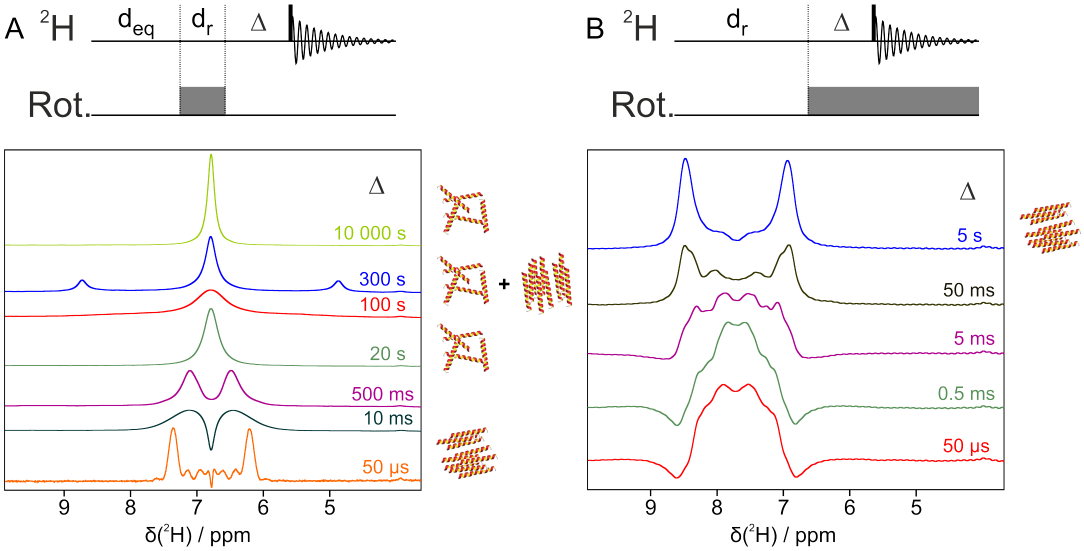

Figure 4.8: Deuterium spectra of a 6 wt% concentration PBLG/CDCl$_3$ with 20 mg Flurbiprofen showing the behavior during switching from rotation to no rotation (A) and vice versa (B). On the right side of the spectra are the values for Δ and next to it helices visualize the corresponding phases. The delays were set to d$_{eq}$ = 500 s, d$_r$ = 10 s for (A) and d$_r$ to 600 s[148].

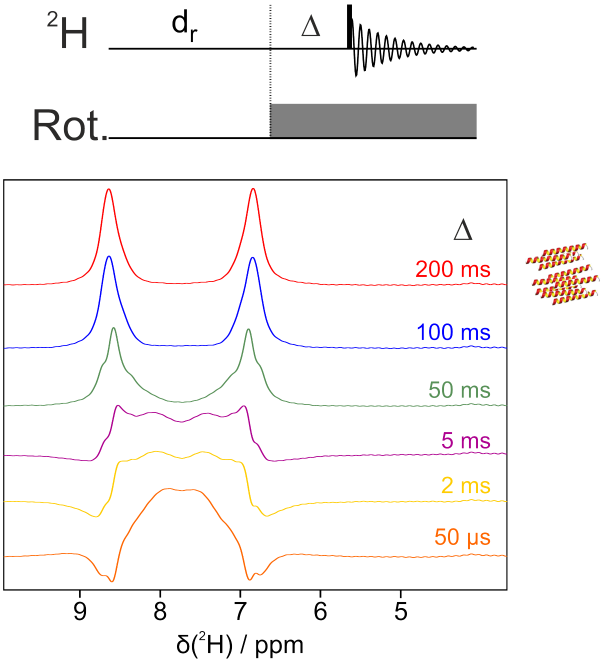

Figure 4.9: Deuterium spectra of a 6 wt% concentration PBLG/CDCl$_3$ with 20 mg Flurbiprofen at 290 K showing the behavior during switching from no rotation to rotation. On the right side of the spectra are the values for Δ and next to it oriented helices visualize the switched phase. The first delay was set to d$_r$ = 600 s[148].

experiments for the 9.5 wt% concentration, the quadrupolar splitting reaches several times values larger than 0.5 for $|\frac{Q_s}{Q_{ns}}|$. As this results in a negative value underneath the square root in Equation 4.2, they were all set to 90°. Figure 4.10 shows the three dilution steps 0, 2 and 4 from Table 4.1 with the approximate concentrations of 15.4 wt%, 9.5 wt% and 8.0 wt% and their tilt angles from the start of shearing until the shear plane is fully reached and the relaxation of the tilt angle back to 90° after cessation of shear over the time interval Δ. All three concentrations show two quadrupolar couplings at 10 ms which indicate the change of the director from parallel to perpendicular to the magnetic field.

Both concentrations above the transition region (15.4 and 9.5 wt%) show some kind of coalescence at this 10 ms where the two couplings are barely noticeable. The 8.0 wt% concentration, on the other hand, shows both quadrupolar couplings clearly. Instead, all spectra until 5 ms after the rotation starts show a coalescence without any visible peaks. After 100 ms all three concentrations are fully developed in the shear plane within their alignment tilt.
After cessation of shear, it takes approximately 1 s until a change of the tilt angle is noticeable. After this time interval, the 8.0 wt% concentration shows four peaks corresponding to two quadrupolar couplings before the magic angle with no quadrupolar coupling is reached after 20 s. There is no sign of a coalescence where two quadrupolar couplings change to another. The 9.5 and 15.4 wt% concentrations, on the other hand, never show two quadrupolar couplings, instead they show a coalescence between 2 and 5 s where any peaks are difficult to detect. After 100 - 200 s, all three concentrations are less than 10° tilted from the magnetic field and after 400 s, the director oscillates between 0° and 5° against the magnetic field which corresponds to a maximum 2 Hz difference between the measured static quadrupolar coupling before the experiments and the quadrupolar couplings after cessation of shear. With a linewidth of minimum 8 Hz for all the deuterium spectra, these 2 Hz can be seen as measurement error. Hence, the director is fully aligned with the magnetic field after 400 s.

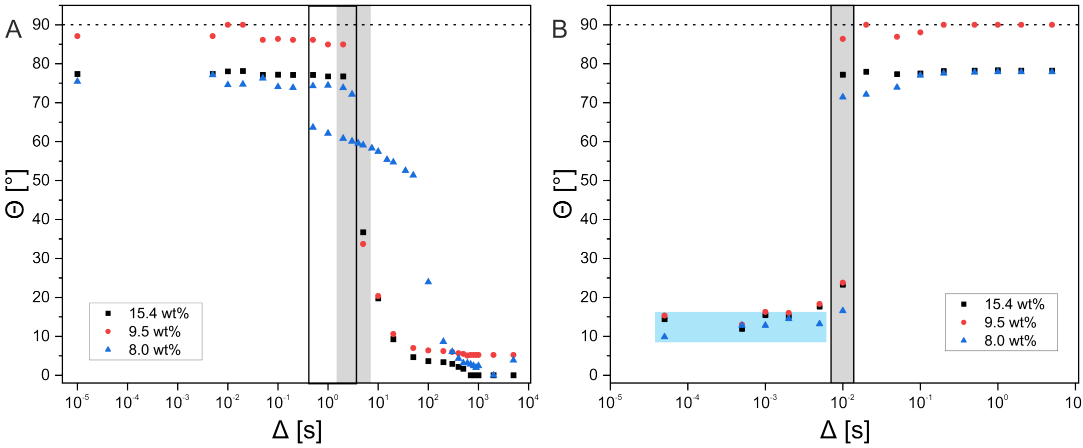

Figure 4.10: The development of the director angle of the 15.4 wt% (black squares), the 9.5 wt% (red dots) and the 8.0 wt% (blue triangles) concentration after shearing started and after cessation of shear. The light grey area indicates the coalescence region of the 15.4 and 9.5 wt% samples and the black framed box indicates a region where the deuterium signal shows two quadrupolar splittings. The full 90° are marked with a dotted line. All data points on this mark are from values where $|\frac{Q_s}{Q_{ns}}| >$ 0.5 and could therefore not calculated with Equation 4.2 due to the negative square root. A) The relaxation of the director back parallel to the magnetic field needed around 1 s until a change in the angle was visible. At this time interval the 8.0 wt% sample showed two signals. After approximately 100 - 200 s, only 10° were left for all concentrations. The 8.0 wt% sample in the biphasic area needed the longest time. B) The switching time into the shear plane was on a much faster time interval. After only 10 ms, the peaks of the shear plane appeared. The two concentrations of 9.5 and 15.4 wt% showed a coalescence around these 10 ms. The 8.0 wt% concentration on the other hand directly started with a coalescence until an interval of 5 ms. The light blue area indicates the coalescence.

It is not the first time that the relaxation behavior of the alignment director parallel to the magnetic field was investigated for PBLG as already mentioned in Section 2.4.3.1. The group of Martins measured several relaxation experiments for PBLG with m-cresol on a 300 MHz spectrometer. The first source of rotation was hereby a simple but sudden rotation of the sample tube inside the magnet by 90° with respect to the magnetic field[137,139]. Afterwards, they measured deuterium spectra of a 14 and 17 wt% PBLG sample for different time intervals until the director was fully back parallel to B^0. On top of that, this group calculated the director distributions for the 14 wt% sample and generated theoretical 1D deuterium spectra out of the calculated director distributions (see Figure 2.17)[139]. Their time intervals, after which the coalescence and the full relaxation parallel to B^0 can be seen, are similar to the ones for the high concentration shown here. Later, the same group measured a 12 and 14 wt% sample under shear with a Couette cell with shear rates from 5 to 150 s^{-1}[138,140]. Even for the relaxation measurements of these low shear rates, the spectra look very similar to the ones shown here. As they already proposed, the relaxation mechanism of the director of PBLG is independent from the shear history, shear rate, and source of rotation.

It seems that the relaxation process of the director parallel to B^0 is independent from the concentration above the transition region and the concentration is only responsible for the amount of anisotropy and the size of the quadrupolar couplings, at least up to 17 wt%. In the transition region, the time interval for the full relaxation parallel to B^0 is similar, but the director changes differently during the relaxation process, as can be seen in Figure 4.10. Below the transition region, this changes even more and when the concentration is significantly low (less than 5 wt%), the influence of the anisotropic behavior is so weak, that the sample is isotropic in less then 10 s after cessation of shear.

The switching time into the shear plane is similar for all concentrations for the high shear rates. Recovery times of 100 - 200 ms are sufficient for most concentrations. Although, as for example the 6 wt% concentration at room temperature shows, some concentrations undergo a disassembly and reassembly process of the director angle and might need a preshearing interval or a change in temperature.

4.1.4 J-resolved

After successfully programming the 1D pulse sequences, the next step was to program 2D spectra. The issue here is that most 2Ds use gradients and therefore cannot be used with TTL signals. However, one type of sequences could be found, the J-resolved experiment, which does not contain gradients and could be used with explicit pulse programming and TTL commands. First, the standard 2D $\mathcal{J}$-resolved sequence for deuterium was recorded and rotated with the waveform generator throughout the sequence. The isotropic $CDCl_3$ split in both directions, the $\mathcal{J}$-dimension and the chemical shift dimension, by 12 Hz, as was the case in the ^{2}H 1D spectrum under rotation. In the next step, the 100 ms switching time required by the rotation for complete alignment was taken and incremented as a second refocusing element. Additionally, explicit pulse programming was used to start the rotation started via the TTL signals of the spectrometer together with the second refocusing element, so that only the F2-dimension could evolve under anisotropic conditions and $\mathcal{J}$-evolution under isotropic conditions. And indeed, this time the 12 Hz splitting only appeared in the F2-dimension by correlating the isotropic coupling of zero with the anisotropic coupling of 12 Hz. Unfortunately, this has so far only worked at lower concentrations. At concentrations above the critical static alignment concentration, the signal seems to be lost during the refocusing period.

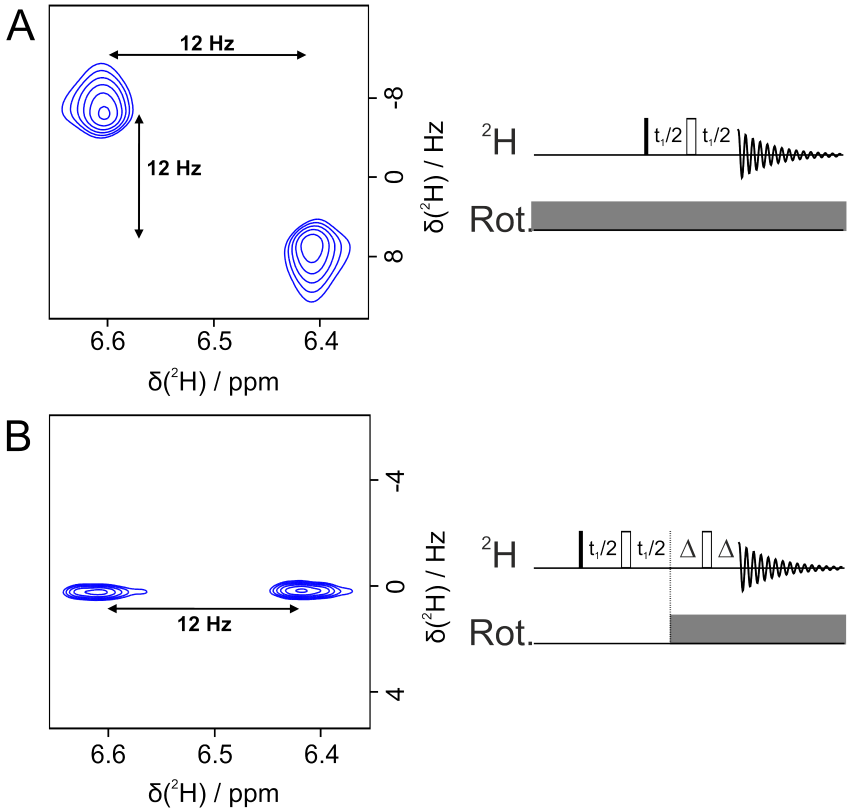

Figure 4.11: The ^{2}H 2D *J*-resolved spectra of a 4 wt% PBLG/CDCl$_3$ sample with ergosterol which is isotropic under static conditions and shows a 12 Hz quadrupolar splitting under sheared conditions together with the corresponding pulse sequences. The conventional deuterium 2D *J*-resolved spectrum under steady 48 Hz rotation from the waveform generator (A) shows the quadrupolar splitting in both dimensions. The extended *J*-resolved experiment where the first refocusing element is under static conditions and the second under shear-induced alignment as well as the acquisition shows the splitting only in one dimension[148].

4.2 Transition state

In the last Section 4.1, a special phenomenon of some liquid crystals as PBLG could be seen. The transition from isotropic to anisotropic is not like a sudden switch, which can be turned on or off, but a process over a small region of up to 0.5 or 1 wt%. During this transition, the amount of the isotropic phase slowly decreases while the amount of the anisotropic phase increases. I recognized this biphasic region in the dilution series of the PBLG/CDCl$_3$ sample with flurbiprofen but at first could not reproduce it with a PBLG sample without a solute molecule. I only saw this phenomenon in samples with guest molecules (next to flurbiprofen also with strychnine or menthol). Preparing three samples with approximately the same amount of PBLG but different concentrations of flurbiprofen (Fig. 4.12) showed again only the biphasic region with the solute molecule. As known from literature, the transition happens without a guest molecule but depends on the used solvent and the length of the liquid crystalline rods[98,99,104]. The quadrupolar splitting during the rotation of the three samples indicated that I probably missed the biphasic region by a small weight percentage without the solute molecule. The results of Sakamoto[98], who found the biphasic region of PBLG (about 12 000 wt) in CDCl$_3$ at approximately 7.5 to 8.5 wt%, supports this assumption.

Therefore, I started a dilution series under non-rheological conditions in NMR tubes carefully sealed with teflon in our 600 MHz spectrometer with three samples all from the same batch of PBLG. One

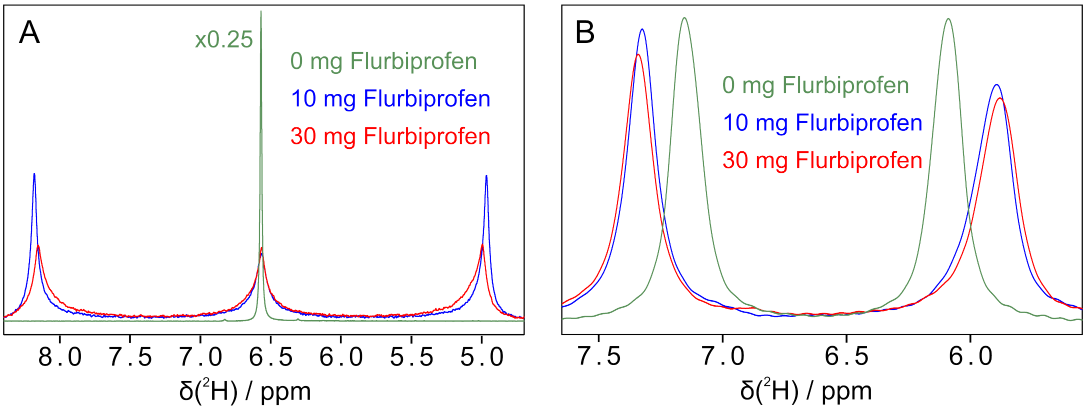

Figure 4.12: Deuterium 1D spectra of A 7.8 wt% sample of PBLG/$CDCl_3$ without a solute molecule, a 8.3 wt% sample with 10 mg flurbiprofen and a 8.5 wt% sample with 30 mg flurbiprofen at 298 K are shown under static conditions (A) and during 48 Hz rotation (B). The total mass of all three components (PBLG, flurbiprofen, chloroform) is identical in all three samples. The static spectrum without flurbiprofen was reduced by one fourth in intensity[148].

without a guest molecule, one with (+)-borneol and one with (-)-camphor as solute molecules. These molecules were chosen due to their structural similarity only differing in their ability to function as hydrogen bond donor and acceptor. Furthermore, both molecules were subject in previous studies and calculations in our group[153,154]. Most of the findings in this chapter were published in 2025 in the publication "The Transition State of PBLG Studied by Deuterium NMR"[155] or in the preprint version[156].

4.2.1 Dilution series without guest

The first sample without the solute molecule had a starting concentration of 10.26 wt% and a quadrupolar splitting of 378 Hz. It was diluted in two steps to 8.5 wt% and then in approximately 0.2 wt% steps until a concentration of 6.79 wt% and a quadrupolar coupling of 188 Hz (see Figure 4.18 in Section 4.2.3). Meanwhile, the quadrupolar coupling decreases linearly with the concentration as shown in the dilution series in Section 4.1.1. This concentration showed for the first time a small peak at the chemical shift of isotropic $CDCl_3$ as can be seen in Figure 4.13. Diluting further in 0.1 wt% steps, the isotropic peak in the middle increases very slowly and the outer anisotropic peaks decrease. The first major change in the spectra could be seen at 6.50 wt%, where the isotropic peak was still small but the anisotropic peaks decreased heavily compared to the previous dilution step. At the next dilution step with 6.41 wt%, all three visible peaks in the 1D spectrum were at approximately the same height. This concentration is the turnover point at which the ratio of isotropic and anisotropic phases changes in favor of the isotropic phase. Afterwards, the middle peak is always higher, indicating a more dominant isotropic phase inside the sample. Until a concentration of 5.89 wt%, the outer peaks decreased further and at 5.79 wt% no anisotropic peaks could be seen anymore. As already mentioned in Section 4.1.1, the quadrupolar splitting stays constant over the biphasic region, here with a value of 186 ± 2 Hz.

This agrees very well with the earlier findings of the dilution study with flurbiprofen where the quadrupolar coupling did not change in the biphasic region as well and only the ratio of the isotropic and anisotropic peak intensities changed. Additionally, it agrees with Robinson who showed in polarized images that in the biphasic region the characteristics of the isotropic and the anisotropic phase do not change, only their proportion to one another. During the whole biphasic region, the isotropic phase is always equal to the pure isotropic phase at the lower concentration limit and the anisotropic phase is always the same as the anisotropic phase at the higher concentration limit[102,105].

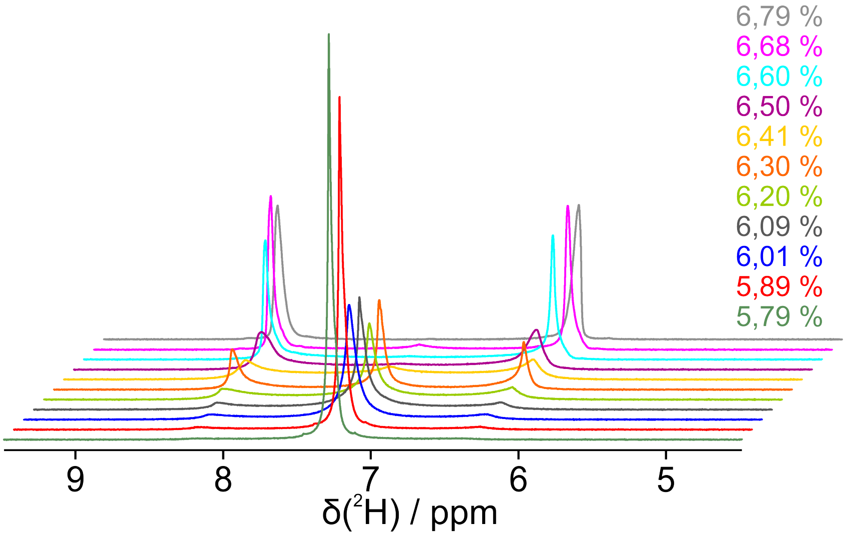

Figure 4.13: The ^{2}H 1D spectra of the biphasic region of PBLG/$CDCl_3$ during step-by-step dilution from the pure anisotropic to the pure isotropic phase. Spectra were acquired approximately 5-10 minutes after the sample was inserted into the magnet[155,156].

4.2.2 Kinetic studies of the biphasic region

The deuterium spectra in Figure 4.13 at concentrations where the isotropic and anisotropic phases are of similar concentrations show very broad lines and the peaks are not always well separated. As known from the kinetic studies in Section 4.1.3, the build up of the alignment parallel to the magnetic field especially at intermediate concentrations takes several minutes. Although, the spectra were recorded 5-10 minutes after insertion into the magnet, the signal of the deuterium spectra could take even longer to build up. Therefore, I prepared a second PBLG/$CDCl_3$ sample without a guest molecule starting at 8 wt%. This time from a different batch of PBLG.

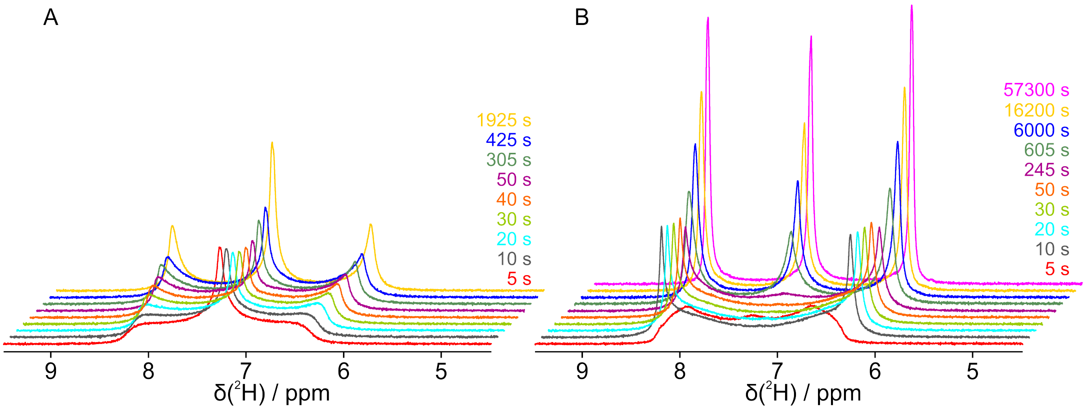

Figure 4.14: The deuterium spectra of PBLG/$CDCl_3$ at 6.03 wt% (A) and 6.19 wt% (B) were measured over a long time period and different time points are shown for the specific concentrations[155,156].

I remeasured the whole series now as a kinetic study on the 600 MHz spectrometer acquiring deuterium spectra at different time points for the same concentration. As the alignment directly builds up after insertion into the magnet, the shim file from the first sample was taken without changing it between the dilution steps. Several deuterium 1D spectra were acquired immediately after insertion into the magnet in a time interval of at least one hour. Contrary to the at least 400 s the alignment needs in the

400 MHz magnet for all concentrations, the pure anisotropic phase needs less than a minute for the full alignment at 600 MHz. Afterwards only an increase in sharpness and intensity can be seen. The same observations could be made for the pure isotropic phase. Also, up to a 5 % ratio isotropic/anisotropic and above a 95 % ratio, the full build up of the two phases does not take longer than a minute with only increasing sharpness and intensity afterwards. Between these ratios, the build up time for the alignment with both phases takes much longer. It takes 10 to 20 minutes for the phase ratios isotropic/anisotropic of 5-20 % and 80-95 % reaching fully separated and sharp signals. A change in intensity and sharpness could still be seen but none in the values for integrals and quadrupolar splitting. Between a 20-40 % and 60-80 % ratio isotropic/anisotropic, the fully separated and sharp signals were reached after 30-40 minutes. Again, integrals and quadrupolar splittings do not change anymore but intensity and sharpness increase further (Fig. 4.14). At equal amounts of both phases - 40-60 % ratio - the alignment needs around 100 minutes until the changes for the integrals and quadrupolar splittings are negligible small. Nevertheless, the major changes are over after 30 minutes but sharpness and intensity are changing heavily for 4 hours and even after half a day a change in sharpness and intensity could be seen.

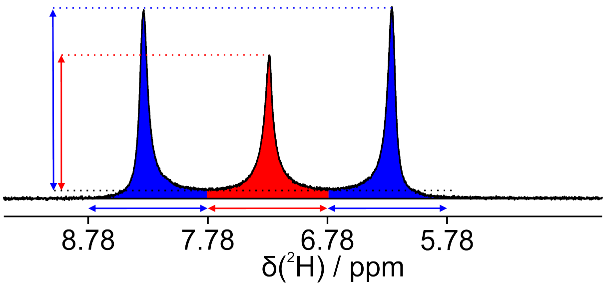

Figure 4.15: The scheme shows how signal heights and integrals of isotropic (red) and anisotropic (blue) peaks were measured as indicator for the amount of both present phases. For comparability reasons, the integral regions were always exactly 92.13 Hz (≙ 1 ppm) starting at 5.78 ppm[155,156].

In the scheme in Figure 4.15 is explained how the absolute signal heights and integrals for the isotropic and anisotropic peaks were measured. The height, which is plotted in Figure 4.16 against the time, was measured as the distance between the top of the peak and the lowest point between an anisotropic signal and the isotropic signal. The sample at 6.19 wt% with all three peaks ending in equal heights needed around 10 seconds before the more dominant anisotropic phase showed their peaks. The isotropic peak in the middle could shortly be seen in the first five seconds and vanished then for over 200 seconds. During this time, the signal height of the outer anisotropic peaks decreased and they decreased even further until the first 500 seconds. However, after 245 seconds the isotropic peak showed up again and increased slightly until the first 500 seconds are over. From this point on, all three signals increased and the longer the time is the faster they increase. After 6000 seconds they reached the final height ratio between isotropic and anisotropic phase proportions where longer waiting times still increase the intensity and signal sharpness but not the relative height to another.

The second concentration at 6.03 wt% behaved similar if compared to the more dominant phases. At this concentration, the isotropic phase was dominant and therefore the middle peak can be seen right from the beginning, decreasing in the first 50 seconds. The outer peaks could not be seen at the beginning, only after 10-20 seconds. For the first 50 seconds they increased slowly and then from this turnover point all three signals increased again faster the longer they are in the magnet until they reach the final height ratio after 2000 seconds.

These measurements showed that in the first few seconds none of the microheterogeneous phases are isotropic or anisotropic. Then, the more dominant phase is built up first until the second phase is built up, delayed by up to 30 s. Only around a height ratio of 50:50 for the two phases, the slightly

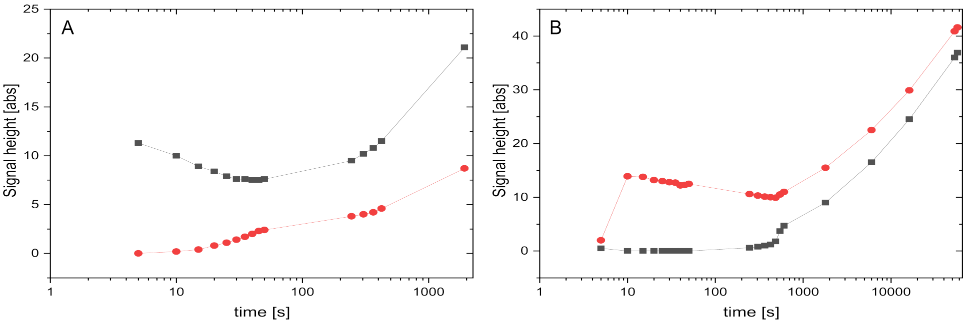

Figure 4.16: The absolute values for the heights of the inner isotropic (black) and outer anisotropic (red) peaks measured from the deuterium spectra in Figure 4.14 are plotted against the time in seconds. (A) is the sample at 6.03 wt& and (B) at 6.19 wt% respectively[155,156].

less dominant phase needed up to 200 s until a peak could be seen. It first started as something which looks similar to a coalescence where all three peaks could be seen with a closer look. This changed then to two broad and overlapping peaks where the center between both peaks showed quite some distance to the actual baseline until after these 200 s the isotropic peak was visible in the center. These 200 s would be nearly enough for all pure anisotropic or pure isotropic phases to fully develop in the 1D deuterium spectra. On top of that, the anisotropic phase at the 50:50 height ratio needed 600 s developing the full distance of the quadrupolar splitting which is ten times slower than for the pure anisotropic phase directly above the biphasic region. The full equilibrium of the 50:50 height ratio takes even on the 600 MHz spectrometer several hours. As the equilibration for pure anisotropic phases takes approximately twice as long on our 400 MHz spectrometer compared to the 600 MHz, it would probably need half a day to a whole day fully equilibrating at 400 MHz.
For all tested concentrations the anisotropic peaks seem to have a faster kinetic as subordinate peaks than the isotropic peaks in a dominant anisotropic phase. Probably, this can be explained with the linewidth. The center between two broad peaks suffers from two overlapping linewidths and hence can be seen later as a peak which is only influenced by one broad linewidth. Additionally, the quadrupolar coupling increases with time until it reaches the final value decreasing the overlapping of both peaks simply by the higher distance between the peaks. In a more dominant anisotropic phase, the isotropic peak can latest be seen when the quadrupolar splitting is fully developed.

Another interesting effect could be seen in this second PBLG/$CDCl_3$ sample without a solute molecule. The concentration range of the biphasic region was shifted by nearly 0.5 wt% compared to the sample from Section 4.2.1 but the quadrupolar coupling inside this region was approximately equal for both samples. As literature tells, the 150k-350k wt PBLG always behaves the same in its physical characteristics[5], which is mostly true as can be seen by comparing the samples.

4.2.3 Dilution series with guests

As mentioned in the beginning of this chapter, I did not only dilute PBLG/$CDCl_3$ samples without a solute molecule but also with the guest molecules borneol and camphor. The naturally occurring bicyclic ketone camphor acts as a hydrogen acceptor with its C=O group. Is this functional group reduced to an alcohol group, the second naturally occurring molecule borneol acting as hydrogen donor is received. Figure 4.17 shows their influence on the concentration especially around the transition from anisotropic to isotropic. The hydrogen donor borneol had the first appearance of the isotropic peak at a concentration of 6.79 wt% similar to the sample without a guest molecule but the isotropic peak in the sample with borneol started already a much higher intensity. Additionally, the outer anisotropic peaks decreased faster and the concentration, where all three signals are equally high, was at 6.47 wt% instead of 6.41 wt% as it was for the sample without a solute. On top of that, the anisotropic peaks vanished at 5.89 wt% and therefore 0.1 wt% earlier than without a guest. With camphor as guest molecule, the story is different. The first sign of the isotropic peak in the middle could be seen at 6.59 wt% which was 0.2 wt% less than for the other two samples. The same 0.2 wt% difference to borneol and 0.14 wt% difference to the sample without a guest for the concentration was where all three signals have the same height, which was at 6.27 wt% for camphor. Unfortunately, the concentration point, where the anisotropic peaks vanish, could not be acquired for camphor, because the sample was destroyed during preparation of the dilution step for 5.89 wt%.

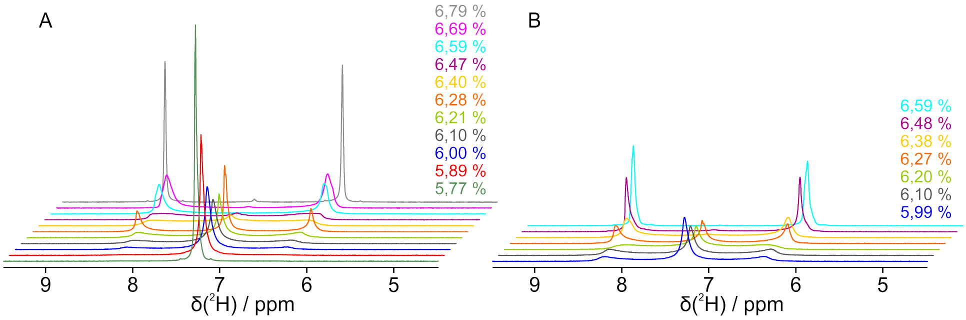

Figure 4.17: The ^{2}H 1D spectra of the biphasic region of PBLG/CDCl$_3$ with either (+)-borneol (A) or (-)-camphor (B) during step-by-step dilution from the pure anisotropic to the pure isotropic phase. Spectra were acquired approximately 5-10 minutes after the sample was inserted into the magnet[155,156].

For better comparison of all three samples, the quadrupolar splittings and the relative signal height of the anisotropic and the isotropic phase proportions are plotted against the concentration in two separate diagrams in Figure 4.18. Looking at the quadrupolar splitting in the pure anisotropic phase, all three samples have a linear decrease with the concentration until they reach the biphasic region as I could see for the dilution series in Section 4.1.1. During this decrease, the camphor sample always had the highest splitting at the same concentration and the other two samples were similar with borneol being slightly underneath the one without the solute molecule. In the biphasic concentration region, I calculated theoretical quadrupolar splittings by using the relative integrals of the signals with Equation 4.3. These theoretical values are equal to the amount of anisotropy left inside the three samples and show an approximately linear decrease of the anisotropy with decreasing concentration. At the same concentration as the other samples, the camphor sample always has a higher theoretical quadrupolar splitting during the biphasic region and borneol has the lowest theoretical quadrupolar splitting. As this theoretical splitting represents the amount of anisotropy, the sample with camphor has more anisotropy left at the same concentration as the other two samples and borneol has the least anisotropy. Similar results showed the relative signal heights of the anisotropic outer peaks compared to the inner isotropic peak where the blue line of camphor is always on top reaching the same relative signal heights at lower concentrations and the red line of borneol is always underneath the sample without a guest molecule.

$$Q_{calc.} = \frac{I_A}{(I_A + I_I)} Q \tag{4.3}$$

One important note should be made here. As shown in Section 4.1, anisotropy can also be induced at pure isotropic concentrations where the quadrupolar splittings decrease exponentially after the biphasic plateau is over. Therefore, the calculated splittings, which reach zero at the concentration of pure isotropy, can only be taken as amount of static anisotropy and not the real possible quadrupolar splittings. Additionally, as already discussed in Section 4.2.1, during the biphasic region, the isotropic and anisotropic phases show exactly the same characteristics as the pure phases which explains the constant quadrupolar splitting of the anisotropic peaks during this region.

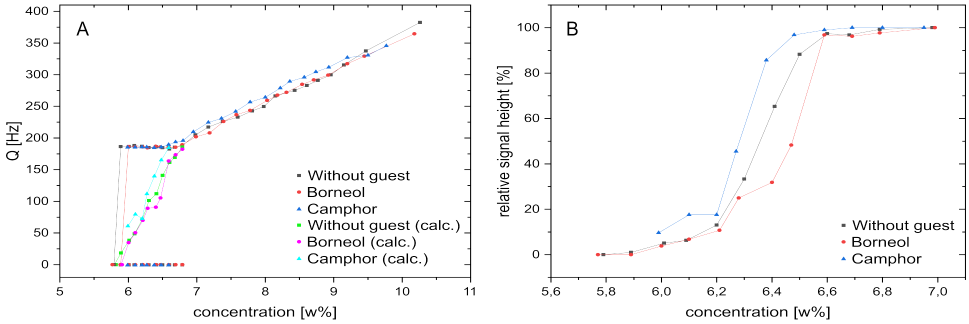

Figure 4.18: The three PBLG/$CDCl_3$ samples with borneol, camphor and without a solute molecule from the same batch are compared in their amount of quadrupolar splitting (A) and relative signal height anisotropic/isotropic(B) over the concentration range. Additionally, in (A) is the 0 Hz coupling of the isotropic peak included after the biphasic region is reached (Q ~185 Hz) and the calculated couplings via the amount of the integrals (see Eq. 4.3)[155,156].

As already mentioned in the kinetic study of the alignment director in Section 4.1.3 where the tilt angle Θ_D of the alignment director to the magnetic field is smaller for samples with strychnine, the solute molecules in this study influence the alignment and the biphasic region as well. A hydrogen donor like Borneol at the same concentration compared to solute free PBLG decreases the quadrupolar splitting and shifts the biphasic region to a slightly higher concentration. A hydrogen acceptor like camphor, on the other hand, shows exactly the opposite results, increasing the quadrupolar splittings at the same concentration and shifting the biphasic region to a slightly lower concentration. The ester carbonyls of the cholesteric PBLG sidechains can form hydrogen bonds with donor molecules, resulting in tight interactions which plays an important role in partial alignment[153]. Borneol is such a donor molecule, which reduces interhelical interaction strengths of PBLG, and therefore the anisotropic character, through its tight bonding with the helix which probably causes this higher transition concentration and the lower quadrupolar splittings. Contrary, a hydrogen bond acceptor like camphor cannot interact this strongly with PBLG as PBLG has no hydrogen donors in the accessible sidechain. However, it could interact with the solvent molecules reducing the amount of available solvent molecules for PBLG which would increase the anisotropic character of PBLG. Hence, quadrupolar splittings increase and the concentration of the phase transition decrease. Another important observation of this dilution study is that the general use of solute molecules does not decrease the PBLG concentration just by their additional weight as borneol and camphor were both added by the same amount and both show opposite effects. The quadrupolar splittings as well as the concentration range of the phase transition are in the middle for the solute free PBLG sample. The samples were prepared with approximately 400 µl $CDCl_3$ ($\approx$ 620 mg) and diluted to nearly 800 µl ($\approx$ 1240 mg) with 70 mg PBLG and 14 mg of the solute molecule which corresponds to 0.2 wt% solute molecule at the beginning and 0.1 wt% at the end. This was exactly the change in weight percentage during each dilution step (at the beginning 0.2 wt% and in the biphasic region 0.1 wt% dilution). Nevertheless, the chosen solute molecule has an influence on the anisotropic character of PBLG, which should be considered before performin experiments. Still, Sarfati et al.[9] were correct that a solute molecule can always be used in a certain concentration range. Some liquids, which do not interact as solvent, on the other hand, have a bigger impact on the anisotropic character of PBLG as mentioned in Section 2.4.3 and extensively discussed by Marx et al.[129].

4.2.4 X-y plane

The 2D ^{2}H imaging experiment with gradients along the z-axis[157] show very nicely, if a sample is homogeneous in the z-direction. However, it cannot tell anything about the homogeneity or general behavior in the x,y-plane. Luckily, a cooperation with Prof. Dr. Gisela Guthausen from the MVM institute at the KIT, gave the opportunity to measure magnetic resonance images. Prof. Guthausen measured deuterium CSI experiments and proton FLASH experiments of three samples. First, a biphasic sample with strychnine and afterwards a fully anisotropic and a fully isotropic sample as comparison. The ^{1}H images are shown in Figure 4.19.

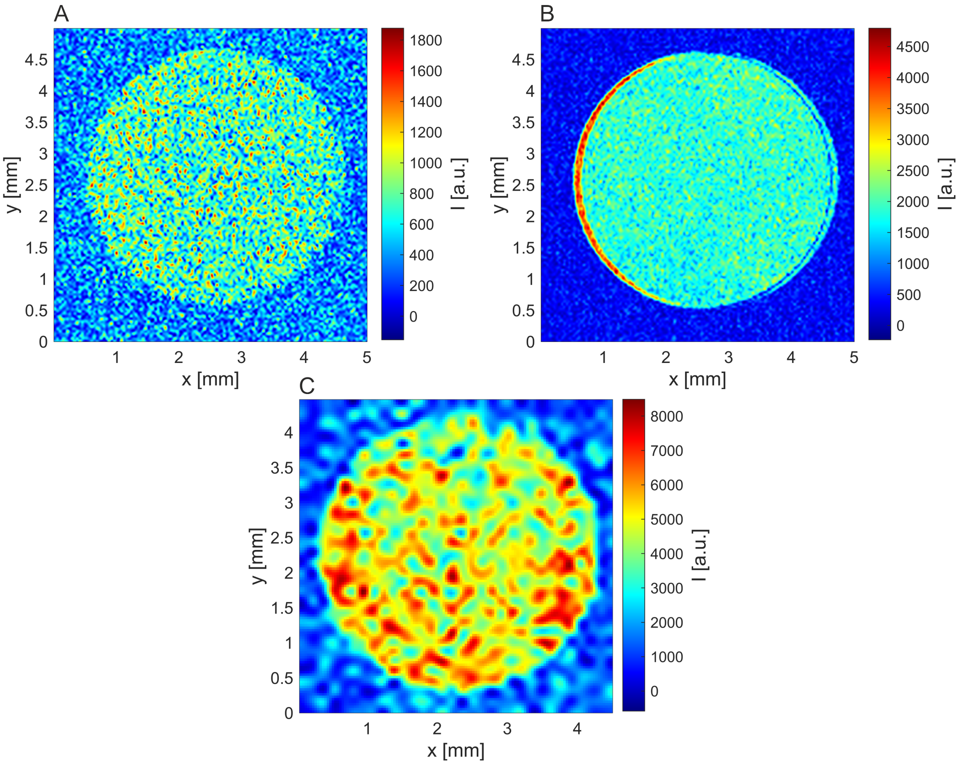

Figure 4.19: ^{1}H FLASH experiments for an isotropic (A), an anisotropic (B) and a biphasic (C) sample are shown. The isotropic and anisotropic samples are both entirely homogeneous. The intense edge in B for the anisotropic sample comes from the susceptibility difference with the NMR tube. The biphasic sample is not homogeneous with "islands" of extremely higher intensity. The typical diameter of the islands is 100-300 µm in the measured sample.

Both ^{1}H images of the anisotropic and the isotropic sample were entirely homogeneous. In both samples a few more intense dots were randomly distributed over the whole sample, indicating noise or minor local fluctuations. No signs of any patterns or other conspicuous characteristics could be seen. The only difference between the anisotropic and isotropic image was the susceptibility difference to the NMR tube at the edge of the anisotropic image. A phenomenon that sometimes can happen in the x-direction during imaging experiments. The image of the biphasic sample looked different. The areas with higher intensity were not dots anymore, they looked more like "islands". Also, they were bigger at the left and right edges and at the bottom edge. These "islands" are probably the spherulites described by Conmar Robinson[103,104]. He observed that spherulites of the anisotropic phase are either dispersed in the continuous isotropic phase or that the anisotropic phase is bound to the walls of the vessel containing the biphasic solution, resulting in a continuous anisotropic phase at the walls and a continuous isotropic phase in the center with dispersed spherulites. As the anisotropic phase had a higher amount of PBLG than the isotropic phase and PBLG provided the most proton signals, the more intense areas should reflect the anisotropic phase and these results agree with the results of Robinson.

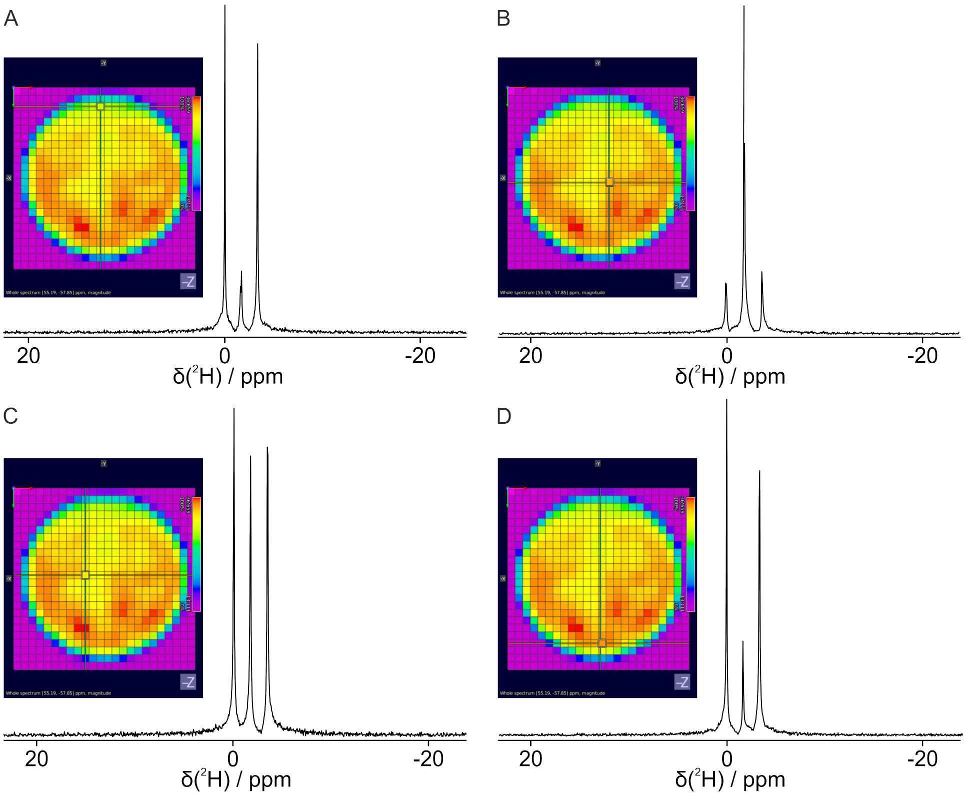

Figure 4.20: The figure shows the ^{2}H CSI experiment of a biphasic PBLG sample as a colored 2D plot. The four 2D plots are all the same in A-D, the cross line simply shows which 250 µm x 250 µm square of the NMR tube is looked at. A) and D) show two squares near the walls of the NMR tube showing mainly an anisotropic phase, B) shows a square directly in the center with mainly an isotropic phase and C) shows a square slightly off the center where all three peaks are equally intense.

The ^{2}H image of the biphasic sample in Figure 4.20 further supports this assumption. The CSI experiment was taken as many individual 1D deuterium spectra within a range of 250 µm in x and y-direction resulting in 20 points in every direction. The 1D deuterium spectra next to the walls of the NMR tube (blue squares in two-dimensional plots) all showed two large anisotropic peaks and only a small isotropic peak in between. Following the squares more to the center, the isotropic peak gained intensity compared to the anisotropic peaks with equal intensity near the center. Directly in the center and one square next to it in every direction, the isotropic peaks had a higher intensity than the anisotropic peaks. The ^{2}H image of the biphasic sample showed that the anisotropic phase was mainly present at the walls of the NMR tube with only small isotropic parts and that the isotropic phase was more strongly represented in the center. Exactly as Robinson found and as assumed after the ^{1}H image. On the other hand, a fully anisotropic phase at the walls as Robinson found, could not be seen. Even the 250 µm x 250 µm squares directly next to the blue squares of the NMR tube always showed a small isotropic peak. Interestingly, the colors in the 2D plot seem to show the total deuterium signal of the solvent and do not reflect the intensity difference of the isotropic and anisotropic phase. This would mean, the whole sample was not perfectly homogeneous in the distribution of the deuterated solvent.

For comparison, Figure 4.21 shows the ^{2}H acCSI experiments of the isotropic and the anisotropic sample. The 1D deuterium spectra in all squares of the 2D plot differed only slightly in intensity, as also shown by the small difference in the 2D color plot.

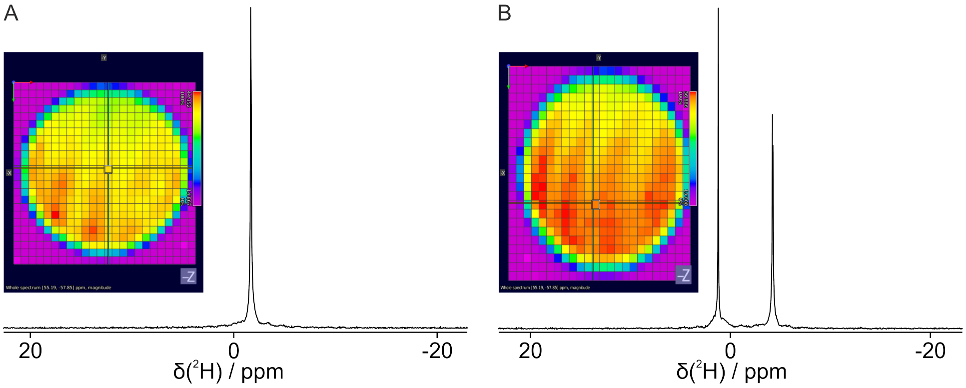

Figure 4.21: The figure shows the ^{2}H CSI experiment of an isotropic (A) and anisotropic (B) PBLG sample as a colored 2D plot. The cross line simply shows which 250 µm x 250 µm square of the NMR tube is looked at.

4.2.5 Phase separation

Anisotropic liquid crystalline solutions are birefringent, whereas isotropic liquid crystalline solutions are not. Two groups took advantage of this difference in birefringence and showed that the two phases have different densities and can separate over time due to their density[90,106]. Both groups used benzyl alcohol as solvent where the isotropic phase could be found at the top due to a lower density. The biphasic sample with strychnine from the previous section was first used for dipolar coupling measurements (see Section 4.3.3) and was left outside the magnet afterwards. After five weeks, a 2D deuterium image of the sample showed this phase separation as well (Fig. 4.22). Outside the magnet, the sample showed a very faint line visible with the eye, which probably showed the phase boundary. Only between two polarizers rotated by 90° relative to each other, filtering out the incident light, this faint line could unambiguously determined as the phase boundary between an isotropic phase and an anisotropic phase. Contrary to Horton et al.[90] and Sasaki et al.[106], the isotropic PBLG phase was the phase with a higher density in this work. Probably due to the high density of the solvent chloroform.

Regarding the simple experimental setup, the first polarization filter produces linearly polarized light, while the second polarization filter analyzes the direction of polarized light. When both polarization filters are in the same direction, the intensity of the linear polarized light is unchanged. Every other combination of directions reduces the intensity after the second polarization filter, leading to zero intensity if both polarization filters are perpendicular to each other. If now a third polarization filter is put between both perpendicular polarization filters with a direction which is not perpendicular to the first one, polarized light will be rotated or projected along the direction of the third filter. Instead of a third polarization filter, any substance which can rotate light (for example birefringent substances) can be used for the same effect[158].

Therefore, the birefringent anisotropic phase rotates the polarized light after the first polarization filter and outcoming light is seen after the second filter. Contrary, the non-birefringent phase does not rotate the polarized light and no outcoming light is seen, just a black background. The biphasic sample shows a transparent phase on the top and a black phase at the bottom, which means the birefringent anisotropic phase is at the top and the isotropic phase at the bottom. Contrary, the polarizing image of the biphasic sample directly after centrifugation showed only one phase with a very light blue color. Showing colors in a polarizer is a common property of LCs. The polarizing image of an anisotropic PBLG sample showed this blue color even stronger. Interestingly, the blue color could faintly be seen in an polarizing image of an isotropic sample with PBLG. It was expected that this sample would show no colors similar to the isotropic sample without PBLG (Fig. 4.22). As the isotropic sample with PBLG was shortly underneath the biphasic region, there might already be some small amounts of anisotropy in this sample. But not enough to show any signs in a deuterium spectrum.

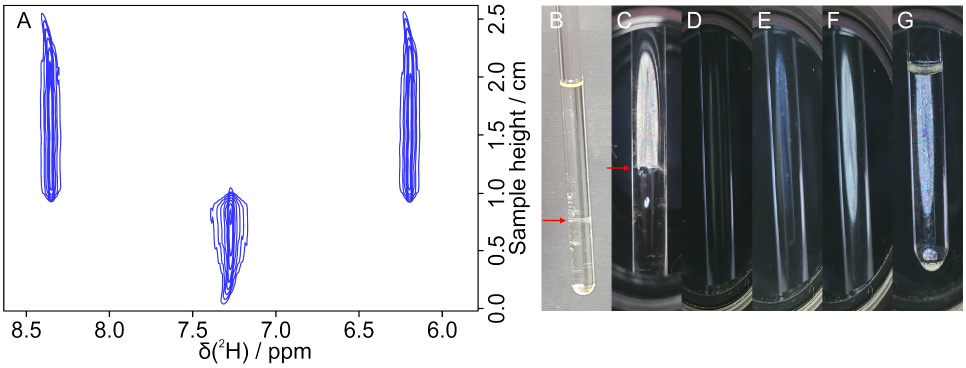

Figure 4.22: Five weeks after the last centrifugation, the biphasic sample showed a phase separation as proven by the 2D deuterium image (A) and an optical polarization filtered image (C). Both show that the non-birefringent isotropic phase is at the bottom. B) A picture under normal light shows that a phase separation can be seen without any additional preparation, just with the eye. The red arrow points to the boundary of both phases. C-G) The polarization filters before and after the sample were rotated 90° relative to each other, filtering out the incident light. C) The birefringent anisotropic phase at the top also rotated the incoming light, resulting in a transparent phase at the top and a black isotropic phase at the bottom. The red arrow points to the boundary of both phases. The polarizing images of an isotropic sample without PBLG (D), of an isotropic sample with PBLG (E) of the biphasic sample directly after centrifugation (E) and of an anisotropic PBLG sample (G) are shown[155,156].

With thorough forth-and-back centrifugation, I was able to recombine the isotropic and anisotropic phases completely homogeneous in z-direction and as the imaging experiments in Section 4.2.4 show, also in the x,y-plane. After successfully recombining the phases, the phase separation was monitored in a 400 MHz spectrometer over 543 hours (approximately three weeks) with 1D and 2D deuterium spectra. The 1D spectra are shown in Figure 4.23 and the 2D spectra in Figure 4.24.

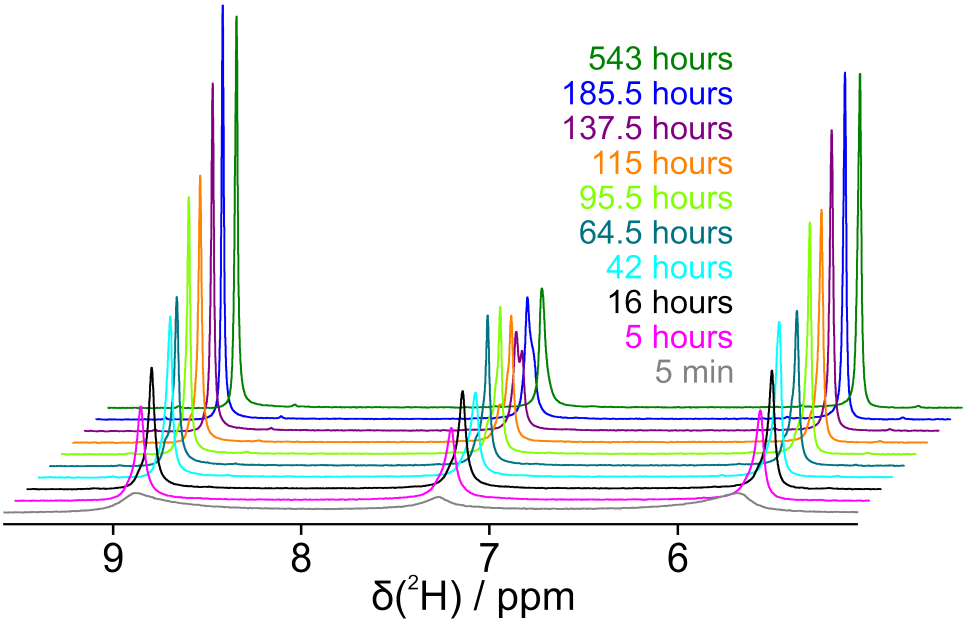

Figure 4.23: The biphasic sample was put into the magnet directly after thoroughly centrifugation recombining the isotropic and anisotropic phase homogeneously along the z-direction. The separation was monitored by 1D and 2D (Fig 4.24) deuterium spectra. The time intervals after which the 1D spectra were acquired can be seen in the figure.

The 2D spectrum shows after 5 minutes that the sample is fully homogeneous. The 1D after 5 minutes showed three nearly equally high peaks with very broad linewidths as expected from the kinetic experiments in previous Section 4.2.2. Five hours after the sample was transferred into the magnet, the peaks were still around the same height, more intense and less broad. Another eleven hours later, only the intensity and the linewidth changed as expected to more narrow peaks. After 42 hours, the signal height of the isotropic peak was reduced, while the signal height of the anisotropic peaks were increased. The linewidth was approximately the same as after 16 hours. Another day later (64.5 hours), the anisotropic peaks were unchanged but the isotropic peak increased again to approximately the same height as the anisotropic peaks. This changed again after 95.5 hours where the isotropic signal approximately stayed at the same intensity as before but the anisotropic peaks increased again heavily to nearly double the height of the isotropic peak. For all other spectra later, the isotropic peak only changed in its appearance due to a change in the shim. The anisotropic peaks, on the other hand, increased in their intensity until 185.5 hours (approximately 8 days) and this intensity does not change for the rest of the three weeks.

Comparing with the 2D spectra, the change of the signal height in the 1Ds after 42 h could be seen in the 2Ds as well, but only very weak. The first real visible change in the 2D spectra could be seen after 95.5 hours where the isotropic signal in the middle did not look completely homogeneous any more and the 1D spectrum had a large intensity increase of the anisotropic peaks. Another two days later (137.5 h), the isotropic signal had a bulk at the bottom and a narrow line at the rest of the spectrum and the anisotropic peaks were considerably narrower at the bottom. Again two days later (185.5 hours $\approx$ 8 days), the phase separation was almost over with only a small overlap of both phases and a few residues of the isotropic phase in the anisotropic phase. This explains why the 1Ds did not change after these 8 days. The 2Ds, on the other hand, still changed slightly showing that the phase separation was not complete yet. After 353 hours ($\approx$ 15 days), there were some minor residues of the isotropic phase in the anisotropic phase and both phases were still overlapping. After approximately 18 days (429 hours), the isotropic phase had completely vanished from the anisotropic phase but a small overlapping of both phases could be seen. After 23 days (543 hours), there was still a minor overlapping between both phases but negligibly small. Surprisingly, the isotropic phase after seven weeks (1200 hours) was much smaller than after three weeks, although the isotropic and anisotropic phase still overlapped in a small area. With the increasing anisotropic phase, it seemed that near the phase boundary some phases changed from isotropic to anisotropic. As there was no sign of evaporation, it could not be an effect of a higher concentration after solvent evaporation. This was the last point taken for this work, but it would be interesting to see how long a change can be observed. However, for the sample studied, the major separation took place between six and eight days after centrifugation.

4.3 Structure determination

NMR is a common tool for structure determination. The two-dimensional structure of small molecules can be easily verified with standard isotropic NMR, and even three-dimensional structures can be determined with NOE measurements under isotropic conditions. However, the quality of such structures strongly depends on the availability of few constraints that are typically limited to ^{1}H, ^{1}H-correlations. Some of these limitations can be overcome by additional constraints measured by anisotropic parameters such as RDCs, RQCs and RCSA[38,40].

The required anisotropy can be induced by stretched polymer gels[12] or by LCs like PBLG[9]. Both methods induce a low degree of molecular order, resulting in spectra in which the anisotropic couplings can be measured similarly to the isotropic couplings. The main advantage of the anisotropic couplings is their dependence on the local angle Θ with respect to the static magnetic field B^0, which leads to structural

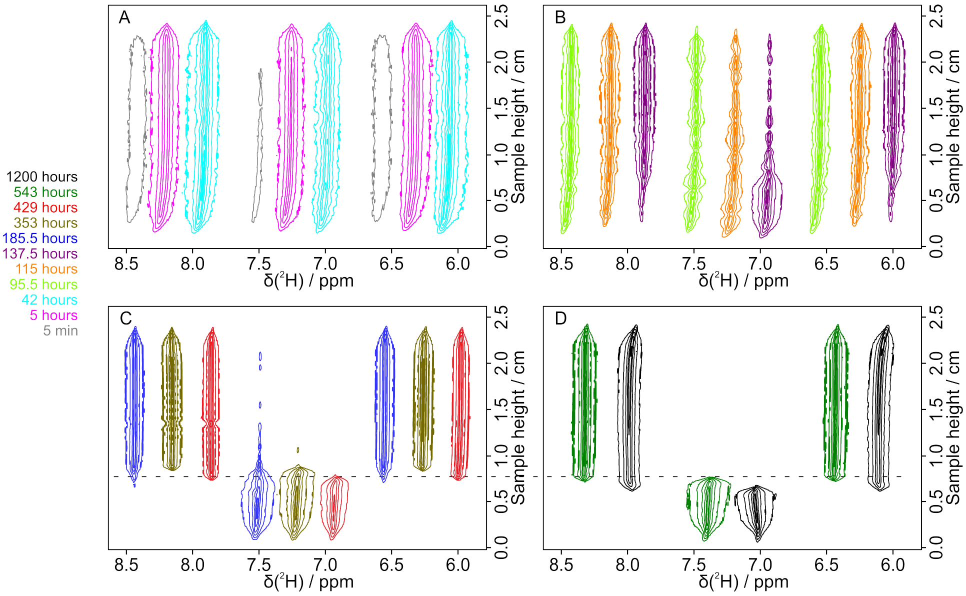

Figure 4.24: The corresponding 2D deuterium imaging spectra of the biphasic sample in Figure 4.23. The time intervals of 16 and 64.5 hours are not shown as the changes were only small. Instead, 2D spectra with time intervals of 353 hours, 429 hours and 1200 hours (7 weeks) were added. The dotted line in C) and D) is directly above the isotropic phase of the green spectrum after 543 hours.

constraints on the relative orientation of the molecule[38]. Furthermore, the angular dependence with respect to Θ_D can be used to create different sets of anisotropic couplings that are scalable in a similar way to stretched polymer gels[14,50]. Chapter 4.1 showed that the shear-force introduced by the rheo-NMR device is able to change the angle of the alignment vector determined by the quadrupolar coupling of the solvent $CDCl_3$. The influence of shear-force on the anisotropic parameters of small molecules in PBLG will be shown in the following chapter, most of which was already published in 2023[148].

4.3.1 Residual dipolar couplings

Courtieu et al.[9] introduced for the first time PBLG in chloroform as a very weak aligning medium for dipolar couplings of water insoluble molecules. Three years later, Thiele and Berger[159] published the stereochemical assignment of geminal protons using RDCs in strychnine obtained from ^{13}C 1D spectra. Independently at the same time, Verdier et al.[160] measured homo- and heteronuclear RDCs in menthol obtained by ^{13}C, ^{13}C- INADEQUATE and $^{1}H,^{13}C$-HSQC spectra. Both works were at the beginning for practically relevant structure determination via RDCs of small molecules in PBLG. Nowadays, the $^{1}H,^{13}C$-CLIP-HSQC is one of the standard experiments for $^{1}D_{CH}$ coupling extractions. Especially in PBLG, one major issue arises. Second-order artifacts caused by large dipolar couplings create significant distortions in corresponding spectra. One possible solution reducing these distortions is using shear-force, as this section will show.

4.3.1.1 Strychnine

The alkaloid strychnine (Fig. 4.25) was often used as a model system for RDCs[14,159]. It has 21 carbon and 22 hydrogen atoms and therefore 22 possible RDCs to measure. Hereby, the geminal protons of a CH_2 group are especially hard to assign without the extra information of the dipolar couplings. Therefore, strychnine is the perfect test molecule for the rheo-device.

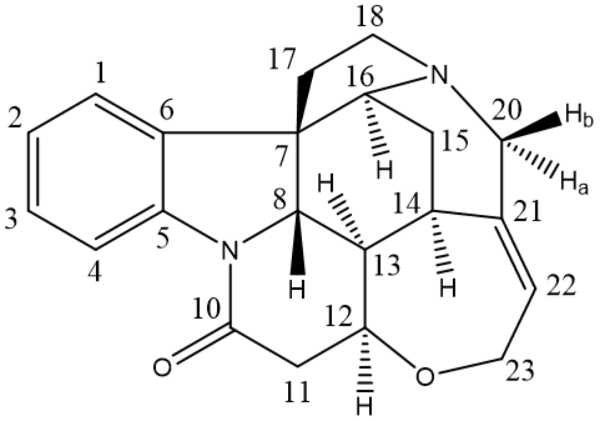

Figure 4.25: Strychnine and its assignment

First, an isotropic CLIP-HSQC determining the $^1J_{CH}$ coupling (Fig. 4.26A) was acquired where all 22 couplings were measured. Then, a 11.3 wt% sample was prepared which showed a quadrupolar coupling of 372 Hz for $CDCl_3$ in the static case. This sample was already attached to the rheo-device with the inner 3 mm tube filled with DMSO-d_6. As can be seen in Figure 4.26B, most signal intensities were below the detection limit due to heavily broadened proton multiplet widths and the reduced active volume because of the inner tube despite increased measurement times. Instead, the T_1-noise from water of the DMSO-d_6 and residual signals of DMSO-d_5 were present. Nevertheless, spinning the same sample at a rotation speed of 48 Hz improved the quality of the spectrum tremendously (Fig. 4.26C). The quadrupolar coupling of $CDCl_3$ was reduced to $\Delta\nu_Q$ = 180 Hz and all other anisotropic parameters were scaled by the factor − 0.48 under these shear-induced alignment conditions. I could now measure 19 out of the 22 possible couplings instead of only 4 in the static case, simply by shearing the sample. Still, the multiplet widths were broad and contained second-order artifacts as indicated by different multiplet lineshapes which resulted in relatively large errors for the couplings. One deterioration of this spectrum was the T_1-noise from water which broadened heavily due to the rotational noise.
The static and the sheared spectra were shimmed on the inner DMSO-d_6 signal, where both deuterium spectra showed a linewidth of 1.1-1.2 Hz of DMSO-d_6. The linewidth of the $CDCl_3$ signal increased from 5 Hz for the static deuterium spectrum to 20 Hz for the sheared spectrum. An increase in the linewidth would mean an increase of the dipolar coupling constant or the correlation time (Eq. 2.100), which could not be observed. The dipolar couplings were decreased by approximately 50%, judged by the decrease of the quadrupolar splitting of approximately 50 %. As shown later in Figure **??**, the viscosity was reduced during shear and the temperature was constant during the experiment except for frictional heat during the shear, which would decrease the viscosity and the correlation time as well. The signal widths, on the other hand, decreased for all couplings, which is why more couplings could be measured. The shown 1D slice in Figure 4.26 had a signal width of 370 Hz and a signal-to-noise ratio of 3.88 for the static measurement. A linewidth for the signal was not measurable. Under shear, the signal width decreased to 290 Hz, the signal-to-noise ratio increased to 12.13 and a linewidth of 80 Hz could be measured. As in all 1D spectra, the linewidth in the static and sheared measurements were approximately constant, the viscosity change was probably only macromolecular and did not change the correlation time of the solute molecule strychnine.

With the knowledge of Figure 4.5, the sample was diluted to approximately 6.7 wt% where the static case showed only an isotropic peak. Under 48 HZ rotation, the deuterium spectrum showed a splitting of $\Delta\nu_Q$ = 67 Hz for $CDCl_3$. Once again, a CLIP-HSQC was measured under spinning conditions (Fig. 4.26D), only this time a third of the measurement time was required for twice the signal intensity. Under these

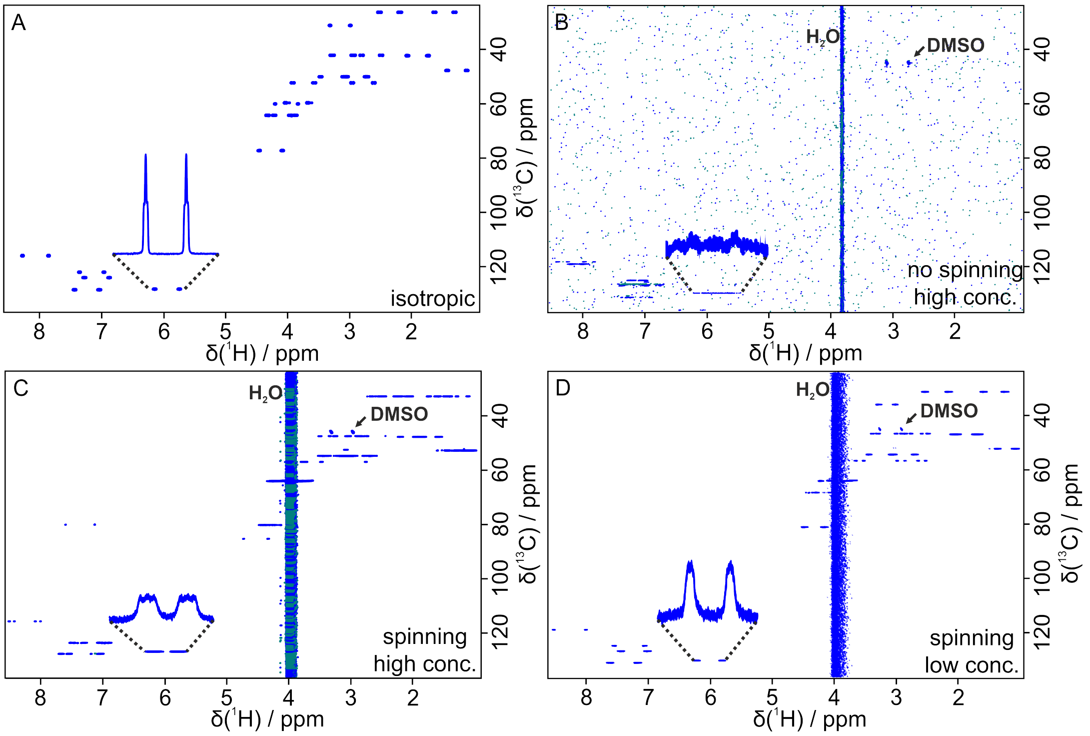

Figure 4.26: CLIP-HSQC spectra for $^1J_{CH}$ and $^1T_{CH}$ coupling determination of strychnine were acquired under isotropic (A), static aligned (B) and sheared aligned (48 Hz rotation) conditions (C-D). The solvent was $CDCl_3$ or a mixture of PBLG/$CDCl_3$ respectively. The overall measurement time for the isotropic case (A) was 15 h 47 min, for the 11.3 wt% sample (B-C) 22 h 5 min and for the 6.7 wt% sample 7 h 22 min. Around 3.8 ppm T_1-noise from water of the DMSO-d_6-filled inner 3 mm NMR tube creates a strong artifact which broadens under shear stress. Additionally, the residual signal from DMSO-d_5 could be seen (B-D). For comparison of signal intensity, a 1D slice through the signal at about 6 ppm is shown in all four spectra. Sets of RDCs measured as the difference of splittings obtained from (B-D) vs (A) are given in Table 4.2[148].

conditions, comparable alignment properties as strychnine measured in stretched polymer gels could be seen[11,161] and the extraction of couplings was significantly enhanced. Unfortunately, the T_1-noise of water was even broader and overlapped with two more couplings than in the original concentration leading to only 17 out of 22 couplings with considerably reduced errors. With the lower concentration of PBLG the signal width decreased to 245 Hz, the linewidth to 37 Hz and the signal-to-noise ratio increased to 19.33 in one only third of the measurement time. The measured couplings of all three conditions are shown in Table 4.2.

As expected, the RDCs showed the same sign change during shear as the quadrupolar coupling of $CDCl_3$ in Section 4.1, which was proven by the Q.E.COSY. Moreover, the couplings under shear for $\Delta\nu_Q$ = 67 Hz were almost one third of the couplings under shear for 180 Hz. The scalability of RDCs with quadrupolar splitting for strychnine in PBLG was already shown by Thiele et al.[14]. Together with a third set of strychnine RDCs measured at a quadrupolar coupling of 125 Hz (Table 4.3, explanation and spectra follows), the scalability of all three sets of RDCs is shown in Figure 4.27. With the exception of four couplings, all couplings were scalable within in their errors. The other four couplings showed some of the largest errors for the RDCs, due to either poor signal intensity or overlapping artifacts. Of these four couplings, C13-H13 and C11-H11b in particular showed poor scalability, with C13-H13 at $\Delta\nu_Q$ = 125 Hz even having the opposite sign compared to the other two. Some of the deviations for all couplings were probably due to the open NMR tube and the evaporation of the solvent during the measurements. The CLIP- and CLAP-HSQCs had acquisition times between 8 and 23 hours depending on the sample. Although I could show that the splitting remains approximately constant for 5-6 days

Table 4.2: $^1D_{CH}$ RDCs measured for strychnine in PBLG/$CDCl_3$ at different alignment conditions. Resulting spectra are shown in Figure 4.26[a]

Assignment	Fig. 4.26B, $\Delta\nu_Q$ = 372 Hz D_{CH}(no spinning) [Hz]	Fig. 4.26C, $\Delta\nu_Q$ = 180 Hz D_{CH}(spinning) [Hz]	Fig. 4.26D, $\Delta\nu_Q$ = 67 Hz D_{CH}(spinning/low) [Hz]
C1-H1	-84.00 or **-232.63** ± 1.01	98.53 ± 4.32	34.27 ± 1.59
C2-H2	**-15.01** or -310.93 ± 2.25	12.66 ± 4.04	3.49 ± 2.89
C3-H3	n.d.	36.54 ± 3.00	13.08 ± 1.78
C4-H4	-97.41 or **-239.59** ± 1.52	120.05 ± 2.09	32.60 ± 0.99
C8-H8	n.d.	23.22 ± 12.68	n.d.
C11-H11a	n.d.	40.17 ± 6.84	15.35 ± 1.77
C11-H11b	n.d.	-60.64 ± 6.84	-21.37 ± 3.53
C12-H12	n.d.	-71.21 ± 3.93	-24.41 ± 2.04
C13-H13	n.d.	-16.39 ± 5.79	-11.76 ± 2.20
C14-H14	n.d.	-62.75 ± 1.33	-28.14 ± 2.00
C15-H15a	n.d.	45.72 ± 5.57	13.07 ± 1.97
C15-H15b	n.d.	4.87 ± 9.74	-1.82 ± 4.44
C16-H16	n.d.	n.d.	n.d.
C17-H17a	n.d.	5.89 ± 2.83	2.83 ± 0.82
C17-H17b	n.d.	5.89 ± 2.83	2.83 ± 0.82
C18-H18a	n.d.	-6.74 ± 3.04	-0.63 ± 1.94
C18-H18b	n.d.	26.45 ± 4.05	6.61 ± 2.91
C20-H20a	n.d.	-24.94 ± 18.24	n.d.
C20-H20b	n.d.	-23.00 ± 3.14	-8.91 ± 2.26
C22-H22	**1.78** or -319.69 ± 3.70	-1.93 ± 0.82	0.003 ± 0.95
C23-H23a	n.d.	n.d.	n.d.
C23-H23b	n.d.	n.d.	n.d.

n.d. = not determined

[a] if total splittings are so large that two values for D are possible, the bold value is the more likely one as judged from the couplings measured under weaker aligning conditions

without rotation and for approximately 18-24 hours with constant rotation, the additional heat during constant rotation can increase the PBLG concentration during a measurement, resulting in broader peaks with higher errors. Another reason why this coupling had an error of more than 12 Hz was that the peaks were at the edge of the spectrum and parts of the peak were cut off.

At this point should be mentioned, not only the seen CLIP-HSQCs were used for the coupling measurements under spinning conditions but also the complementary antiphase CLAP-HSQCs, which are shown in Figure 4.28. Measuring the couplings with the CLIP/CLAP approach[146] has several advantages. The addition and subtraction of inphase and antiphase signals increases the signal-to-noise ratio and often allows the correct determination of overlapping CH_2 signals. Furthermore, the signal intensity in a CLAP-HSQC during the coherence transfer is close to 100 % for all couplings and does not scale with $\sin\pi(^1J_{CH} + D_{CH})\Delta$ as in a CLIP-HSQC. The 90° pulses are independent of the applied delays during the coherence transfer for the CLAP-HSQC. Especially for molecules such as strychnine with a very broad range of dipolar couplings, the acquisition of a CLAP-HSQC significantly improves the determination of dipolar couplings.

After I could prove that the rheo-device works very well, gaining sheared sets of RDCs, I finally wanted to get rid of the T_1 noise of DMSO/water. A first attempt was to reduce the temperature beneath

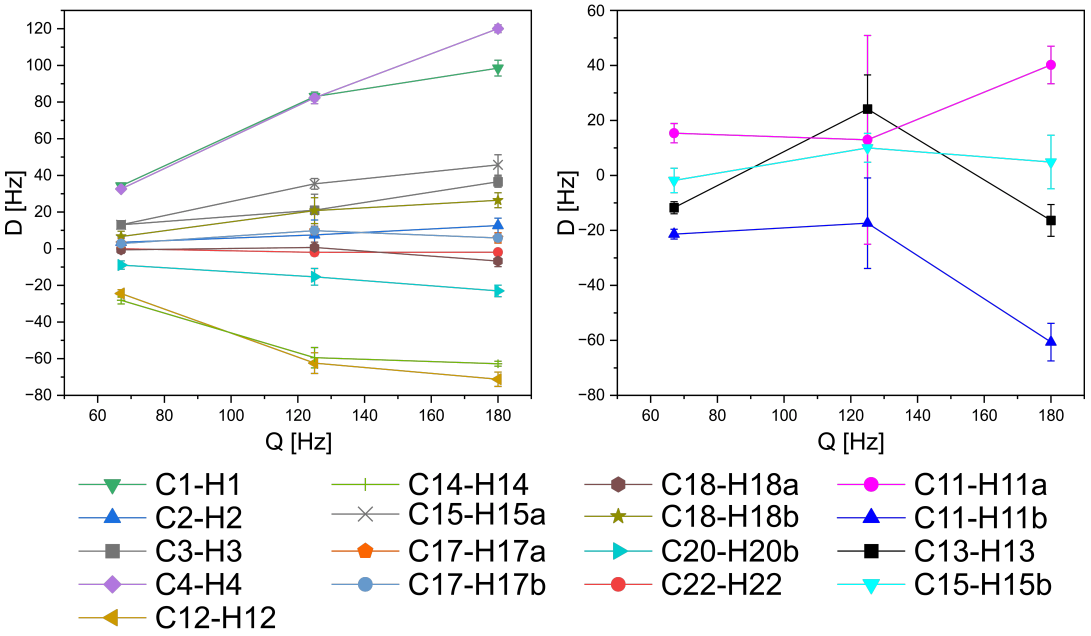

Figure 4.27: The RDCs (D) of Table 4.2 and 4.3 are shown for each coupling over the quadrupolar coupling (Q) of $CDCl_3$ with PBLG. Only the couplings are shown, which have values for all three quadrupolar splittings. All couplings which show the linear behavior within a small error can be seen in A) and the four couplings which do not show a nice linear behavior can be seen in B).

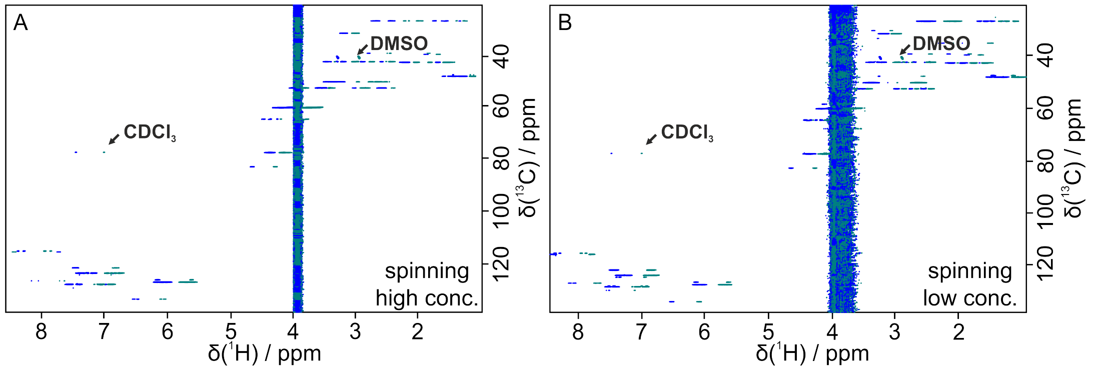

Figure 4.28: The corresponding CLAP-HSQC spectra to Figure 4.26C and D. For compatibility, both CLAP spectra are recorded the same way as the CLIP spectra[148].

the freezing temperature of DMSO of 18 °C (291 K). Spectra were measured at 285 K using a freshly filled 3 mm inner NMR tube with waterfree DMSO-d_6 after shimming on the DMSO-d_6 signal at room temperature. Most of the DMSO-d_6 signal in the 1D deuterium spectrum at 285 K disappeared due to freezing, thus it was necessary to shim at room temperature. The effects in the CLIP-HSQC spectra were as expected. The DMSO-d_5 signal and the T_1 noise both disappeared completely from the spectra. Now, the two couplings underneath the broad noise could be measured and only one C-H coupling of strychnine was not measurable due to low signal intensity of these peaks. The CLIP- and CLAP-HSQCs are shown in Figure 4.29 and the measured couplings in Table 4.3. Unfortunately, after one week the T_1 noise and the DMSO-d_5 peaks in the 1D and 2D spectra came back due to water in the air dissolving in DMSO-d_6 inside the open 3 mm tube. Looking at the phase diagram of DMSO/water, the freezing temperature of the mixture decreases strongly with small amounts of water, down to a minimum of − 70 °C[162]. The used spectrometer could not go below 284 K, which made it impossible to freeze the mixture. Luckily, a small change in the apparatus made it possible using sealed 3 mm NMR tubes. Therefore, the 3 mm tube could be filled with DMSO-d_6 from a freshly opened vial under argon atmosphere. This way, the DMSO-d_6 stays waterfree and there is no need to change the DMSO-d_6 every week before the measurements.

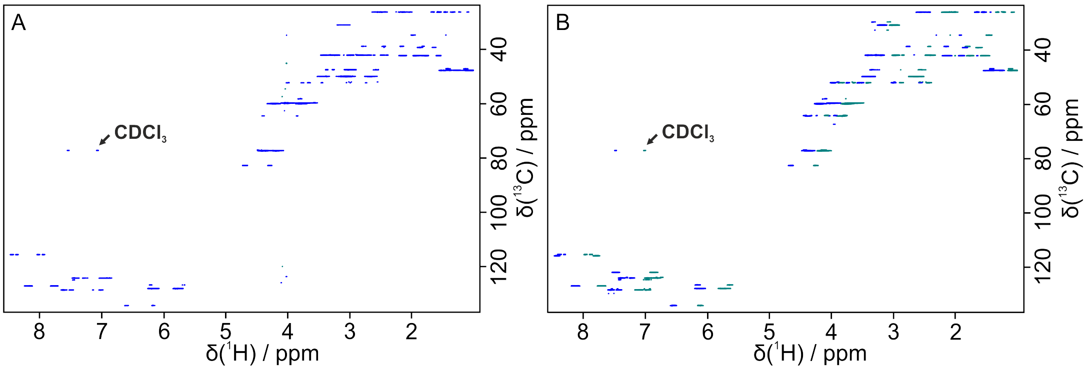

Figure 4.29: CLIP- (A) and CLAP- (B) HSQC spectra of strychnine in PBLG/CDCl$_3$. The sample was diluted to approx. 9 wt% with a static quadrupolar splitting of CDCl$_3$ of around 260 Hz and a quadrupolar splitting of 125 Hz during rotation. The couplings were measured after shimming at room temperature on the DMSO signal in the inner 3mm tube and lowering the temperature to 285 K (freezing temperature of waterfree DMSO. This removed most of the DMSO-d_6 signal from the deuterium 1D , the complete DMSO-d_5 signal from the CLIP-HSQC and the spectral artifacts caused by T_1 noise of DMSO/water. Therefore, a larger number of $^1T_{CH}$-couplings (21 out of 22 C-H couplings) could be measured (Table 4.3)[148].

Table 4.3: $^1D_{CH}$ RDCs measured for strychnine in PBLG/CDCl$_3$ with a quadrupolar splitting of 125 Hz. Resulting spectra are shown in Figure 4.29

Assignment	Fig. 4.29, $\Delta\nu_Q$ = 125 Hz D_{CH} [Hz]
C1-H1	83.03 ± 2.33
C2-H2	7.54 ± 8.12
C3-H3	21.03 ± 8.75
C4-H4	82.33 ± 3.19
C8-H8	-8.30 ± 22.56
C11-H11a	12.93 ± 16.46
C11-H11b	-17.37 ± 37.97
C12-H12	-62.40 ± 5.65
C13-H13	24.16 ± 12.39
C14-H14	-59.47 ± 5.56
C15-H15a	35.40 ± 2.92
C15-H15b	10.02 ± 5.26
C16-H16	21.82 ± 0.83
C17-H17a	9.82 ± 1.71
C17-H17b	9.82 ± 1.71
C18-H18a	0.69 ± 2.95
C18-H18b	20.79 ± 7.08
C20-H20a	-10.84 ± 8.44
C20-H20b	-15.34 ± 4.55
C22-H22	-1.98 ± 1.93
C23-H23a	n.d.
C23-H23b	-32.16 ± 4.90

n.d. = not determined

The last step after the successful measurement of various data sets with RDCs for strychnine at different concentrations was the comparison of the data with back-calculated RDCs using the program PALES by M. Zweckstetter[46,47]. In addition, the obtained RDCs were compared with other strychnine data from the Thiele group measured in PBLG/$CDCl_3$ with a VASS probe at different angles below the magic angle ($\Theta_r < 54.7°$)[14] (Fig. 4.30). First, the comparison with the data from the Thiele group is shown. The measurement of the 6.7 wt% sample with $\Delta\nu_Q$ = 67 Hz of $CDCl_3$ could be compared with their measurement at an angle of 48.5° and $\Delta\nu_Q$ = 76 Hz, the measurement of the 9 wt% sample with $\Delta\nu_Q$ = 125 Hz with their measurement at an angle of 43.7° and $\Delta\nu_Q$ = 137 Hz and the measurement of the 11.3 wt% sample with $\Delta\nu_Q$ = 180 Hz with their measurement at an angle of 40.3° and $\Delta\nu_Q$ = 179 Hz. Interestingly, less than 10° of the angle change the quadrupolar splitting of $CDCl_3$ by 100 Hz. All three data sets agreed well with the sets of the Thiele group with a Pearson's correlation factor R of at least 0.948. Only a few outliers were not on or near the regression line, most of which had large measurement errors due to low signal intensity or strong artifacts. One important thing should be noted here. There are two ways of calculating the dipolar coupling which differs by a factor of two. One can either take the whole splitting of the two signals or divide the splitting by two, which is the difference to the chemical shift of the original isotropic signal. In our group, we are using the whole splitting and the Thiele group is dividing their signals by two. The factor of two has no influence on the structure determination. Similarly, the comparison of three data sets with the back-calculated RDCs using PALES agreed well with Pearson's R factors of 0.933 (67 Hz), 0.942 (125 Hz) and 0.905 (180 Hz) and Saupe Q values of 0.259 (67 Hz), 0.213 (125 Hz) and 0.299 (180 Hz), respectively. See the appendix 6.2 for the PALES output files.

The lower concentration sample with a quadrupolar splitting of 67 Hz during rotation offered a new way of calculating RDCs. Without rotation, the 1D deuterium spectrum showed a single line for $CDCl_3$, which meant the sample was isotropic. Theoretically, a CLIP-HSQC of this sample without rotation should give the isotropic $^1J_{CH}$ couplings. As can be seen in Figure 4.31, this assumption was correct. The C-H couplings were all equal in size for the strychnine sample in $CDCl_3$ without PBLG and strychnine in 6 wt% PBLG/$CDCl_3$. Even the aromatic region with very high RDCs under anisotropic conditions showed a maximum difference of 0.4 Hz to the isotropic sample without PBLG. However, the four couplings of two CH_2 groups (17 and 20) showed a difference of 1 Hz due to the broad linewidth of 7 Hz, and one CH_2 group (18) showed the highest difference of 1.5 Hz and 2.4 Hz, as the two hydrogens are so close to each other that the mean signal overlaps, which explains this minimally higher difference (see the appendix for Tab. 6.1). The broader linewidth was an effect of the dipolar couplings. Although dipolar interactions are canceled out in isotropic samples, they still exist and increase the linewidth in isotropic spectra. An increase in linewidth due to a bad shim could be excluded as it was automatically shimmed on the $CDCl_3$ signal, resulting in a $CDCl_3$ linewidth of 1.0 Hz without apodization. Another effect could be seen in this sample, which will be discussed in more detail in subsection 4.3.2. Especially in the aromatic region, strong ^{13}C chemical shift differences up to 1 ppm could be seen. Both spectra were referenced to the TMS signal.

Subsequently, the sample could be measured with rotation and the isotropic $^1J_{CH}$ couplings and the anisotropic $^1T_{CH}$ couplings could be obtained within the same sample (Fig. 4.32) without changing other parameters (e.g. shim). Only the two C-H couplings from the CH_2 group (23) next to the oxygen in the seven-membered hetero cycle did not have enough signal intensity in the sheared CLIP- and CLAP-HSQCs and 20 out of 22 C-H couplings were obtained (see the appendix for Tab. 6.2). PALES calculated a Pearson's R factor of 0.937 and a Saupe Q factor of 0.235 for this set of RDCs (see the appendix for the PALES file 6.2.4). This showed that using PBLG underneath the critical concentration for static alignment could be used for structure determination with RDCs. Unlike the gain in signal intensity due to shearing in Figure 4.26, this time less signal was received. In the isotropic case without rotation, the dipolar couplings were averaged to zero, but shear-induced anisotropy led to visible RDCs

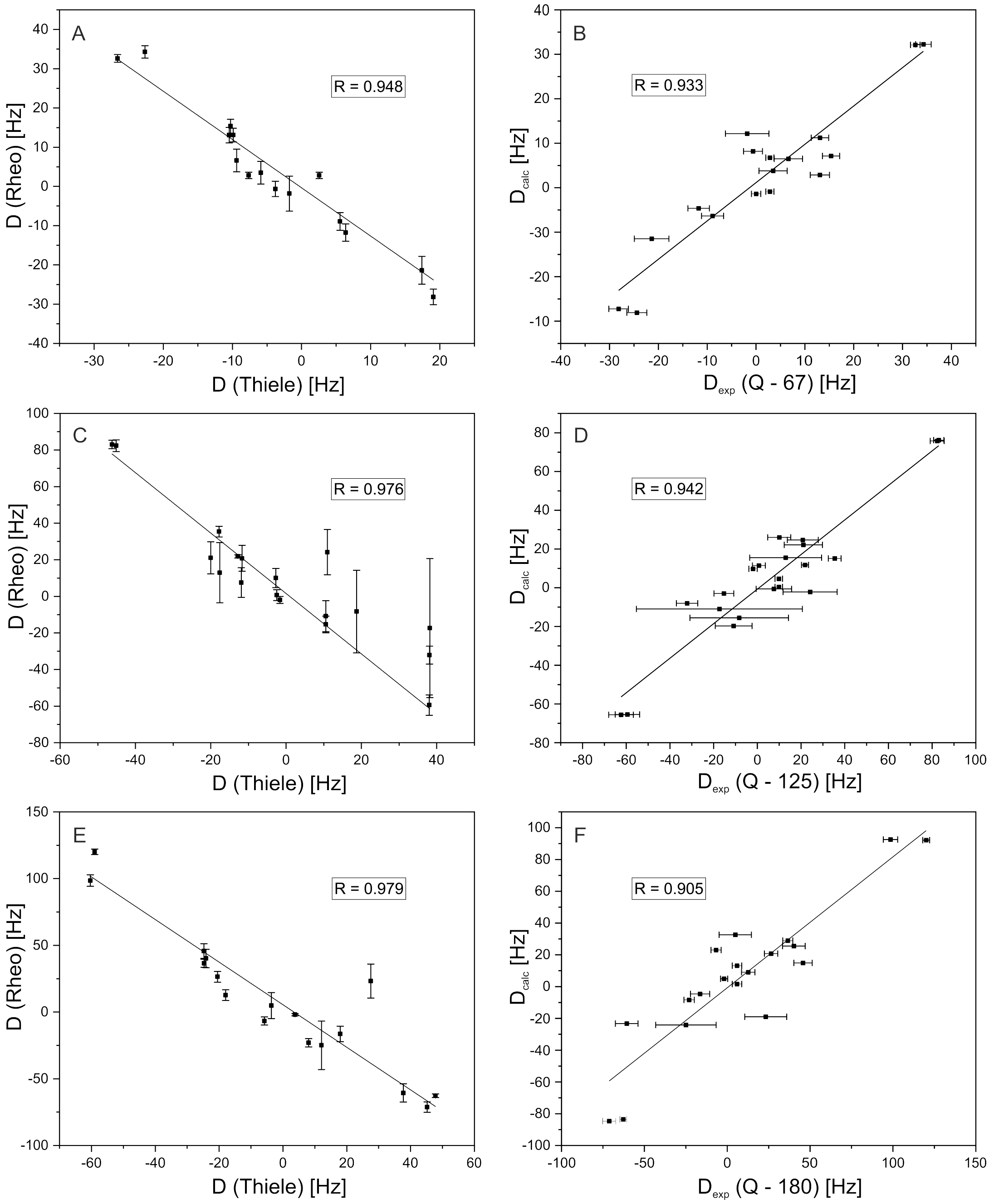

Figure 4.30: Comparison of the measured RDCs from Figure 4.26, 4.28 and 4.29 with measurements of the Thiele group[14] at (A) 67 Hz (Rheo), 76 Hz (Thiele) (C) 125 Hz (Rheo), 137 Hz (Thiele) (E) 180 Hz (Rheo), 179 Hz (Thiele) $CDCl_3$ splitting[148] as well as with back-calculated ones by PALES[46,47] (B,D,F). The Pearson's factor R for each correlation is shown in the spectra.

in the spectrum and the signal intensity was reduced by the induced dipolar couplings as well as by the multiplet structure due to the dipolar couplings. Therefore, the only advantage of this way of measuring RDCs is that the expensive polymer is saved. The other advantage related to the RCSA will be explained later.

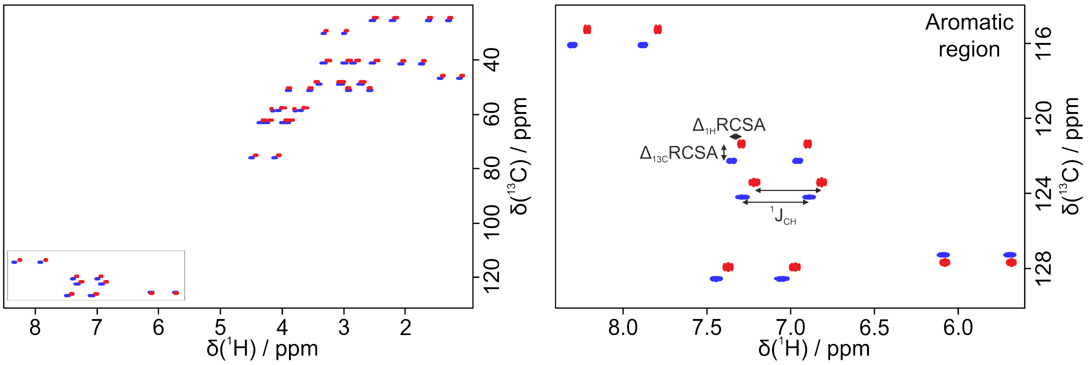

Figure 4.31: On the left, a CLIP-HSQC of strychnine in $CDCl_3$ (red) is overlayed with a CLIP-HSQC of strychnine in 6 wt% PBLG/$CDCl_3$ (blue). On the right, the aromatic region of the same spectra are shown where arrows indicate the isotropic $^1J_{CH}$ coupling and the chemical shift difference (ΔRCSA).

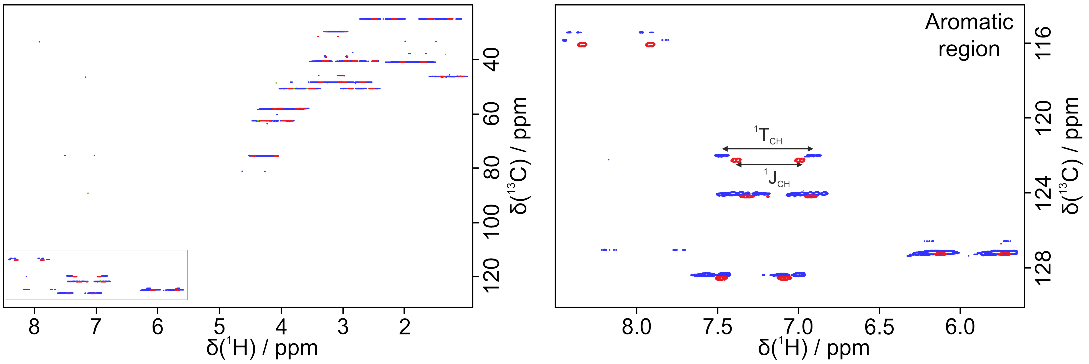

Figure 4.32: Two CLIP-HSQCs of strychnine in 6 wt% PBLG/$CDCl_3$ (left), one with 48 Hz rotation (blue) and one without (red), are shown. The overall measurement time for both spectra was each 7 h 46 min. For more details, the right spectrum is zoomed into the aromatic region, where the isotropic $^1J_{CH}$ couplings and the anisotropic $^1T_{CH}$ couplings are shown.

4.3.1.2 1-Fluornaphthalene

So far, only strychnine was used in this work as a model for dipolar coupling measurements. Due to its strong interaction with PBLG, the RDCs were large with heavy line broadening, which made it nearly impossible to measure RDCs without rotation in the spectrometer operating at 9.4 T. Therefore, I changed the solute molecule to 1-fluornaphthalene, which should interact weakly with PBLG due to its missing hydrogen donor groups. Furthermore, it has only 7 C-H couplings, all located in the aromatic region (Fig. 4.33). All couplings could be measured with relatively high signal intensity in an approximately 9 wt% PBLG/$CDCl_3$ sample under both conditions - static and under shear. This made it possible to calculate the dipolar coupling through two different anisotropic states without the need of an isotropic state. Only one calculation was required before. Both anisotropic conditions showed the total couplings according to Equation 2.62, where the Legendre polynomial can be fitted for the two alignment tilt angles in the static case (Θ_D = 0°) and in the sheared case (Θ_D = 75-90°). For easier calculation, the value of the Legendre polynomial is referenced by κ_L and can be calculated by the quadrupolar couplings of the solvent with Equation 4.1.

$$\kappa_L = 3\cos^2(\Theta_D) - 1 = \frac{2Q_s}{Q_{ns}} \tag{4.4}$$

In both cases, the isotropic *J*-coupling is the same and κ_L = 2 at 0°. If the total coupling under spinning is now subtracted from the total coupling under static conditions, the isotropic *J*-coupling is canceled out and only the dipolar couplings remain, which are $2D$ in the static case and $\kappa_L D$ in the sheared case.

$$^{1}T_{CH}(nonspinning) -^{1} T_{CH}(spinning) = (2 - \kappa_L)^{1}D_{CH} \tag{4.5}$$

With Equation4.5 and a calculated κ_L of -0.88 for this sample, the values in Table 4.4 were obtained. As expected, the dipolar couplings were much smaller than for strychnine. The aromatic RDCs of 1-fluornaphthalene had a maximum value of -14.4 Hz and the ones for strychnine went up to 41.5 Hz at 125 Hz quadrupolar splitting of $CDCl_3$ during rotation which was a bit less than the 138 Hz for 1-fluornaphthalene. The 41.5 Hz belonged to the C1-H1 coupling in Table 4.3, which was originally given as 83.03 Hz. However, since the RDCs for 1-fluornaphthalene are divided by 2.88 according to Equation 4.5, the 83.03 Hz also had to be divided by two for a correct comparison. The calculation with PALES gave a Pearson's R factor of 0.977 and a Saupe Q factor of 0.044 which is very close to perfection but with only seven couplings this is not very surprising (see the appendix for the PALES file 6.2.6). For the Saupe tensor at least 5 couplings are needed and 1-fluornaphthalene is a completely flat molecule with its aromatic rings.

Table 4.4: $^{1}T_{CH}$ couplings and corresponding RDCs of 1-fluornaphthalene in PBLG/$CDCl_3$. The spectrum is shown in Figure 4.33

Assignment	$\Delta\nu_Q$ = -315 Hz T_{CH}(no spinning)[Hz]	$\Delta\nu_Q$ = 138 Hz T_{CH}(spinning)[Hz]	(2-κ_L) = 2.88 D_{CH}[Hz]
C1-H1	150.647	170.069	-6.744
C2-H2	141.517	169.162	-9.599
C3-H3	131.934	172.526	-14.094
C4-H4	146.028	166.97	-7.272
C6-H6	143.463	167.5	-8.346
C7-H7	138.65	170.695	-11.127
C8-H8	135.105	176.687	-14.438

However, the measurements with 1-fluornaphthalene showed that it is possible to determine a set of RDCs without knowing the isotropic *J*-coupling. The *J*-coupling can be calculated from the total couplings and the determined RDCs. As Table 4.5 shows, there was only a small difference between the calculated *J*-couplings and the ones measured under isotropic conditions. However, due to the short measurement time (only 256 points in the indirect dimension) the carbon splitting of C8 by the neighboring fluor atom could only be seen in the isotropic spectrum. Both anisotropic spectra showed a tilt due to this splitting but were not resolved in individual peaks. More points in the indirect dimension should solve this issue. This way of measuring RDCs could be particularly useful for samples where no isotropic sample can be measured, e.g. a very expensive substance that cannot initially be produced as an isotropic sample.

The rheo-device offered several different methods for the determination of RDCs with high quality. This quality is obtained on a 400 MHz spectrometer with a sample volume of 300 µl. Normally, a sample for small molecules would contain between 400 and 500 µl and would be measured at 600-800 MHz for spectra with higher quality. Especially, if alignment is produced by polymeric LCs. The spectra under shear offered comparable spectral quality. One could use the rheo-device at higher magnetic fields but the shear-force needs to be stronger than the magnetic force for a changed alignment. I tried the

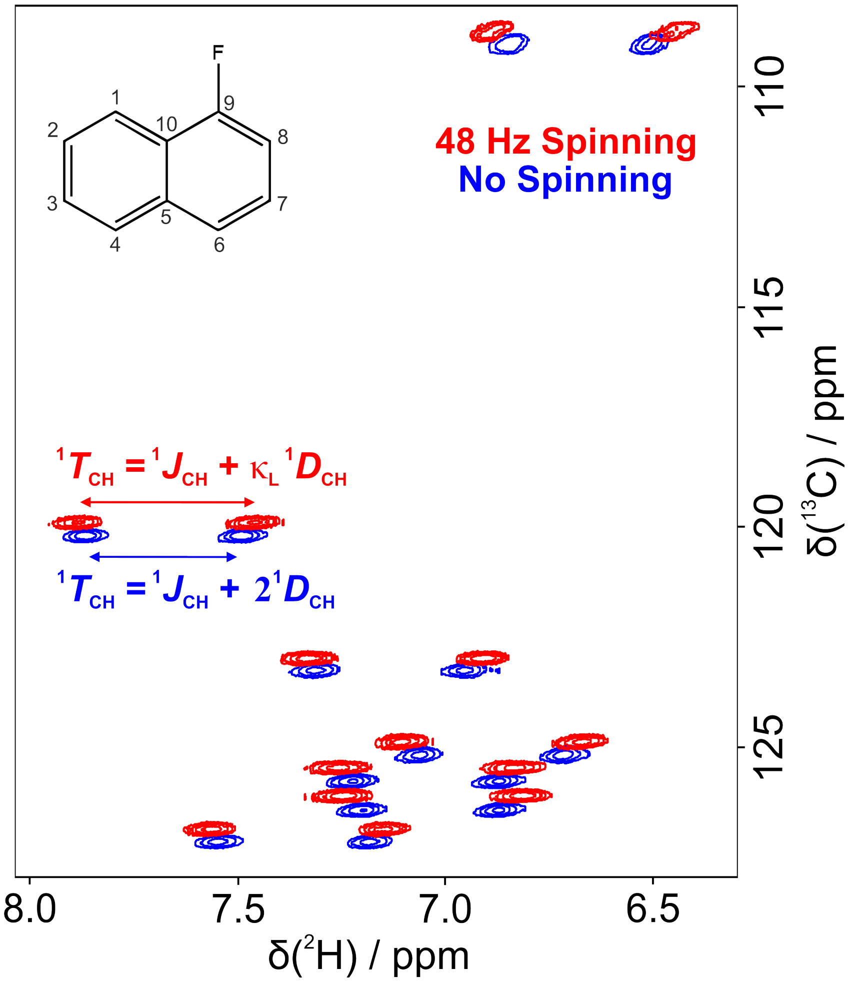

Figure 4.33: The two aromatic CLIP-HSQCs under static (blue) and sheared (red) conditions are overlayed. The corresponding quadrupolar couplings of $CDCl_3$ are -314.9 Hz at static conditions and 137.5 Hz at sheared conditions resulting in a κ_L of -0.88 under rotation. The spectra were acquired with 8192 points in the direct dimension, 256 points in the indirect dimension and two scans. The measurement time was 15 min.

Table 4.5: The calculated J-couplings from the total couplings and RDCs are compared with measured J-couplings for an isotropic sample.

assignment	calculated coupling [Hz]	mesaured coupling [Hz]	difference between both [Hz]
C1-H1	164.13	162.82	1.31
C2-H2	160.72	161.03	-0.31
C3-H3	160.19	160.12	0.07
C4-H4	160.57	159.86	0.71
C6-H6	160.16	159.58	0.58
C7-H7	160.90	160.04	0.86
C8-H8	163.98	161.77	2.21

apparatus one time at a 600 MHz spectrometer but several issues stopped these measurements. In the future, it is planned to redo these experiments as the few measurements showed that the shear-force

induced by 50 Hz rotation speed might be still strong enough for a tilted alignment.
However, the main advantage of the rheo-device are the low LC concentration measurements. Inducing residual anisotropic parameters in concentrations under the critical concentration reduces the linewidth and increases the signal-to noise ratio significantly. The obtained RDCs offered still the same structural information. Therefore, it is unnecessary to use PBLG concentrations higher than 10 wt%. The alignment at 10 wt% is already very strong and the line broadening gets worse for higher concentrations. Especially for molecules like strychnine, which are interacting strongly with PBLG, the lower concentrations are highly advantageous.

Similar results as for shearing with the rheo-device can be obtained with VASS. A VASS probehead can spin at every angle between 0° and 90°, where the angle does not rely on the equilibrium between the shear-force and the magnetic force. This probehead is a costum-made product similar to the rheo-device, only that the VASS probehead costs over 50 000 € and the used apparatus here costs less than 10 000 € including the approximately 1 month construction time. Also, the shear force by spinning in a VASS probehead is different from the shear-force in a rheometer. In a rheometer, the substance is actively sheared between walls. For concentrations above the critical concentration, it would not matter which shear-force is used. The sample is anisotropic and will show the angle dependent alignment strength. Below the critical concentration, it probably does matter how the sample is sheared. The shear-force needed for an isotropic PBLG sample to change into flow aligning anisotropy, is higher than for an anisotropic PBLG sample. The passive shear-force from spinning the sample in a VASS probe is probably too weak for anisotropic aligning of a low concentration PBLG sample, but since this has not been tested, it is only speculative.

4.3.2 RCSA

In Figure 4.31 and 4.32, there is a difference in the chemical shift between the two isotropic spectra (with and without PBLG) acquired on a 400 MHz spectrometer, and a difference between the spectra with PBLG during rotation and without rotation. The first one is the chemical shift difference due to the different susceptibility of pure $CDCl_3$ and $CDCl_3$ with PBLG and the effect of aromatics on chemical shifts. Hereby, it does not matter if it is referenced to the TMS signal or the $CDCl_3$ signal. Both show a chemical shift difference for all the other signals. However, if it is referenced to TMS, as TMS should be least affected according to theory with its tetrahedral geometry, $CDCl_3$ has the highest chemical shift difference of 1.087 ppm. The truth is probably somewhere in the middle, because the solvent susceptibility definitely affects the chemical shift of $CDCl_3$ and TMS[53].
The second one are RCSAs measured by the difference of isotropic versus spinning-induced anisotropic spectra. If the susceptibility changes here as well, it could not be measured. It was still the same sample in the same solvent with the same amount of PBLG which does not change the susceptibility. Courtieu et al.[13] showed in their work on VASS that the anisotropy of the magnetic susceptibility depends, among other things, on the angle Θ_D and the viscosity. But whether this relationship can also be used in rheo-NMR, where the director is tilted by shear-force, has never been shown. Nevertheless, the viscosity under shear for PBLG in $CDCl_3$ decreases by more than a factor of 10 (see Sec. 4.4), which can probably cause a change in susceptibility. The chemical shifts of the isotropic spectrum with 6 wt% PBLG are between the chemical shifts of the isotropic spectrum without PBLG and the anisotropic spectrum with 6 wt% PBLG. Hence, the probable susceptibility change for the PBLG sample during rotation is added positively to the susceptibility change from 0 wt% PBLG to 6 wt% PBLG. The effects of rotation on other reference molecules are examined in the next section 4.3.2.1.

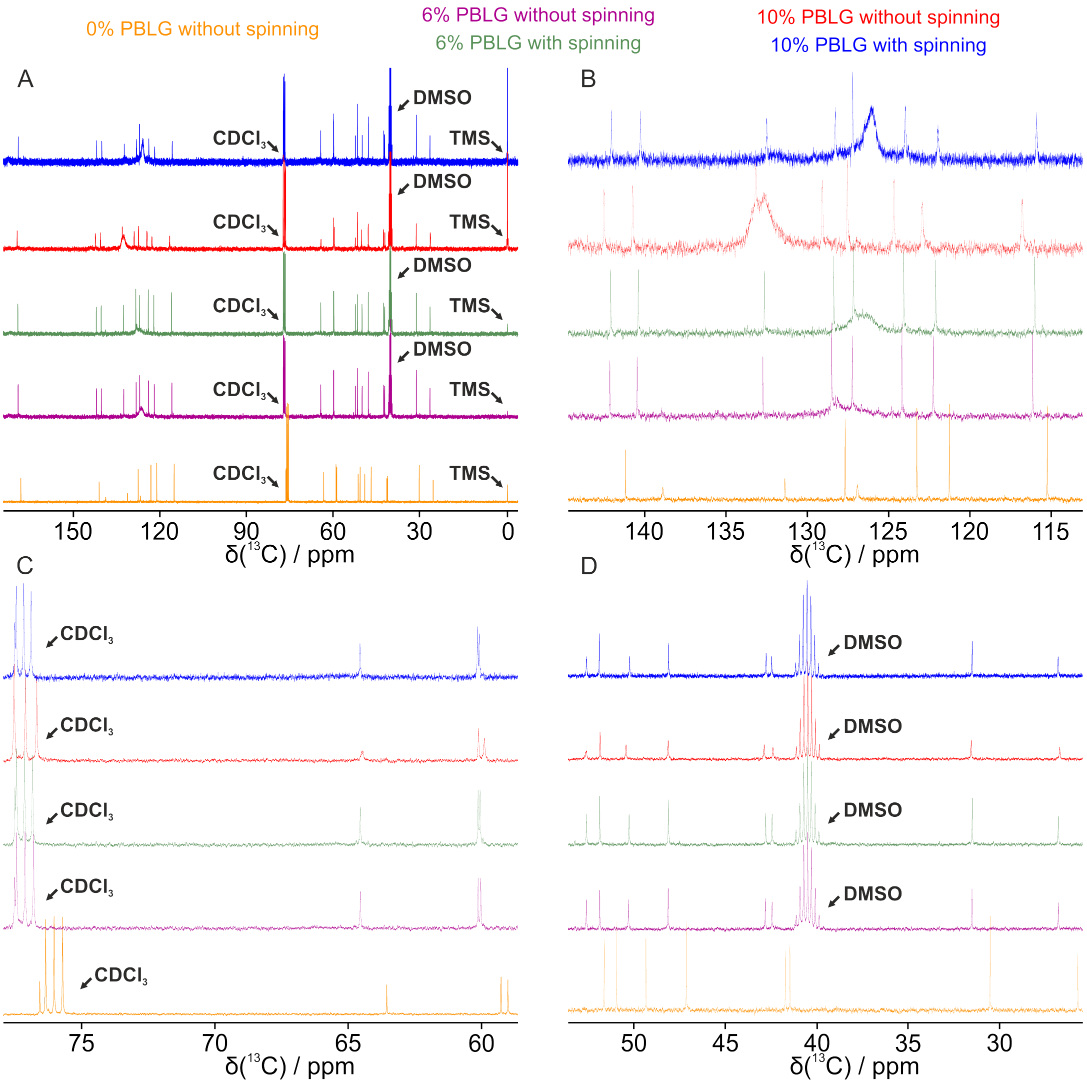

Figure 4.34: The ^{13}C 1Ds of strychnine in $CDCl_3$ are shown for different amounts of PBLG and during rotation or without rotation. In A) the whole spectra are shown, in B), C) and D) only parts of the spectra. The orange spectrum without PBLG was not taken inside the rheo-device and is therefore missing the DMSO signal at 39.5 ppm. Between 125 and 135 ppm an up to 300 Hz broad peak arises in the spectra with PBLG which corresponds to the aromatic benzyl signals of PBLG (see SDBS for γ-benzyl-l-glutamate).

In addition to the 6 wt% sample, another PBLG sample from the same batch was measured with a concentration of 10 wt%. For some of the peaks, the chemical shifts are between both isotropic samples, for the other peaks, the chemical shifts show larger distances to the isotropic shifts without PBLG than to those with 6 wt% PBLG.

The higher amount of PBLG changes the susceptibility, but not as much as different amounts of PBLG compared to the sample without PBLG. A second effect plays a role, namely the influence of the magnetic anisotropy of aromatics. As often reported in the literature, a change from a non-aromatic solvent (e.g. $CDCl_3$) to benzene or another aromatic solvent changes the chemical shifts of the molecule of interest. Not all signals change to the same extent, but some chemical shifts are more affected than others[163]. For this reason alone, it is not possible to measure an RCSA between an isotropic solution in pure $CDCl_3$ and an anisotropic solution in $CDCl_3$ in the presence of PBLG, since the effect of benzyl groups are not predictable a priori.

Table 4.6: The comparison of the chemical shift differences of strychnine between the isotropic sample without PBLG, the isotropic 6 wt% PBLG sample and the anisotropic 6 wt% PBLG sample.

assignment	0 wt% PBLG [ppm]	static 6 wt% PBLG [ppm]	$\Delta\delta$ to 0 wt% [ppb]	sheared 6 wt% PBLG [ppm]	RCSA to static 6 wt% [ppb]
1	121.264	122.246	982	122.102	-144
2	123.255	124.170	915	124.064	-106
3	127.667	128.492	825	128.370	-122
4	115.242	116.137	895	116.004	-133
5	141.179	142.131	952	142.074	-57
6	131.368	132.720	1352	132.628	-92
7	50.942	51.858	916	51.858	0
8	59.004	60.024	1020	60.047	23
10	168.228	169.257	1029	169.187	-70
11	41.455	42.430	975	42.430	0
12	76.565	77.504	939	77.491	-13
13	47.119	48.114	995	48.105	-9
14	30.508	31.495	987	31.485	-10
15	25.709	26.769	1060	26.779	10
16	59.263	60.121	858	60.123	2
17	41.702	42.800	1098	42.782	-18
18	49.331	50.285	954	50.251	-34
20	51.616	52.588	972	52.584	-4
21	138.770	140.453	1683	140.381	-72
22	126.914	127.220	306	127.151	-69
23	63.548	64.537	989	64.541	4
$CDCl_3$	76.025	77.114	1089	77.137	23

The RCSA is largest in the aromatic region of strychnine. Up to -144 ppb RCSA can be measured here for the sheared 6 wt% sample referenced to the static one. In the aliphatic region, two peaks within the linewidth of 2.5 Hz show no signs of RCSA. However, three signals show an RCSA of maximum ± 4 ppb ($\approx$ 0.4 Hz), which is about six times smaller than the linewidth. The same peaks show a higher RCSA for the sheared 10 wt% sample referenced to the static 10 wt% one, in which the linewidth is 4.5 Hz. All 24 possible RCSA values (including $CDCl_3$) show the same sign and most of the RCSA values are six to seven times larger for the 10 wt% sample than for the 6 wt% sample.

Interestingly, it seems as the chemical shift differences of the static and sheared 10 wt% sample referenced to the static 6 wt% sample are also scalable with the RCSA values of the sheared 6 wt% sample. The chemical shift differences between both static PBLG concentrations are mostly four to five times larger with a sign change for all values. The chemical shift differences of the sheared 10 wt% sample referenced to the static 6 wt% sample are about twice as large as the RCSAs of the sheared 6 wt% sample. The only RCSA value, which does not scale with the other values, is the one from the solvent $CDCl_3$. The same comparison of the chemical shift differences referenced to the isotropic sample without PBLG shows no sign of scalability due to the previously mentioned effect of aromatics on the chemical shift.

Even more interesting is the comparison between the chemical shift differences of the sheared and static 10 wt% measurements referenced to the static 6 wt% measurement. They show approximately the same scaling factor of approximately -0.5 as RDCs changed from static to shear-induced alignment. It seems that within a small error due to the concentration of the benzyl group, a lower concentration of PBLG, which is isotropic to the eye under static conditions, can be taken as an isotropic reference for higher concentrated PBLG samples. However, if the same concentration of PBLG can be used for referencing, this should always be the choice.

Table 4.7: The comparison of the chemical shift differences of strychnine between the isotropic 6 wt% PBLG sample and the anisotropic 10 wt% PBLG sample and the RCSA of the 10 wt% sample.

assignment	**static 10 wt% PBLG [ppm]**	**$\Delta\delta$ to static 6 wt% [ppb]**	**sheared 10 wt% PBLG [ppm]**	**$\Delta\delta$ to static 6 wt% [ppb]**	**RCSA to static 10 wt% [ppb]**
1	122.918	672	121.956	-290	-953
2	124.662	492	123.962	-208	-700
3	129.069	577	128.259	-233	-810
4	116.770	633	115.888	-249	-882
5	142.488	357	142.028	-103	-460
6	133.163	443	132.483	-237	-680
7	51.838	-20	51.882	24	44
8	59.885	-139	60.079	55	194
10	169.516	259	169.111	-146	-405
11	42.381	-49	42.452	22	71
12	77.523	19	77.504	0	-19
13	48.117	3	48.096	-18	-21
14	31.538	43	31.484	-11	-54
15	26.694	-75	26.785	16	91
16	60.104	-17	60.142	21	38
17	42.862	62	42.755	-45	-107
18	50.419	134	50.221	-64	-198
20	52.589	1	52.581	-7	-8
21	140.722	269	140.251	-202	-471
22	127.527	307	127.193	-27	-334
23	64.447	-90	64.550	13	103
$CDCl_3$	77.099	15	77.166	52	67

Since all spectra were referenced to TMS, no RCSA of TMS was measurable and the effect of shear force on the chemical shift of TMS remains unanswered. Nevertheless, a small RCSA of TMS is expected, as previously reported[51,52]. Therefore, an attempt was made to evaluate the shearing influence on tetrahedral molecules as can be seen in the next section.

4.3.2.1 Tetrahedral molecules

TMS is a well-established chioce for a reference molecule. However, RDCs and RCSA were reported for TMS many times probably due to distortions of the tetrahedral symmetry through e.g. vibrational motion in a nematic phase[51,52]. Also, the carbon atoms in TMS are not truly tetrahedral, the silicon is. Therefore, small distortions and measurable RDCs and RCSA are not surprising. There are other tetrahedral molecules were the carbon is tetrahedral, methane and all its tetrasubstituted versions

(CX_4). These tetrahedral molecules can show the same distortions and hence measurable RDCs and RCSA. Burnell et al.[51] showed this for a few tetrahedral molecules in nematic phases, one of them was methane. The small hydrogen atom does not provide a completely rigid structure.
However, there might be some atoms providing a better approximation to a symmetric tetrahedral structure without distortions in nematic phases - halomethanes. Chlorine, bromine and especially iodine are very large atoms and the tetrahalomethanes might be ideal for showing no RCSA. Therefore, I tried the three molecules CCl_4, CBr_4 and CI_4. Unfortunately, I could not detect any signal for CI_4. I tried several ways, including 1 hour relaxation time for ^{13}C experiments at the highest possible concentration of CI_4 (around 100 mM), but no success. Looking into the literature, there is only one paper claiming to have measured the carbon signal of tetraiodomethane[164], all other halomethane related references measured all possible halomethanes, but never CI_4. As I could not find a way to detect CI_4, the final sample under investigation for RCSA contained $CDCl_3/CHCl_3$ (1:1), TMS, CCl_4, CBr_4 and 5.2 wt% PBLG.

For optimal comparison of the chemical shifts and the RCSA of all substances, all spectral preparations like shimming were done before the first ^{13}C or ^{29}Si spectrum. After the static ^{13}C spectra were acquired, the rotation was turned on by the waveform generator and after one minute adjusting time for the rotation, the spectra under spinning conditions were acquired. After the rotation was stopped, 20 minutes were waited until the second nucleus was changed to silicon and the spectra were acquired the same way. The chemical shifts in Table 4.8 were determined without further referencing from the spectra shown in Figure 4.35.

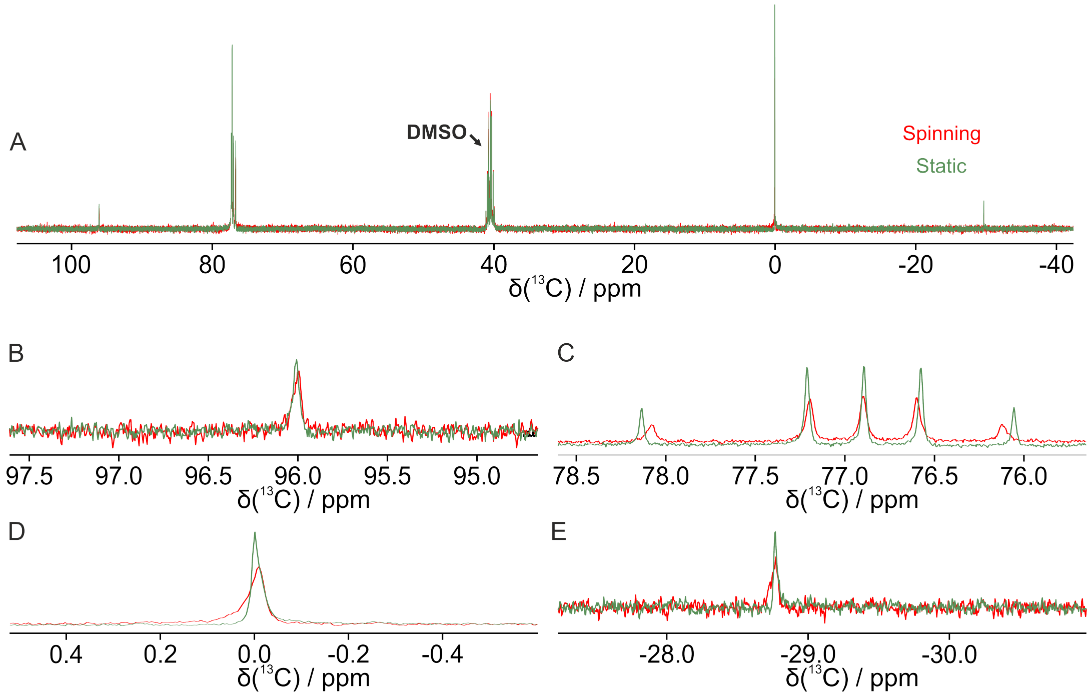

Figure 4.35: ^{13}C 1Ds of several threefold molecules in $CDCl_3/CHCl_3$ and 5.2 wt% PBLG are shown. The green spectra were acquired under static conditions, the red spectra under sheared conditions. In A) the entire spectra are shown, in B) the CCl_4 signal, in C) the solvent signals, in D) the TMS signal, and in E) the CBr_4 signal. A, B, D and E show the decoupled spectra, C shows the coupled spectra. The decoupled spectra were acquired as inverse gated decoupling with Ernst-angle excitation with 4096 scans in 1 h 19 min and the coupled spectra only with Ernst-angle excitation with 4096 scans in 1 h 19 min.

CCl_4 showed the largest chemical shift difference of -13.8 ppb, which is very small. The rest had a difference of less than 10 ppb, where only the two chloroform solvents showed no shift difference at all. Even the signal of DMSO-d_6 showed a difference of 2.2 ppb under shearing. This was unexpected,

Table 4.8: The threefold molecules TMS, CCl_4 and CBr_4 are measured in $CDCl_3/CHCl_3$ (1:1) for 5.2 wt% PBLG. Additionally, the signal of DMSO-d_6 in the inner tube is measured. Spectra were measured under static and spinning conditions.

substance	static [ppm]	spinning [ppm]	difference [ppb]
CBr_4	-29.7098	-29.7145	-4.7
TMS	0.0000	-0.0093	-9.3
DMSO-d_6	40.4489	40.4511	2.2
$CHCl_3$	77.1591	77.1591	0.0
$CDCl_3$	76.9573	76.9573	0.0
CCl_4	96.0679	96.0541	-13.8

because DMSO-d_6 is not affected by PBLG, and should not show any chemical shift difference. In view of the shown results, the solvent signals would be a better reference than TMS for an RCSA. Even CBr_4 would be better with its smaller shift difference compared to TMS. More experiments were acquired, but unfortunately due to experimental problems, they did not yield the same results. Repetition was not yet possible due to time constraints.

The chemical shift difference of the silicon in the ^{29}Si spectra was -1 ppb (≈ -0.08 Hz at 79.5 MHz ^{29}Si frequency). It might be an RCSA or it might be due to some minimal change in the spectrometer or magnet. Similar to the carbon spectra, these measurements need to be repeated.

Lastly, in the coupled ^{13}C spectra the C-D and C-H couplings of $CDCl_3$ and $CHCl_3$ could be determined. Both static spectra showed a C-D coupling of 31.8 Hz and a C-H coupling of 209.3 Hz and during rotation the C-D coupling decreased to 30.1 Hz and the C-H coupling to 196.6 Hz.

4.3.3 Biphasic sample

During the dilution experiments on the biphasic area of PBLG, a thought arose as to how RDCs and RCSA are affected in this area. Does the solute molecule feel both phases simultaneously and averages the isotropic and anisotropic influences or is it possible to see the isotropic and anisotropic influences separately as two independent sets of signals in the spectra as Recchia et. al.[165] showed in 2020 for strychnine in PBLG. For this reason, the biphasic sample from Section 4.2.4 and 4.2.5 was prepared with strychnine as solute molecule and measured in a 600 MHz spectrometer with cryo-probe. First, a Q.E.COSY (Fig. 4.36) was acquired, showing the anisotropic and isotropic solvent peaks. The anisotropic multiplet shows the quadrupolar coupling of -199.8 Hz indicated by a left tilt. The isotropic multiplet shows no quadrupolar coupling and thus the antiphase peaks in the middle cancel each other, resulting in only four peaks. The C-D coupling is 37.8 Hz and the C-H coupling 32.3 Hz.

The proton 1D of the biphasic sample in comparison to an isotropic and anisotropic proton 1D do not show any sign of two different strychnine data sets (Fig. 4.37). The lines are broader than the possible RCSA for protons. At least, proton chemical shifts and some multiplets are still visible compared to the pure anisotropic spectrum at 10 wt%. The proton-decoupled carbon 1D, on the other hand, shows well resolved peaks. Compared to the isotropic spectrum without any PBLG, twice as many signals can be observed as shown in Figure 4.38. From the deuterium spectrum, it was known that the sample has a higher anisotropic proportion than isotropic, which is why the more intense peaks of each signal pair are the chemical shifts of strychnine under anisotropic conditions. This was later confirmed with CLIP- and CLAP-HSQCs. The chemical shifts of strychnine under isotropic and anisotropic conditions and the RCSA are given in Table 4.9. Judging from the ^{13}C 1Ds, five signals do not show any RCSA or at

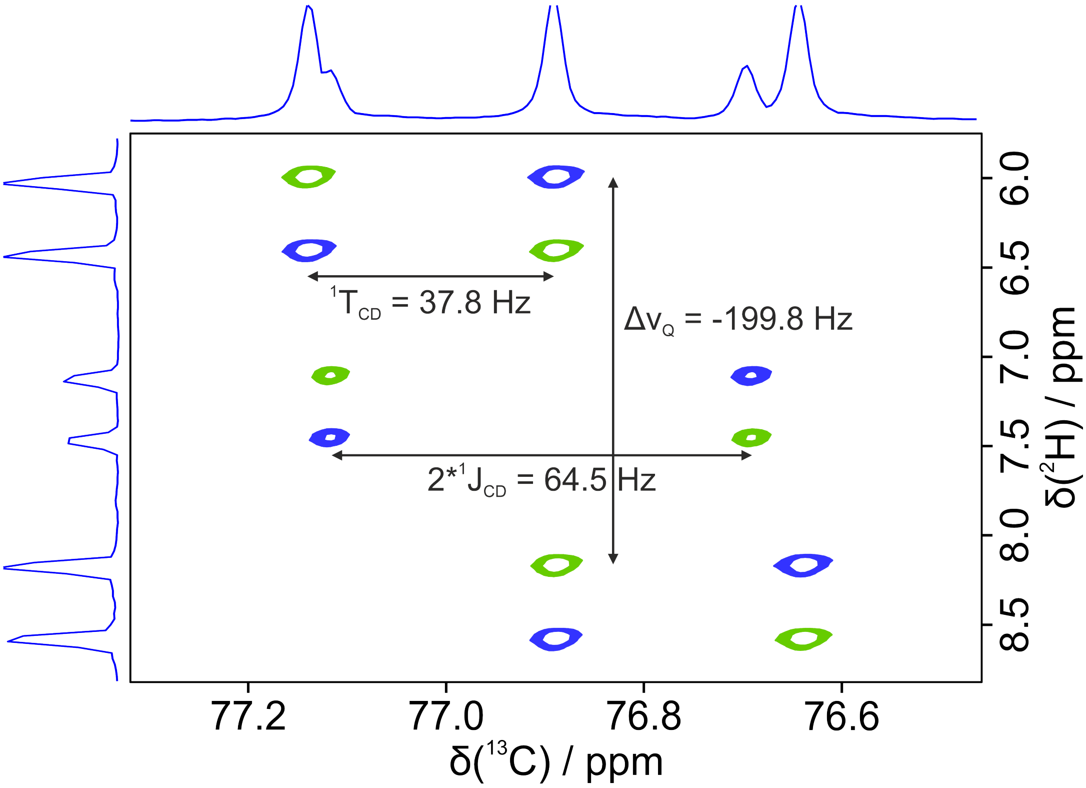

Figure 4.36: The Q.E.COSY of the biphasic sample is shown. The anisotropic part showed a quadrupolar coupling of -199.8 Hz, the isotropic part in the middle showed no quadrupolar coupling. The C-D coupling is 37.8 Hz and the C-H coupling 32.3 Hz.

least an RCSA which is smaller than the line width of 2-3 Hz. Three peaks belong to strychnine, the fourth is the TMS peak and the fifth the solvent $CDCl_3$. However, the Q.E.COSY shows a small RCSA for the solvent peaks of 15 ppb which corresponds to approximately 2.3 Hz for carbon at 150 MHz. This is smaller than the linewidth in the ^{13}C 1Ds, explaining missed out RCSA. It is unclear, if the other four signals also have an RCSA smaller than the linewidth. The peak of C12 at 77.5 ppm shows a small shoulder upon closer inspection. ^{13}C, ^1H 2Ds like the CLIP- and CLAP-HSQCs would be able to give an answer.

At first, standard CLIP- and CLAP-HSQC spectra were acquired for strychnine. Unfortunately, the total couplings of strychnine showed a range between 30 and 245 Hz, which could not be measured with only a CLIP-HSQC spectrum due to the signal loss during the coherence transfer for couplings far away from the set *J*-coupling. Although the signal intensity is close to 100 % in a CLAP-HSQC for all couplings[146], a CLIP-HSQC was needed as the two sets of isotropic and anisotropic couplings in one spectrum reduced the overall signal intensity and many signals overlapped, which could only be resolved with the addition and subtraction of inphase and antiphase spectra. Instead of recording several different HSQCs, which takes a lot of time, the so called COB3-CLIP- and COB3-CLAP-HSQCs were acquired. COB stands for couplings, offsets, and B^1-field inhomogeneities, which is an insensitive nuclei enhanced by polarization transfer (INEPT) building block developed in our group[166]. It compensates for a wider range of couplings of around 120-250 Hz and the COB3-INEPT transfer element is an extension of the COB-INEPT element covering 120-750 Hz couplings, which was also developed in our group[167]. Although it is not optimized for couplings lower than 120 Hz, it gives still slightly higher signal intensity for these low couplings compared to the conventional CLIP- and CLAP-HSQCs. Additionally, the indirect carbon dimension was reduced to 30 ppm adjusted around the aromatic region for a better FID resolution. As the direct dimension still covered the full 10 ppm necessary for all proton

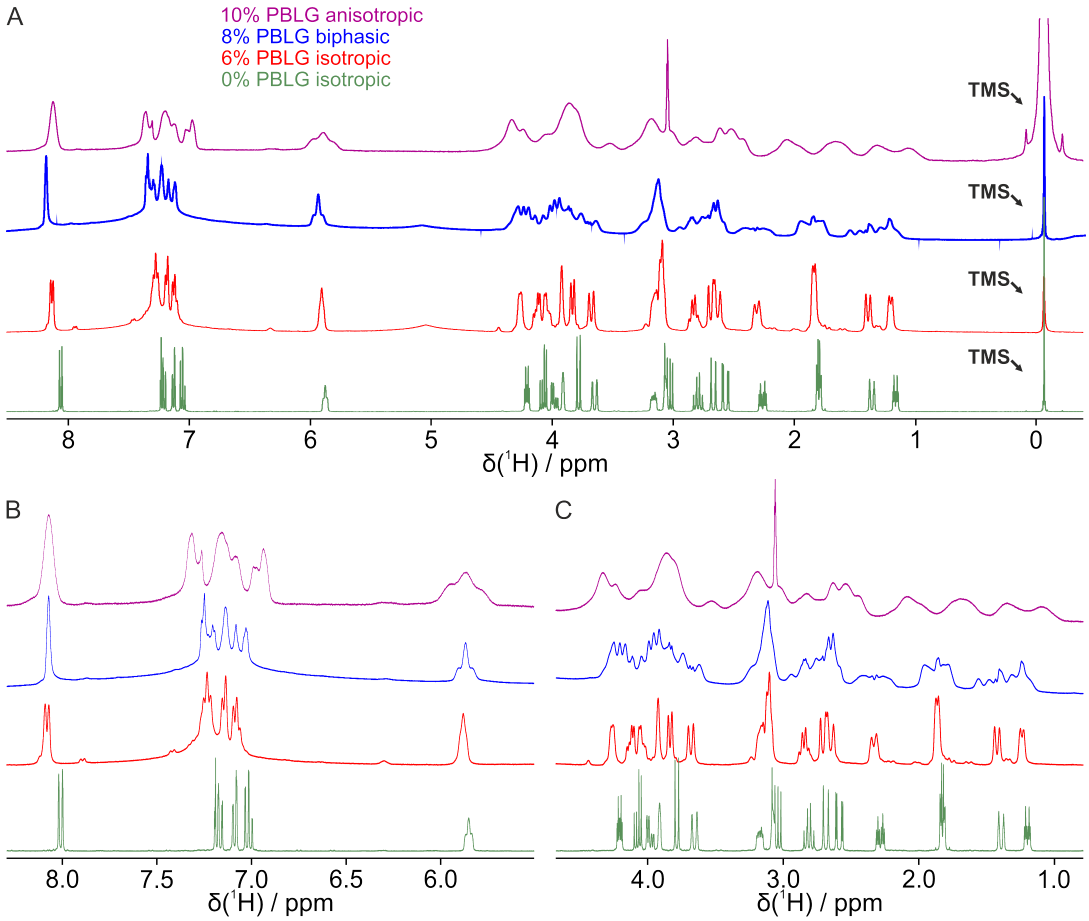

Figure 4.37: The ^{1}H 1Ds of strychnine at different PBLG concentrations in $CDCl_3$. The concentrations were 0 wt% (green), 6 wt% (red), 8 wt% (blue) and 10 wt% (violet). In A) the whole spectra are shown, in B) the aromatic region and in C) the aliphatic region. In the ^{1}H 1Ds it is impossible to tell if two sets of strychnine peaks were obtained.

signals, the non aromatic signals of strychnine were folded into the spectral range, as can be seen in Figure 4.39.

In the COB3-CLIP- and COB3-CLAP-HSQCs, 17 out of 22 total couplings could be obtained for the anisotropic data set and the total coupling of residual $CHCl_3$. The isotropic data set shows all possible $\mathcal{J}$-couplings including $CHCl_3$ and TMS (Tab. 4.10). Due to the broad anisotropic multiplets, the isotropic peaks have a higher intensity in this spectrum. As the carbon chemical shifts of the isotropic peaks have the same shifts as the smaller peaks in the ^{13}C 1D, the assignment of isotropic and anisotropic peaks was clear. All not determined anisotropic total couplings show peaks with either broad multiplets and low signal intensity or overlapped strongly with the isotropic $\mathcal{J}$-coupling. The only exception is TMS, which does not show any sign of a total coupling. As it does not show any sign of an RCSA either, the total coupling of TMS has to be equal to the $\mathcal{J}$-coupling within ± 1 Hz. The range of the total couplings for strychnine is between 30.3 Hz and 245.1 Hz, which results in RDCs ranging from -127.6 Hz up to 95.7 Hz for a quadrupolar splitting of $CDCl_3$ of 200 Hz. Compared to the RDCs under spinning conditions with 180 Hz quadrupolar splitting (Tab. 4.2), all but two RDCs show opposite signs as expected for a comparison between RDCs at static and spinning conditions. The two, which do not show the opposite sign, were estimated with errors of approximately 50% of their size. Compared to the RDCs from the Thiele group from the VASS measurements at 40.3° with 179 Hz quadrupolar splitting[14], all obtained RDCs in the biphasic sample show the same sign. Independent from the sign, all RDCs

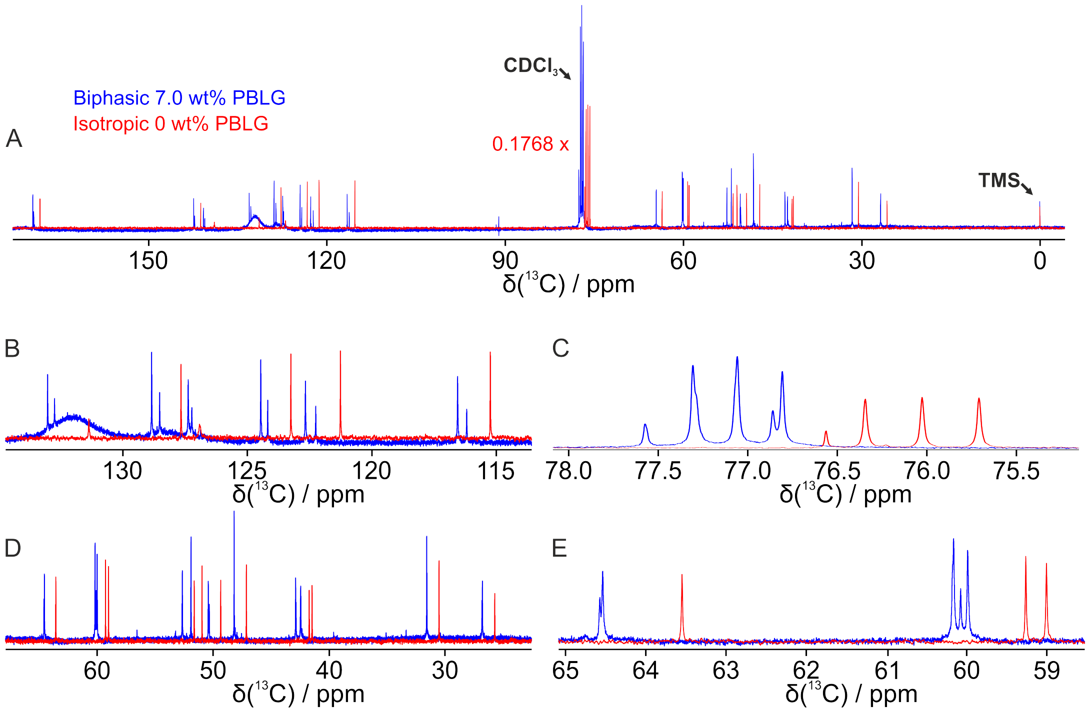

Figure 4.38: The ^{13}C 1Ds of strychnine without and with PBLG at a biphasic concentration in CDCl$_3$. In the biphasic sample (blue), strychnine showed twice as many peaks. In A) the entire spectra are shown, in B) the aromatic region, in C) the solvent peaks and C12 of strychnine, in D) the aliphatic region and in E) C8, C16 and C23 in more details.

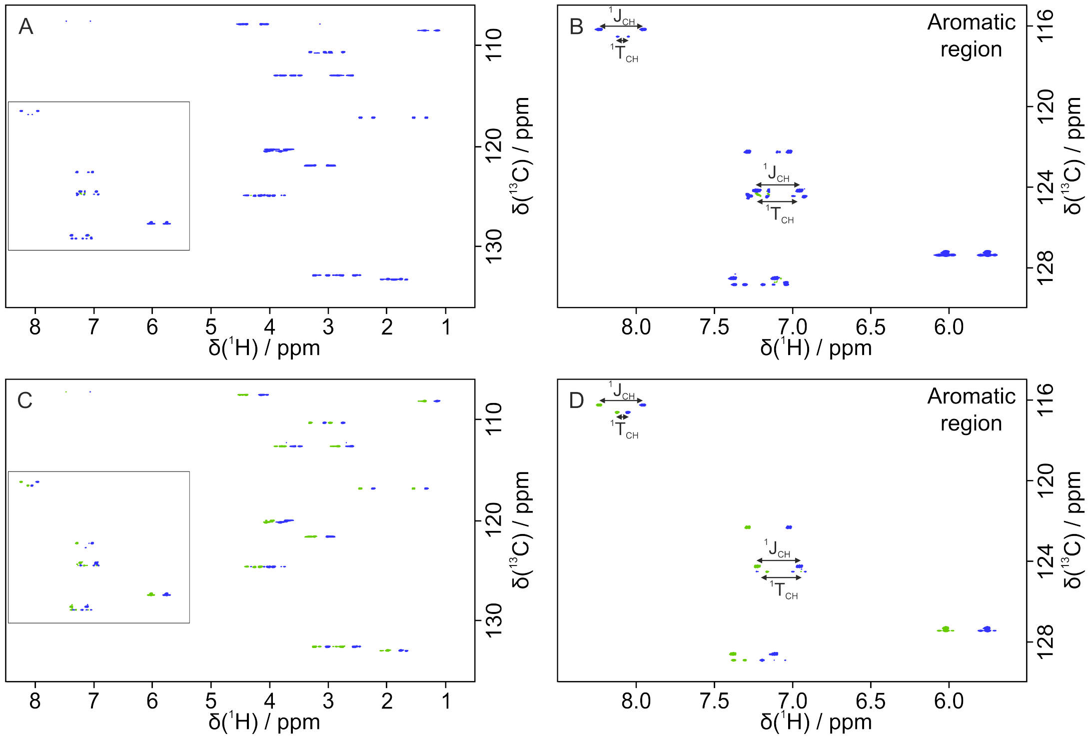

Figure 4.39: The COB3-CLIP- and COB3-CLAP-HSQC spectra folded in a ^{13}C range from 105-135 ppm of strychnine measured on a 600 MHz spectrometer are shown. In A) and C) the full 30 ppm range spectra of the CLIP (A) and CLAP (C) are shown and in B) and D) the aromatic regions, respectively.

Table 4.9: The RCSA of strychnine in the biphasic PBLG sample.

assignment	isotropic signal [ppm]	anisotropic signal [ppm]	RCSA [ppb]
1	122.254	122.668	414
2	124.183	124.463	280
3	128.525	128.846	321
4	116.190	116.555	365
5	142.192	142.371	179
6	132.746	133.025	279
7	51.910	51.890	-20
8	60.071	59.985	-86
10	169.272	169.437	165
11	42.460	42.435	-25
12*	77.565	77.574	9
13	48.200	48.200	0
14	31.557	31.574	17
15	26.812	26.772	-40
16	60.170	60.159	-11
17	42.837	42.878	41
18	50.321	50.405	84
20	52.642	52.642	0
21	140.501	140.724	223
22	127.233	127.378	145
23	64.534	64.534	-36
$CDCl_3$*2	77.074	77.059	15
TMS	0.000	0.000	0

* determined with HETCOR experiment

*2 determined with Q.E.COSY experiment

show roughly the same size for the three compared data sets. The Pearson's correlation factor between the biphasic sample and the Thiele group is R = 0.999 (Fig. 4.40). Like the other samples before, the RDCs are compared with backcalculated RDCs from PALES, which resulted in a Pearson's factor of R = 0.965 and a Saupe Q value of 0.183 (see the appendix for the PALES file 6.2.5). Therefore, it was possible to obtain a nearly full set of RDCs in the biphasic sample, where the isotropic J-couplings originated from the same sample without changing the experimental conditions.

However, some signals of the biphasic sample show a very small RCSA that could not be resolved with the used CLIP-HSQCs using a COB3 INEPT transfer element. The total couplings and J-couplings overlap too strongly and the resolution in the indirect carbon dimension was not good enough. Recently, Yannik T. Woordes from our group, developed a carbon detected heteronuclear correlation (HETCOR) experiment further, where he adjusted BIRD filters with a COB-BIRD^r element. During this sequence, all but geminal ^{1}H-^{1}H couplings are decoupled over the indirect dimension, while $^1J_{CH}$-couplings are allowed to evolve[168]. This experiment was used for better resolution in the carbon dimension as shown in Figure 4.41. A resolution of 1.4 Hz in the direct carbon dimension was achieved, with all but three carbon signals (2 from strychnine and TMS) separated. The two signals from strychnine show a possible RCSA of less than 1.5 Hz, but the multiplet structure of the anisotropic signal and the small

Table 4.10: The RDCs of strychnine in the biphasic PBLG sample in a 14.1 T magnet compared with the RDCs under spinning conditions from Fig 4.26 at 180 Hz quadrupolar splitting of $CDCl_3$.

assignment	J_{CH} **[Hz]**	T_{CH} **[Hz]**	D_{CH} **[Hz]**	**Tab. 4.2**, $\Delta\nu_Q$ = 180 Hz [Hz]
C1-H1	157.91	30.32	-127.61 ± 2.22	98.53 ± 4.32
C2-H2	161.44	152.41	-9.03 ± 8.53	12.66 ± 4.04
C3-H3	159.53	111.50	-48.03 ± 1.97	36.54 ± 3.00
C4-H4	168.82	41.62	-127.20 ± 0.87	120.05 ± 2.09
C8-H8	144.78	193.90	49.12 ± 14.11	23.22 ± 12.68
C11-H11a	126.29	206.11	79.82 ± 3.29	-60.64 ± 6.84
C11-H11b	135.00	81.59	-53.41 ± 5.48	40.17 ± 6.84
C12-H12	149.39	245.12	95.73 ± 0.03	-71.21 ± 3.93
C13-H13	125.14	n.d.	n.d.	16.39 ± 5.79
C14-H14	131.73	226.83	95.10 ± 4.79	-62.75 ± 1.33
C15-H15a	131.17	n.d.	n.d.	45.72 ± 5.57
C15-H15b	130.08	120.79	-9.29 ± 4.11	4.87 ± 9.74
C16-H16*	147.20	122.20	-25.00 ± 21.65	n.d.
C17-H17a	133.22	124.51	-8.69 ± 1.47	5.89 ± 2.83
C17-H17b	133.22	124.51	-8.69 ± 1.47	5.89 ± 2.83
C18-H18a	147.38	139.02	-8.36 ± 7.41	-6.74 ± 3.04
C18-H18b	131.01	96.50	-34.49 ± 4.81	26.45 ± 4.05
C20-H20a	138.48	161.12	22.64 ± 2.53	-24.94 ± 18.24
C20-H20b	139.27	164.81	25.64 ± 3.52	-23.00 ± 3.14
C22-H22	158.82	160.22	1.40 ± 0.03	-1.93 ± 0.82
C23-H23a	146.57	n.d.	n.d.	n.d.
C23-H23b	136.53	n.d.	n.d.	n.d.
$CHCl_3$	209.40	246.60	37.20 ± 0.03	n.d.
TMS	118.31	118.31	0.0 ± 1.00	n.d.

n.d. = not determined

* determined with HETCOR experiment

RDCs made it impossible to verify this as RCSA. TMS shows no evidence of an RCSA or RDCs in the HETCOR experiment. Nevertheless, an additional RCSA value compared to the ^{13}C 1D and a RDC value for compared to the COB3-CLIP- and CLAP-HSQC could be determined (marked with an asterisk in the Tables 4.9 and 4.10). For C12, which shows a shoulder in the 1D spectrum, an RCSA of 9 ppb (≈ 1.4 Hz) could be determined. This is less then the linewidth in the ^{13}C 1D and exactly the resolution of the HETCOR experiment. The additional RDC for C16 has an error of ≈ 20 Hz, due to low signal intensity of the anisotropic coupling and overlap with the isotropic signal. With its RCSA of 11 ppb, it is at the edge of the resolution. At least, the overlap is slightly less than in the COB3-CLIP- and COB3-CLAP-HSQCs and the RDC could be determined. A disadvantage of the HETCOR experiment is the poor signal intensity for natural abundance measurements of ^{13}C. Improvements in signal intensity for this sequence might follow in the future as I was told by personal communication.

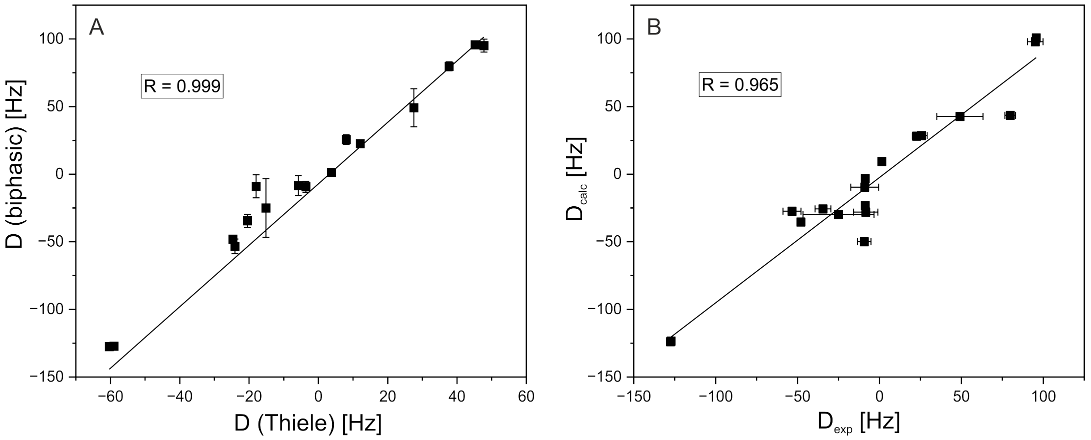

Figure 4.40: The obtained RDCs from the biphasic sample are compared with RDCs measured by the Thiele group at a similar quadrupolar splitting of CDCl₃ (A) and with backcalculated RDCs from PALES (B). The Pearson's R factor for both correlations is shown in the spectra.

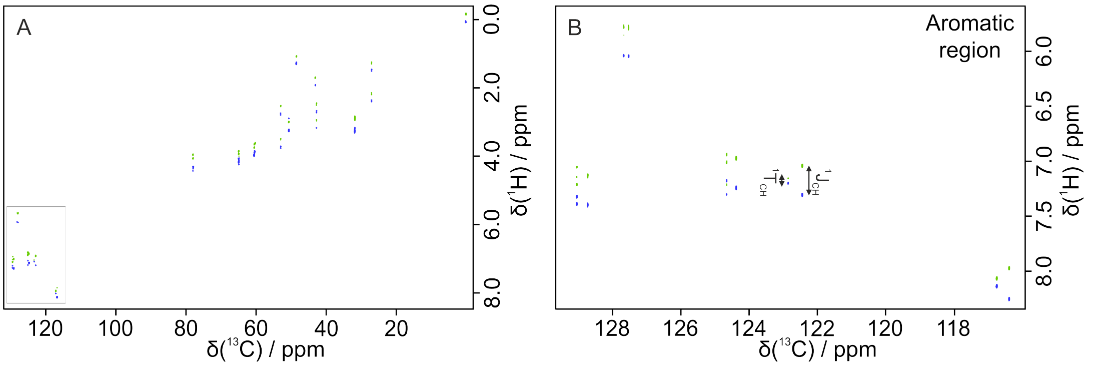

Figure 4.41: The biphasic sample was measured with a ^{13}C-detected ^{1}H decoupled INEPT-type sequence using a COB-BIRD^{r} element for ^{1}H-^{1}H decoupling over the indirect dimension, while $^{1}J_{CH}$-couplings were allowed to evolve.

None of the spectra of the biphasic sample show any sign of an RCSA or RDCs for TMS. As the linewidths is about 1.5 Hz, the possible RCSA has to be smaller than 1 Hz. From my knowledge, this was the very first time, TMS could be measured isotropically and anisotropically without any change in susceptibility changes or other influences.

Nevertheless, the biphasic sample confirms the assumption that TMS represents a reference that changes less than 5 ppb per 100 Hz quadrupolar splitting $\Delta\nu_Q$ for PBLG in CDCl₃. This result may be used to intrinsically reference other partially aligned samples with the same alignment medium. Additionally, it was possible to determine the RCSA of a solute molecule without the need of a reference as the isotropic and anisotropic chemical shifts are simultaneously present in one sample unaffected by the environment similar to the findings of Recchia et. al.[165]. The situation seems to be the same as for alignment in a gel-compression device[169], but the compression device physically separates isotropic and anisotropic phase[170], leading to enormous RCSA values. The microheterogeneous biphasic PBLG in CDCl₃, instead, leads to identical bulk susceptibilities and corresponding errors are minimized. For the measurement of RDCs, on the other hand, the total couplings and *J*-couplings are overlapping often in the experiments used, particularly when RCSA is so small that signals cannot be distinguished. As these couplings are less affected by susceptibility changes, two separate isotropic and anisotropic spectra as with the experiments reported in Section 4.3.1.1 are the better choice.

4.4 Viscosity measurements

The rheo-device used in this work had a large gap size and the 3 mm NMR tube in the center, which sheared the sample inside the 5 mm tube, did not rotate concentrically. Furthermore, there were no transducers attached so that no rheological parameters such as viscosity could be measured with this device. Since the literature on PBLG only contains rheological data with m-cresol instead of $CDCl_3$, viscosity measurements with $CDCl_3$ were carried out on an ARES-G2 shear rheometer in the group of Prof. Dr. M. Wilhelm at the Institute of Technical Chemistry and Polymeric Chemistry at KIT.

Two samples, one with 4 wt% and one with 8.5 wt% PBLG, were prepared for these measurements. These concentrations were chosen as they were close to the biphasic transitions region, with one sample being isotropic and the other anisotropic. The measurements were repeated several times for both samples and the results were consistent for all measurements. Due to the small sample volume and strong evaporation, the number of points for the measurements was reduced. For all but the first test measurements, only six data points between 30 and 300 s^{-1} were acquired. Figure 4.42 shows the obtained viscosity data. As the viscosity measurements are always displayed logarithmically in the literature, the same was done here. As expected, the viscosity of PBLG showed the same shear-thinning behavior in m-cresol with a higher viscosity for isotropic solutions than for anisotropic solutions (see 2.15). In only two measurements, the viscosity at 300 s^{-1} was slightly above 1 Pas. In all other measurements, the viscosity was already below 1 Pas, and always around ten times lower than at 30 s^{-1}. The shear plateau from region II could not be determined in these measurements. However, a bend around a shear rate of 10 s^{-1} and a viscosity of 8 Pas could be seen in the plot in Figure 4.42, which would agree with the plateau regions in the literature[3,109]. The shear thinning between 0.01 and 5 s^{-1} as well as the very high viscosity values in this area are most likely artifacts due to the fast and not optimal sample loading, which was required for $CDCl_3$. Although it looks similar to region I shear-thinning, this region is normally not found for PBLG concentrations of less than 30 wt%. Therefore, it is very unlikely that this is region I shear-thinning.

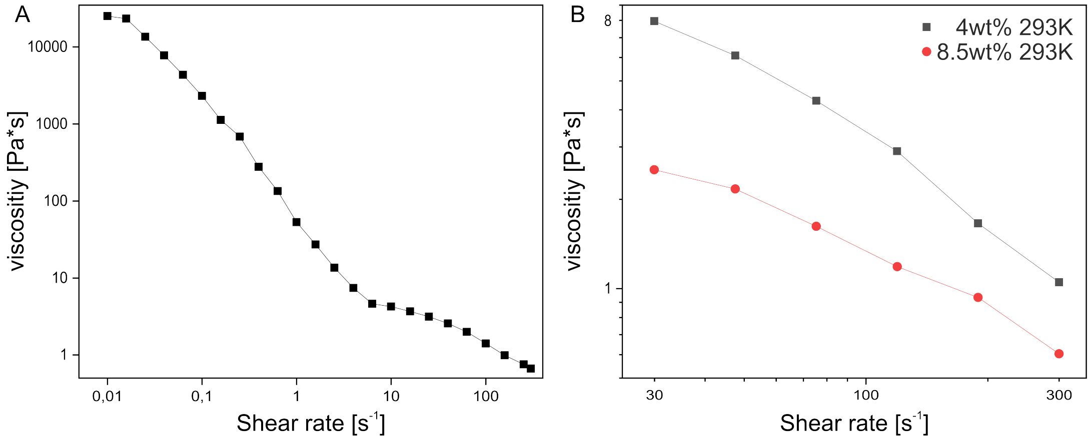

Figure 4.42: A) The first measurement in the ARES rheometer of the 8.5 wt% PBLG sample was acquired between 0.01 and 300 s^{-1} for test purposes. B) As $CDCl_3$ is evaporating very fast, the number of points for the measurements were reduced to six points in a range of 30 - 300 s^{-1}. Two measurements at concentrations of 4 wt% (black) and 8.5 wt% (red) are compared at 293 K.

The measurements at the ARES rheometer showed that at shear rates higher than 10 s^{-1} the behavior was similar to the one with m-cresol in the literature. Therefore, the overall behavior of PBLG in m-cresol can be transferred to PBLG in chloroform, which is in agreement with the obtained data on the alignment director. As the focus of this work was on the alignment director and its value for NMR, more precise rheological data were not necessary as it has no added value.

4.5 Other liquid crystals

Although PBLG is one of the most investigated LC in rheology, a change of the alignment director could be observed for many other LCs as well[79,81,82,86,115,171]. In the beginning of this work, several other LCs and two polymeric amino acids were tested. The two polymeric amino acids (poly-L-lysine and poly-L-glutamine) are known to exhibit α-helical order under certain conditions. It was tested whether anisotropy could be induced by shear flow similar to PBLG under the critical concentration. However, this was not achieved. All samples tested under different conditions never showed any alignment. Similar, the known LC graphene oxide (GO)[172] was tested without success. The sample used was probably too old as no alignment was visible under static conditions. Measurements with DNA showed an alignment under static conditions with quadrupolar splittings of 40-70 Hz depending on the temperature, but the highest shear rates of 896.6 s^{-1} changed the quadrupolar splitting of D_2O only by 2-3 Hz under all conditions. The same was observed for the ACN-d_3 signal, which showed a quadrupolar splitting of 80-100 Hz during the experiments.

The only other LC tested that showed static alignment and a change in the director due to shear were the Pf1 phages, as the following section will show.

4.5.1 PF1 phages

The filamentous bacteriophage Pf1 from *Pseudomonas aeruginosa* is a well known water-based LC crystal[142,144]. The induced alignment is tunable already at low concentrations. Two samples at a concentration of 10 mg/ml were tested during this work[148]. The first one contained only D_2O as deuterated solvent and showed a static quadrupolar splitting of 6.4 Hz. During rotation, it showed a splitting of 1.1 Hz at a shear rate of 896.6 s^{-1} and a splitting of 1.7 Hz at a shear rate of 408.4 s^{-1}. The second sample also contained 10 % ACN-d_3. The quadrupolar splitting of the D_2O signal was again 6.4 Hz and the quadrupolar splitting of ACN-d_3 was 9.4 Hz. At shear rates of 896.6 s^{-1}, they showed quadrupolar splittings of 1.4 Hz and 2.5 Hz, respectively. Although most of the kinetic experiments with different temperatures and shear rates were performed on the first sample without ACN-d_3, the linewidth of the D_2O signal was mostly broader than the splitting and in more than 80 % of the spectra only a broad peak without splitting could be detected. For this reason, ACN-d_3 was added to the second sample. Figure 4.43 shows the deuterium 1Ds under static and spinning conditions, Figure 4.44 shows the corresponding Q.E.COSY of the ACN-d_3 signal.

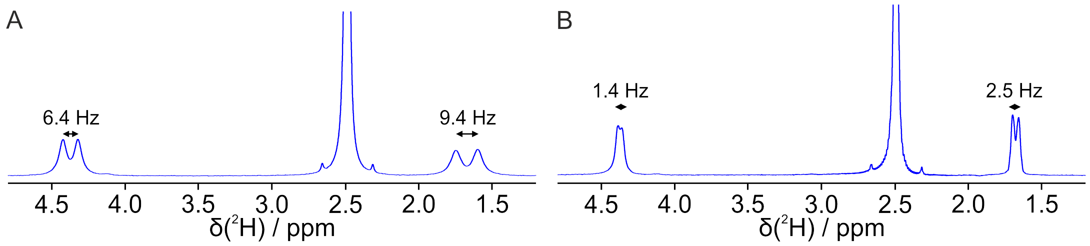

Figure 4.43: The 1D ^2H spectra of pf1 phage in D_2O/ACN-d_3 (9:1) are shown under static conditions (A) and under rotation with a shear rate of 896.6 s^{-1} (B). The signal in the center (2.5 ppm) is the isotropic DMSO-d_6 signal from the inner NMR tube, the left signal (4.5 pp) is D_2O and the right signal (1.7 ppm) is ACN-d_3[148].

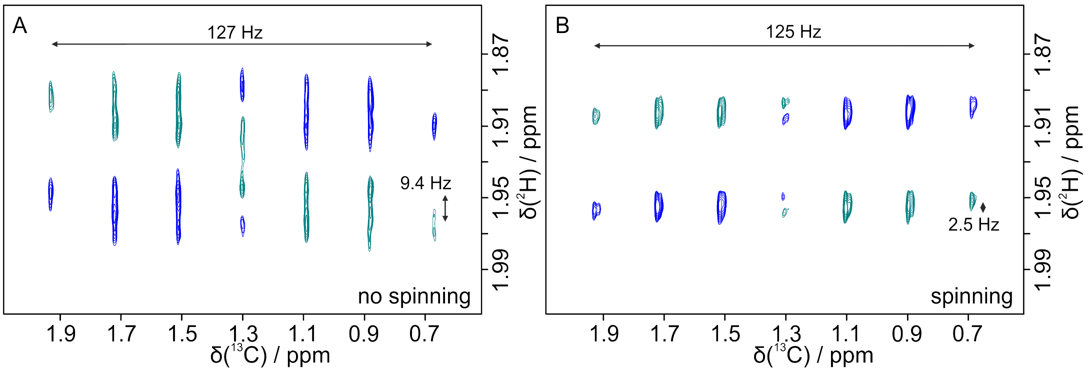

Figure 4.44: The Q.E.COSY of Pf1 phage in D_2O/ACN-d_3 (9:1) are shown under static conditions (A) and under rotation with a shear rate of 896.6 s^{-1} (B). The sign change due to shearing can be observed for the ACN-d_3 signal and the quadrupolar splitting of 9.4 Hz is reduced to 2.5 Hz. Additionally, the C-D coupling reduces only slightly from 21.2 Hz to 20.8 Hz (or from 127 Hz to 125 Hz measured as the total distance of all seven signals)[148].

The kinetic studies of the deuterium 1Ds (Fig. 4.45) showed similar results as the one from PBLG in Section 4.1.3 for the relaxation of director angle back to 0°. However, the switching time from 0° in the shear-plane could not be determined. For both samples, all experiments trying to determine the switching time into the shear-plane resulted in broad lines without any splitting. Up to 500 s were tested for the first sample and 20 s for the second sample. Without the rotation by explicit pulse programming and rotating at constant speed with the waveform generator, a splitting under sheared conditions could be seen within 1-2 s. Also the 10 s rotating delay d_r in the relaxation experiment was enough for a visible splitting under rotation. The linewidth was about twice as high in the experiments in which the rotation was started before acquisition compared to the relaxation experiments and compared to the rotation with the waveform generator. No conclusive explanation can be given here to this reproducible effect, which most probably is caused by the pulse sequence used for this switching time.

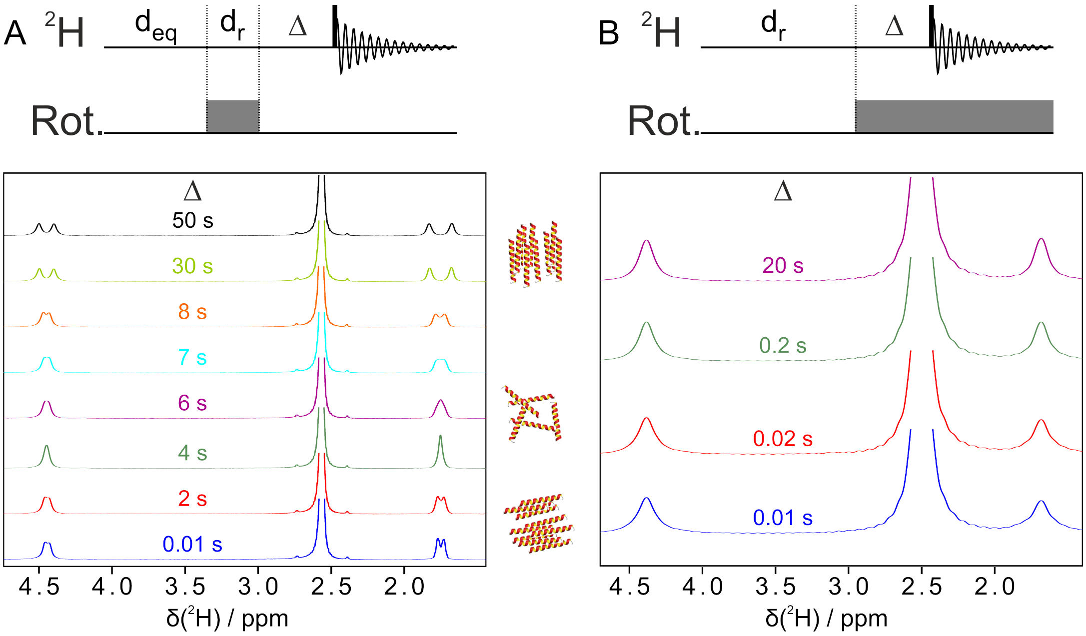

Figure 4.45: The 1D ^2H spectra of pf1 phage in D_2O/ACN-d_3 (9:1) are shown for switching from rotation to no rotation (A) and vice versa (B). The signal in the center (2.5 ppm) is the isotropic DMSO-d_6 signal from the inner NMR tube, the left signal (4.5 pp) is D_2O and the right signal (1.7 ppm) is ACN-d_3. The delays were set to d_{eq} = 500 s, d_r = 10 s for (A) and d_r to 600 s in (B).

The Pf1 phage relaxed back to parallel orientation to the magnetic field faster than PBLG. For the D_2O signal, the splitting was so small that hardly any splitting could be observed in the first two seconds. The ACN-d_3 signal showed the larger splitting by approximately the same linewidth as the D_2O signal. The splitting of the ACN-d_3 signal increased in the first second from 2.5 to 3.4 Hz and decreased to zero after three seconds. The increase of the splitting could not be explained as the experiments under constant rotation showed only a splitting of 2.5 Hz. The rotation may have created a concentration gradient for a short time interval. Nevertheless, the zero splitting persisted about three seconds until a splitting of 2.3 Hz was seen again after seven seconds. This splitting increased for 30 s, and after 50 s there was no more change. After a few hundred seconds, the signal quality decreased which was not observed for the first sample. The sample was inhomogeneous after the long delays, but careful centrifugation homogenized the sample again. Even after prolonged rotation by the waveform generator, an inhomogeneity could be observed that did not require external centrifugation, but only a few hours of rest until the original quadrupolar splitting could be observed again. As the Pf1 phage is a biological substance, the shear rates and rotation speeds could be too high and the addition of acetonitrile could accelerate the inhomogenization.

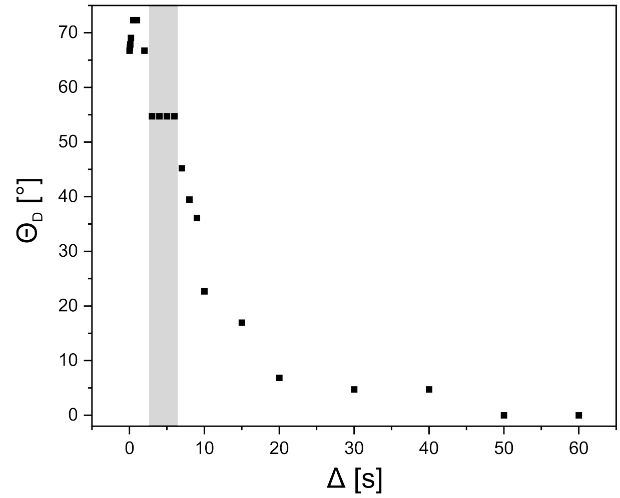

Figure 4.46: The angular distribution of Θ_D for the Pf1 phage from the shear-plane back parallel to the magnetic field. In the grey shaded area, the quadrupolar splitting was zero and the tilt angle at the magic angle (54.7°) indicating the sign change of the quadrupolar splitting. No evaluable data could be obtained for the switching time parallel to the magnetic field into the shear-plane.

The director angle Θ_D was close to 0° after 20 s (Fig.4.46), but needed 50 s until it was fully parallel to the magnetic field. It seemed as if the director stayed around the magic angle for about 4 s. The linewidth changed from 2.1 Hz to 4.0 Hz during these four seconds, which was probably broader than the observable splitting. Nevertheless, the Pf1 phage offers a water-based LC for measurements under sheared alignment conditions and the relaxation time is faster than for PBLG. The stability for RDCs and RCSA measurements need to be tested in the future, but as a master thesis in New Zealand showed[141], it is possible. In the rheo-device used in this work, the shear rates should probably be reduced and the concentration possibly increased to 20 mg/ml to achieve better splitting of the D_2O signal under shear.

Since PBLG has a higher alignment strength and showed larger differences between static and sheared alignment, PBLG was chosen after testing different alignment media. Furthermore, of the alignment media tested, isotropic concentrations could only be changed to anisotropy for PBLG.

5 Summary

In this work, the alignment properties of PBLG in $CDCl_3$ were investigated using a homemade rheo-NMR device that fits into almost any standard-bore NMR spectrometer. A 3 mm NMR tube, controlled by a motor, rotates the sample inside a 5 mm NMR tube. The motor is controllable either by an external waveform generator or by the spectrometer itself through explicit pulse programming. In the course of this work, the rheo-device was further optimized. Not only the known anisotropic phase above the critical concentration was the subject of this study, but also the isotropic phase below the critical concentration and the biphasic region at the phase transition were investigated.

For the LC phase it has been shown that the shear force of the rheo-device reduces the quadrupolar splitting of the solvent $CDCl_3$ by almost 50 %(Sec. 4.1). The Q.E.COSY experiment unambiguously has confirmed a sign change of the quadrupolar splitting and the possible angles of the director in this work were between 75° and 90° under shear.

Above the critical concentration, the static and shear-induced splitting decreased linearly with decreasing concentration (Sec. 4.1.1). In the transition region to isotropic concentrations, the static and shear-induced splitting remained approximately constant over the entire region and only relative intensities of isotropic and anisotropic subphases changed. For lower concentrations, the isotropic PBLG no longer showed any quadrupolar splitting. However, it could be shown that the shear forces exerted by our device were strong enough to induce flow-aligning anisotropy in the sample and quadrupolar splitting was observed in otherwise isotropic concentration ranges. The quadrupolar splitting under shear decreased approximately exponentially upon lowering the concentrations to 1 wt%, where quadrupolar splittings of 2-4 Hz were observed. The director angle and quadrupolar splitting also depend on shear rate and temperature, with little difference at the relatively high shear rates used in this work (Sec. 4.1.2). The temperature, on the other hand, shows larger effects. In addition to decreased quadrupolar splittings at higher temperatures, the linewidth of the signals increased strongly at higher temperatures, indicating a wide range of differently aligned solvent molecules.

Kinetic studies with self-written pulse programs using explicit pulse programming showed that the alignment director above the critical concentration requires up to 500 s in a 9.4 T magnet in order to (re-)orient parallel to the magnetic field (Sec. 4.1.3). Nevertheless, the high shear rates in this work were able to completely change the angle of the director nearly perpendicular to the magnetic field in less than 200 ms. Similar kinetics were achieved for biphasic concentrations. Concentrations, which are isotropic under static conditions, still showed the same switching time of 100-200 ms perpendicular to the magnetic field, but the isotropic state after relaxation was reached in less than 20 s.

The transition of PBLG from isotropic to anisotropic takes place within a 0.5-1 wt% wide range in which both phases coexist (Sec. 4.2). The exact range depends on the molecular weight and persistence length of PBLG, the sample temperature, and the solute molecule. A higher persistence length and molecular weight of PBLG and a decrease in sample temperature increase the anisotropic behavior. With this increased anisotropic behavior, the transition region is shifted to lower concentration ranges. The influence of the solute molecule on the transition occurs through molecular interactions (Sec. 4.2.3). Hydrogen bond donors such as borneol interact tightly with PBLG and reduce the interhelical interaction strength of PBLG and thus its anisotropic character. On the other hand, hydrogen acceptors such as camphor do not interact with PBLG but with the solvent molecules in the sample, which reduces the number of available solvent molecules for PBLG, increasing its anisotropic character. Therefore, it seems that the transition region for solute molecules acting as hydrogen donors shifts to lower concentration ranges and for solute molecules acting as hydrogen acceptors to higher concentration ranges. These results, however, need to be verified by a larger number of molecules.

The equilibration time alignment at the phase transition region strongly depends on the amount of isotropic and anisotropic subphases (Sec. 4.2.2). At the edge of the transition region, where mainly one of the phases is present, the time is almost equal to the time in the purely anisotropic phase. However, the more evenly both phases are distributed, the longer it takes for the alignment to be fully established. It goes so far that with equal proportions of isotropic and anisotropic phases, the alignment in a 14.1 T magnet takes several hours instead of 10 inutes for a purely anisotropic phase.

The isotropic and anisotropic phases are homogeneously distributed along the z-axis. In the x,y-plane (Sec. 4.2.4), the isotropic phase is more likely to be found in the center of the sample and the anisotropic phase at the walls of the NMR tube. Over time, both phases begin to separate (Sec. 4.2.5). Due to the high density of the solvent $CDCl_3$, the isotropic phase was located at the bottom of the NMR tube underneath the anisotropic phase. In this work, the separation process began after 3-4 days and was mostly finished after 8 days. After 7 weeks, the 2D deuterium image showed a clearly visible separation along the z-direction.

The main purpose of using the LC PBLG in the rheo-device was its use as an alignment medium for small molecule NMR (Sec. 4.3). The influence of shear force on residual parameters (RDCs, RCSA) was demonstrated using the example of strychnine, which has been widely used in the literature and for which severe problems in data extraction due to too strong alignment with PBLG are well documented[159] (Sec. 4.3.1.1). Similar to the quadrupolar couplings, the dipolar couplings and the chemical shift anisotropy during shear are reduced by approximately -0.5 due to the director angle being nearly perpendicular to the magnetic field. This scalability strongly influences the signal width of the $^1J_{CH}$ couplings in the HSQC spectra. The proton multiplet width decreases and the signal intensity significantly increases. Signals that are almost undetectable under static conditions suddenly become detectable by simply shearing the sample. Instead of measuring a sample above the critical concentration, which induces strong partial alignment, the sample could now be measured at concentrations below the critical concentration, where the shear induced lower partial alignment and the multiplet widths were reduced even more. The measurement time could be reduced to a third and the signal intensity was still higher compared to samples above the critical concentration.

Shear-induced alignment offers a new way measuring RCSA. RCSA generally requires a comparison of chemical shift once measured under isotropic and once under anisotropic conditions. Contrary to conventional RCSA, measurements above the phase transition of PBLG and shear-induced alignment of concentrations below the phase transition allows to acquire these two data sets under exactly the same (chemical) conditions, once under static conditions and once under sheared (Sec.4.3.2). The obtained RCSAs at different concentrations were scalable. TMS was used as internal reference for each spectrum. Since published data on RDCs and RCSA of TMS have been determined[51,52], TMS was measured in the presence of two other tetrahedral molecules (CCl_4 and CBr_4)(Sec. 4.3.2.1). The goal was to determine the RCSA for these three molecules together with the RCSA of $CDCl_3$ and $CHCl_3$. All RCSAs were less than 15 ppb, but for more precise results, the experiments need to be repeated.

The comparison of NMR spectra of PBLG samples under static and rheological conditions allows to measure RDCs and chemical shift changes due to different alignments withing a single sample, but the biphasic sample offers another striking possibility to measure RDCs and RCSA (Sec. 4.3.3). In a static biphasic sample, two sets of peaks of the solute molecule are obtained. These correspond to an isotropic and an anisotropic set, leading to ${}^{1}J_{CH}$ couplings and ${}^{1}T_{CH}$ couplings, where RDCs can be obtained in the same sample without changing the alignment director. Both sets of peaks also show different chemical shifts in most cases clearly indicating the possibility to measure RCSA under fully identical bulk susceptibility. This makes complicated fitting procedures obsolete and enhances significantly the reliability of structural parameters. For TMS, on the other hand, it could be clearly shown that its RCSA is smaller than 1 Hz and only leads to a small error compared to the shear induced RCSA when TMS is taken as a reference.

In conclusion, this work characterized the biphasic transition region of PBLG by NMR and PBLG in $CDCl_3$ in a homemade rheo-NMR device. Furthermore, this work demonstrates the potential of LCs in rheo-NMR for structure determination using RDCs and RCSA. By reducing the amount of PBLG and still inducing anisotropy in isotropic PBLG samples under static conditions, rheo-NMR significantly improves the spectral quality and is a more cost effective method for changing the director angle compared to VASS. Furthermore, the low concentrations of PBLG enable adjustable alignment strengths under shear, where even 2-4 Hz quadrupolar splittings can be achieved, and are thus competitive with the elaborately produced stretched polymer gels.

Acronyms

ACN acetonitrile

$CDCl_3$ deuterochloroform

$CHCl_3$ chloroform

CLAP clean antiphase

CLIP clean inphase

CSI chemical shift imaging

DBA deuterated benzyl alcohol

DMF dimetyhlformamide

DMSO dimethlysulfoxid

EDTA ethylenediaminetetraacetic acid

FID free-induction decay

FLASH fast low angle shot

FWHM full width at half-maximum

GO graphene oxide

HETCOR heteronuclear correlation

HSQC heteronuclear single quantum coherence

INEPT insensitive nuclei enhanced by polarization transfer

LC liquid crystal

MRI magnetic resonance imaging

NMR nuclear magnetic resonance

NOE nuclear Overhauser enhancement

PBDG poly-γ-benzyl-D-glutamate

PBLG poly-γ-benzyl-L-glutamate

PDMS poly(dimethylsiloxane)

PEEK polyether ether ketone

PEG polyethylenglycol

PGSE pulsed gradient spin echo

PIB poly(isobutylene)

ppm parts per million

PWM pulse-width-modulated

RCSA residual chemical shift anisotropy

RDCs residual dipolar couplings

RQCs residual quadrupolar couplings

SVD singular value decomposition

TCU temperature control unit

TFA trifluoroacetic acid

THF tetrahydrofuran

TMS tetramethylsilane

Tris tris(hydroxylmethyl)aminomethane

TTL transistor-transistor logic

VASS variable-angle sample spinning

List of Figures

List of Tables

Bibliography

(1) Hanby, W. E.; Waley, S. G.; Watson, J. 632. Synthetic Polypeptides. Part II. Polyglutamic Acid. *J. Chem. Soc.* **1950**, 3239.

(2) Ambrose, E. J.; Elliott, A. The Structure of Synthetic Polypeptides. II. Investigation with Polarized Infra-Red Spectroscopy. *Proc. R. Soc. Lond. A* **1951**, *205*, 47–60.

(3) Kiss, G.; Porter, R. S. Rheology of Concentrated Solutions of Poly(γ-Benzyl-Glutamate). *J. Polym. Sci. Polym. Symp.* **1978**, *65*, 193–211.

(4) Baek, S.-G.; Magda, J. J.; Larson, R. G. Rheological Differences among Liquid-crystalline Polymers. I. The First and Second Normal Stress Differences of PBG Solutions. *J. Rheol.* **1993**, *37*, 1201–1224.

(5) Walker, L. M.; Mortier, M.; Moldenaers, P. Concentration Effects on the Rheology and Texture of PBG/m–Cresol Solutions. *J. Rheol.* **1996**, *40*, 967–981.

(6) Hongladarom, K.; Burghardt, W. R. Molecular Alignment of Polymer Liquid Crystals in Shear Flows. 2. Transient Flow Behavior in Poly(Benzyl Glutamate) Solutions. *Macromolecules* **1993**, *26*, 785–794.

(7) Samulski, E. T.; and Tobolsky, A. V. The Liquid Crystal Phase of Poly-γ-benzyl-L-glutamate in Solution and in the Solid State. *Mol. Cryst.* **1969**, *7*, 433–442.

(8) Samulski, E. T.; Tobolsky, A. V. Distorted α-Helix for Poly (γ-Benzyl L-glutamate) in the Nematic Solid Stale. *Biopolymers* **1971**, *10*, 1013–1019.

(9) Sarfati, M.; Lesot, P.; Merlet, D.; Courtieu, J. Theoretical and Experimental Aspects of Enantiomeric Differentiation Using Natural Abundance Multinuclear Nmr Spectroscopy in Chiral Polypeptide Liquid Crystals. *Chem. Commun.* **2000**, 2069–2081.

(10) Sarfati, M.; Courtieu, J.; Lesot, P. First Successful Enantiomeric Discrimination of Chiral Alkanes Using NMR Spectroscopy. *Chem. Commun.* **2000**, 1113–1114.

(11) Kummerlöwe, G.; Halbach, F.; Laufer, B.; Luy, B. Precise Measurement of RDCs in Water and DMSO Based Gels Using a Silicone Rubber Tube for Tunable Stretching. *TOSPECJ* **2008**, *2*, 29–33.

(12) Kummerlöwe, G.; McCord, E. F.; Cheatham, S. F.; Niss, S.; Schnell, R. W.; Luy, B. Tunable Alignment for All Polymer Gel/Solvent Combinations for the Measurement of Anisotropic NMR Parameters. *Chem. Eur. J.* **2010**, *16*, 7087–7089.

(13) Courtieu, J.; Alderman, D. W.; Grant, D. M.; Bayles, J. P. Director Dynamics and NMR Applications of Nematic Liquid Crystals Spinning at Various Angles from the Magnetic Field. *J. Chem. Phys.* **1982**, *77*, 723–730.

(14) Thiele, C. M. Scaling the Alignment of Small Organic Molecules in Substituted Polyglutamates by Variable-Angle Sample Spinning. *Angew. Chem. Int. Ed.* **2005**, *44*, 2787–2790.

(15) Nakatani, A. I.; Poliks, M. D.; Samulski, E. T. NMR Investigation of Chain Deformation in Sheared Polymer Fluids. *Macromolecules* **1990**, *23*, 2686–2692.

(16) Callaghan, P. T. Rheo NMR and Shear Banding. *Rheol. Acta* **2008**, *47*, 243–255.

(17) Callaghan, P. T., *Rheo-NMR: A New Window on the Rheology of Complex Fluids*; John Wiley & Sons, Ltd: Chichester, UK, 2002.

(18) Morimoto, D.; Walinda, E.; Iwakawa, N.; Nishizawa, M.; Kawata, Y.; Yamamoto, A.; Shirakawa, M.; Scheler, U.; Sugase, K. High-Sensitivity Rheo-NMR Spectroscopy for Protein Studies. *Anal. Chem.* **2017**, *89*, 7286–7290.

(19) Moino, C.; Artusio, F.; Pisano, R. Shear Stress as a Driver of Degradation for Protein-Based Therapeutics: More Accomplice than Culprit. *Int. J. Pharm.* **2024**, *650*, 123679.

(20) Jayaratne, J. S.; Codd, S. L.; Al-Kaby, R. N.; Maley, J.; Brox, T. I.; Galvosas, P.; Seymour, J. D. Large Amplitude Oscillatory Shear Rheo-NMR Velocimetry. *Phys. Fluids* **2023**, *35*, 093105.

(21) Xiong, Y.; Xia, Z.; Lu, A.; Chen, W. Time-Resolved Extensional Rheo-NMR Spectroscopy for Investigating Polymer Nanocomposites under Deformation. *Anal. Chem.* **2023**, *95*, 7545–7551.

(22) Leal, C. R.; Feio, G. M.; Almeida, P. L. Rheo-NMR Velocimetry Characterisation of PBLG/m-Cresol. *Liq. Cryst.* **2023**, *50*, 1541–1546.

(23) Lepper, C.; Edwards, P. J. B.; Schuster, E.; Brown, J. R.; Dykstra, R.; Callaghan, P. T.; Williams, M. A. K. Rheo-NMR Studies of the Behavior of a Nematic Liquid Crystal in a Low-Shear-Rate Regime: The Transition from Director Alignment to Reorientation. *Phys. Rev. E Stat. Nonlin. Soft Matter Phys.* **2010**, *82*, 041712.

(24) Rabi, I. I.; Zacharias, J. R.; Millman, S.; Kusch, P. A New Method of Measuring Nuclear Magnetic Moment. *Phys. Rev.* **1938**, *53*, 318–318.

(25) Purcell, E. M.; Torrey, H. C.; Pound, R. V. Resonance Absorption by Nuclear Magnetic Moments in a Solid. *Phys. Rev.* **1946**, *69*, 37–38.

(26) Bloch, F.; Hansen, W. W.; Packard, M. The Nuclear Induction Experiment. *Phys. Rev.* **1946**, *70*, 474–485.

(27) Nobel Prize in Physics 1944, https://www.nobelprize.org/prizes/physics/1944/summary/.

(28) Nobel Prize in Physics 1952, https://www.nobelprize.org/prizes/physics/1952/summary/.

(29) Nobel Prize in Chemistry 1991, https://www.nobelprize.org/prizes/chemistry/1991/summary/.

(30) Ernst, R. R.; Anderson, W. A. Application of Fourier Transform Spectroscopy to Magnetic Resonance. *Rev. Sci. Instrum.* **1966**, *37*, 93–102.

(31) Nobel Prize in Chemistry 2002, https://www.nobelprize.org/prizes/chemistry/2002/summary/.

(32) Williamson, M. P.; Havel, T. F.; Wüthrich, K. Solution Conformation of Proteinase Inhibitor IIA from Bull Seminal Plasma by 1H Nuclear Magnetic Resonance and Distance Geometry. *J. Molec. Biol.* **1985**, *182*, 295–315.

(33) Zweckstetter, M.; Holak, T. A.; Schwalbe, M., Magnetische Resonanzspektroskopie von Biomolekülen In *Bioanalytik*, Kurreck, J., Engels, J. W., Lottspeich, F., Eds.; Springer: Berlin, Heidelberg, 2022, pp 489–526.

(34) Levitt, M., *Spin Dynamics: Basics of Nuclear Magnetic Resonance*, 2nd Edition; John Wiley & Sons, Ltd: 2008.

(35) Keeler, J., *Understanding NMR Spectroscopy*, 2nd Edition; John Wiley & Sons, Ltd: 2010.

(36) Kramer, F.; Deshmukh, M.; Kessler, H.; Glaser, S. Residual Dipolar Coupling Constants: An Elementary Derivation of Key Equations. *Concepts Magn. Reson.* **2004**, *21A*, 10–21.

(37) Li, F.; Lee, J. H.; Grishaev, A.; Ying, J.; Bax, A. High Accuracy of Karplus Equations for Relating Three-Bond J Couplings to Protein Backbone Torsion Angles. *ChemPhysChem* **2015**, *16*, 572–578.

(38) Prestegard, J. H.; Al-Hashimi, H. M.; Tolman, J. R. NMR Structures of Biomolecules Using Field Oriented Media and Residual Dipolar Couplings. *Q. Rev. Biophys.* **2000**, *33*, 371–424.

(39) Koos, M. R. M.; Navarro-Vázquez, A.; Anklin, C.; Gil, R. R. Computer-Assisted 3D Structure Elucidation (CASE-3D): The Structural Value of 2JCH in Addition to 3JCH Coupling Constants. *Angew. Chem. Int. Ed.* **2020**, *59*, 3938–3941.

(40) Emsley, J.; Lindon, J., *NMR Spectroscopy Using Liquid Crystal Solvents*; Pergamon Press Ltd.: Oxford, 1975.

(41) Kummerlöwe, G.; Luy, B. Residual Dipolar Couplings as a Tool in Determining the Structure of Organic Molecules. *TrAC* **2009**, *28*, 483–493.

(42) Prestegard, J. H.; Bougault, C. M.; Kishore, A. I. Residual Dipolar Couplings in Structure Determination of Biomolecules. *Chem. Rev.* **2004**, *104*, 3519–3540.

(43) Deloche, B.; Samulski, E. T. Short-Range Nematic-like Orientational Order in Strained Elastomers: A Deuterium Magnetic Resonance Study. *Macromolecules* **1981**, *14*, 575–581.

(44) Saupe, A.; Englert, G. High-Resolution Nuclear Magnetic Resonance Spectra of Orientated Molecules. *Phys. Rev. Lett.* **1963**, *11*, 462–464.

(45) Saupe, A. Recent Results in the Field of Liquid Crystals. *Angew. Chem. Int. Ed.* **1968**, *7*, 97–112.

(46) Zweckstetter, M.; Bax, A. Prediction of Sterically Induced Alignment in a Dilute Liquid Crystalline Phase: Aid to Protein Structure Determination by NMR. *J. Am. Chem. Soc.* **2000**, *122*, 3791–3792.

(47) Zweckstetter, M.; Bax, A. Evaluation of Uncertainty in Alignment Tensors Obtained from Dipolar Couplings. *J. Biomol. NMR* **2002**, *23*, 127–137.

(48) Meirovitch, E.; Samulski, E. T.; Leed, A.; Scheraga, H. A.; Rananavare, S.; Nemethy, G.; Freed, J. H. Deuterium NMR Study of the Structure and Dynamic of the Side Chains of Several Solid Polyglutamates. *J. Phys. Chem.* **1987**, *91*, 4840–4851.

(49) Poliks, M. D.; Park, Y. W.; Samulski, E. T. Poly-γ-Benzyl-L-Glutamate: Order Parameter, Oriented Gel, and Novel Derivatives. *Mol. Cryst. Liq. Cryst. Incorporating. Nonlinear Opt.* **1987**, *153*, 321–345.

(50) Kummerlöwe, G.; Grage, S. L.; Thiele, C. M.; Kuprov, I.; Ulrich, A. S.; Luy, B. Variable Angle NMR Spectroscopy and Its Application to the Measurement of Residual Chemical Shift Anisotropy. *J. Magn. Reson.* **2011**, *209*, 19–30.

(51) Burnell, E. E.; de Lange, C. A. Effects of Interaction between Molecular Internal Motion and Reorientation on NMR of Anisotropic Liquids. *J. Magn. Reson.* **1980**, *39*, 461–480.

(52) Snyder, L. C.; Meiboom, S. NMR of Tetrahedral Molecules in a Nematic Solvent. *J. Chem. Phys.* **1966**, *44*, 4057–4058.

(53) Hoffman, R. E. Variations on the Chemical Shift of TMS. *J. Magn. Reson.* **2003**, *163*, 325–331.

(54) Courtieu, J.; Bayle, J. P.; Fung, B. M. Variable Angle Sample Spinning NMR in Liquid Crystals. *Prog. Nucl. Magn. Reson. Spectrosc.* **1994**, *26*, 141–169.

(55) Liu, Y.; Cohen, R. D.; Martin, G. E.; Williamson, R. T. A Practical Strategy for the Accurate Measurement of Residual Dipolar Couplings in Strongly Aligned Small Molecules. *J. Magn. Reson.* **2018**, *291*, 63–72.

(56) Lesot, P.; Berdagué, P.; Silvestre, V.; Remaud, G. Exploring the Enantiomeric 13C Position-Specific Isotope Fractionation: Challenges and Anisotropic NMR-based Analytical Strategy. *Anal. Bioanal. Chem.* **2021**, *413*, 6379–6392.

(57) Reinitzer, F. Beiträge zur Kenntniss des Cholesterins. *Monatshefte für Chemie* **1888**, *9*, 421–441.

(58) Lehmann, O., *Flüssige Kristalle sowie Plastizität von Kristallen im allgemeinen, molekulare Umlagerungen und Aggregatzustandsänderungen*; Verlag von Wilhelm Engelmann: Leipzig, 1904.

(59) Physics Success Stories - Physics On Display, https://archive.ph/Unpb, 2012.

(60) Nobel Prize in Physics 1991, https://www.nobelprize.org/prizes/physics/1991/summary/.

(61) Chandrasekhar, S.; Sadashiva, B. K.; Suresh, K. A. Liquid Crystals of Disc-like Molecules. *Pramana - J Phys* **1977**, *9*, 471–480.

(62) Lei, L. Bowlic Liquid Crystalsl. *Mol. Cryst. Liq. Cryst.* **1987**, *146*, 41–54.

(63) Martin, J. D.; Keary, C. L.; Thornton, T. A.; Novotnak, M. P.; Knutson, J. W.; Folmer, J. C. W. Metallotropic Liquid Crystals Formed by Surfactant Templating of Molten Metal Halides. *Nature Mater.* **2006**, *5*, 271–275.

(64) Lesot, P.; Aroulanda, C.; Berdagué, P.; Meddour, A.; Merlet, D.; Farjon, J.; Giraud, N.; Lafon, O. Multinuclear NMR in Polypeptide Liquid Crystals: Three Fertile Decades of Methodological Developments and Analytical Challenges. *Prog. Nucl. Magn. Reson. Spectrosc.* **2020**, *116*, 85–154.

(65) Bloembergen, N.; Purcell, E. M.; Pound, R. V. Relaxation Effects in Nuclear Magnetic Resonance Absorption. *Phys. Rev.* **1948**, *73*, 679–712.

(66) Debye, P. J. W., *Polar Molecules*; The Chemical Catalog Company, inc.: New York, 1929.

(67) Macosko, C. W., *Rheology: Principles, Measurements, and Applications*; Wiley-VCH: New York, 1994.

(68) Callaghan, P. T. Rheo-NMR: Nuclear Magnetic Resonance and the Rheology of Complex Fluids. *Rep. Prog. Phys.* **1999**, *62*, 599–670.

(69) Larson, R. G., *The Structure and Rheology of Complex Fluids*; Topics in Chemical Engineering; Oxford University Press: Oxford, New York, 1999.

(70) Mezger, T. G., *Das Rheologie Handbuch*, 5th ed.; Vincentz Network: Hannover, 2016.

(71) Couette, M. M. Etudes Sur Le Frottement Des Liquides. *Ann. Chim. Phys* **1890**, *Ser. VI*, 433–510.

(72) Hagen, G. H. L. Ueber Die Bewegung Des Wassers in Engen Cylindrischen Röhren. *Pogg. Ann.* **1839**, *46*, 423–442.

(73) Poiseuille, L. J., *Comptes Rendus Hebdomadaires Des Séances de l'Académie Des Sciences*; publiés avec le concours du Centre national de la recherche scientifique par MM. les secrétaires perpétuels: Paris, 1840; Vol. t.11, 961 and 1041.

(74) Rheological measurements, https://wiki.anton-paar.com/at-de/grundlagen-der-rheologie/rheometer-messungen/.

(75) Samulski, E. T. Investigations of Polymer Chains in Oriented Fluid Phases with Deuterium Nuclear Magnetic Resonance. *Polymer* **1985**, *26*, 177–189.

(76) Abbott, J. R.; Tetlow, N.; Graham, A. L.; Altobelli, S. A.; Fukushima, E.; Mondy, L. A.; Stephens, T. S. Experimental Observations of Particle Migration in Concentrated Suspensions: Couette Flow. *J. Rheol.* **1991**, *35*, 773–795.

(77) Altobelli, S. A.; Givler, R. C.; Fukushima, E. Velocity and Concentration Measurements of Suspensions by Nuclear Magnetic Resonance Imaging. *J. Rheol.* **1991**, *35*, 721–734.

(78) Graham, A. L.; Altobelli, S. A.; Fukushima, E.; Mondy, L. A.; Stephens, T. S. Note: NMR Imaging of Shear-induced Diffusion and Structure in Concentrated Suspensions Undergoing Couette Flow. *J. Rheol.* **1991**, *35*, 191–201.

(79) Xia, Y.; Callaghan, P. T. Study of Shear Thinning in High Polymer Solution Using Dynamic NMR Microscopy. *Macromolecules* **1991**, *24*, 4777–4786.

(80) Xia, Y.; Callaghan, P. T. The Measurement of Diffusion and Flow in Polymer Solutions Using Dynamic NMR Microscopy. *Makrom. Chemie. Macromolecular Symposia* **1990**, *34*, 277–286.

(81) Rofe, C. J.; Lambert, R. K.; Callaghan, P. T. Nuclear Magnetic Resonance Imaging of Flow for a Shear-thinning Polymer in Cylindrical Couette Geometry. *J. Rheol.* **1994**, *38*, 875–887.

(82) Grabowski, D. A.; Schmidt, C. Simultaneous Measurement of Shear Viscosity and Director Orientation of a Side-Chain Liquid-Crystalline Polymer by Rheo-NMR. *Macromolecules* **1994**, *27*, 2632–2634.

(83) Räntzsch, V.; Ratzsch, K.-F.; Guthausen, G.; Schlabach, S.; Wilhelm, M. Molecular Dynamics of Polymer Composites Using Rheology and Combined RheoNMR on the Example of TiO2-Filled Poly(n-Alkyl Methacrylates) and Trans-1,4-Polyisoprene. *Soft Mater.* **2014**, *12*, S4–S13.

(84) Callaghan, P. T.; Gil, A. M. 1 H NMR Spectroscopy of Polymers under Shear and Extensional Flow. *Rheol. Acta* **1999**, *38*, 528–536.

(85) Atkin, J. M.; Cormier, R. J.; Callaghan, P. T. Time-Dependence of Nuclear Magnetic Resonance Quadrupole Interactions for Polymers under Shear. *J. Magn. Reson.* **2005**, *172*, 91–97.

(86) Siebert, H.; Grabowski, D. A.; Schmidt, C. Rheo-NMR Study of a Non-Flow-Aligning Side-Chain Liquid Crystal Polymer in Nematic Solution. *Rheol. Acta* **1997**, *36*, 618–627.

(87) Callaghan, P. T., Velocimetry In *Translational Dynamics and Magnetic Resonance: Principles of Pulsed Gradient Spin Echo NMR*, Callaghan, P. T., Ed.; Oxford University Press: 2011, p 0.

(88) Britton, M. M.; Callaghan, P. T. Nuclear Magnetic Resonance Visualization of Anomalous Flow in Cone-and-Plate Rheometry. *J. Rheol.* **1997**, *41*, 1365–1386.

(89) Shukla, P. Thermodynamics and Kinetics of Gelation in the Poly(γ-Benzyl α,l-Glutamate)—Benzyl Alcohol System. *Polymer* **1992**, *33*, 365–372.

(90) Horton, J. C.; Donald, A. M. Phase Separation in the Poly(γ-Benzyl-α,l-Glutamate)/Benzyl Alcohol System and Its Role in Gelation. *Polymer* **1991**, *32*, 2418–2427.

(91) Doty, P.; Bradbury, J. H.; Holtzer, A. M. Polypeptides. IV. The Molecular Weight, Configuration and Association of Poly-γ-benzyl-L-glutamate in Various Solvents. *J. Am. Chem. Soc.* **1956**, *78*, 947–954.

(92) Sridhar, C. G.; Hines, W. A.; Samulski, E. T. Polypeptide Liquid Crystals: Magnetic Susceptibility, Twist Elastic Constant, Rotational Viscosity Coefficient, and poly-γ-benzyl-L-glutamate Sidechain Conformation. *J. Chem. Phys.* **1974**, *61*, 947–953.

(93) DuPré, D. B.; Duke, R. W. Temperature, Concentration, and Molecular Weight Dependence of the Twist Elastic Constant of Cholesteric Poly-γ-Benzyl-L-glutamate. *J. Chem. Phys.* **1975**, *63*, 143–148.

(94) Doi, M.; Edwards, S. F., *The Theory of Polymer Dynamics*; Clarendon Press: 1988.

(95) Mead, D. W.; Larson, R. G. Rheooptical Study of Isotropic Solutions of Stiff Polymers. *Macromolecules* **1990**, *23*, 2524–2533.

(96) Onsager, L. The Effects of Shape on the Interaction of Colloidal Particles. *Ann. N.Y. Acad. Sci* **1949**, *51*, 627–659.

(97) Flory, P. L. Phase Equilibria in Solutions of Rod-like Particles. *Proc. R. Soc. Lond. Ser. A* **1956**, *234*, 73–89.

(98) Sakamoto, R. Phase Separation of Poly(γ-Benzyl L-glutamate) to Liquid Crystal and Isotropic Solution in Various Helicogenic Solvents. *Colloid Polym. Sci.* **1984**, *262*, 788–792.

(99) Miller, W. G.; Kou, L.; Tohyama, K.; Voltaggio, V. Kinetic Aspects of the Formation of the Ordered Phase in Stiff-Chain Helical Polyamino Acids. *J. Polym. Sci., C Polym. Symp.* **1978**, *65*, 91–106.

(100) Wu, L.; Müller, E. A.; Jackson, G. Understanding and Describing the Liquid-Crystalline States of Polypeptide Solutions: A Coarse-Grained Model of PBLG in DMF. *Macromolecules* **2014**, *47*, 1482–1493.

(101) Ginzburg, B. M.; Shepelevskii, A. A. Construction Of The Full Phase Diagram For The System Of Poly(γ-Benzyl-l-Glutamate)/Dimethylformamide On The Basis Of The Complex Of Literature Data. *J. Macromol. Sci., Part B* **2003**, *42*, 1–56.

(102) Miller, W. G.; Wee, E. L. Liquid Crystal-Isotropic Phase Equilibriums in the System Poly(.Gamma.-Benzyl .Alpha.-L-glutamate)-Methylformamide. *J. Phys. Chem.* **1971**, *75*, 1446–1452.

(103) Robinson, C. The Cholesteric Phase in Polypeptide Solutions and Biological Structures. *Mol. Cryst.* **1966**, *1*, 467–494.

(104) Robinson, C. Liquid-Crystalline Structures in Solutions of a Polypeptide. *Trans. Faraday Soc.* **1956**, *52*, 571–592.

(105) Miller, W. G.; Wu, C. C.; Wee, E. L.; Santee, G. L.; Rai, J. H.; Goebel, K. G. Thermodynamics and Dynamics of Polypeptide Liquid Crystals. *Pure and Applied Chemistry* **1974**, *38*, 37–58.

(106) Sasaki, S.; Tokuma, K.; Uematsu, I. Phase Behavior of Poly(γ-Benzyl L-glutamate) Solutions in Benzyl Alcohol. *Polymer Bulletin* **1983**, *10*, 539–546.

(107) Yang, J. T. Non-Newtonian Viscosity of Poly-γ-benzyl-L-glutamate Solutions. *J. Am. Chem. Soc.* **1958**, *80*, 1783–1788.

(108) Gleeson, J. T.; Larson, R. G.; Mead, D. W.; Kiss, G.; Cladis, P. E. Image Analysis of Shear-Induced Textures in Liquid-Crystalline Polymers. *Liq. Cryst.* **1992**, *11*, 341–364.

(109) Kiss, G.; Porter, R. S. Rheology of Concentrated Solutions of Helical Polypeptides. *J. Polym. Sci. Polym. Phys. Ed.* **1980**, *18*, 361–388.

(110) Hermans, J. The Viscosity of Concentrated Solutions of Rigid Rodlike Molecules (Poly-γ-Benzyl-l-Glutamate in m-Cresol). *J. Colloid. Sci.* **1962**, *17*, 638–648.

(111) Onogi, S.; Asada, T., Rheology and Rheo-Optics of Polymer Liquid Crystals In *Rheology: Volume 1: Principles*, Astarita, G., Marrucci, G., Nicolais, L., Eds.; Springer US: Boston, MA, 1980, pp 127–147.

(112) Wissbrun, K. F. Rheology of Rod–like Polymers in the Liquid Crystalline State. *J. Rheol.* **1981**, *25*, 619–662.

(113) Walker, L. M.; Wagner, N. J.; Larson, R. G.; Mirau, P. A.; Moldenaers, P. The Rheology of Highly Concentrated PBLG Solutions. *J. Rheol.* **1995**, *39*, 925–952.

(114) Larson, R. G.; Mead, D. W. Time and Shear–Rate Scaling Laws for Liquid Crystal Polymers. *J. Rheol.* **1989**, *33*, 1251–1281.

(115) Cidade, M. T.; Filipe, S.; Barroso, V. C.; Wilhelm, M. Experimental Results on Fourier Transform Rheology of PBLG/m-Cresol and HPC/Water Liquid Crystalline Solutions. *Mol. Cryst. Liq. Cryst.* **2008**, *495*, 247/[599]–258/[610].

(116) Hongladarom, K.; Burghardt, W. R.; Baek, S. G.; Cementwala, S.; Magda, J. J. Molecular Alignment of Polymer Liquid Crystals in Shear Flows. 1. Spectrographic Birefringence Technique, Steady-State Orientation, and Normal Stress Behavior in Poly(Benzyl Glutamate) Solutions. *Macromolecules* **1993**, *26*, 772–784.

(117) Dadmun, M. D.; Han, C. C. A Neutron Scattering Study of the Orientation of a Liquid Crystalline Polymer by Shear Flow. *Macromolecules* **1994**, *27*, 7522–7532.

(118) Magda, J. J.; Baek, S. G.; DeVries, K. L.; Larson, R. G. Shear Flows of Liquid Crystal Polymers: Measurements of the Second Normal Stress Difference and the Doi Molecular Theory. *Macromolecules* **1991**, *24*, 4460–4468.

(119) Larson, R. G.; Doi, M. Mesoscopic Domain Theory for Textured Liquid Crystalline Polymers. *J. Rheol.* **1991**, *35*, 539–563.

(120) Vermant, J.; Mortier, M.; Moldenaers, P.; Mewis, J. An Evaluation of the Larson-Doi Model for Liquid Crystalline Polymers Using Recoil. *Rheol. Acta* **1999**, *38*, 537–547.

(121) Larson, R. G. Arrested Tumbling in Shearing Flows of Liquid-Crystal Polymers. *Macromolecules* **1990**, *23*, 3983–3992.

(122) Bedford, B. D.; Burghardt, W. R. Molecular Orientation and Instability in Plane Poiseuille Flow of a Liquid–Crystalline Polymer. *J. Rheol.* **1994**, *38*, 1657–1679.

(123) Chidambaram, S.; Butler, P. D.; Hamilton, W. A.; Dadmun, M. D., What Is a Model Liquid Crystalline Polymer Solution?: Solvent Effects on the Flow Behavior of LCP Solutions In *Scattering from Polymers*, Cebe, P., Ed.; ACS Symposium Series; American Chemical Soc: Washington, DC, 2000, pp 356–373.

(124) Marx, A.; Thiele, C. M. Orientational Properties of Poly-Gamma-Benzyl-L-glutamate: Influence of Molecular Weight and Solvent on Order Parameters of the Solute. *Chem. Eur. J.* **2009**, *15*, 254–260.

(125) Lesot, P.; Merlet, D.; Meddour, A.; Courtieu, J.; Loewenstein, A. Visualization of Enantiomers in a Polypeptide Liquid-Crystal Solvent through Carbon-13 NMR Spectroscopy. *J. Chem. Sci. Faraday Trans.* **1995**, *91*, 1371.

(126) Tzvetkova, P.; Luy, B.; Simova, S. Configuration Verification via RDCs on the Example of a Tetra-Substituted Pyrrolidine Ring. *Magn. Reson. Chem.* **2012**, *50*, S92–S101.

(127) Madiot, V.; Lesot, P.; Grée, D.; Courtieu, J.; Gree, R. Highly Enantioselective Propargylic Monofluorination Established by Carbon-13 and Fluorine-19 NMR in Chiral Liquid Crystals. *Chem. Commun.* **2000**, 169–170.

(128) Duke, R. W.; Du Pre, D. B.; Hines, W. A.; Samulski, E. T. Poly(.Gamma.-Benzyl L-glutamate) Helix-Coil Transition. Pretransition Phenomena in the Liquid Crystal Phase. *J. Am. Chem. Soc.* **1976**, *98*, 3094–3101.

(129) Marx, A.; Böttcher, B.; Thiele, C. M. Enhancing the Orienting Properties of Poly(γ-Benzyl-L-glutamate) by Means of Additives. *Chem. Eur. J.* **2010**, *16*, 1656–1663.

(130) Aroulanda, C.; Lesot, P. Molecular Enantiodiscrimination by NMR Spectroscopy in Chiral Oriented Systems: Concept, Tools, and Applications. *Chirality* **2022**, *34*, 182–244.

(131) Solgadi, A.; Jean, L.; Lasne, M.-C.; Rouden, J.; Courtieu, J.; Meddour, A. NMR in Chiral Polypeptide Liquid Crystals: The Problem of Amines. *Tetrahedron: Asymmetry* **2007**, *18*, 1511–1516.

(132) Lesot, P.; Serhan, Z.; Billault, I. Recent Advances in the Analysis of the Site-Specific Isotopic Fractionation of Metabolites Such as Fatty Acids Using Anisotropic Natural-Abundance 2H NMR Spectroscopy: Application to Conjugated Linolenic Methyl Esters. *Anal. Bioanal. Chem.* **2011**, *399*, 1187–1200.

(133) Lesot, P.; Merlet, D.; Loewenstein, A.; Courtieu, J. Enantiomeric Visualization Using Proton-Decoupled Natural Abundance Deuterium NMR in Poly(γ-Benzyl-l-Glutamate) Liquid Crystalline Solutions. *Tetrahedron: Asymmetry* **1998**, *9*, 1871–1881.

(134) Martin, G. J.; Martin, M. L. Deuterium Labelling at the Natural Abundance Level as Studied by High Field Quantitative 2H NMR. *Tetrahedron Letters* **1981**, *22*, 3525–3528.

(135) Merlet, D.; Ancian, B.; Courtieu, J.; Lesot, P. Two-Dimensional Deuterium NMR Spectroscopy of Chiral Molecules Oriented in a Polypeptide Liquid Crystal: Applications for the Enantiomeric Analysis through Natural Abundance Deuterium NMR. *J. Am. Chem. Soc.* **1999**, *121*, 5249–5258.

(136) Gouilleux, B.; Moussallieh, F.-M.; Lesot, P. Anisotropic 1H STD-NMR Spectroscopy: Exploration of Enantiomer-Polypeptide Interactions in Chiral Oriented Environments. *ChemPhysChem* **2023**, *24*, e202200508.

(137) Veron, A.; Gomes, A. E.; Leal, C. R.; van der Klink, J.; Martins, A. F. NMR Study of Flow and Viscoelastic Properties of PBLG/m-Cresol Lyotropic Liquid Crystal. *Mol. Cryst. Liq. Cryst. Sci. Technol.* **1999**, *331*, 499–507.

(138) Orian, L.; Feio, G.; Veron, A.; Martins, A. F.; Polimeno, A. Rheo-NMR and Numerical Study of the Nematodynamics in Cylindrical Couette Geometry. *Mol. Cryst. Liq. Cryst.* **2003**, *394*, 63–75.

(139) Martins, A. F.; Gomes, A. E.; Polimeno, A.; Orian, L. Simulations of Flow-Induced Director Structures in Nematic Liquid Crystals through Leslie-Ericksen Equations. II. Interpretation Of NMR Experiments in Liquid Crystal Polymers. *Phys. Rev. E Stat. Nonlin. Soft Matter Phys.* **2000**, *62*, 2301–2309.

(140) Leal, C. R.; Klink, J.; Martins, A. F. Some Aspects of the Rheo-NMR Behavior of the Lyotropic Liquid Crystal Poly(γ-Benzyl-L-glutamate) in m -Cresol. *Mol. Cryst. Liq. Cryst.* **2004**, *420*, 35–45.

(141) Munro, B. An Investigation of Rheo-NMR Techniques to Improve the Capture of Residual Dipolar Couplings, MA thesis, Palmerston North, New Zealand: Massey University, 2015.

(142) Hansen, M. R.; Hanson, P.; Pardi, A. Filamentous Bacteriophage for Aligning RNA, DNA, and Proteins for Measurement of Nuclear Magnetic Resonance Dipolar Coupling Interactions. *Methods Enzymol.* **2000**, *317*, 220–240.

(143) Hansen, M. R.; Rance, M.; Pardi, A. Observation of Long-Range 1H-1H Distances in Solution by Dipolar Coupling Interactions. *J. Am. Chem. Soc.* **1998**, *120*, 11210–11211.

(144) Hansen, M. R.; Mueller, L.; Pardi, A. Tunable Alignment of Macromolecules by Filamentous Phage Yields Dipolar Coupling Interactions. *Nature Struct. Biol.* **1998**, *5*, 1065–1074.

(145) Jackson, C. L.; Shaw, M. T. Polymer Liquid Crystalline Materials. *Int. Mater. Rev.* **1991**, *36*, 165–186.

(146) Enthart, A.; Freudenberger, J. C.; Furrer, J.; Kessler, H.; Luy, B. The CLIP/CLAP-HSQC: Pure Absorptive Spectra for the Measurement of One-Bond Couplings. *J. Magn. Reson.* **2008**, *192*, 314–322.

(147) Brox, T. I.; Douglass, B.; Galvosas, P.; Brown, J. R. Observations of the Influence of Taylor-Couette Geometry on the Onset of Shear-Banding in Surfactant Wormlike Micelles. *J. Rheol.* **2016**, *60*, 973–982.

(148) Hoffmann, F.; Kouřil, K.; Berger, S. T.; Meier, B.; Luy, B. Rheo-NMR at the Phase Transition of Liquid Crystalline Poly-γ-benzyl-l-glutamate: Phase Kinetics and a Valuable Tool for the Measurement of Residual Dipolar Couplings. *Macromolecules* **2023**, *56*, 7782–7794.

(149) Tzvetkova, P.; Luy, B. Q.E.COSY: Determining Sign and Size of Small Deuterium Residual Quadrupolar Couplings Using an Extended E.COSY Principle. *Magn. Reson. Chem.* **2016**, *54*, 351–357.

(150) Fung, B. M.; Martin, T. H. Magnetic Relaxation and Quadrupole Splitting for Liquid Crystalline Solutions of poly-γ-benzyl-L-glutamate in CDCl3 and CD2Cl2. *J. Chem. Phys.* **1974**, *61*, 1698–1702.

(151) Moseley, M. E. Anisotropic Solvent Translational Diffusion in Solutions of Poly(.Gamma.-Benzyl-L-glutamate). *J. Phys. Chem.* **1983**, *87*, 18–20.

(152) Lepper, C.; Edwards, P. J. B.; Dykstra, R.; Williams, M. A. K. Rheo-NMR Studies of a Nematic Worm-like Micelle System in a High-Shear-Rate Regime. *Soft matter* **2011**, *7*, 10291.

(153) Sager, E.; Tzvetkova, P.; Lingel, A.; Gossert, A. D.; Luy, B. Hydrogen Bond Formation May Enhance RDC-based Discrimination of Enantiomers. *Magn. Reson. Chem.* **2024**, *62*, 639–647.

(154) Elsing, D.; Luy, B.; Kozlowska, M. Enantiomer Differentiation by Interaction-Specific Prediction of Residual Dipolar Couplings in Spherical-like Molecules. *J. Chem. Theory Comput.* **2024**, *20*, 6454–6469.

(155) Hoffmann, F. M.; Luy, B. The Transition State of PBLG Studied by Deuterium NMR. *Polymers* **2025**, *17*, 3280.

(156) Hoffmann, F.; Luy, B. The Transition State of PBLG Studied by Deuterium NMR. *ChemRxiv* **2025**, DOI: `10.26434/chemrxiv-2025-wdl2n`.

(157) Trigo-Mouriño, P.; Merle, C.; Koos, M. R. M.; Luy, B.; Gil, R. R. Probing Spatial Distribution of Alignment by Deuterium NMR Imaging. *Chem. Eur. J.* **2013**, *19*, 7013–7019.

(158) Meschede, D., Wellenoptik In *Gerthsen Physik*, Meschede, D., Ed.; Springer: Berlin, Heidelberg, 2015, pp 533–583.

(159) Thiele, C. M.; Berger, S. Probing the Diastereotopicity of Methylene Protons in Strychnine Using Residual Dipolar Couplings. *Org. Lett.* **2003**, *5*, 705–708.

(160) Verdier, L.; Sakhaii, P.; Zweckstetter, M.; Griesinger, C. Measurement of Long Range H,C Couplings in Natural Products in Orienting Media: A Tool for Structure Elucidation of Natural Products. *J. Magn. Reson.* **2003**, *163*, 353–359.

(161) Luy, B.; Kobzar, K.; Kessler, H. An Easy and Scalable Method for the Partial Alignment of Organic Molecules for Measuring Residual Dipolar Couplings. *Angew. Chem. Int. Ed.* **2004**, *43*, 1092–1094.

(162) Rasmussen, D. H.; Mackenzie, A. P. Phase Diagram for the System Water–Dimethylsulphoxide. *Nature* **1968**, *220*, 1315–1317.

(163) Claridge, T. D. W., Chapter 3 - Practical Aspects of High-Resolution NMR In *High-Resolution NMR Techniques in Organic Chemistry (Third Edition)*, Claridge, T. D. W., Ed.; Elsevier: Boston, 2016, pp 61–132.

(164) Howarth, O.; and Lynch, R. 13C N.M.R. of Tetraiodomethane. *Mol. Phys.* **1968**, *15*, 431–431.

(165) Recchia, M. J. J.; Cohen, R. D.; Liu, Y.; Sherer, E. C.; Harper, J. K.; Martin, G. E.; Williamson, R. T. "One-Shot" Measurement of Residual Chemical Shift Anisotropy Using Poly-γ-benzyl-l-glutamate as an Alignment Medium. *Org. Lett.* **2020**, *22*, 8850–8854.

(166) Ehni, S.; Luy, B. A Systematic Approach for Optimizing the Robustness of Pulse Sequence Elements with Respect to Couplings, Offsets, and B1-field Inhomogeneities (COB). *Magn. Reson. Chem.* **2012**, *50 Suppl 1*, S63–72.

(167) Ehni, S.; Luy, B. Robust INEPT and Refocused INEPT Transfer with Compensation of a Wide Range of Couplings, Offsets, and B1-field Inhomogeneities (COB3). *J. Magn. Reson.* **2014**, *247*, 111–117.

(168) Woordes, Y. T.; Reinsperger, T.; Ehni, S.; Luy, B. Robust Bilinear Rotations. *Sci. Adv. submitted.*

(169) Gil-Silva, L. F.; Santamaría-Fernández, R.; Navarro-Vázquez, A.; Gil, R. R. Collection of NMR Scalar and Residual Dipolar Couplings Using a Single Experiment. *Chem. Eur. J.* **2016**, *22*, 472–476.

(170) Hellemann, E.; Teles, R. R.; Hallwass, F.; Barros Jr., W.; Navarro-Vázquez, A.; Gil, R. R. Mechanical Behavior of Polymer Gels for RDCs and RCSAs Collection: NMR Imaging Study of Buckling Phenomena. *Chem. Eur. J.* **2016**, *22*, 16632–16635.

(171) Edwards, P. J. B.; Kakubayashi, M.; Dykstra, R.; Pascal, S. M.; Williams, M. A. K. Rheo-NMR Studies of an Enzymatic Reaction: Evidence of a Shear-Stable Macromolecular System. *Biophys. J.* **2010**, *98*, 1986–1994.

(172) França, J. A. A.; Navarro-Vázquez, A.; Lei, X.; Sun, H.; Griesinger, C.; Hallwass, F. Complete NMR Assignment and Conformational Analysis of 17-α-Ethinylestradiol by Using RDCs Obtained in Grafted Graphene Oxide. *Magn. Reson. Chem.* **2017**, *55*, 297–303.

6 Appendix

6.1 Figures

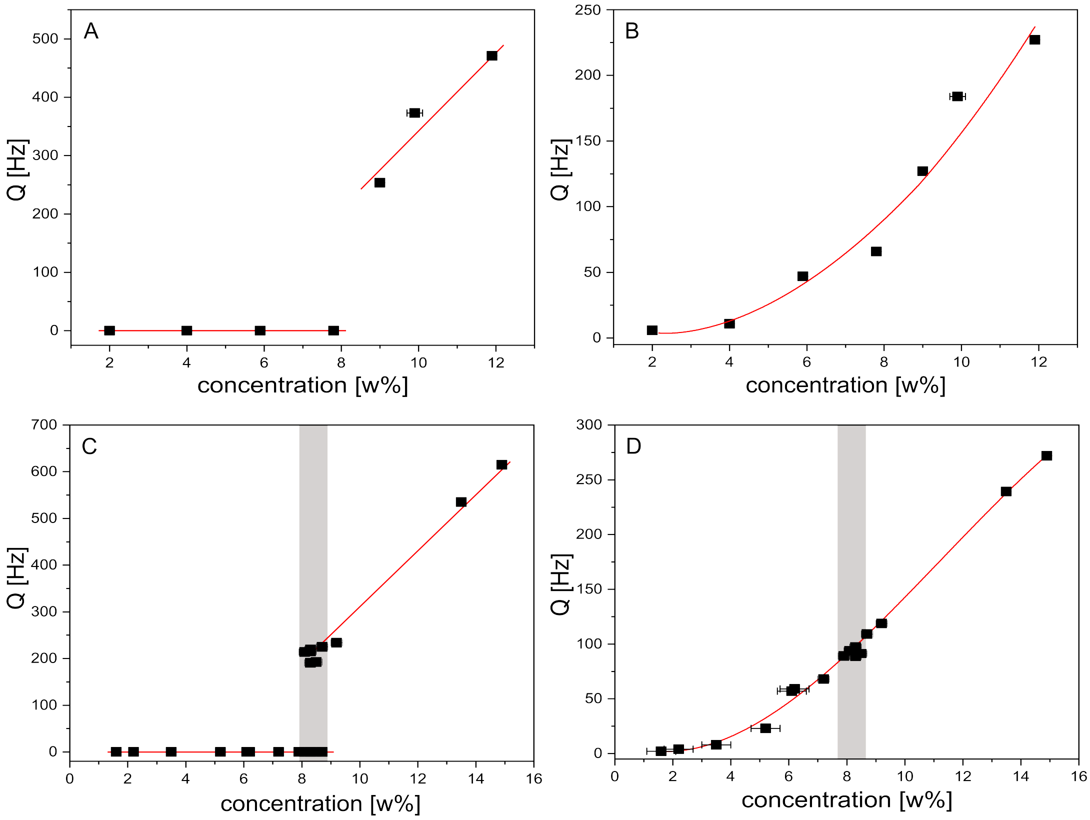

Figure 6.1: The linear representation of the change in the quadrupolar splitting of the dilution series from Figure 4.2. A), B) show the splitting of $CDCl_3$ at different PBLG concentrations without a guest molecule, C) and D) show the splitting of $CDCl_3$ at different PBLG concentrations with the guest molecule 1-flurbiprofen (20 mg). The static splittings are given under A), C) and the shear-induced splittings in B) and D). The biphasic region, in which the isotropic and anisotropic signals can be seen simultaneously, is indicated by the grey shaded area.

Table 6.1: The isotropic *J*-couplings of a 0 and 6 wt% PBLG sample (Fig. 4.31) are compared and their difference Δ is shown.

Assignment	J_{CH} 6 wt% PBLG [Hz]	J_{CH} 0 wt% PBLG [Hz]	Δ [Hz]
C1-H1	158.66 ± 0.03	158.26 ± 0.01	0.40
C2-H2	162.09 ± 0.03	162.19 ± 0.01	-0.10
C3-H3	160.21 ± 0.03	160.21 ± 0.01	0.00
C4-H4	168.83 ± 0.03	168.43 ± 0.01	0.40
C8-H8	145.08 ± 0.02	144.88 ± 0.01	0.20
C11-H11a	135.32 ± 0.11	135.22 ± 0.01	0.10
C11-H11b	125.58 ± 0.06	125.68 ± 0.01	-0.10
C12-H12	149.42 ± 0.07	149.42 ± 0.01	0.00
C13-H13	125.47 ± 0.10	125.17 ± 0.01	0.30
C14-H14	131.54 ± 0.07	131.24 ± 0.01	0.30
C15-H15a	130.85 ± 0.08	131.05 ± 0.01	-0.20
C15-H15b	129.84 ± 0.06	130.04 ± 0.01	-0.20
C16-H16	146.93 ± 0.01	147.13 ± 0.01	-0.20
C17-H17a	133.87 ± 1.02	132.87 ± 0.01	1.00
C17-H17b	133.87 ± 1.02	132.87 ± 0.01	1.00
C18-H18a	146.22 ± 5.11	148.62 ± 1.42	-2.40
C18-H18b	131.25 ± 4.54	132.75 ± 1.15	-1.50
C20-H20a	138.47 ± 0.04	139.47 ± 0.01	-1.00
C20-H20b	138.19 ± 0.03	139.29 v 0.01	-1.10
C22-H22	159.21 ± 0.02	159.01 ± 0.01	0.20
C23-H23a	145.30 ± 1.25	145.60 ± 0.01	-0.30
C23-H23b	136.92 ± 0.63	137.22 ± 0.01	-0.30

Table 6.2: The J- and T-couplings of a 6 wt% PBLG sample (Fig. 4.32) are shown together with the RDCs.

Assignment	J_{CH} 6 wt% PBLG [Hz]	T_{CH} 6 wt% PBLG [Hz]	D_{CH} [Hz]
C1-H1	158.66 ± 0.03	232.78 ± 2.58	74.12 ± 2.58
C2-H2	162.09 ± 0.03	171.40 ± 0.93	9.31 ± 0.93
C3-H3	160.21 ± 0.03	187.50 ± 1.14	27.29 ± 1.14
C4-H4	168.83 ± 0.03	248.05 ± 1.81	79.22 ± 1.81
C8-H8	145.08 ± 0.02	120.40 ± 8.78	-24.68 ± 8.78
C11-H11a	135.32 ± 0.11	167.23 ± 3.15	31.91 ± 3.15
C11-H11b	125.58 ± 0.06	68.15 ± 18.35	-57.43 ± 18.35
C12-H12	149.42 ± 0.07	89.40 ± 1.10	-60.02 ± 1.10
C13-H13	125.47 ± 0.10	101.67 ± 1.86	-23.80 ± 1.86
C14-H14	131.54 ± 0.07	71.07 ± 3.95	-60.47 ± 3.95
C15-H15a	130.85 ± 0.08	165.78 ± 2.16	34.93 ± 2.16
C15-H15b	129.84 ± 0.06	132.25 ± 8.82	2.41 ± 8.82
C16-H16	146.93 ± 0.01	164.10 ± 0.20	17.17 ± 0.20
C17-H17a	133.87 ± 1.02	141.68 ± 1.99	7.81 ± 1.99
C17-H17b	133.87 ± 1.02	141.68 ± 1.99	7.81 ± 1.99
C18-H18a	146.22 ± 5.11	151.24 ± 3.04	5.02 +/+ 3.04
C18-H18b	131.25 ± 4.54	149.42 ± 5.47	18.17 ± 5.47
C20-H20a	138.47 ± 0.04	126.65 ± 1.28	-11.82 ± 1.28
C20-H20b	138.19 ± 0.03	122.81 ± 2.56	-15.38 ± 2.56
C22-H22	159.21 ± 0.02	157.20 ± 0.79	-2.01 ± 0.79
C23-H23a	145.30 ± 1.25	n.d.	n.d.
C23-H23b	136.92 ± 0.63	n.d.	n.d.

n.d. = not determined

6.2 PALES files

6.2.1 PALES output file of strychnine at 67 Hz spinning

```
REMARK Molecular Alignment Simulation.

REMARK Simulation parameters.

DATA PALES_MODE DC

DATA TENSOR_MODE SVD (Order Matrix Method)


REMARK Order matrix.

DATA SAUPE_MATRIX     S(zz)       S(xx-yy)      S(xy)      S(xz)      S(yz)
DATA SAUPE        -6.5981e-004  6.8601e-004 -8.6744e-005  1.9165e-004 -7.2111e-005

DATA IRREDUCIBLE_REP    A0          A1R          A1I         A2R         A2I
DATA IRREDUCIBLE    -1.0460e-003 -2.4808e-004 -9.3342e-005  4.4399e-004  1.1228e-004
DATA IRREDUCIBLE GENERAL_MAGNITUDE   1.2861e-003


REMARK Mapping of coordinates.

DATA MAPPING_COOR   Szz_d(x)  Szz_d(y)  Syy_d(x)  Syy_d(y)  Sxx_d(x)  Sxx_d(y)
DATA MAPPING       -0.13192   0.14437   0.40779   1.41069   1.42412  -0.06873
DATA MAPPING INV    2.97699  -0.14437  -0.09305  -1.41069  -1.71006   0.06873


REMARK Eigensystem & Euler angles for clockwise rotation about z, y', z''.

DATA EIGENVALUES (Sxx_d,Syy_d,Szz_d)   -2.0600e-005 -6.9206e-004  7.1266e-004
DATA EIGENVECTORS          (x_coor      y_coor      z_coor)
DATA EIGENVECTORS X_AXIS  1.4248e-001  9.8741e-001 -6.8673e-002
DATA EIGENVECTORS Y_AXIS -1.3303e-001  8.7855e-002  9.8721e-001
DATA EIGENVECTORS Z_AXIS  9.8082e-001 -1.3152e-001  1.4387e-001

DATA Q_EULER_SOLUTIONS    ALPHA     BETA    GAMMA
DATA Q_EULER_ANGLES  1    93.98    81.73   187.64
DATA Q_EULER_ANGLES  2   273.98    81.73   187.64
DATA Q_EULER_ANGLES  3    86.02    98.27     7.64
DATA Q_EULER_ANGLES  4   266.02    98.27     7.64


REMARK Euler angles (psi/theta/phi) for rotation about x, y, z.

DATA EULER_SOLUTIONS 2
DATA EULER_ANGLES  -42.43  -78.76  136.97
DATA EULER_ANGLES  137.57  258.76  -43.03

DATA Da  3.563278e-004
DATA Dr  2.238187e-004


DATA Aa  7.126556e-004
DATA Ar  4.476374e-004
```

```
DATA Da_HN       7.691407e+000
DATA Rhombicity  6.281258e-001


REMARK Dipolar couplings.

DATA N                    17
DATA RMS                  6.202
DATA Chi2                 653.958
DATA CORR R               0.933
DATA Q SAUPE              0.259
DATA REGRESSION OFFSET    1.158 +/- 1.468 [Hz]
DATA REGRESSION SLOPE     0.862 +/- 0.086 [Hz]
DATA REGRESSION BAX SLOPE 0.926 +/- 0.061 [Hz]

VARS    RESID_I RESNAME_I ATOMNAME_I RESID_J RESNAME_J ATOMNAME_J DI D_OBS D D_DIFF DD W
FORMAT  %4d %4s %4s %4d %4s %4s %9.2f %9.3f %9.3f %9.3f %.2f %.2f

    1    C   C1    1    C   H1  46706.23   34.2690   32.2527    2.0163  1.0000 1.00
    1    C   C2    1    C   H2  46662.29    3.4890    3.8028   -0.3138  1.0000 1.00
    1    C   C3    1    C   H3  46714.54   13.0840   11.2252    1.8588  1.0000 1.00
    1    C   C4    1    C   H4  46675.13   32.6040   32.0960    0.5080  1.0000 1.00
    1    C  C11    1    C 1H11  46561.48  -21.3710  -11.4587   -9.9123  1.0000 1.00
    1    C  C11    1    C 2H11  46639.25   15.3470    7.1437    8.2033  1.0000 1.00
    1    C  C12    1    C  H12  46706.22  -24.4140  -28.0757    3.6617  1.0000 1.00
    1    C  C13    1    C  H13  46663.05  -11.7560   -4.6246   -7.1314  1.0000 1.00
    1    C  C14    1    C  H14  46731.14  -28.1440  -27.2339   -0.9101  1.0000 1.00
    1    C  C15    1    C 1H15  46700.57   13.0650    2.8672   10.1978  1.0000 1.00
    1    C  C15    1    C 2H15  46531.13   -1.8230   12.1754  -13.9984  1.0000 1.00
    1    C  C17    1    C 1H17  46665.41    2.8330   -0.8638    3.6968  1.0000 1.00
    1    C  C17    1    C 2H17  46576.63    2.8330    6.7496   -3.9166  1.0000 1.00
    1    C  C18    1    C 1H18  46651.35   -0.6300    8.2016   -8.8316  1.0000 1.00
    1    C  C18    1    C 2H18  46681.32    6.6130    6.4993    0.1137  1.0000 1.00
    1    C  C20    1    C 2H20  46645.73   -8.9110   -6.3480   -2.5630  1.0000 1.00
    1    C  C22    1    C  H22  46671.79    0.0030   -1.3773    1.3803  1.0000 1.00
```

6.2.2 PALES output file of strychnine at 125 Hz spinning

```
REMARK Molecular Alignment Simulation.

REMARK Simulation parameters.

DATA PALES_MODE DC

DATA TENSOR_MODE SVD (Order Matrix Method)


REMARK Order matrix.

DATA SAUPE_MATRIX     S(zz)       S(xx-yy)      S(xy)      S(xz)      S(yz)
DATA SAUPE        -1.3375e-003  1.8311e-003 -2.5785e-004  4.9849e-004 -4.2889e-004

DATA IRREDUCIBLE_REP    A0          A1R          A1I         A2R         A2I
DATA IRREDUCIBLE    -2.1204e-003 -6.4526e-004 -5.5516e-004  1.1851e-003  3.3376e-004
DATA IRREDUCIBLE GENERAL_MAGNITUDE   2.9962e-003
```

```
REMARK Mapping of coordinates.

DATA MAPPING_COOR   Szz_d(x)  Szz_d(y)  Syy_d(x)  Syy_d(y)  Sxx_d(x)  Sxx_d(y)
DATA MAPPING       -0.16725   0.18227   0.62906   1.24835   1.30466  -0.26295
DATA MAPPING INV    2.92230  -0.18227  -0.36649  -1.24835  -1.72895   0.26295


REMARK Eigensystem & Euler angles for clockwise rotation about z, y', z''.

DATA EIGENVALUES (Sxx_d,Syy_d,Szz_d)   -1.8610e-004 -1.5357e-003  1.7218e-003
DATA EIGENVECTORS          (x_coor      y_coor      z_coor)
DATA EIGENVECTORS X_AXIS  2.1044e-001  9.4242e-001 -2.5993e-001
DATA EIGENVECTORS Y_AXIS -1.2756e-001  2.9008e-001  9.4846e-001
DATA EIGENVECTORS Z_AXIS  9.6925e-001 -1.6644e-001  1.8126e-001

DATA Q_EULER_SOLUTIONS    ALPHA     BETA    GAMMA
DATA Q_EULER_ANGLES  1   105.33    79.56   189.74
DATA Q_EULER_ANGLES  2   285.33    79.56   189.74
DATA Q_EULER_ANGLES  3    74.67   100.44     9.74
DATA Q_EULER_ANGLES  4   254.67   100.44     9.74


REMARK Euler angles (psi/theta/phi) for rotation about x, y, z.

DATA EULER_SOLUTIONS 2
DATA EULER_ANGLES  -42.56  -75.75  148.78
DATA EULER_ANGLES  137.44  255.75  -31.22

DATA Da  8.609096e-004
DATA Dr  4.498740e-004


DATA Aa  1.721819e-003
DATA Ar  8.997479e-004


DATA Da_HN       1.858291e+001
DATA Rhombicity  5.225565e-001


REMARK Dipolar couplings.

DATA N                    21
DATA RMS                  11.879
DATA Chi2                 2963.567
DATA CORR R               0.942
DATA Q SAUPE              0.213
DATA REGRESSION OFFSET    -0.698 +/- 2.605 [Hz]
DATA REGRESSION SLOPE     0.892 +/- 0.073 [Hz]
DATA REGRESSION BAX SLOPE 0.949 +/- 0.052 [Hz]

VARS    RESID_I RESNAME_I ATOMNAME_I RESID_J RESNAME_J ATOMNAME_J DI D_OBS D D_DIFF DD W
FORMAT  %4d %4s %4s %4d %4s %4s %9.2f %9.3f %9.3f %9.3f %.2f %.2f

    1    C   C1    1    C   H1  46706.23   83.0250   76.2335    6.7915  1.0000 1.00
    1    C   C2    1    C   H2  46662.29    7.5430   -0.5930    8.1360  1.0000 1.00
    1    C   C3    1    C   H3  46714.54   21.0330   22.1698   -1.1368  1.0000 1.00
    1    C   C4    1    C   H4  46675.13   82.3320   75.8272    6.5048  1.0000 1.00
    1    C   C8    1    C   H8  46704.93   -8.3020  -15.5427    7.2407  1.0000 1.00
    1    C  C11    1    C 1H11  46561.48  -17.3740  -10.9383   -6.4357  1.0000 1.00
```

```
    1    C  C11    1    C 2H11  46639.25   12.9340   15.5312   -2.5972  1.0000 1.00
    1    C  C12    1    C  H12  46706.22  -62.4010  -65.5700    3.1690  1.0000 1.00
    1    C  C13    1    C  H13  46663.05   24.1600   -2.1559   26.3159  1.0000 1.00
    1    C  C14    1    C  H14  46731.14  -59.4680  -65.4373    5.9693  1.0000 1.00
    1    C  C15    1    C 1H15  46700.57   35.3980   15.1130   20.2850  1.0000 1.00
    1    C  C15    1    C 2H15  46531.13   10.0220   26.0161  -15.9941  1.0000 1.00
    1    C  C16    1    C  H16  46663.11   21.8210   11.7506   10.0704  1.0000 1.00
    1    C  C17    1    C 1H17  46665.41    9.8180    0.3841    9.4339  1.0000 1.00
    1    C  C17    1    C 2H17  46576.63    9.8180    4.6392    5.1788  1.0000 1.00
    1    C  C18    1    C 1H18  46651.35    0.6870   11.4766  -10.7896  1.0000 1.00
    1    C  C18    1    C 2H18  46681.32   20.7860   24.6690   -3.8830  1.0000 1.00
    1    C  C20    1    C 1H20  46724.46  -10.8440  -19.7314    8.8874  1.0000 1.00
    1    C  C20    1    C 2H20  46645.73  -15.3390   -2.9557  -12.3833  1.0000 1.00
    1    C  C22    1    C  H22  46671.79   -1.9760    9.7862  -11.7622  1.0000 1.00
    1    C  C23    1    C 2H23  46712.16  -32.1560   -8.0281  -24.1279  1.0000 1.00
```

6.2.3 PALES output file of strychnine at 180 Hz spinning

```
REMARK Molecular Alignment Simulation.

REMARK Simulation parameters.

DATA PALES_MODE DC

DATA TENSOR_MODE SVD (Order Matrix Method)


REMARK Order matrix.

DATA SAUPE_MATRIX     S(zz)       S(xx-yy)      S(xy)      S(xz)      S(yz)
DATA SAUPE        -1.8064e-003  2.0629e-003 -2.2183e-004  5.2081e-004 -4.5165e-004

DATA IRREDUCIBLE_REP    A0          A1R          A1I         A2R         A2I
DATA IRREDUCIBLE    -2.8637e-003 -6.7415e-004 -5.8463e-004  1.3351e-003  2.8714e-004
DATA IRREDUCIBLE GENERAL_MAGNITUDE   3.6774e-003


REMARK Mapping of coordinates.

DATA MAPPING_COOR   Szz_d(x)  Szz_d(y)  Syy_d(x)  Syy_d(y)  Sxx_d(x)  Sxx_d(y)
DATA MAPPING       -0.13133   0.14854   0.51600   1.31657   1.37753  -0.20477
DATA MAPPING INV    2.97567  -0.14854  -0.27411  -1.31657  -1.69843   0.20477


REMARK Eigensystem & Euler angles for clockwise rotation about z, y', z''.

DATA EIGENVALUES (Sxx_d,Syy_d,Szz_d)   -6.9879e-005 -1.9730e-003  2.0429e-003
DATA EIGENVECTORS          (x_coor      y_coor      z_coor)
DATA EIGENVECTORS X_AXIS  1.5973e-001  9.6599e-001 -2.0334e-001
DATA EIGENVECTORS Y_AXIS -1.1634e-001  2.2297e-001  9.6786e-001
DATA EIGENVECTORS Z_AXIS  9.8028e-001 -1.3094e-001  1.4800e-001

DATA Q_EULER_SOLUTIONS    ALPHA     BETA    GAMMA
DATA Q_EULER_ANGLES  1   101.86    81.49   187.61
DATA Q_EULER_ANGLES  2   281.86    81.49   187.61
DATA Q_EULER_ANGLES  3    78.14    98.51     7.61
DATA Q_EULER_ANGLES  4   258.14    98.51     7.61
```

```
REMARK Euler angles (psi/theta/phi) for rotation about x, y, z.

DATA EULER_SOLUTIONS 2
DATA EULER_ANGLES  -41.50  -78.60  143.93
DATA EULER_ANGLES  138.50  258.60  -36.07

DATA Da  1.021455e-003
DATA Dr  6.343837e-004


DATA Aa  2.042909e-003
DATA Ar  1.268767e-003


DATA Da_HN       2.204830e+001
DATA Rhombicity  6.210591e-001


REMARK Dipolar couplings.

DATA N                    19
DATA RMS                  20.519
DATA Chi2                 7999.200
DATA CORR R               0.905
DATA Q SAUPE              0.299
DATA REGRESSION OFFSET    -0.721 +/- 4.570 [Hz]
DATA REGRESSION SLOPE     0.824 +/- 0.094 [Hz]
DATA REGRESSION BAX SLOPE 0.915 +/- 0.068 [Hz]

VARS    RESID_I RESNAME_I ATOMNAME_I RESID_J RESNAME_J ATOMNAME_J DI D_OBS D D_DIFF DD W
FORMAT  %4d %4s %4s %4d %4s %4s %9.2f %9.3f %9.3f %9.3f %.2f %.2f

    1    C   C1    1    C   H1  46706.23   98.5290   92.5817    5.9473  1.0000 1.00
    1    C   C2    1    C   H2  46662.29   12.6590    9.0801    3.5789  1.0000 1.00
    1    C   C3    1    C   H3  46714.54   36.5440   28.9485    7.5955  1.0000 1.00
    1    C   C4    1    C   H4  46675.13  120.0480   92.1535   27.8945  1.0000 1.00
    1    C   C8    1    C   H8  46704.93   23.2180  -18.9556   42.1736  1.0000 1.00
    1    C  C11    1    C 1H11  46561.48  -60.6400  -23.2729  -37.3671  1.0000 1.00
    1    C  C11    1    C 2H11  46639.25   40.1740   25.5458   14.6282  1.0000 1.00
    1    C  C12    1    C  H12  46706.22  -71.2090  -84.6527   13.4437  1.0000 1.00
    1    C  C13    1    C  H13  46663.05  -16.3870   -4.6120  -11.7750  1.0000 1.00
    1    C  C14    1    C  H14  46731.14  -62.7510  -83.5315   20.7805  1.0000 1.00
    1    C  C15    1    C 1H15  46700.57   45.7210   14.8736   30.8474  1.0000 1.00
    1    C  C15    1    C 2H15  46531.13    4.8690   32.6356  -27.7666  1.0000 1.00
    1    C  C17    1    C 1H17  46665.41    5.8860    1.6500    4.2360  1.0000 1.00
    1    C  C17    1    C 2H17  46576.63    5.8860   13.1611   -7.2751  1.0000 1.00
    1    C  C18    1    C 1H18  46651.35   -6.7410   23.0408  -29.7818  1.0000 1.00
    1    C  C18    1    C 2H18  46681.32   26.4550   20.8073    5.6477  1.0000 1.00
    1    C  C20    1    C 1H20  46724.46  -24.9350  -24.1728   -0.7622  1.0000 1.00
    1    C  C20    1    C 2H20  46645.73  -22.9980   -8.3200  -14.6780  1.0000 1.00
    1    C  C22    1    C  H22  46671.79   -1.9270    4.9153   -6.8423  1.0000 1.00
```

6.2.4 PALES output file of strychnine in a 6 wt% sample

```
REMARK Molecular Alignment Simulation.

REMARK Simulation parameters.
```

```
DATA PALES_MODE DC

DATA TENSOR_MODE SVD (Order Matrix Method)


REMARK Order matrix.

DATA SAUPE_MATRIX     S(zz)       S(xx-yy)      S(xy)      S(xz)      S(yz)
DATA SAUPE        -1.5235e-003  1.5837e-003 -2.1243e-004  3.8572e-004 -1.8087e-004

DATA IRREDUCIBLE_REP    A0          A1R          A1I         A2R         A2I
DATA IRREDUCIBLE    -2.4152e-003 -4.9928e-004 -2.3412e-004  1.0250e-003  2.7497e-004
DATA IRREDUCIBLE GENERAL_MAGNITUDE    2.9485e-003


REMARK Mapping of coordinates.

DATA MAPPING_COOR   Szz_d(x)  Szz_d(y)  Syy_d(x)  Syy_d(y)  Sxx_d(x)  Sxx_d(y)
DATA MAPPING       -0.13972   0.12829   0.36831   1.41855   1.41466  -0.08154
DATA MAPPING INV    2.97606  -0.12829  -0.10815  -1.41855  -1.71649   0.08154


REMARK Eigensystem & Euler angles for clockwise rotation about z, y', z''.

DATA EIGENVALUES (Sxx_d,Syy_d,Szz_d)   -4.7583e-005 -1.5864e-003  1.6340e-003
DATA EIGENVECTORS          (x_coor      y_coor      z_coor)
DATA EIGENVECTORS X_AXIS  1.5034e-001  9.8527e-001 -8.1454e-002
DATA EIGENVECTORS Y_AXIS -1.1471e-001  9.9217e-002  9.8843e-001
DATA EIGENVECTORS Z_AXIS  9.8196e-001 -1.3926e-001  1.2793e-001

DATA Q_EULER_SOLUTIONS    ALPHA     BETA    GAMMA
DATA Q_EULER_ANGLES  1    94.71    82.65   188.07
DATA Q_EULER_ANGLES  2   274.71    82.65   188.07
DATA Q_EULER_ANGLES  3    85.29    97.35     8.07
DATA Q_EULER_ANGLES  4   265.29    97.35     8.07


REMARK Euler angles (psi/theta/phi) for rotation about x, y, z.

DATA EULER_SOLUTIONS 2
DATA EULER_ANGLES  -47.43  -79.10  142.66
DATA EULER_ANGLES  132.57  259.10  -37.34

DATA Da  8.169857e-004
DATA Dr  5.129352e-004


DATA Aa  1.633971e-003
DATA Ar  1.025870e-003


DATA Da_HN       1.763480e+001
DATA Rhombicity  6.278386e-001


REMARK Dipolar couplings.

DATA N                    20
DATA RMS                  12.937
```

```
DATA Chi2                 3347.253
DATA CORR R               0.937
DATA Q SAUPE              0.235
DATA REGRESSION OFFSET    0.975 +/- 2.860 [Hz]
DATA REGRESSION SLOPE     0.877 +/- 0.077 [Hz]
DATA REGRESSION BAX SLOPE 0.938 +/- 0.055 [Hz]

VARS    RESID_I RESNAME_I ATOMNAME_I RESID_J RESNAME_J ATOMNAME_J DI D_OBS D D_DIFF DD W
FORMAT  %4d %4s %4s %4d %4s %4s %9.2f %9.3f %9.3f %9.3f %.2f %.2f

    1    C   C1    1    C   H1  46706.23   74.1000   74.1828   -0.0828  1.0000 1.00
    1    C   C2    1    C   H2  46662.29    9.3000    8.3323    0.9677  1.0000 1.00
    1    C   C3    1    C   H3  46714.54   27.3000   26.3300    0.9700  1.0000 1.00
    1    C   C4    1    C   H4  46675.13   79.2000   73.9253    5.2747  1.0000 1.00
    1    C   C8    1    C   H8  46704.93  -24.7000  -22.6112   -2.0888  1.0000 1.00
    1    C  C11    1    C 1H11  46561.48  -57.4000  -27.1348  -30.2652  1.0000 1.00
    1    C  C11    1    C 2H11  46639.25   31.9000   17.4735   14.4265  1.0000 1.00
    1    C  C12    1    C  H12  46706.22  -60.0000  -65.6738    5.6738  1.0000 1.00
    1    C  C13    1    C  H13  46663.05  -23.8000  -10.3286  -13.4714  1.0000 1.00
    1    C  C14    1    C  H14  46731.14  -60.5000  -63.7940    3.2940  1.0000 1.00
    1    C  C15    1    C 1H15  46700.57   34.9000    6.5526   28.3474  1.0000 1.00
    1    C  C15    1    C 2H15  46531.13    2.4000   30.1209  -27.7209  1.0000 1.00
    1    C  C16    1    C  H16  46663.11   17.2000   19.4134   -2.2134  1.0000 1.00
    1    C  C17    1    C 1H17  46665.41    7.8000    0.5503    7.2497  1.0000 1.00
    1    C  C17    1    C 2H17  46576.63    7.8000   13.8246   -6.0246  1.0000 1.00
    1    C  C18    1    C 1H18  46651.35    5.0000   18.5400  -13.5400  1.0000 1.00
    1    C  C18    1    C 2H18  46681.32   18.2000   12.5238    5.6762  1.0000 1.00
    1    C  C20    1    C 1H20  46724.46  -11.8000  -18.9697    7.1697  1.0000 1.00
    1    C  C20    1    C 2H20  46645.73  -15.4000  -14.5045   -0.8955  1.0000 1.00
    1    C  C22    1    C  H22  46671.79    2.0000   -3.5695    5.5695  1.0000 1.00
```

6.2.5 PALES output file of strychnine in the biphasic sample

```
REMARK Molecular Alignment Simulation.

REMARK Simulation parameters.

DATA PALES_MODE DC

DATA TENSOR_MODE SVD (Order Matrix Method)


REMARK Order matrix.

DATA SAUPE_MATRIX     S(zz)       S(xx-yy)      S(xy)      S(xz)      S(yz)
DATA SAUPE         2.3632e-003 -2.8240e-003  3.0457e-004 -6.6197e-004  2.2960e-004

DATA IRREDUCIBLE_REP    A0          A1R          A1I         A2R         A2I
DATA IRREDUCIBLE     3.7465e-003  8.5686e-004  2.9720e-004 -1.8277e-003 -3.9425e-004
DATA IRREDUCIBLE GENERAL_MAGNITUDE   4.7616e-003


REMARK Mapping of coordinates.

DATA MAPPING_COOR   Szz_d(x)  Szz_d(y)  Syy_d(x)  Syy_d(y)  Sxx_d(x)  Sxx_d(y)
DATA MAPPING       -0.11235   0.13375   0.38239   1.41990   1.44458  -0.06944
DATA MAPPING INV    3.00118  -0.13375  -0.08986  -1.41990  -1.68944   0.06944
```

```
REMARK Eigensystem & Euler angles for clockwise rotation about z, y’, z’’.

DATA EIGENVALUES (Sxx_d,Syy_d,Szz_d)    2.5185e-004  2.4661e-003 -2.7179e-003
DATA EIGENVECTORS          (x_coor      y_coor      z_coor)
DATA EIGENVECTORS X_AXIS  1.2212e-001  9.9009e-001 -6.9380e-002
DATA EIGENVECTORS Y_AXIS -1.2425e-001  8.4604e-002  9.8864e-001
DATA EIGENVECTORS Z_AXIS  9.8471e-001 -1.1211e-001  1.3335e-001

DATA Q_EULER_SOLUTIONS    ALPHA     BETA    GAMMA
DATA Q_EULER_ANGLES  1    94.01    82.34   186.50
DATA Q_EULER_ANGLES  2   274.01    82.34   186.50
DATA Q_EULER_ANGLES  3    85.99    97.66     6.50
DATA Q_EULER_ANGLES  4   265.99    97.66     6.50


REMARK Euler angles (psi/theta/phi) for rotation about x, y, z.

DATA EULER_SOLUTIONS 2
DATA EULER_ANGLES  -40.05  -79.97  134.50
DATA EULER_ANGLES  139.95  259.97  -45.50

DATA Da -1.358955e-003
DATA Dr -7.380736e-004


DATA Aa -2.717911e-003
DATA Ar -1.476147e-003


DATA Da_HN      -2.933332e+001
DATA Rhombicity  5.431184e-001


REMARK Dipolar couplings.

DATA N                    18
DATA RMS                  16.224
DATA Chi2                 4737.650
DATA CORR R               0.965
DATA Q SAUPE              0.183
DATA REGRESSION OFFSET    -2.471 +/- 3.876 [Hz]
DATA REGRESSION SLOPE     0.927 +/- 0.063 [Hz]
DATA REGRESSION BAX SLOPE 0.961 +/- 0.044 [Hz]

VARS    RESID_I RESNAME_I ATOMNAME_I RESID_J RESNAME_J ATOMNAME_J DI D_OBS D D_DIFF DD W
FORMAT  %4d %4s %4s %4d %4s %4s %9.2f %9.3f %9.3f %9.3f %.2f %.2f

    1    C   C1    1    C   H1  46706.23 -127.6000 -123.9342   -3.6658  1.0000 1.00
    1    C   C2    1    C   H2  46662.29   -9.0000   -9.5445    0.5445  1.0000 1.00
    1    C   C3    1    C   H3  46714.54  -48.0000  -35.3514  -12.6486  1.0000 1.00
    1    C   C4    1    C   H4  46675.13 -127.2000 -123.4108   -3.7892  1.0000 1.00
    1    C   C8    1    C   H8  46704.93   49.1000   42.7187    6.3813  1.0000 1.00
    1    C  C11    1    C 1H11  46561.48   79.8000   43.5914   36.2086  1.0000 1.00
    1    C  C11    1    C 2H11  46639.25  -53.4000  -27.3457  -26.0543  1.0000 1.00
    1    C  C12    1    C  H12  46706.22   95.7000  100.7597   -5.0597  1.0000 1.00
    1    C  C14    1    C  H14  46731.14   95.1000   97.9559   -2.8559  1.0000 1.00
    1    C  C15    1    C 2H15  46531.13   -9.3000  -49.9607   40.6607  1.0000 1.00
    1    C  C16    1    C  H16  46663.11  -25.0000  -29.8928    4.8928  1.0000 1.00
    1    C  C17    1    C 1H17  46665.41   -8.7000   -3.1708   -5.5292  1.0000 1.00
```

```
    1    C  C17    1    C 2H17  46576.63   -8.7000  -23.1679   14.4679  1.0000 1.00
    1    C  C18    1    C 1H18  46651.35   -8.4000  -28.0648   19.6648  1.0000 1.00
    1    C  C18    1    C 2H18  46681.32  -34.5000  -25.6901   -8.8099  1.0000 1.00
    1    C  C20    1    C 1H20  46724.46   22.6000   28.1535   -5.5535  1.0000 1.00
    1    C  C20    1    C 2H20  46645.73   25.6000   28.5844   -2.9844  1.0000 1.00
    1    C  C22    1    C  H22  46671.79    1.4000    9.4010   -8.0010  1.0000 1.00
```

6.2.6 PALES output file of 1-fluornaphthalene

```
REMARK Molecular Alignment Simulation.

REMARK Simulation parameters.

DATA PALES_MODE DC

DATA TENSOR_MODE SVD (Order Matrix Method)


REMARK Order matrix.

DATA SAUPE_MATRIX     S(zz)       S(xx-yy)      S(xy)      S(xz)      S(yz)
DATA SAUPE        -4.7532e-004  1.4098e-004  5.0354e-005  0.0000e+000  0.0000e+000

DATA IRREDUCIBLE_REP    A0          A1R          A1I         A2R         A2I
DATA IRREDUCIBLE    -7.5353e-004 -0.0000e+000  0.0000e+000  9.1246e-005 -6.5178e-005
DATA IRREDUCIBLE GENERAL_MAGNITUDE   7.7004e-004


REMARK Mapping of coordinates.

DATA MAPPING_COOR   Szz_d(x)  Szz_d(y)  Syy_d(x)  Syy_d(y)  Sxx_d(x)  Sxx_d(y)
DATA MAPPING        0.00000   1.57080   0.31014  -0.00000   1.88093  -0.00000
DATA MAPPING INV    0.00000  -1.57080  -2.83146   0.00000  -1.26066   0.00000


REMARK Eigensystem & Euler angles for clockwise rotation about z, y’, z’’.

DATA EIGENVALUES (Sxx_d,Syy_d,Szz_d)    1.5103e-004  3.2429e-004 -4.7532e-004
DATA EIGENVECTORS          (x_coor      y_coor      z_coor)
DATA EIGENVECTORS X_AXIS -3.0519e-001  9.5229e-001  0.0000e+000
DATA EIGENVECTORS Y_AXIS  9.5229e-001  3.0519e-001  0.0000e+000
DATA EIGENVECTORS Z_AXIS  0.0000e+000  0.0000e+000  1.0000e+000

DATA Q_EULER_SOLUTIONS    ALPHA     BETA    GAMMA
DATA Q_EULER_ANGLES  1    72.23     0.00     0.00
DATA Q_EULER_ANGLES  2   252.23     0.00     0.00
DATA Q_EULER_ANGLES  3   287.77   180.00     0.00
DATA Q_EULER_ANGLES  4   107.77   180.00     0.00


REMARK Euler angles (psi/theta/phi) for rotation about x, y, z.

DATA EULER_SOLUTIONS 2
DATA EULER_ANGLES    0.00   -0.00   72.23
DATA EULER_ANGLES  180.00  180.00  252.23

DATA Da -2.376584e-004
DATA Dr -5.775267e-005
```

```
DATA Aa -4.753169e-004
DATA Ar -1.155053e-004


DATA Da_HN      -5.129905e+000
DATA Rhombicity  2.430070e-001


REMARK Dipolar couplings.

DATA N                    7
DATA RMS                  0.611
DATA Chi2                 2.616
DATA CORR R               0.977
DATA Q SAUPE              0.044
DATA REGRESSION OFFSET    0.458 +/- 0.984 [Hz]
DATA REGRESSION SLOPE     0.955 +/- 0.093 [Hz]
DATA REGRESSION BAX SLOPE 0.978 +/- 0.066 [Hz]

VARS    RESID_I RESNAME_I ATOMNAME_I RESID_J RESNAME_J ATOMNAME_J DI D_OBS D D_DIFF DD W
FORMAT  %4d %4s %4s %4d %4s %4s %9.2f %9.3f %9.3f %9.3f %.2f %.2f

    1    C   C1    1    H   H1  45040.73    6.7430    7.3586   -0.6156  1.0000 1.00
    1    C   C2    1    H   H2  45020.40    9.5990   10.3760   -0.7770  1.0000 1.00
    1    C   C3    1    H   H3  45072.70   14.0940   14.2430   -0.1490  1.0000 1.00
    1    C   C4    1    H   H4  45007.81    7.2720    7.5994   -0.3274  1.0000 1.00
    1    C   C6    1    H   H6  44979.15    8.3460    7.4044    0.9416  1.0000 1.00
    1    C   C7    1    H   H7  45051.13   11.1270   10.3577    0.7693  1.0000 1.00
    1    C   C8    1    H   H8  45125.30   14.4380   14.2796    0.1584  1.0000 1.00
```

6.3 Pulse Programs

The Pulse programs shown were all programmed with explicit pulse programming. Hereby, the channels are separated by the "exec_on_chan", "exec_enable", "exec_on_other" and "exec_wait" commands for simultaneous operation. The explicit channel (here f1) is started with "exec_on_chan:f1" the other channel is started with "exec_on_other". The termination of the channel depends on which channel is terminated first. The first receives "exec_wait" and the second "exec_enable". The rotation is controlled by the TTL signals, whereby four TTL signals are available by default and one has to find the correct one on the spectrometer. In our case it was TTL4 and we had to program the speeds as TTL4_LOW (for the 0V signal) and TTL4_HIGH (for the 5V signal), with the waiting set as a delay in front of the TTL commands. Both delays were 1 ms in total, and 700 µs for the 5V signal and 300 µs for the 0V signal, for example for the duty cycle of 0.70. These TTL commands belong to the time unit and therefore always need to be after "exec_on_other".

6.3.1 Rheozg2hoff for kinetic measurements after rotation is switched off

```
;rheozg2hoff
;avance-version (12/01/11)
;deuterium (2H) 1D for rheo-NMR setup
;measures equilibration processes after rotation is switched off.
;2H channel assumed to be lock channel
;sample rotation controlled by TTL signal (here: TTL4)
;TTL channel depends on specific spectrometer and needs to be adjusted
;
;initial rotation speed TTL-controlled (d50/d51/l11), then delay d2 without rotation before acquisition.
;
;Fabian Hoffmann, Karel Kouril, Stefan T. Berger, Benno Meier, Burkhard Luy,
;Macromolecules, submitted (2023).
;
;$CLASS=HighRes
;$DIM=2D
;$TYPE=
;$SUBTYPE=
;$COMMENT=


#include <Avance.incl>
#include <De.incl>
#include <Sysconf.incl>


"d11=30m"

"acqt0=-p1*2/3.1416"

"l11=((d1)/(d50+d51))-0.5"


1 ze
  d11 LOCKDEC_ON
  d11 H2_PULSE

2 30m
  30m H2_LOCK
  d10
```

```
5 TTL4_LOW
  d51
  TTL4_HIGH
  d50
  lo to 5 times l11

  d2
  d11 H2_PULSE
  p1:D ph1


  go=2 ph31
  30m mc #0 to 2 F0(zd)

  d11 H2_LOCK
  d11 LOCKDEC_OFF
exit


ph1=0 2 2 0 1 3 3 1
ph2=0 2 2 0 1 3 3 1
ph3=2 0 0 2 3 1 1 3
ph31=0 2 2 0 1 3 3 1


;pl1 : f1 channel - power level for pulse (default)
;p1 : f1 channel -  90 degree high power pulse (deuterium)
;d11: delay for disk I/O                             [30 msec]
;d1 : relaxation delay with rotation on
;d2 : delay between switching off rotation and H2_PULSE
;d50 : TTL4_HIGH 5V blanking delay [700u]
;d51 : TTL4_LOW  0V unblanking delay [300u]
;ns: 1 * n

;locnuc: off



;$Id: rheozg2hoff,v 3.2 2022/10/31 17:49:26 bulu Exp $
```

6.3.2 Rheozg2hon for kinetic measurements after rotation is switched on

```
;rheozg2hon
;avance-version (12/01/11)
;deuterium (2H) 1D for rheo-NMR setup
;measures equilibration processes after rotation is switched on.
;2H channel assumed to be lock channel
;sample rotation controlled by TTL signal (here: TTL4)
;TTL channel depends on specific spectrometer and needs to be adjusted
;pulse program uses explicit channel adressing
;
;initial rotation speed TTL-controlled (d50/d51/l11), then delay d2 with rotation before acquisition.
;
;Fabian Hoffmann, Karel Kouril, Stefan T. Berger, Benno Meier, Burkhard Luy,
;Macromolecules, submitted (2023).
;
;$CLASS=HighRes
;$DIM=2D
```

```
;$TYPE=
;$SUBTYPE=
;$COMMENT=


#include <Avance.incl>
#include <De.incl>
#include <Sysconf.incl>


"d11=30m"

"acqt0=-p1*2/3.1416"

"l11=((d2+aq)/(d50+d51))-0.5"


1 ze
  d11 LOCKDEC_ON
  d11 H2_PULSE

2 30m
  200m
  d1
  exec_on_chan:f1
  d2
  p1:D ph1
  ACQ_START(ph30,ph31)
  aq DWELL_GEN:f1

  exec_enable

  exec_on_other
5 d51 TTL4_LOW
  d50 TTL4_HIGH
  lo to 5 times l11
  exec_wait

  10u
  rcyc=2
  30m mc #0 to 2 F0(zd)

  d11 H2_LOCK
  d11 LOCKDEC_OFF
exit


ph1=0 2 2 0 1 3 3 1
ph2=0 2 2 0 1 3 3 1
ph3=2 0 0 2 3 1 1 3
ph30=0
ph31=0 2 2 0 1 3 3 1


;pl1 : f1 channel - power level for pulse (default)
;p1 : f1 channel -  90 degree high power pulse
;d11: delay for disk I/O                             [30 msec]
;d1 : relaxation delay with rotation off
;d2 : delay between switching on rotation and acquisition
;d50 : TTL4_HIGH 5V blanking delay [700u]
```

```
;d51 : TTL4_LOW  0V unblanking delay [300u]
;ns: 1 * n

;locnuc: off



;$Id: rheozg2hon,v 3.2 2022/10/31 17:49:26 bulu Exp $
```

6.3.3 Rheo2h2Djres for a 2D J-resolved experiment

```
;rheo2h2Djres
;avance-version (12/01/11)
;2D deuterium j-resolved experiment allowing J-evolution in the
;indirect dimension under static conditions and direct acquisition
;under rotating conditions using a rheo-NMR setup
;2H channel assumed to be lock channel
;sample rotation controlled by TTL signal (here: TTL4)
;TTL channel depends on specific spectrometer and needs to be adjusted
;pulse program uses explicit channel addressing
;
;initial rotation speed TTL-controlled (d50/d51/l11), then delay d2 with rotation before acquisition.
;
;Fabian Hoffmann, Karel Kouril, Stefan T. Berger, Benno Meier, Burkhard Luy,
;Macromolecules, submitted (2023).
;
;$CLASS=HighRes
;$DIM=2D
;$TYPE=
;$SUBTYPE=
;$COMMENT=


#include <Avance.incl>
#include <De.incl>
#include <Sysconf.incl>


"d11=30m"

"acqt0=-p1*2/3.1416"

"l11=((d2+d2+p2+aq)/(d50+d51))-0.5"

"in0=inf1/2"


1 ze
  d11 LOCKDEC_ON
  d11 H2_PULSE

2 30m
3 200m
  d1
  p1:D ph1
  d0
  p2:D ph1
  d0
```

```
  exec_on_chan:f1
  d2
  p2:D ph1
  d2
  ACQ_START(ph30,ph31)
  aq DWELL_GEN:f1
  exec_enable

  exec_on_other
5 d51 TTL4_LOW
  d50 TTL4_HIGH
  lo to 5 times l11
  exec_wait

  10u
  rcyc=2
  30m mc #0 to 2 F1QF(caldel(d0, +in0))

  d11 H2_LOCK
  d11 LOCKDEC_OFF
exit


ph1=0 2 2 0 1 3 3 1
ph2=0 2 2 0 1 3 3 1
ph3=2 0 0 2 3 1 1 3
ph30=0
ph31=0 2 2 0 1 3 3 1


;pl1 : f1 channel - power level for pulse (default)
;p1 : f1 channel -  90 degree high power pulse
;d11: delay for disk I/O                             [30 msec]
;d1 : relaxation delay with rotation of
;d2 : half delay between switching off rotation and acquisition
;d50 : TTL4_HIGH 5V blanking delay [700u]
;d51 : TTL4_LOW  0V unblanking delay [300u]
;ns: 1 * n

;locnuc: off



;$Id: rheo2h2Djres,v 3.2 2022/10/31 17:49:26 bulu Exp $
```

6.4 Python scripts

The Python scripts are written for the Bruker Topspin Python API and directly take the data out of Topspin and can manipulate data in TopSpin (e.g. processing via Python in TopSpin).

6.4.1 RDCs of CH groups with Bruker Topspin Python API

```
#
# Bruker Python program to calculate RDCs with the CLIP/CLAP approach
# Using crosscorrelation between the subtracted and added CLIP/CLAP 1Ds
# External information needed
# Fabian Hoffmann 10.10.2023
#
from bruker.api.topspin import Topspin
from bruker.data.nmr  import *
from bruker.publish.plot import *

from datetime import datetime

from matplotlib import pyplot as plt
import numpy as np
import re
import sys
import tkinter as tk
#____________________________________________________________

#____________________________________________________________
top = Topspin()
dp = top.getDataProvider()

# get the instance of NMR Data set
folder = "E:/Fabian/NMRDATA/Ernst/250113_PBLG_Strychnin"
CLIP = folder + "/56/pdata/476"
CLAP = folder + "/59/pdata/476"
clip = dp.getNMRData(CLIP)
clap = dp.getNMRData(CLAP)

res = clip.getSpecDataPoints()
res2 = clap.getSpecDataPoints()

if res.get(EXCEPTION):
    print('Error␣:',res.get(EXCEPTION).details())
    exit(-1)

if res2.get(EXCEPTION):
    print('Error␣:',res2.get(EXCEPTION).details())
    exit(-1)
#____________________________________________________________
```

```
#__________________________________________________________
# controls if the correct CLIP 1D slice is open
proton = dp.getCurrentDatasetIdentifier()
if proton != CLIP:
    print('Error:␣open␣CLIP␣1D␣slice␣first')
    exit(-1)
#__________________________________________________________

#__________________________________________________________
#gets the information of the current open dataset
curdat = top.getDataProvider().getCurrentDataset()
SI = int(curdat.getPar("SI"))
SWH = int(float(curdat.getPar("SWH")))
HZpPT = SWH/SI
top.executeCommand("sino")

def linewidth(i):
        max2 = numpy.max(i)
        indexmax2=numpy.argmax(i)
        error_list=numpy.argwhere(i>=max2*0.5)
        error_left=error_list[0]
        error_right=error_list[-1]
        linewidth = (error_right-error_left)*HZpPT
        linewidth = float(linewidth)
        return linewidth
#__________________________________________________________

#__________________________________________________________
# request sino values in external field
root = tk.Tk()

label3 = tk.Label(root, text="sino").grid(row=0)

sino = tk.Entry(root)

sino.grid(row=0, column=1)
schaltf1 = tk.Button(
     root, text="Enter", command=root.quit
     ).grid(row=3, column=0, pady=4)

root.mainloop()
#__________________________________________________________

#__________________________________________________________
# get the complete FID and Spectrum (Real,Imaginary)
startTime = datetime.now()

rawData  = clip.getRawDataPoints()
```

```
rawData2   = clap.getRawDataPoints()

specData = clip.getSpecDataPoints()
if specData.get(EXCEPTION):
    print('Error␣:',specData.get(EXCEPTION).details())
    exit(-1)

specData2 = clap.getSpecDataPoints()
if specData2.get(EXCEPTION):
    print('Error␣:',specData2.get(EXCEPTION).details())
    exit(-1)

imagData = clip.getSpecDataPoints(component= PROCDATA_IMAG)
imagData2 = clap.getSpecDataPoints(component= PROCDATA_IMAG)

endTime = datetime.now()
print("Elapsed␣Time␣(3␣component␣read):" + str(endTime - startTime))
#____________________________________________________________

#____________________________________________________________
#Calculate sum and substraction
data = specData['dataPoints']
data2 = specData2['dataPoints']
data3 = []
for i in range(len(data)):
    data3.append(data[i] + data2[i])
specData3 = specData.copy()
specData3['dataPoints'] = data3

data4 = []
for i in range(len(data)):
    data4.append(data[i] - data2[i])
specData4 = specData.copy()
specData4['dataPoints'] = data4
#____________________________________________________________

#____________________________________________________________
# plot crosscorrelation
fig = plt.figure()
ax1 = fig.add_subplot(211)

# crosscorrelation of addition and substraction
ccf = ax1.xcorr(
     specData3['dataPoints'],specData4['dataPoints'],usevlines=False,
     maxlags=(SI-1), normed=True, lw=2
     )
ax1.grid(True)
ax1.axhline(0, color='blue', lw=2)
#____________________________________________________________
```

```
#____________________________________________________________
max = numpy.max(ccf[1])    # maximum of crosscorrelation function
indexmax=numpy.argmax(ccf[1])    # index of the maximum
T = (SI-indexmax)*HZpPT    # your total coupling in Hz
cnst = 4    # cnst for sino and linewidth correlation. Modify if necessary
sino = float(sino.get())
error = linewidth(data2)/(sino*cnst)    # error calculation for total coupling
print('your␣total␣coupling␣T␣is', T, '+/-', error)

#important to be before the final tk root.
#Otherwise the plot will not be shown
plt.show()
#____________________________________________________________

#____________________________________________________________
root = tk.Tk() #will be shown as soon as the plot is closed
coupling = 'Your␣total␣coupling␣T␣is', T, '+/-', error
label = tk.Label(root, text=coupling)
label.pack()
root.mainloop()
```

6.4.2 RDCs of CH_2 groups with Bruker Topspin Python API

```
#
# Bruker Python program to calculate RDCs with the CLIP/CLAP approach
# Using crosscorrelation between the subtracted and added CLIP/CLAP 1Ds
# External information needed
# Fabian Hoffmann 10.10.2023
#
from bruker.api.topspin import Topspin
from bruker.data.nmr import *
from bruker.publish.plot import *

from datetime import datetime

from matplotlib import pyplot as plt
import numpy as np
import re
import sys
import tkinter as tk
#____________________________________________________________

#____________________________________________________________
dp = top.getDataProvider()

# get the instance of NMR Data set
folder = "E:/Fabian/NMRDATA/Ernst/250113_PBLG_Strychnin"
CLIP = folder + "/56/pdata/1127"
```

```
CLAP = folder + "/59/pdata/1127"
clip = dp.getNMRData(CLIP)
clap = dp.getNMRData(CLAP)

res = clip.getSpecDataPoints()
res2 = clap.getSpecDataPoints()

if res.get(EXCEPTION):
    print('Error␣:',res.get(EXCEPTION).details())
    exit(-1)

if res2.get(EXCEPTION):
    print('Error␣:',res2.get(EXCEPTION).details())
    exit(-1)
#___________________________________________________________

#___________________________________________________________
# controls if the correct CLIP 1D slice is open
proton = dp.getCurrentDatasetIdentifier()
if proton != CLIP:
    print('Error:␣open␣CLIP␣1D␣slice␣first')
    exit(-1)
#___________________________________________________________

#___________________________________________________________
#gets the information of the current open dataset
curdat = top.getDataProvider().getCurrentDataset()
SI = int(curdat.getPar("SI"))
SWH = int(curdat.getPar("SWH"))
HZpPT = SWH/SI
top.executeCommand("sino")

def linewidth(i):
        max2 = numpy.max(i)
        indexmax2=numpy.argmax(i)
        error_list=numpy.argwhere(i>=max2*0.5)
        error_left=error_list[0]
        error_right=error_list[-1]
        linewidth = (error_right-error_left)*HZpPT
        linewidth = float(linewidth)
        return linewidth
#___________________________________________________________

#___________________________________________________________
# request sino values in external field
root = tk.Tk()

label1 = tk.Label(root, text="ppm␣left").grid(row=0)
label2 = tk.Label(root, text="ppm␣right").grid(row=1)
```

```
label3 = tk.Label(root, text="sino").grid(row=2)

sino = tk.Entry(root)
leftppm = tk.Entry(root)
rightppm = tk.Entry(root)

leftppm.grid(row=0, column=1)
rightppm.grid(row=1, column=1)
sino.grid(row=2, column=1)
schaltf1 = tk.Button(
      root, text="Enter", command=root.quit
      ).grid(row=4, column=0, pady=4)

root.mainloop()
#___________________________________________________________

#___________________________________________________________
# get the complete FID and Spectrum (Real,Imaginary)
startTime = datetime.now()

left = float(leftppm.get())
right = float(rightppm.get())

rawData  = clip.getRawDataPoints()
rawData2  = clap.getRawDataPoints()

specData = clip.getSpecDataPoints(physRange = [PhysicalRange(right,left)])
if specData.get(EXCEPTION):
     print('Error␣:',specData.get(EXCEPTION).details())
     exit(-1)

specData2 = clap.getSpecDataPoints(physRange = [PhysicalRange(right,left)])
if specData2.get(EXCEPTION):
     print('Error␣:',specData2.get(EXCEPTION).details())
     exit(-1)

imagData = clip.getSpecDataPoints(component= PROCDATA_IMAG)
imagData2 = clap.getSpecDataPoints(component= PROCDATA_IMAG)

endTime = datetime.now()
print("Elapsed␣Time␣(3␣component␣read):" + str(endTime - startTime))
#___________________________________________________________

#___________________________________________________________
#Calculate sum and substraction
data1 = specData['dataPoints']
data2 = specData2['dataPoints']
data3 = []
for i in range(len(data1)):
```

```
    data3.append(data1[i] + data2[i])
specData3 = specData.copy()
specData3['dataPoints'] = data3

data4 = []
for i in range(len(data1)):
    data4.append(data1[i] - data2[i])
specData4 = specData.copy()
specData4['dataPoints'] = data4
points = len(data1)-1 #the number of points used in the given physicalRange
#_____________________________________________________________

#_____________________________________________________________
# plot crosscorrelation
fig = plt.figure()
ax1 = fig.add_subplot(211)

# crosscorrelation of addition and substraction
ccf = ax1.xcorr(
      specData3['dataPoints'],specData4['dataPoints'],usevlines=False,
      maxlags=points, normed=True, lw=2
      )
ax1.grid(True)
ax1.axhline(0, color='blue', lw=2)
#_____________________________________________________________

#_____________________________________________________________
# calculate total coupling
max = numpy.max(ccf[1])    # maximum of crosscorrelation function
indexmax=numpy.argmax(ccf[1])    # index of the maximum
T = (points-indexmax)*HZpPT     # your total coupling in Hz
cnst = 4    # cnst for sino and linewidth correlation. Modify if necessary
sino = float(sino.get())
error = linewidth(data2)/(sino*cnst)  # error calculation for total coupling
print('your␣total␣coupling␣T␣is', T, '+/-', error)

#important to be before the final tk root.
#Otherwise the plot will not be shown
plt.show()
#_____________________________________________________________

#_____________________________________________________________
root = tk.Tk() #will be shown as soon as the plot is closed
coupling = 'Your␣total␣coupling␣T␣is', T, '+/-', error
label = tk.Label(root, text=coupling)
label.pack()
root.mainloop()
```